Clip-off Chemistry Applied to the Synthesis of Rh(II)-based Complexes via Rational Cleavage of Metal-Organic-Polyhedra

Anna Broto Ribas

UAB
Universitat Autònoma de Barcelona

Clip-off Chemistry Applied to the Synthesis of Rh(II)-based Complexes via Rational Cleavage of Metal-Organic-Polyhedra

Anna Broto Ribas

Doctoral Thesis

PhD in Chemistry

Supervisors:

Dr. Inhar Imaz

Prof. Dr. Daniel Maspoch

Catalan Institute of Nanoscience and Nanotechnology (ICN2)

Autonomous University of Barcelona

Department of Chemistry – Faculty of Sciences

2023

Memòria presentada per aspirar al Grau de Doctor per Anna Broto Ribas

Anna Broto Ribas

Vist i plau

Prof. Dr. Daniel Maspoch

ICREA Research Professor & Group Leader

Supramolecular Nanochemistry & Materials Group

Catalan Institute of Nanoscience and Nanotechnology

Autonomous University of Barcelona

Dr. Inhar Imaz

Senior Researcher &Division Coordinator

Supramolecular Nanochemistry & Materials Group

Catalan Institute of Nanoscience and Nanotechnology

Autonomous University of Barcelona

Bellaterra, 27 de juliol del 2023

Table of contents

Abstract

Innovations in chemical synthesis have historically led to the discovery of new materials and molecules. Each new reaction and methodology not only expand the accessible chemical space but also inspires researchers to explore novel ways of thinking and further innovate in the iterative design and preparation of new chemical targets. The most common synthetic approaches involve bottom-up strategies, where bonds link atoms or molecules to form larger compounds. In this Thesis, our aim is to explore a new approach to develop a novel synthetic methodology called Clip-off Chemistry. This new synthetic strategy aims to generate new materials and molecules by selectively and rationally cleaving covalent bonds in reticular materials, providing precise spatial control over the final structure. This controllable bond cleavage occurs at the molecular level through the ozonolysis of alkene bonds. Within this Thesis, our focus is to show the synthesis of the first products made using "Clip-off Chemistry"; herein, through the cleavage of Rh_2-Metal-Organic Polyhedra (MOPs), releasing coordination compounds that would otherwise be inaccessible by direct synthesis.

Chapter 1 briefly explains the basic concepts of reticular materials and their evolution throughout history. This chapter also offers a review of reported destructive synthetic strategies applied to reticular materials. Afterwards, Chapter 2 introduces the objectives of this Thesis.

Chapter 3 focuses on the first example of synthesis using "Clip-off Chemistry". As a proof of concept, we have synthesized an homoleptic Rh_2-MOP with olefinic bonds in known crystallographic positions and cleaved it in half, resulting in two Rh_2-clusters fully functionalized with aldehyde groups.

In Chapter 4, we have successfully synthesized a family of 12 heteroleptic trigonal antiprismatic Rh_2-MOPs to expand the catalogue of Clip-off starting materials. We have discovered that depending on the combination of complementary ligands, two possible heteroleptic cage isomers can be assembled. Moreover, all these MOPs exhibit microporosity in the solid state, further expanding the limited list of porous cages.

In Chapter 5, we have synthesized a triangular Rh_2-macrocycle by cleaving one of the heteroleptic trigonal antiprismatic Rh_2-MOPs from Chapter 4 in half. We have optimized the reaction conditions to obtain the fully functionalized triangular Rh_2-macrocycle with carboxylic acid groups.

Finally, in Chapter 6, we have successfully synthesized a *cis*-Rh_2-cluster through the Clip-off cleavage of a trigonal antiprismatic Rh_2-MOP with olefinic bonds in both of its ligands. First, starting conceptually from one of the previously reported trigonal antiprismatic Rh_2-MOPs, we have synthesized a new trigonal antiprismatic Rh_2-MOP with two ligands containing olefinic bonds using reticular chemistry. Then, we have cleaved this new MOP resulting in the expected *cis*-Rh_2-cluster fully functionalized with aldehyde groups.

Resum

Les innovacions en mètodes sintètics han permès, al llarg de la història, descobrir nous materials i molècules. Cada nova reacció o metodologia sintètica no només ajuda a expandir el catàleg de materials i molècules sinó que també inspira noves maneres de pensar i innovar en estratègies sintètiques. Avui en dia, els mètodes sintètics més comuns consisteixen en la formació d'enllaços creant estructures més grans i complexes a partir d'unitats més petites. L'objectiu d'aquesta Tesi és explorar una nova metodologia sintètica anomenada "Clip-off-Chemistry". Aquest nou mètode sintètic consisteix a generar nous materials i molècules a través del trencament selectiu i racional d'enllaços covalents d'un material reticular proporcionant un control espacial precís de l'estructura final. Aquest trencament controlat d'enllaços es dona a escala molecular a través de l'ozonólisi d'enllaços dobles. En aquesta Tesi hem dut a terme la síntesi dels primers productes per "Clip-off Chemistry". Concretament ens hem centrat en el trencament de poliedres metal·loorgànics (MOPs) alliberant diversos compostos de coordinació.

En el Capítol 1 s'expliquen breument els conceptes bàsics de materials reticulars i la seva evolució a través de la història. Aquest capítol també ofereix un resum de l'estat actual de les estratègies destructives en materials reticulars. Posteriorment, en el Capítol 2 s'introdueixen els objectius de la Tesi.

En el Capítol 3 es detalla el primer exemple de síntesi utilitzant la "Clip-off Chemistry". Com a prova del concepte, s'ha sintetitzat un Rh_2-MOP homolèptic amb enllaços dobles en posicions cristal·logràfiques conegudes i s'ha trencat per la meitat alliberant dos Rh_2-clústers totalment funcionalitzats amb grups aldehids.

En el Capítol 4 es detalla la síntesi d'una família de 12 Rh_2-MOPs heterolèptics amb geometria d'antiprisma trigonal per tal d'expandir el catàleg de materials disponibles per a ser usats com a precursors en la "Clip-off-Chemistry". S'ha descobert que, depenent de la combinació de lligands complementaris, es poden formar dos possibles isòmers de caixes heterolèptiques. A més a més, tots aquests MOPs són microporosos en l'estat sòlid allargant així la curta llista de caixes poroses reportades.

En el Capítol 5 s'ha detallat la síntesi d'un macrocicle trigonal de rodi trencant per la meitat un dels MOPs amb geometria d'antiprisma trigonal del Capítol 4. S'han optimitzat les condicions de reacció fins a aconseguir el macrocicle completament funcionalitzat amb grups àcid carboxílic.

Finalment, el Capítol 6 consta de la síntesi d'un *cis*-Rh_2-clúster mitjançant el trencament d'un MOP amb geometria d'antiprisma trigonal amb dobles enllaços en els dos lligands. Primer, començant conceptualment per un dels MOPs amb geometria d'antiprisma trigonal prèviament reportats, es va sintetitzar un nou MOP amb la mateixa geometria però format per dos lligands que contenien dobles enllaços. Seguidament, es va trencar aquest MOP alliberant un *cis*-Rh_2-clúster totalment funcionalitzat amb grups aldehid.

Acknowledgements

Primer de tot voldria agrair al Prof. Daniel Maspoch l'haver-me donat l'oportunitat de realitzar la meva Tesi doctoral sota la seva supervisió. NanoUp és, sens dubte, un dels millors grups on hagués pogut dur a terme la Tesi tant per la novetat i la bellesa de les idees com pels mitjans per dur-les a terme. Em sento molt afortunada d'haver tingut aquesta sort. Voldria agrair-li també haver-me allargat el contracte quan el finançament de GÈNESIS es va acabar i haver-me donat l'oportunitat de participar en diversos congressos.

M'agradaria donar les gràcies al Dr. Inhar Imaz per ser el meu director de Tesi. Voldria donar-li les gràcies per proposar-me tants projectes paral·lels a GÈNESIS a l'inici de la Tesi, per la llibertat que m'ha donat durant tot el seu transcurs, per proporcionar-me múltiples estructures per resoldre durant el confinament, per donar-me l'oportunitat d'anar tants cops al sincrotró, per explicar-me com podia millorar *abstractes* i *papers* sense fer-ho ell, per ensenyar-me a valorar i explicar la novetat d'idees i projectes, per confiar cegament en mi i per no dubtar mai de la meva capacitat per aconseguir els objectius, però sobretot, pel seu recolzament constant i per fer-me costat durant els moments més complicats d'aquesta Tesi.

M'agradaria donar les gràcies a totes les persones amb qui he compartit laboratori i/o oficina durant els anys que he passat a NanoUp. Totes i cada una d'elles han influït en mi d'una manera o altra. I particularly wish to thank Ceren, Luis Carlos, and Civan for their support, advice, and help at the beginning of this Thesis. I would also like to thank Najmeh for her strong energy and sense of humour. I really enjoyed sharing the office with you. I want to express my gratitude to Yang for his kindness and always being available to lend a helping hand. També voldria agrair a l'Arnau i el Troyano el seu sentit de l'humor i les seves curioses converses que van fer que els meus inicis a NanoUp no fossin gens avorrits. Voldria agrair sobretot a l'Arnau les

nostres converses esporàdiques sobre PIMs a l'inici de la Tesi i, més tard, la seva guia i consell durant les meves primeres síntesis de Rh_2-MOPs. També m'agradaria agrair-li el fet que mai em posés problemes per utilitzar el rodi. Special thanks to my PhD brothers Borja and Yunhui, with whom I have shared the biggest part of my PhD journey. Voldria donar les gràcies al José per tots els BETs que m'ha mesurat i per respectar sempre l'ordre de la cua de mostres. Sense ell no crec que hagués estat possible la síntesi de PIMs porosos. També m'agradaria agrair a la Thais per ensenyar-me múltiples mètodes i trucs per cristal·litzar. Aprecio molt el coneixement que em va transmetre. I would like to express my gratitude to Cornelia, whose arrival gave me new energy. I really appreciate our scientific discussions as well as your positive and energetic character. I want to extend my gratitude to Sofia and Michele because, despite their brief stay with us, I will never forget Sofia's incredible personality and Michele's goodness and kindness. You both helped make enjoyable my last months in the laboratory regardless of the pressure. M'agradaria dona les gràcies a la Sara per acabar el projecte i al Jorge per ajudar-la. Thank also to the more recent incorporations: Marcel, Kornel, Roberto, Lingxin and Javier. I have good memories with all of you. I want to specifically thank Lingxin for his support, our basketball games, and our conversations during my writing breaks. También me gustaría agradecer a Javier por valorarme como científica y como persona desde el momento en que llego, por explicarme sus brillantes ideas y sus proyectos cuando yo ya no podía hacer los míos, por todo el tiempo que hemos pasado juntos este último año, por su felicidad intrínseca, por su apoyo infinito y, sobre todo, por nuestra amistad.

També voldria dona les gràcies a totes les persones de la UAB, ICN2, sincrotró, UB i ICMM que han contribuït d'alguna manera al treball científic d'aquesta Tesi. M'agradaria dona les gràcies concretament a l'Oscar Palacios, la Judith Juanhuix, la Irene Fernández, el Marcos Rosado, la Jessica Padilla,

el Felipe Gándara, el Pau Nolis, el Teodor Parella i l'Eva Monteagudo. Especialment voldria agrair a l'Oscar Palacios del servei d'anàlisi química de la UAB i a la Irene Fernández del servei d'anàlisi química de la UB per l'esforç i la cura amb què han analitzat les meves mostres, a la Judith Juanhuix per totes les hores que ha passat ajudant-nos al sincrotró ALBA, al Felipe Gándara per la seva rapidesa en mesurar i resoldre els cristalls que li enviava, i a l'Eva Monteagudo del servei de NMR de la UAB per la seva amabilitat i per resoldre els múltiples problemes tècnics que he tingut. També m'agradaria agrair a l'Elena Jiménez la seva ajuda en els tràmits per al dipòsit de la tesi.

Voldria agrair als professors que m'han donat l'oportunitat de fer classes a la UAB durant aquest últim any i també a tots els professors i alumnes amb qui he compartit assignatures teòriques o laboratoris. Tots i cada un d'ells han fet que hagi gaudit molt de la meva primera experiència com a professora.

M'agradaria agrair als meus amics: la Bero, l'Helena, l'Emma, l'Albert, el Manrique, el Bernat, la Marta, l'Andrea, l'Aragó, el Marc, l'Àlex, el Jordi i el David per ser els meus amics. M'agradaria agrair especialment a l'Helena, l'Emma i l'Aragó que compartissin amb mi els sentiments i vivències experimentats durant les seves respectives Tesis. Voldria agrair a l'Helena i l'Emma tots els Skypes i els viatges que hem fet durant aquest període, a l'Aragó les múltiples quedades a l'inici de la Tesi, a la Bero els sopars, cines, vins i sortides, a l'Andrea, el Manrique i l'Albert que es riguessin de mi, de les situacions que estava vivint i de tot i de tothom en general i al Bernat, la Marta, el Manrique, l'Albert i l'Aragó per cada tarda i nit de jocs de taula que hem fet durant aquest període. Finalment, m'agradaria donar les gràcies amb especial èmfasi AL Marc amb qui he compartit despatx els últims mesos d'escriptura. Gràcies per estar allà cada dia i pel teu suport. Sense tu el final d'aquesta Tesi no hauria estat el mateix.

Per acabar, m'agradaria donar les gràcies a la meva família per haver-me acompanyat i donat suport durant tota la meva vida.

Chapter 1

Introduction to reticular materials and their synthesis through synthetic “destructive” strategies

1.1 Introduction: Materials through history

The development of materials by civilizations has been intimately connected to the improvement of their people's quality of life. For that reason, the earlier stages of human history were named after the predominant material used for their tools: stone, bronze, and iron ages. Ancient tribes made use of matter found in their environments, such as wood, rock, soil, and animal tissues. The discovery of fire allowed the heating and shaping of metals such as gold and copper. The use of copper became very frequent due to its plasticity and its ability to be melted but it was too soft for many applications. Around 3000 BCE, mixtures of copper with other metals were done, forming alloys with higher hardness, which were called bronze. Later came the development of glass, paper, other metal alloys and plastics pushing the progress of civilizations.

Until the latter half of the eighteen century, the discovery and improvement of new materials were done thanks to macroscopic empirical observations (naked eye observations). Due to the accumulated empirical knowledge about chemical substances and operations from medicine, metallurgy and alchemy, the understanding of materials and substances on a microscopic or nanoscopic scale was possible, and with it, the development of modern chemistry.[1] In chemistry, it is widely accepted that the structures of molecules and materials determine their properties. As suggested in the famous Feynman citation *“I can hardly doubt that when we have some control of the arrangement of things on a small scale we will get an enormously greater range of possible properties that substances can have, and of different things that we can do“*,[2] understanding and controlling the arrangement of atoms in molecules and materials make possible the precise design and prediction of physical and chemical properties.

The development of X-ray crystallography marked a significant advancement in structural determination, enabling the definitive characterization of molecules and materials, and facilitating the correlation between form and function. X-ray diffraction is a characterization technique in which an incident X-ray beam collides with a crystalline structure, causing it to diffract in many different directions. A three-dimensional picture of the density of electrons inside the crystal can be determined from the angles and intensities of these diffracted beams. This electron density map can be used to determine the precise locations of the atoms inside the crystal. The accumulation of data on structure-property relationships enabled the imagination and design of new molecules and materials with an expected concrete function. When envisioning a new molecule or material, the need arises to construct it from basic starting materials or molecules. A reaction pathway for the desired compound is first designed, then executed and optimized, transforming chemists into architects and builders. This series of operations is highly refined in organic chemistry, enabling the design and synthesis of any feasible molecule. Conversely, the rational chemical synthesis of metal complexes is less developed due to the ability of metal ions to adopt various coordination numbers and geometries, which introduces uncertainty. Additionally, the relatively lower stability of metal complexes limits the step-by-step synthetic approach commonly employed in organic compounds, thereby introducing a significant trial-and-error component to metal-organic chemistry.

1.2 Reticular Materials

Reticular chemistry is an example that perfectly illustrates the precise design and synthesis of metal-organic compounds. Reticular chemistry is based on the precise arrangement of molecular building blocks with predefined geometries to create periodic crystalline extended networks. The formation of crystalline structures is possible thanks to the reversibility of the

bonds formed between building blocks. The incessant formation and cleavage of bonds allow structural defects to be fixed forming crystalline structures.

The development of reticular chemistry began in 1989, when Hoskins and Robson proposed the deliberate design and construction of three-dimensional infinite metal-organic structures through the union of the appropriate building blocks.[3] There are two parameters to be considered when linking molecules: (1) the type and directionality of interactions used in such linkages; and (2) the geometry of the molecular building units; length, size, and angles between binding sites. Prof. Hoskins and Prof. Robson pioneered the field of network rational design inspired by Prof. Wells[4] and its conceptual simplification of crystals as nets constructed from nodes and links. They constructed scaffolding-like materials by connecting centres with tetrahedral or octahedral geometries through rod-like connecting units. They synthesized the first periodic 3D framework binding tetrahedral Cu(I) centres with tetrahedral tetra(4-cyanophenyl)methane ligands (Figure 1.1a).[5] In 1995, Prof. Yaghi published another 3D network built by the linkage of trigonal planar Cu(I) centres with lineal 4,4'-bipyridine ligands, introducing for the first time the term Metal-Organic-Framework (MOF) to describe a 3D Metal-Organic Network (Figure 1.1b).[6]

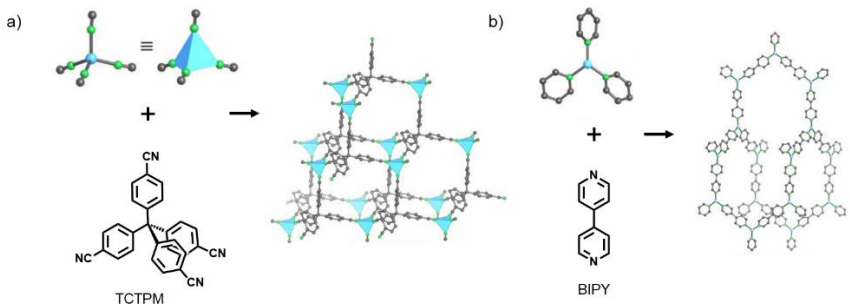

Figure 1.1. (a) Periodic 3D framework formed by binding tetrahedral Cu^+ centres with tetrahedral tetra(4-cyanophenyl)methane ligands. (b) 3D network built by the linkage of trigonal planar Cu^+ centres with lineal 4,4'-bipyridine ligands. Image adapted with permission from reference 7. Copyright 2019 John Wiley and Sons.

After these first examples, several 3D networks constructed by building blocks with defined geometries linked each other by coordinative bonds between metals and N-donor ligands were reported.[8–10] These initial reported MOFs were characterized by their lack of stability due to the fragile nature of the coordination bonds formed between single metal cations and N-donor monodentate ligands. Additionally, they did not exhibit permanent microporosity, as the removal of guest molecules from their pores resulted in the collapse of their flexible structures. In 1998, Prof. Yaghi and co-workers synthesized the first permanent microporous MOF, named MOF-2. MOF-2 is constructed by connecting dinuclear Zn^{2+} paddlewheel clusters with ditopic 1,4-benzenedicarboxylate (BDC) ligands forming a two-dimensional framework (Figure 1.2).[11] Permanent microporosity was possible thanks to the introduction of carboxylate ligands. These ligands coordinate to multiple metal centres, forming poly-nuclear metal clusters. The incorporation of charged chelating ligands enhanced the bond strength between metals and ligands, thereby improving the stability of the network. Additionally, the use of polycarboxylate ligands allowed the formation of neutral frameworks, as the charge on the ligand could balance the charge of the cationic metals, eliminating the need for counter ions to fill the pores. This property increased the stability of the frameworks allowing the removal of all solvent molecules from the pores, without collapsing the reticular material structure and creating permanent microporosity. The creation of MOF-2 played a crucial role on the development of reticular chemistry, as it showed that poly-nuclear clusters serve as perfect building blocks for rational design as they are rigid, stable and have defined geometries. This resulted in the creation of an extensive variety of carboxylate-based MOFs. Most of these MOFs were permanently porous making them attractive for applications such as gas storage, gas separation, water adsorption and catalysis.

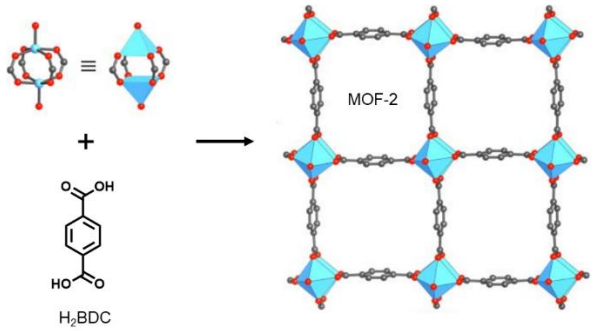

Figure 1.2. Representation of the structure of MOF-2. Dinuclear Zn^{2+} paddlewheel SBUs are linked by ditopic BDC ligands forming a two-dimensional extended structure. All hydrogen atoms are omitted for clarity. Colour code: Zn, blue; N, green; C, grey; O, red. Image adapted with permission from reference 7. Copyright 2019 John Wiley and Sons.

The vast number of newly published MOFs in only few years, resulting from the infinite combinations of metal clusters and organic ligands, gave rise to the need for rationalizing their structures. To simplify the analysis and design of MOFs, Prof. Yaghi and colleagues introduced the concept of Secondary Building Units (SBUs). SBUs serve as a conceptual simplification of metal cluster building blocks, providing information about the binding sites and their directionalities within the metal clusters. SBUs can be employed to analyse and understand three-dimensional networks from a geometric perspective, as well as to facilitate the design of novel networks.

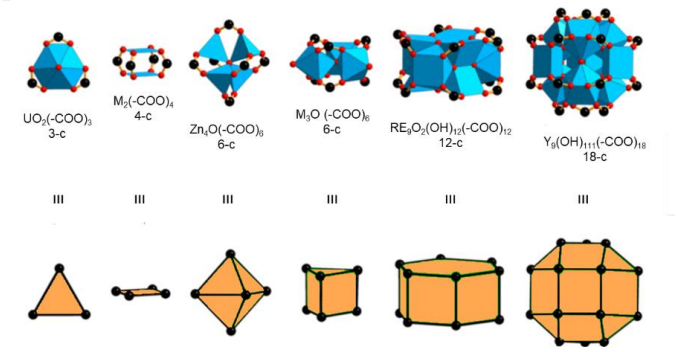

Figure 1.3. Some examples of secondary building units (SBUs). Image adapted with permission from reference 12. Copyright 2020 Springer Nature.

The SBU approach has significantly facilitated the design of reticular materials, contributing to the consolidation of reticular chemistry as a field (Figure 1.3). The combination of SBUs and ligands that have not been previously mixed together allows the creation of entirely new frameworks. Additionally, existing frameworks can be conceptually modified by systematically varying pore size or functionality. For instance, in a given structure, if the distance between SBUs is increased by substituting the ligands with larger analogues (ligands with the same angle between binding sites but larger in size), the structural geometry of the framework remains unchanged while the pore size increases, resulting in a "reticular expansion" (Figure 1.4). The pioneering work by Prof. Yaghi introduced the first examples of such reticular synthesis, where sixteen isoreticular frameworks (named IRMOFs) were designed and synthesized.[13] This work suggests that, once the necessary synthetic conditions for the *in situ* generation of the SBU are identified, it becomes feasible to tune the functionalities and dimensions of the network. This approach opened up possibilities for tailored reticular materials with desired properties.

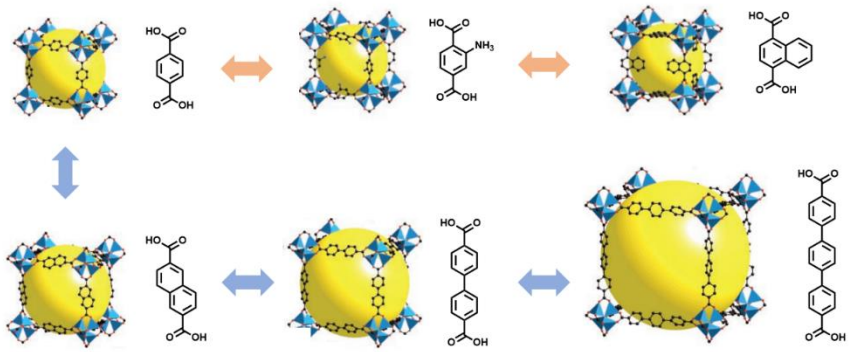

Figure 1.4. Schematic representation of IRMOF series obtained through isoreticular chemistry, by functionalization (orange) or expansion (blue).

In 2005, the concept of reticular synthesis was extended to the field of organic chemistry. Prior to this, organic chemistry was primarily focused on synthesizing individual molecules and polymers. With the reticular synthetic strategy, it became possible to create the first crystalline and porous organic two-dimensional and three-dimensional extended structures.[14] The idea of constructing crystalline infinite extended structures using molecular building blocks with predefined geometries linked using reversible bonds was applied to synthesize crystalline organic networks. Instead of combining metal SBUs with carboxylate organic ligands through coordination bonds, researchers began combining one or two types of organic ligands with reactive functionalities. These ligands contained functional groups capable of undergoing reversible reactions with themselves in the case of homoleptic systems or with each other in the case of heteroleptic systems (Figure 1.5). These reactions resulted in the formation of covalent two-dimensional or three-dimensional crystalline extended materials, which are known as Covalent Organic Frameworks (COFs). Similar to MOFs, COFs exhibit permanent porosity, allowing for potential applications in areas such as gas storage, separation, and catalysis.

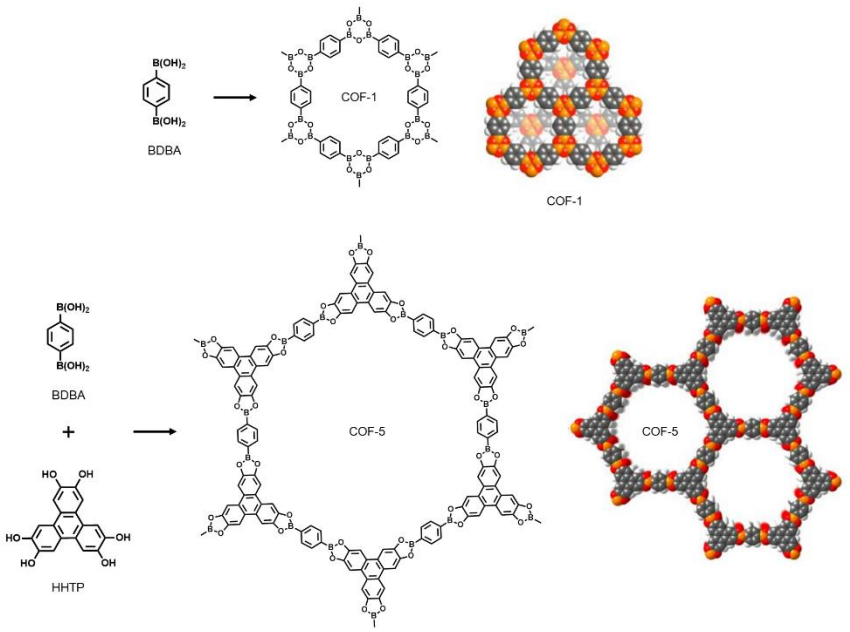

Figure 1.5. Scheme of the formation of two of the first examples of covalent organic frameworks. The formation of boronate ester linkages between BDBA leads to COF-1 (top), whereas the formation of boronate ester linkages between BDBA and HHTP leads to COF-5 (bottom). Colour code: B, orange; O, red: C, grey; H, white.[14] Image adapted with permission from reference 7. Copyright 2019 John Wiley and Sons.

The current consensus is that reticular materials are extended two-dimensional or three-dimensional crystalline structures formed by connecting molecular building blocks through strong bonds. However, if one or more building blocks has a bend angle between binding sites, their linkage can create a closed or a caged structure. Therefore, the concept of reticular synthesis can also be applied to create discrete zero-dimensional compounds known as Metal-Organic Polyhedra (MOPs). MOPs are molecular cages built by the self-assembly of organic polycarboxylate ligands and metal ions through coordination bonds (Figure 1.6). MOPs can also be viewed as "isolated MOF pores" having both the properties of permanent porous solids and molecular compounds. Their molecular nature confers them with

solubility in various solvents, which facilitates their liquid processability,[15,16] their use in the liquid phase for recognition and transport of molecules,[17,18] and the stoichiometric control over post-synthetic functionalizations.[19,20]

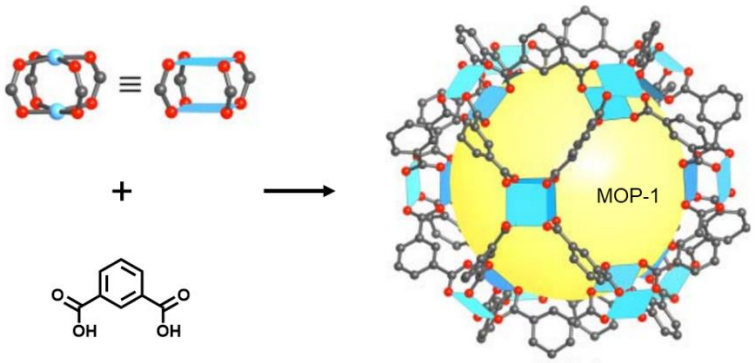

Figure 1.6. Schematic representation of the formation of MOP-1. MOP-1 is built from $Cu_2(–COO)_4$ paddlewheel SBUs and bent m-H_2BDC ligands.[21] All hydrogen atoms are omitted for clarity. Color code: Cu, blue; O, red; C, gray. Image adapted with permission from reference 7. Copyright 2019 John Wiley and Sons.

1.3 Introduction to material “destructive techniques”: Ancient and novel chemical etching processes to make materials

In modern times, the most common strategies to obtain the desired molecules or materials involve constructive strategies where several compounds are linked forming larger and more complex products. However, in earlier cultures, the strategies to develop materials were based on the controlled destruction of existing ones. Ancient tribes, lacking the knowledge and skills to synthesize new materials, had to rely on cutting, shaping, carving, or polishing naturally occurring materials such as wood, rocks, and animal tissues to acquire the desired tools or clothing.

Even with the advent of novel materials like metals, metal alloys, and glass, destructive strategies continued to be employed for engraving or shaping them. Ancient artisans used techniques such as etching, which involved engraving complex patterns onto metal or glass surfaces using

methods that could be considered destructive by today's standards. These techniques allowed them to create intricate designs and decorative elements on these materials.

Chemical etching is the process of using strong acids or corrosive fluids to destroy the unprotected parts of a metal surface creating a design incised in the material. In traditional etching, a metal plate of copper, zinc, or steel is first coated with a layer of wax or another protective substance. Then, a needle or a similar tool is used to scratch off the wax, exposing certain areas of the metal surface. Once the desired design is created, the plate is immersed in a bath of acid. The acid reacts with the plate and corrodes the exposed metal, oxidizing it and creating recessed areas. The depth of the resulting etched design is determined by factors such as the duration of the exposure to the acid and the strength of the acid used. After the desired etching has been achieved, the plate is removed from the acid bath. The remaining wax or protective coating is then cleaned off the plate, revealing the etched design. This technique has been historically employed for various purposes, such as engraving armor or metal plates, and the creation of templates for printing (Figure 1.7). In the printing process, the etched plate is inked, ensuring that the ink remains in the recessed areas created by the etching. The surface ink is then wiped clean, leaving ink only in the etched lines. The plate is then pressed together with a sheet of paper using a high-pressure printing press, transferring the ink from the etched lines onto the paper, resulting in a print.

Figure 1.7. Example of etching art by ancient artist.

The chemical etching carried out on an industrial scale is known as chemical milling or industrial etching. Chemical milling is the manufacturing process of using baths of etching chemicals to create an object with the desired shape by destroying and removing parts of an already existing material. It is performed following the subsequent steps: (1) Cleaning: the surface of the material is cleaned to remove any contaminants that could affect the etching process. (2) Masking: a protective mask is applied to the surface to prevent the etchant from reaching certain areas during the etching process. Common protective mask includes neoprene elastomers or isobutylene-isoprene copolymers. (3) Scribing: the mask is selectively removed from the areas that are intended to be etched, exposing those regions to the etchant. (4) Etching: the material is immersed in an etching bath and the exposed areas are destroyed. (5) Demasking: after the desired etching has been achieved, the residual etchant and mask are thoroughly cleaned off the material's surface.

Photoengraving works on similar premises as chemical etching but uses a light-sensitive photoresist as a mask. That photoresist is resistant to the particular etching compound and, typically, becomes harder when it receives exposure to light (some photoresists are initially hard and became softer). First, the material is covered by the photoresist and an image of ultraviolet light is projected on its surface creating harder and softer parts. Then, a solvent is used to wash away the soft parts exposing part of the material surface, which is subsequently destroyed by the etching compound. Finally, the remaining photoresist is removed. Photoengraving allows a very high degree of precision, and can be used to make printed circuit boards, foil-stamping dies, flat springs, levers, gears, and other useful components that would otherwise be cut from sheet metal.

In the initial stages of chemical etching processes for glass or metal surfaces, the optimization and control of parameters were often achieved

through empirical methods, such as visual observations. Factors like the choice of protective mask material, exposure time, and etching agent concentration could be adjusted by trial and error by iteratively testing different combinations until the desired results were achieved. This empirical approach allowed the development and optimization of chemical etching processes, which was understood and controlled on a macroscopic level. The deep understanding of the underlying material structure and microscopic interactions occurring within the material was not necessarily required for achieving the desired etching results. Instead, the main concept was that the unprotected parts of the material would be destroyed when exposed to the etching agent, whereas the protected areas would remain unchanged, irrespective of their chemical structure.

It is worth noting that, as scientific knowledge and techniques advanced, a more comprehensive understanding of the atomic-scale processes and material interactions involved in chemical etching was gained. This understanding has led to more precise control and optimization of the etching processes, allowing for enhanced reproducibility and efficiency. By carefully controlling the degradation process at the nanoscale, it becomes possible to modify and tailor the properties of the resulting materials. Specific parts of reticular materials, for example, can be selectively destroyed, leading to the formation of new structures or the introduction of desired functionalities. This nanoscopic control over degradation enables the synthesis of materials with targeted properties, opening up possibilities for various applications.

These destructive synthetic strategies, when combined with the constructive approaches, offer a comprehensive toolkit for designing and synthesizing complex materials with precise control over their structures and properties. Both constructive and destructive strategies play important roles

in advancing synthetic methodologies and expanding the scope of materials chemistry.

1.4 Destructive synthetic strategies applied to reticular materials (nanoscopic control)

Reticular materials are typically synthesized using constructive strategies: MOFs and MOPs are formed by coordinating metals and ligands creating networks or cages whereas COFs are built by the formation of covalent bonds between organic building blocks forming networks. Additionally, new reticular materials can be created through post-synthetic modifications by forming or cleaving bonds. Constructive postsynthetic modifications (up-bottom strategies), which consist of the formation of bonds between ligands and additional organic moieties, between ligand free coordinating groups and additional metal ions, or between metals and additional ligands, have been exhaustively studied. In contrast, destructive postsynthetic modifications (up-bottom strategies), which involve selective cleaving of existing bonds to form smaller or less connected systems from bigger or more connected ones, are not as exhaustively explored as the constructive strategies. This section will focus on those destructive synthetic methods that have shown control at the nanoscopic level.

When all clusters or ligands of a reticular material are broken by cleaving covalent ligand bonds or the coordination bonds between metals and ligands, the reticular material is completely destroyed. To create new reticular materials from pre-existing ones, only some of the metal clusters or ligands must be broken, leaving the others unaltered. There are mainly two ways to accomplish this: one consists of randomly destroying some parts of the reticular material, frequently the most accessible ones, like the surface of the MOF particles or pores; and the other consists of quantitatively destroying some concrete kind of bond by using a selective chemical reaction. The

cleavage of all these specific types of bonds must not result in the complete destruction of the reticular material, so alternative ways of connecting some of the ligands and some of the clusters must exist.

1.4.1 Destruction of the most accessible or unstable parts of the reticular material

When a reticular material is exposed to harsh conditions, such as high temperatures, strong acids or bases, or extreme environments, it can undergo partial or total degradation. In most cases, the bonds that are broken are the weaker bonds of the framework which are usually the coordination bonds between metal ions and organic ligands. The control of the concentration of the destruction agent and the time of exposure can avoid the complete degradation of the material. According to which parts of MOF particles are preferentially attacked by the etching agent, we have classified the examples found in the literature in three groups: (1) degradation of the surface of the MOF particles; (2) degradation of the interior of the MOF particles; and (3) degradation of the surface of the micropores of the MOF fusing them into mesoporous or macropores.

1.4.1.1 Degradation of the surface of MOF particles: shape modulation

Similar to how traditional etching is used to shape metals by attacking their exposed surfaces, this technique can also be used for shaping MOF crystals. In 2015, Prof. Maspoch *et al.* reported a selective surface acidic etching process to obtain cubic, tetrahedral and hollow-box-shaped ZIF-8/67 crystals, based on the fact that their different crystal MOF faces have different stabilities in presence of an etching agent.[22]

ZIF-8 and ZIF-67 are isoreticular MOFs formed by the coordination of 2-methylimidazole ligand with zinc or cobalt, respectively. Their crystals are limited by different types of facets, edges, and vertices, which have

different chemical compositions depending on their concentration of ligands, metals and bonds between metals and ligands. In the reported study, the etchant acid was used to protonate the 2-methylimidazole ligands and break their coordination bonds with Zn or Co carving the external crystal surfaces. The crystal faces with the highest density of Zn/Co-2-methylimidazole bonds were preferentially destroyed. As shown in Figure 1.8, the <100> and <211> crystallographic planes of ZIF-8 traverse metal-ligand bonds, whereas the planes <110> and <111> only pass through the ligands. The faces of the ZIF-8 particles that cross the <100> and <211> crystallographic planes degrade more quickly because the metal-ligand bonds are sensitive to the etching conditions while the ligands are stable to those conditions. In the case of truncated rhombic dodecahedron to cube, the plane <100> coincide with the square face of the ZIF-8 particle, whereas the plane <211> coincide with the vertex of the ZIF-8 particle. The <100> planes are therefore more exposed than the <211> planes. For that reason, the etching occurred preferentially in the <100> direction gradually enlarging the square faces until the formation of a cube (Figure 1.8).

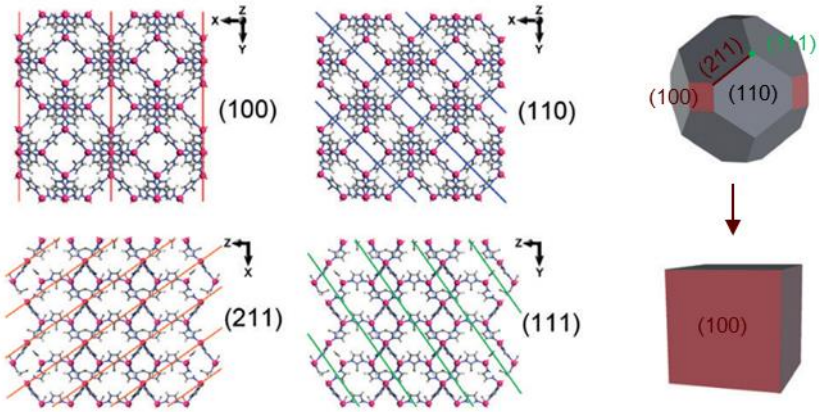

Figure 1.8. (left) ZIF-8 crystal structure represented along different directions. The exposed crystallographic planes are highlighted. (right) Illustration of the change in crystal morphology during the chemical etching of truncated rhombic dodecahedral ZIF-8 particles to form cubic particles. Image adapted with permission from reference 22. Copyright 2015 John Wiley and Sons.

Depending on the initial crystal morphology, which determines the most exposed crystallographic planes, and on the aggressivity of the etching conditions, different crystal morphologies were obtained (Figure 1.9). By simply adjusting the pH of the etchant solution, the etched morphology could be controlled, showing that various homogeneous crystal morphologies can be created from the same initial crystal.[22]

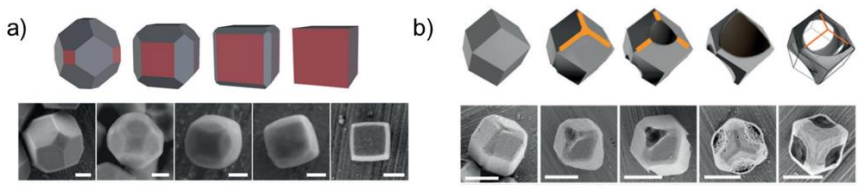

Figure 1.9. Illustration and corresponding SEM images of the change in crystal morphology during the etching of (a) truncated rhombic dodecahedral and (b) rhombic dodecahedral ZIF-8 crystals. Image reprinted with permission from reference 22. Copyright 2015 John Wiley and Sons.

Later, in 2018, Moon *et al.* synthesized similar hollow-box-shaped ZIF-8 particles adjusting the etching solution pH to tune the wall thickness of the hollow ZIF-8 boxes from ≈ 30 nm to ≈ 100 nm and the ZIF-8 macropores from 200 nm to 100 nm.[23] Also in 2018, Chen *et al.* used the same facet-dependent anisotropic etching rate principle for synthetizing hexapod shaped ZIF-8 particles from truncated rhombic dodecahedral particles. These authors proved that the partial removal of metal ions or ligands from ZIF-8 not only leads to a change of the particle shape, but also generates nanostructured roughness increasing the accessible catalytic sites and with them, the catalytic activity of the obtained hexapod ZIF-8 colloids.[24]

1.4.1.2 Degradation of the interior of MOF particles: formation of core-shell particles

Selective etching of the inner parts in MOF particles has been successfully employed to synthesize empty MOFs with core-shell structures. This selective etching was possible thanks to the fact that the different regions of the same MOF particle had different stabilities. To obtain core shell particles, the inner parts of the particles should have lower stability than the outer part. The lower stabilities in the interior of the MOF particles can be achieved by following two possible strategies: (1) decreasing the stability of the inner parts of the particles; or (2) increasing the stability of the particle surfaces. MOF porosity allows small etching agents to reach any point on the MOF particles, allowing them to arrive to the inner parts and degrade them.

The instability of the inner parts of MOF particles can be favoured by increasing the concentration of defects in those parts. This is because parts with higher concentrations of defects are less stable than those parts with lower concentrations of defects. Defects in the interior of MOF particles are favoured by rapid nucleation and aggregation during the first steps of MOF particle synthesis. Generally, the synthesis of MOF nanocrystals can be divided into three steps: (1) nucleation; (2) nuclei aggregation; and (3) growth of aggregates into nanocrystals. If the solute concentration is significantly higher than the critical nucleation point, many small coordination polymer units nucleate and quickly aggregate. Following that, as the concentration of organic ligands and metal ions rapidly falls below the minimum supersaturation level, no more nucleation takes place and aggregates slowly grow forming MOF crystals. For that reason, the inside core of each MOF particle has more defects and is chemically less stable than the outside shell which is considered more robust. This inhomogeneity in MOF particles and the fact that small destroying agents, such as H^+, can diffuse through the pores of the MOF particles, enable the inner area to be preferentially etched. In

2017, Huo *et al.* took advantage of this MOF inhomogeneity and developed a facile method to fabricate single-crystalline multi-shelled hollow MIL-101 crystals through step-by-step crystal growth.[25] Step-by-step crystal growth favoured the formation of defects at the start of each growing step, resulting in particles with multiple layers of unstable-stable regions. Following that, the unstable regions were destroyed by acetic acid etching processes resulting in multi-shelled hollow crystals (Figure 1.10).

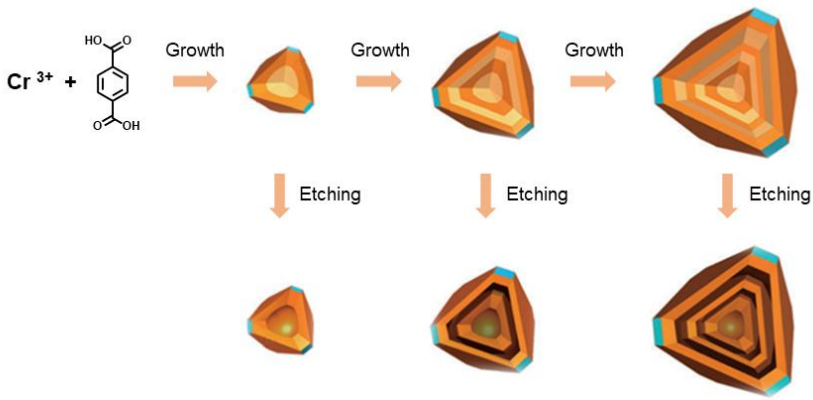

Figure 1.10. Schematic showing the fabrication of single-, double-, and triple-shelled hollow MIL-101 particles. Image adapted with permission from reference 25. Copyright 2017 John Wiley and Sons.

The stability of the surface of MOF particle can be enhanced by using additional compounds that interact with it, protecting this surface from degradation. One example illustrating this approach was reported by Caruso *et al.* They used phenolic acid as an etching agent as well as a surface protector.[26] Phenolic acid molecules were attached the surfaces of MOFs particles protecting them while releasing free protons which diffuse into the particles, etching their interiors and forming hollow MOF crystals. Yamauchi *et al.* synthesized uniform-sized Prussian Blue (PB) hollow particles by etching them with HCl in the presence of polyvinylpyrrolidone (PVP). PVP molecules can be adsorbed on the surface of PB particles surfaces due to the

attractive interactions between the amide units of PVP and the iron ions of the PB. Thus, the PVP layers protect the PB particles slowing down the etching rate on their surfaces creating the hollow PB particles.[27]

1.4.1.3 Degradation of random parts inside MOF particles: fusion of micropores into mesopores

Since MOFs are porous materials, the etching agents can diffuse inside them randomly breaking some of the chemical bonds of the framework. That partial destruction of some parts of the reticular material makes possible the fusion of MOF micropores into mesopores (Figure 1.11).

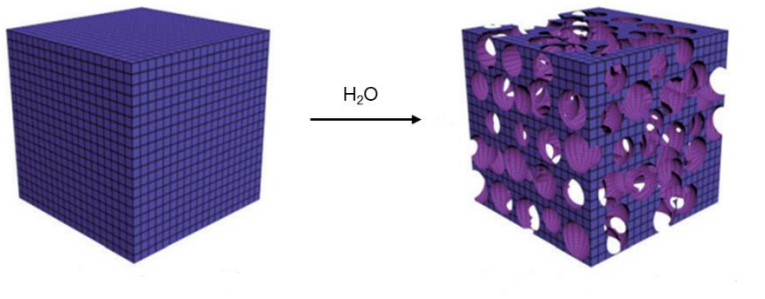

Figure 1.11. Schematic showing the hydrolytic post-synthetic transformation in a MOF, resulting in larger pores by partial removal of constituents. Image adapted with permission from reference [28]. Copyright 2015 John Wiley and Sons.

There are several examples where this idea has been used to synthetize hierarchical micro and mesoporous MOFs applying different destroying strategies. These strategies include the use of water[28] or phosphoric acid[29] to break some of the metal-ligand bonds; the use of hot methanol to reduce some of the Cu^{2+} ions of HKUST to Cu^{+}, changing the original coordination mode of Cu nodes and partially breaking their coordination bonds[30]; the transition of $Fe(III)_3$ cluster to an $Fe(II)Fe(III)_2$ cluster due the decarboxylation of some of the ligands;[31] and the incomplete

replacement of bridging ligands (dicarboxylic acids) by monocarboxylic acids.[32]

In previously mentioned studies, the MOF particles are partially degraded as a result of being exposed to an environment where they are unstable. The degree of degradation is determined by the aggressivity of the etching conditions which causes the cleavage of a greater or a lower number of bonds. The degree of degradation can be more precisely controlled by completely cleaving one type of bond rather than partially cleaving some bonds of one type. To completely cleave one specific type of bond without totally destroying the framework structure, there must be routes of connecting the clusters free of cleavable connections. One possible strategy is to build a reticular material with two geometrically equivalent ligands, one cleavable and one non-cleavable. The degree of MOF degradation can be controlled by the ratio between cleavable ligands and non-cleavable ligands.

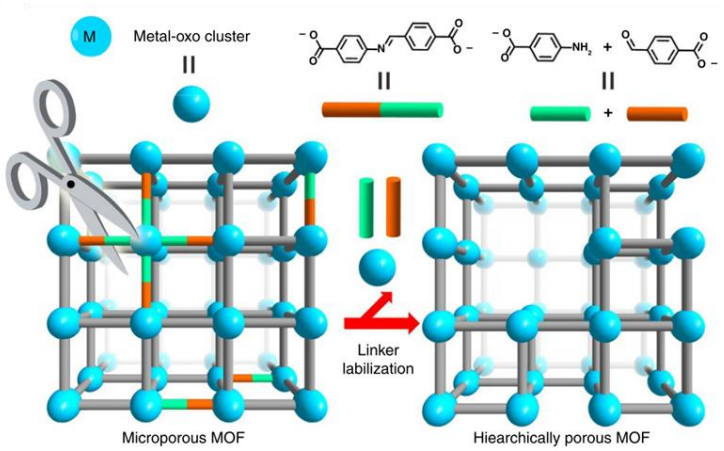

Figure 1.12. Schematic representation of a MOF built by non-cleavable (grey) and cleavable ligands (green and orange) and the breaking of cleavable ligands fusion micropores into mesopores. The amount and size of mesopores is controlled by the concentration of cleavable ligands and the concentration of the etching agent: acid acetic. Image reprinted with permission from reference 33. Open Access CC BY 3.0.

Several instances of selective bond cleavage targeting specific types of bonds have been described.[33–35] In those examples, MOFs were synthesized using two types of ligands: one that is sensitive to the cleavage reaction and the other that is resistant to the cleavage reaction. These two kinds of ligands were analogous between them in terms of length and connectivity, which resulted in their random distribution in the reticular material. When the cleavage reaction was applied, the non-cleavable ligands remained unaltered while the cleavable ligands broke fusing the micropores into mesopores (Figure 1.12 and Figure 1.13). When the number of cleavable ligands rose but remained less than half of the total amount of MOF ligands, the pore size of the resultant MOF grew. Thus, the total pore volume increased while the surface area decreased due to the loss of microporosity and the appearance of mesoporosity. However, when the concentration of cleavable ligands increased to an excessive level, there were not enough non-cleavable ligands left to sustain the MOF structure after the cleavage reaction and the material collapsed, losing both its crystallinity and its porosity.

Three examples of this idea with different pairs of ligands, different cleavable bonds and different cleavable reactions have been reported. In 2017, the Zhou group introduced the concept of labilization that preconize the introduction of analogous labilizable and no labilizable ligands randomly distributed in the MOF. They chose 4-carboxybenzylidene-4-aminobenzate (CBAB), that contain an imine bond, as the labilizable ligand and azobenzene-4,4'-dicarboxylate (AZDC), which contain an azo bond, as the non-labilizable ligand (Figure 1.12 and Figure 1.13a). The labilizable CBAB ligands were selectively eliminated by cleaving the imine bonds in presence of acetic acid, as it is known that in acid media the imine bonds are broken into aldehyde and amine groups (Figure 1.12 and Figure 1.13d). The terminal benzoates are much more labile than the bridging ligand and they could be replaced by acetates or a pair of terminal –OH/H_2O ligands.[33] By carefully

controlling the relation between the labilizable and the non-labilizable ligands and the acid concentration, they were able to tune the MOF pore size from 1.5 nm to a maximum of 18 nm. Later, the same research group applied the same idea by synthesizing a MOF built by terephthalic acid without functionalization and functionalized with amino groups and selectively cleaving the M-L bond by the decarboxylation of amino ligands (Figure 1.13b and Figure 1.13e).[34] By controlling the ratio of thermolabile ligand, the time of heating and the thermolysis temperature, they were able to tune the pore sizes from 0.8 nm to 15 nm. Following a similar approach, Maspoch group explored the generation of mesoporosity in metal–organic frameworks (MOFs) by double bond cleavage via solid gas ozonolysis.[35] Ozonolysis of alkenes is a well-studied organic reaction which allows the selective cleavage of olefinic bonds and the regiospecific formation of carboxylic acids, ketones, or aldehydes. Using this approach, they applied ozonolysis to a mixed-ligand Zr-fcu-MOFs based on organic ligand pairs, in which one ligand has an ozone-cleavable olefinic bonds and the other ligand is ozone-resistant (Figure 1.13c and Figure 1.13f). They were able to selectively break the cleavable ligand via ozonolysis to trigger the fusion of micropores into mesopores within the MOF framework. They were able to tune the total pore volume from 1.27 cm^3/g to 1.44 cm^3/g by changing the ratio of ozone-cleavable ligand.

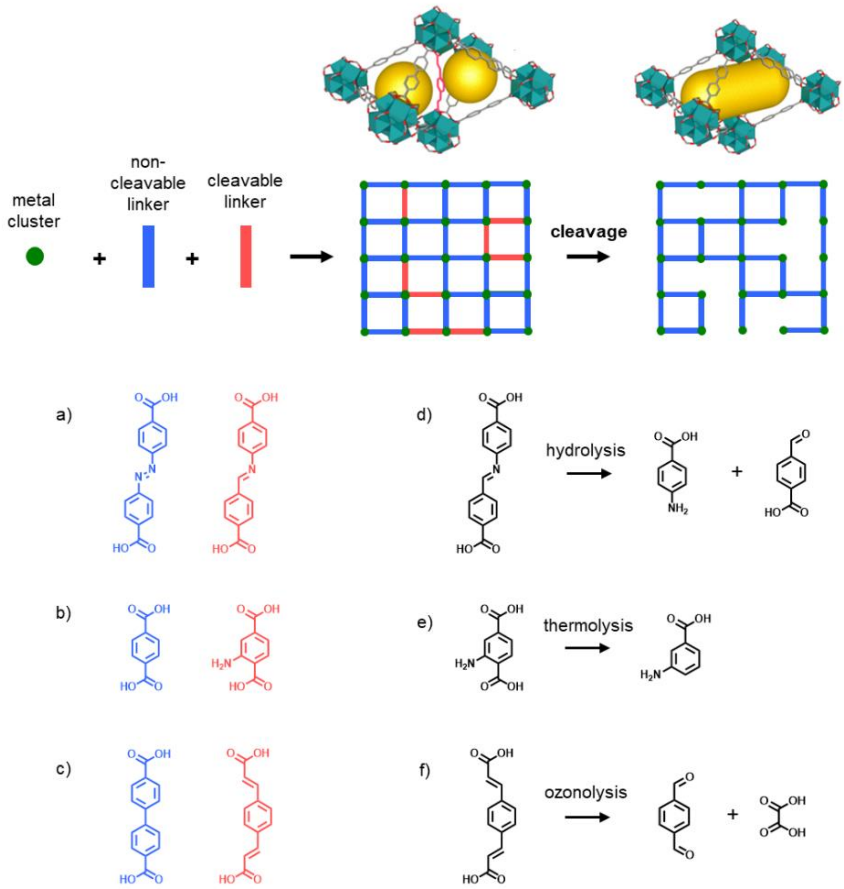

Figure 1.13. Schematic representation of the synthesis of a MOF built by two kinds of ligands, one of them sensitive to the cleavage reaction (in red) and the other resistant to it (in blue), randomly distributed around the MOF, and the subsequent cleavage of the cleavable ones. (a) Azo ligand (in blue) and imine ligand (in red). (b) Non-functionalized terephthalic acid (in blue) and amino-functionalized terephthalic acid (in red). (c) Ligand without double bonds and ligand containing doble bonds. (d) Hydrolysis of the imine ligand. (e) Thermolysis of the amino-functionalized ligand. (f) Ozonolysis of the ligand containing double bonds. Image adapted with permission from reference 35. Copyright 2018 American Chemical Society.

Chapter 2

Objectives

As presented in the previous Chapter, reticular materials are an emerging class of materials that include MOFs, COFs, and MOPs. The most common synthetic methods to obtain reticular materials are based on constructive strategies, where metals and ligands are assembled forming bigger molecules or extended materials. On the other hand, destructive strategies, where bonds are destroyed forming less connected systems or smaller molecules, have not been studied to create new reticular materials. Thus far, these destructive methods have only been used to post-synthetically modify MOFs at the most accessible or unstable parts of them or in a random way. In this Thesis, our aim is to prove that bond breaking can be a new tool to design and synthesize new molecules and materials using reticular materials as precursors. This new synthetic strategy, called Clip-off Chemistry is based on knowing the exact crystallographic positions of the cleavable bonds in a reticular material in a way that, when we apply the cleavage reaction, we will obtain well-defined molecules or materials (Figure 2.1).

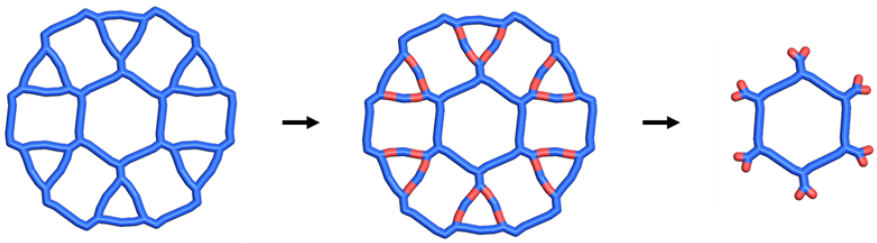

Figure 2.1. Schematic representation of the concept of Clip-off Chemistry. This scheme shows how the introduction of cleavable bonds (in red) in known positions of a COF can allow the synthesis of functionalized macrocycles when the cleavage reaction is applied.

Thus, depending on the starting reticular material and the position of the cleavable bonds, different kinds of compounds such as three-dimensional structures with different topologies, two-dimensional nanosheets, one-dimensional chains or zero-dimensional systems can, in theory, be synthesized (Figure 2.2).

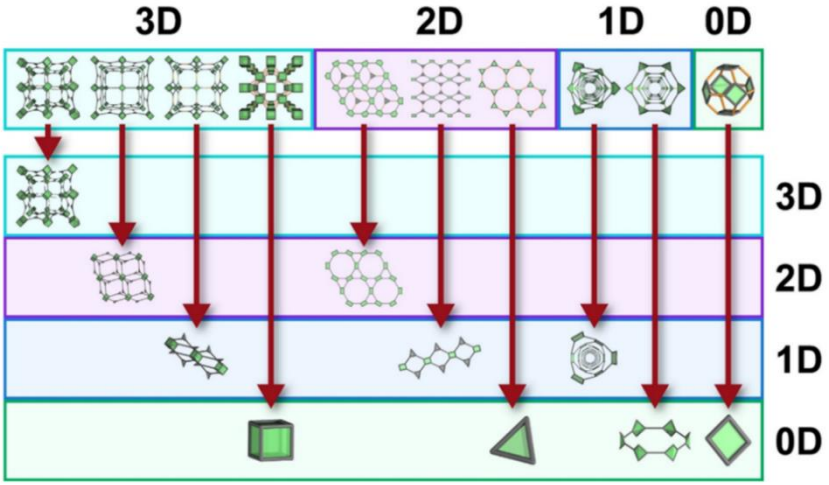

Figure 2.2. Clip-off Chemistry for the synthesis of molecular architectures of different dimensionality. Schematic illustrating the potential outcomes of Clip-off Chemistry, in which the dimensionality of the parent reticular materials dictates the dimensionality of the target molecules and structures. Image reprinted with permission from reference 36. Copyright 2021 John Wiley and Sons.

The main objective of this Thesis is to prove the principles of Clip-off Chemistry (e.g. selective and quantitative bond breaking in reticular materials) and use it to synthesize metal complexes from MOP precursors. More specifically, this Thesis will be divided into 4 major objectives:

- Design and synthesis of a functionalized homoleptic Rh_2-cluster via the cleavage of an homoleptic MOP with cleavable bonds in known positions.
- Synthesis of a family of heteroleptic MOPs to diversify the catalogue of available MOP precursors.
- Design and synthesis of a functionalized Rh_2-macrocycle via the cleavage of an heteroleptic MOP.
- Design and synthesis of a mixed-ligand Rh_2-cluster via the cleavage of an heteroleptic MOP.

Chapter 3

Synthesis of an homoleptic Rh_2-cluster via rational cleavage of an homoleptic MOP

3.1 Introduction

The reaction of ozone with olefins was reported for the first time by Prof. Schonbein in 1855.[37] Prof. Schonbein discovered that ozone and ethylene react to form carbonic acid, formaldehyde, and formic acid (Reaction 3.1). This reaction, which was named ozonolysis, is still one of the most general and reliable methods of selective double-bond cleavage.

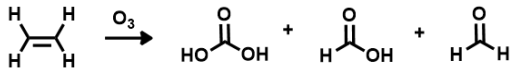

(3.1)

The ozonide, which is the ozonolysis intermediate formed by the addition of the ozone to the olefin prior to the cleavage, was first identified and isolated by Prof. Houzeau and Prof. Dieckhoff.[38,39] Later, Prof. Criegee proposed a mechanism to explain the formation of this ozonide (Reaction 3.2).[40]

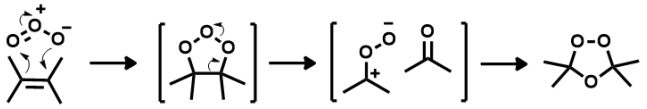

(3.2)

In brief, this mechanism consists of two 1,3-dipolar cycloadditions forming two 5 membered rings and a ring cleavage forming a carbonyl oxide and a carbonyl compound. Ozone and carbonyl oxide can be considered 1,3-dipolar compounds because they have delocalized electrons and a separation of charge over three atoms. The three steps of the mechanisms are: (1) the 1,3-dipolar cycloaddition of ozone to the alkene, creating a primary ozonide or 1,2,3-trioxolane; (2) the primary ozonide decomposition into a carbonyl oxide and a carbonyl compound; and (3) 1,3-dipolar cycloaddition of the carbonyl oxide to the carbonyl compound producing a secondary ozonide or 1,2,4-trioxolane. A significant amount of experimental data has been reported to support this mechanism since Prof. Criegee proposed it.[40]

Ozonide intermediates are unstable and difficult to isolate. They can easily decompose via cleaving the C-C bond that was originally double bonded. Depending on the initial reagents and the experimental conditions, ketone, aldehyde and/or carboxylic acid groups can be obtained from these ozonide intermediates. For example, while quaternary double bonds produce ketones, secondary double bonds can produce aldehyde and/or carboxylic acid groups depending on experimental parameters, such as reaction solvent, co-reagents, etc. However, reductive and oxidative work-up allows the selective formation of aldehyde and carboxylic acid groups, respectively (Reaction 3.3).[41] On one hand, the reductive work-up is carried out by adding a reductive agent, which decomposes the ozonide intermedia forming aldehyde groups. The most employed reductive agents are zinc (Zn) and dimethyl sulfide (Me_2S). Whereas the zinc is oxidized to zinc oxide (ZnO), the dimethyl sulfide is oxidized to dimethyl sulfoxide (DMSO). On the other hand, the oxidative work-up is carried out by adding hydrogen peroxide (H_2O_2), which forms carboxylic acid groups and water (H_2O).

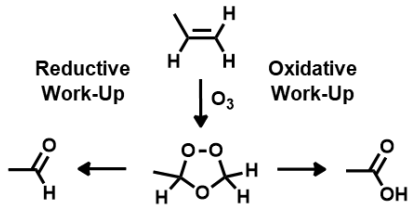

(3.3)

The ozonolysis reaction has two main applications: localizing unsaturations for structural analysis and cleaving double bonds generating functional groups for synthetic purposes. Ozonolysis has been widely used in organic chemistry to create aldehydes, ketones, and carboxylic acids in a regiospecific manner. Beyond functionalizing molecules, ozonolysis can also be utilized to generate novel molecular skeletons. For example, new oligomers have been synthesized by the cleavage of organic polymers.[42,43]

Prof. Walba *et al.* further developed this concept by synthesizing organic rings via ozonolysis.[44,45] Prof. Walba *et al.* synthesized the first Möbius strip and its untwisted cylindrical isomer.[46] The Möbius strip consists of a large macrocycle folded around itself creating a twist. This folding is fixed by double bonds (Figure 3.1a). Otherwise, the untwisted cylindrical isomer is formed by two rings which are placed in parallel and linked each other by double bonds (Figure 3.1b). In both systems, the ozonolysis reaction was used to break the double bonds generating ketones and releasing new molecules. Whereas the cleavage of the Möbius strip via ozonolysis leads to one large ring (Figure 3.1a), ozonolysis of the untwisted cylindrical isomer in half yields two separate rings (Figure 3.1b).[45]

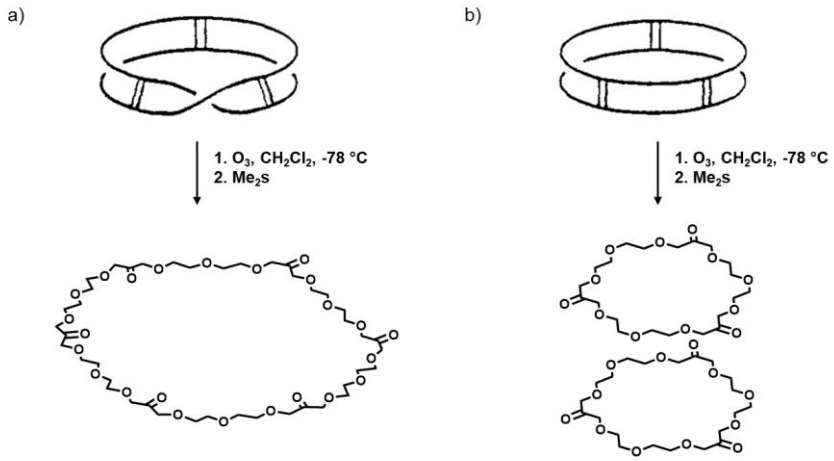

Figure 3.1. Schematic representation of (a) the synthesis of one large ring by the cleavage of a twisted Möbius Ladder and (b) the synthesis of two separate rings by the cleavage of an untwisted belt. Image adapted from reference 44. Copyright 1982 American Chemical Society.

3.1.1 Ozonolysis reaction in reticular materials

Our research group has reported a solid-gas post-synthetic functionalization of an olefinic MOF by ozonolysis.[47] The pendant ethylene groups of the MOF were quantitatively transformed into 1,2,4-trioxolane

moieties. In solid state, this chemical transformation occurred within the pores of the MOF, increasing the stability of the ozonide. Indeed, the 1,2,4-trioxolane ring could be isolated and characterized via single crystal X-ray diffraction. 1,2,4-trioxolane was subsequently converted to aldehyde and carboxylic moieties by a reductive and an oxidative work-up, respectively (Figure 3.2).

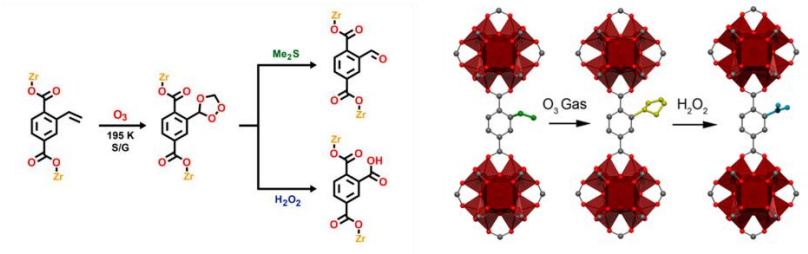

Figure 3.2. Single-crystal-to-single-crystal ozonolysis of an olefinic MOF to generate a 1,2,4-trioxolane ring. This 1,2,4-trioxolane ring is cleaved to form aldehyde or carboxylic acid groups. Image reprinted with permission from reference 47. Copyright 2018 American Chemical Society.

Later, as previously mentioned in *Chapter 1*, ozonolysis was applied to mixed-ligand Zr-fcu-MOFs based on two organic ligands, one of which had ozone-cleavable olefinic bonds and the other was ozone-resistant. These two kinds of ligands were geometrically analogous, making them to be randomly distributed around the reticular material.[48] Several MOFs with different ratio of ozone-cleavable/ozone-resistant ligands were synthesized. While the ozone-cleavable olefinic ligands were broken via ozonolysis, the ozone-resistant ligands remained unaltered. When the ozone-cleavable/ozone-resistant ratio increased, total pore volume increased, and surface area decreased due to the fusing of micropores into mesopores. However, when the concentration of ozone-cleavable ligands was too high, the system lost its crystallinity and its porosity after the ozonolysis reaction since many ligands were broken, and the system could not maintain its

robustness (Figure 1.13). The total pore volume was successfully increased from 1.27 cm^3/g to 1.44 cm^3/g after determining the optimum ratio of ozone-cleavable/ozone-resistant ligands. One of the limitations of ozonolysis and other destructive methods, when applied in reticular materials with mixed ligands, is their poor specificity and selectivity. Random distribution of the cleavable and non-cleavable ligand does not allow to anticipate the final structure of reticular materials after this postsynthetic treatment. In this Thesis, we aim to go a step further and explore the selective cleavage of reticular materials in which we know the exact position of the cleavable bonds. In doing so, we create previously designed coordination compounds that would otherwise be inaccessible by direct synthesis. Specifically, this Thesis will be focused on the cleavage of MOPs by ozonolysis.

MOPs are a subclass of molecular cages constructed from the self-assembly of metal ions and organic ligands. Reticular chemistry can be used in MOPs due to the known coordination modes of the metals and the geometric variability of the organic ligands. This chemistry allows to locate cleavable bonds in known crystallographic positions and therefore, rationally design new MOPs. As a proof of concept of the use of MOPs as precursors in Clip-off Chemistry, we begin from an homoleptic-paddlewheel-MOP that is built by one type of ligand. Among the homoleptic-paddlewheel-MOPs, we work with those made by dimetal paddlewheel M_2 clusters.

Dimetal paddlewheel M_2, mostly Cu_2, building blocks are one of the most often utilized SBUs in the construction of MOFs and MOPs. Depending on the angles between binding sites of the ligands, paddlewheel SBUs can create a broad range of closed structures, including lantern cages, triangles, squares, tetrahedrons, octahedrons, and cuboctahedrons. The most frequently reported homoleptic paddlewheel-MOPs are the cuboctahedron-MOP,[21,49] the octahedron-MOP[50] and the lantern-MOP.[51] Cuboctahedron-MOPs are built by 24 ligands with a 120° angle between binding sites that connect 12

clusters, creating six square windows and eight triangular windows. Octahedron-MOPs are made of six paddlewheel clusters connected by 12 ligands with a 90° angle between binding sites, leading to eight triangular windows. Lantern-MOPs consists of two paddlewheel clusters connected by four ligands with a 0° angle between binding sites (Figure 3.3).

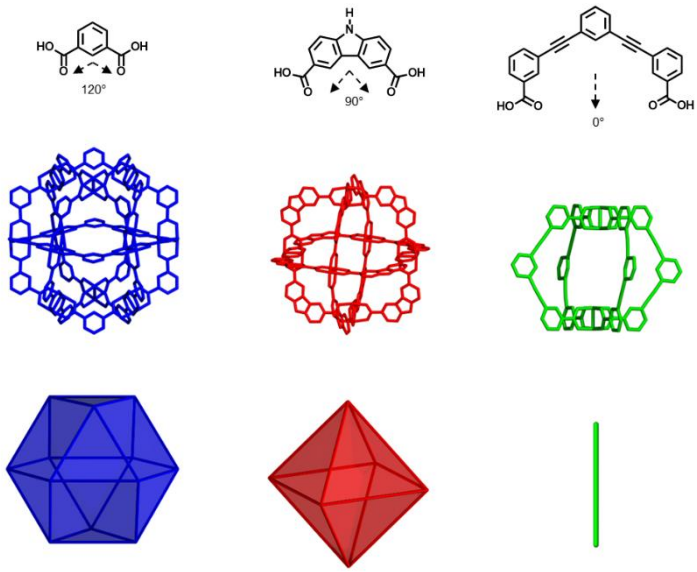

Figure 3.3. From up to down: MOP ligands (up), MOP schematic representation (middle) and MOP geometry linking the centre of each cluster (down). From left to right: cuboctahedron-MOP (left, in blue), octahedron-MOPs (middle, in red) and lantern-MOP (right, in green). Hydrogen atoms have been omitted for clarity.

As mentioned above, we start applying Clip-off Chemistry to homoleptic-MOPs. To synthesize an homoleptic MOP with double bonds in known crystallographic positions, all the ligands of the MOP must be equal and therefore, must present double bonds. When applying the cleavage reaction to this homoleptic MOP, all ligands are broken releasing the functionalized M_2-clusters (Figure 3.4).

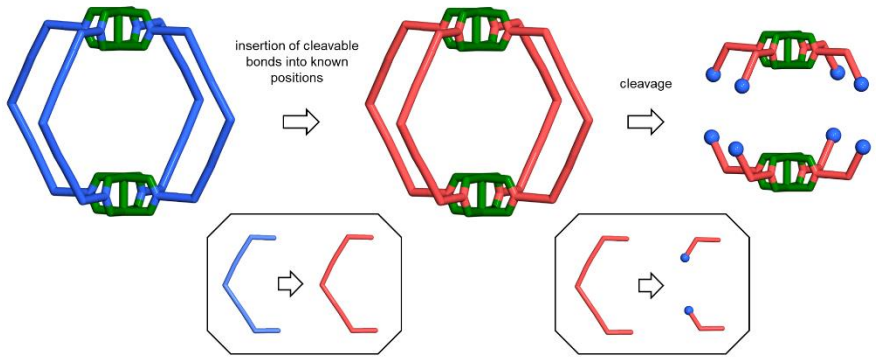

Figure 3.4. Insertion of cleavable bonds into known positions of a homotopic-MOP via reticular chemistry and its cleavage to release an homoleptic Rh_2-cluster.

The synthesis of functionalized metal complexes (e.g., M_2-clusters, MOPs, etc.) with coordinative groups is challenging since these coordinative groups can also interact with metals, forming undesired compounds. One possible strategy is to protect the reactive groups. Then, the M_2-complex must be synthesized and finally, the groups must be deprotected. For example, this protection-deprotection strategy was used in the synthesis of Rh_2-clusters functionalized with carboxylic acid groups in *para*[52] and *meta*[53], as well as in the synthesis of MOPs functionalized with carboxylic acid and amino groups.[20] In this Chapter, we propose an alternative strategy to obtain an aldehyde functionalized Rh_2-cluster, which consists in the cleavage of a preexisting lantern Rh_2-MOP which avoids the use of protection-deprotection strategies.

3.2 Results and Discussion

3.2.1 Selection of the precursor material: lantern Rh_2-MOP

In this Thesis, we focus on Rh_2-compounds due to their kinetic stability with respect to carboxylate exchange at room temperature and their robustness in presence of air and water; characteristics that allow Rh_2-compounds to be used as precursor materials for the synthesis of new compounds.[17,54] In other words, Rh_2-MOPs are suitable precursor materials for Clip-off Chemistry. The synthesis of MOPs is based on the reversibility of the carboxylate-metal ion bonds, which permits the correction of defects by assembly-disassembly reactions until the formation of the thermodynamic product. It should be mentioned that the relative inertness of the equatorial carboxylates of Rh_2-paddlewheel clusters makes difficult their use for the formation of extended structures through ligand-exchange reactions.

In 2016, Prof. Furukawa and Prof. Kitagawa *et al.* reported the first Rh_2-MOPs which had cuboctahedral and anticuboctahedral topologies.[55] Later, in 2018, a lantern Rh_2-MOP, $Rh_4\mathbf{L^{3.1}}_4$, was also published.[51] The lantern M_2-MOP is the most basic M_2-MOP ever reported since it is built just by two paddlewheel M_2-clusters linked together to form a cage with the shape of a giant paddlewheel. The two paddlewheel units of the lantern M_2-MOP are linked together by four ligands with 0° angles between binding sites.[51] The reported lantern Rh_2-MOP, $Rh_4\mathbf{L^{3.1}}_4$, was built by ligands formed by three aromatic rings linked together by two triple bonds, $\mathbf{L^{3.1}}$ (Figure 3.5). Since ozonolysis reaction can also cleave triple bonds,[56] we decided to start using this reported $Rh_4\mathbf{L^{3.1}}_4$ as our first precursor material. Using this MOP, once the four ligands of this $Rh_4\mathbf{L^{3.1}}_4$ are cleaved, homoleptic Rh_2-clusters functionalized in *meta* position should in principle be released (Figure 3.5).

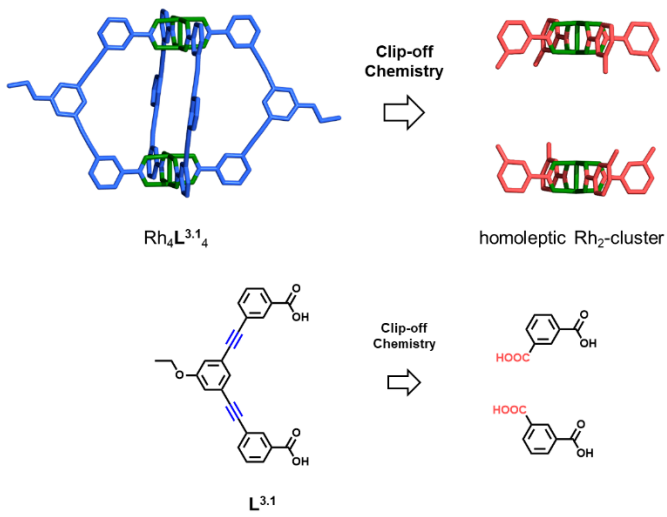

Figure 3.5. Cleavage of a triple bond $Rh_4L^{3.1}_4$ releasing an homoleptic Rh_2-cluster functionalized with carboxylic acid groups.

3.2.2 Establishment of the Clip-off methodology: characterization during the optimization process

Our Clip-off synthetic approach requires the cleavage of a certain type of covalent bond that is situated in well-known positions inside the reticular material. This specific type of bond must be clipped selectively while all other covalent bonds of the ligands and coordination bonds between metals and ligands must remain unaltered. Therefore, to identify and optimize the experimental conditions of a Clip-off procedure, it is necessary to follow both the splitting of the cleavable bonds as well as the stability of the other types of MOP bonds. Specifically, the stability of Rh_2-paddlewheel clusters, which are two Rh^{2+} linked together by four carboxylic acid groups, can be followed qualitatively by simply analysing the colour. Whereas Rh_2-paddlewheel clusters are green, the clusters turn yellow when oxidized to Rh^{3+} and black when reduced to Rh^0. The presence of Rh_2-paddlewheel clusters can also be confirmed by measuring their characteristic band (from

550 nm to 630 nm) via ultraviolet-visible spectroscopy (UV-vis). This band corresponds to the orange-red absorption that gives their characteristic green colour (Figure 3.6).[57,58]

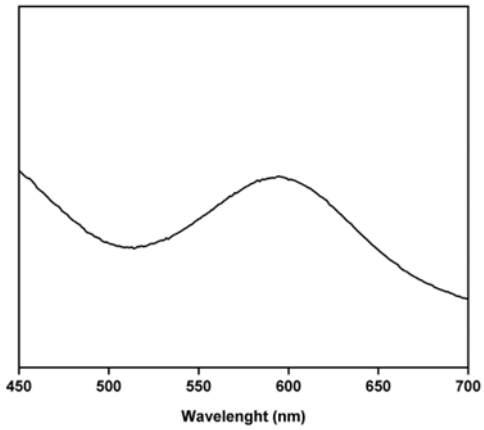

Figure 3.6. Example of the UV-vis band of a Rh_2-MOP.

The coordination of the ligands to Rh_2 units can be confirmed by the shift of their peaks in ^{1}H-NMR respect to the positions of the free ligand proton peaks. The cleavage of the ligand with cleavable bonds and the stability of the ligand with no cleavable bonds can easily be confirmed by ^{1}H-NMR of the digested sample. The digestion consists in solubilizing the sample in 0.45 mL DMSO-d and 2 µL of D-Cl and heating at 100 ºC for 6 h. It should be mentioned that, when the sample is solubilized in DMSO, it turns red due to the coordination of DMSO to the Rh^{2+} paddlewheels. During the digestion, the rhodium paddlewheels are cleaved releasing the organic moieties into the solution and the colour of the solution changes from red to yellow due to the oxidation of Rh^{2+} to Rh^{3+}. Without the effect caused by the rhodium coordination, the free organic moieties can be easy analysed by ^{1}H-NMR. Once the experimental ozonolysis conditions are completely determined, the resulting product can be fully characterized by mass spectroscopy (ESI or MALDI-TOF) and single crystal X-ray diffraction.

3.2.3 Cleavage of the lantern Rh_2-MOP, $Rh_4L^{3.1}{}_4$, containing triple bonds

As mentioned above, we first attempted to break the lantern Rh_2-MOP, $Rh_4\mathbf{L}^{3.1}{}_4$, built with ligands that contain triple bonds, $\mathbf{L}^{3.1}$ (Figure 3.6, in blue).[51] It is known that triple bonds can be broken by ozonolysis reaction while adding H_2O to form carboxylic acid groups (Reaction 3.4).[56,59]

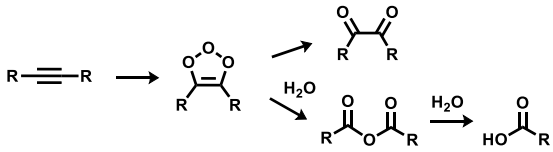

(3.4)

First, we synthesized the $Rh_4\mathbf{L}^{3.1}{}_4$ following the same method that was previously reported.[51] We started the $Rh_4\mathbf{L}^{3.1}{}_4$ cleavage by bubbling ozone into a green solution of 2 mg of MOP in 2 mL of dimethylacetamide (DMA) and 50 μL of water for 1 h. The ^{1}H-NMR analysis revealed that the ligand had been completely cleaved and that the expected isophthalic acid had been formed. However, the solution turned yellow, indicating that the paddlewheel Rh_2-clusters were destroyed (Figure 3.7c). To overcome this problem, we reduced the reaction time to 30 minutes. However, we found that this time was insufficient to cleave the ligand although the reaction crude also turned yellow, indicating that the Rh_2-paddlewheel clusters were again cleaved (Figure 3.7b). Therefore, we concluded that, under these reaction conditions, the Rh_2-clusters are less stable than the triple bonds.

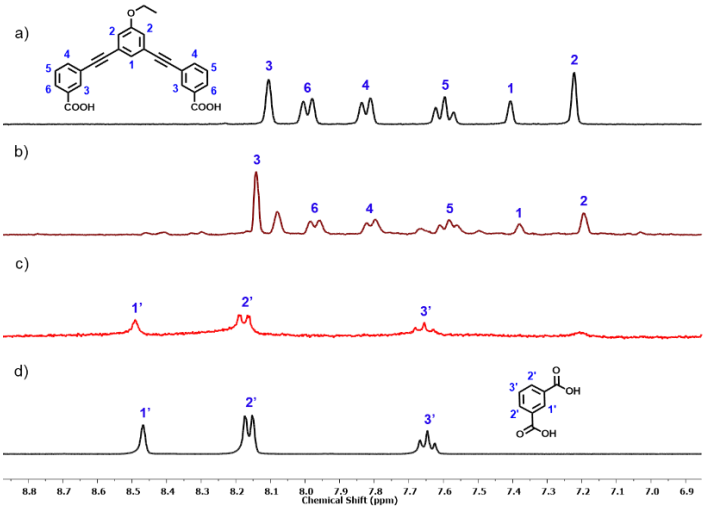

Figure 3.7. ^{1}H-NMR spectra (400 MHz, DMSO-d_6) of (a) $\mathbf{L^{3.1}}$; (b) digested sample obtained after ozonising the $Rh_4\mathbf{L^{3.1}}_4$ during 30 min; (c) digested sample obtained after ozonising the $Rh_4\mathbf{L^{3.1}}_4$ for 1 h; and (d) isophthalic acid.

To identify any condition in which all the triple bonds of the MOP cleaved while the Rh_2-clusters remained unaffected, we attempted various experimental conditions, including different reaction solvents and the addition of pyridines that coordinate to the Rh_2-clusters acting as protecting groups. Unfortunately, we were unsuccessful in finding such conditions. Consequently, we decided to change the precursor material used in our Clip-off Chemistry approach by designing a new lantern M_2-MOP. To do so, we considered two strategies: (1) creating a MOP with metal-ligand bonds that are more stable against the cleavage reaction than Rh-carboxylic bonds; and (2) constructing a MOP composed of ligands that contain cleavable bonds more susceptible to ozonolysis than the triple bonds of $\mathbf{L^{3.1}}$. We chose the second strategy by modifying the $\mathbf{L^{3.1}}$ ligand while retaining the Rh-carboxylic bonds in our new MOP design.

3.2.4 Design and synthesis of a new lantern Rh_2-MOP, $Rh_4L^{3.2}{}_4$, with olefinic bonds

Double bonds are more sensitive to ozonolysis than triple bonds. For that reason, we designed and synthesized a lantern Rh_2-MOP that contains olefinic bonds instead of the triple bonds of the previously reported $Rh_4\mathbf{L}^{3.1}{}_4$ (Figure 3.8, red).

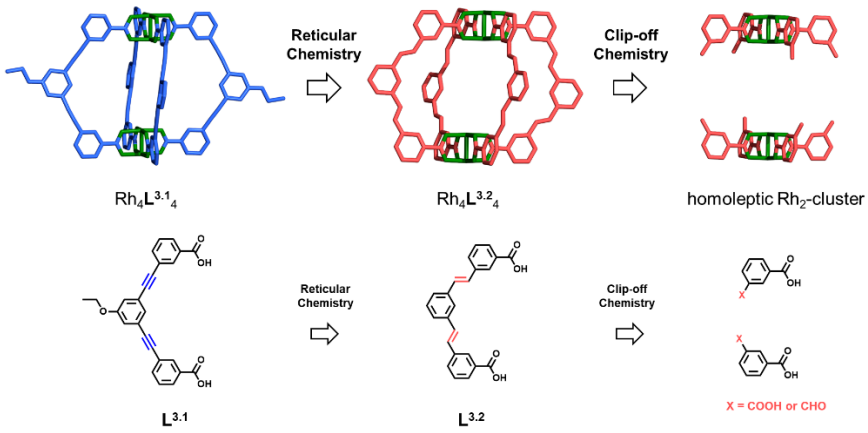

Figure 3.8. Synthesis of a new MOP by reticular synthesis (changing of a ligand that contains triple bonds with a ligand that contains double bonds) and Clip-off Synthesis of the new cluster obtained from the MOP.

First, we designed an analogous ligand to the triple bond lantern Rh_2-MOP ligand, $\mathbf{L}^{3.1}$, but with double bonds instead of triple bonds, $\mathbf{L}^{3.2}$. We synthesized $\mathbf{L}^{3.2}$ via the Heck reaction of 3-vinylbenzoic acid and 1,3-diiodobenzene in the presence of triphenylphosphine, triethylamine, and palladium (II) acetate in tetrahydrofuran (THF) at 80ºC (Reaction 3.4). The obtained crude was purified by precipitation from THF and, subsequently, washed with methanol. Finally, the ligand was characterized by ^{1}H-NMR (Figure 3.9 and Figure S3.1-S3.4).

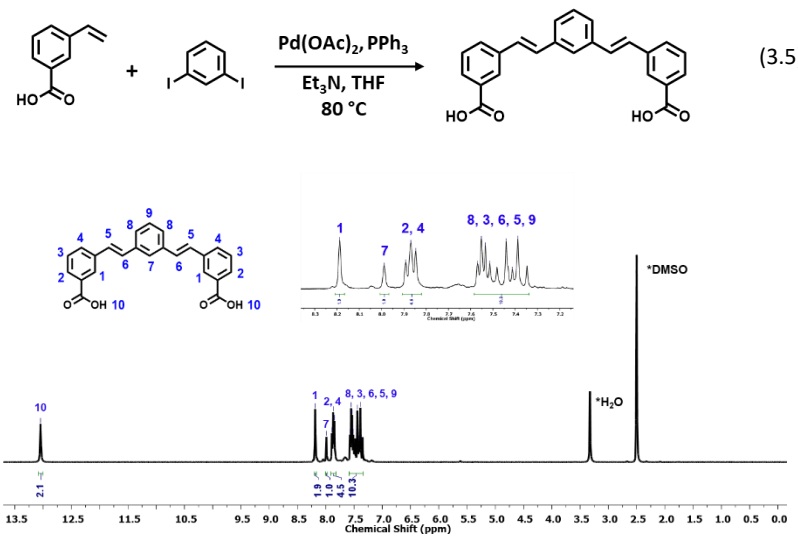

Figure 3.9. ^{1}H-NMR spectrum (400 MHz, DMSO-d$_6$) of $\mathbf{L^{3.2}}$.

Once we had the ligand containing the olefinic bonds, we proceeded with the synthesis of the new $Rh_4\mathbf{L^{3.2}}_4$. We solvothermally reacted 5 equivalents of the obtained $\mathbf{L^{3.2}}$ with rhodium acetate in the presence of Na_2CO_3 in dimethylacetamide (DMA) solvent at 100ºC for 72 h. This reaction yielded a brown solution, which was centrifuged to eliminate the Na_2CO_3 and the insoluble polymers formed during the reaction. The supernatant was added drop by drop to cold MeOH inducing the precipitation of a green powder. This green powder was cleaned three times with MeOH and characterized by ^{1}H-NMR, UV-vis, DOSY, and MALDI-TOF (Figure 3.10). The ^{1}H-NMR spectrum indicates that the ligands are coordinated, as observed from the broadening and slight displacement of the peaks compared to the positions of the free ligands. The DOSY shows that all the aromatic peaks correspond to the same molecule, or to several molecules with the same size. The UV-vis spectrum of $Rh_4\mathbf{L^{3.2}}_4$ in DMA shows the characteristic band centred at 595 nm. This band is attributed to the $\pi^* \rightarrow \sigma^*$ transition of Rh(II) paddlewheel clusters, further confirming the presence and stability of the

Rh_2-paddlewheel structure. MALDI-TOF spectrum of the product shows a peak that concurs with the expected molecular mass for a MOP made from the assembly of two Rh(II) paddlewheel SBUs and four $\mathbf{L^{3.2}}$ ligands $[Rh_4\mathbf{L^{3.2}}_4 + H]^+$ (expected = 1885.0; found = 1883.9).

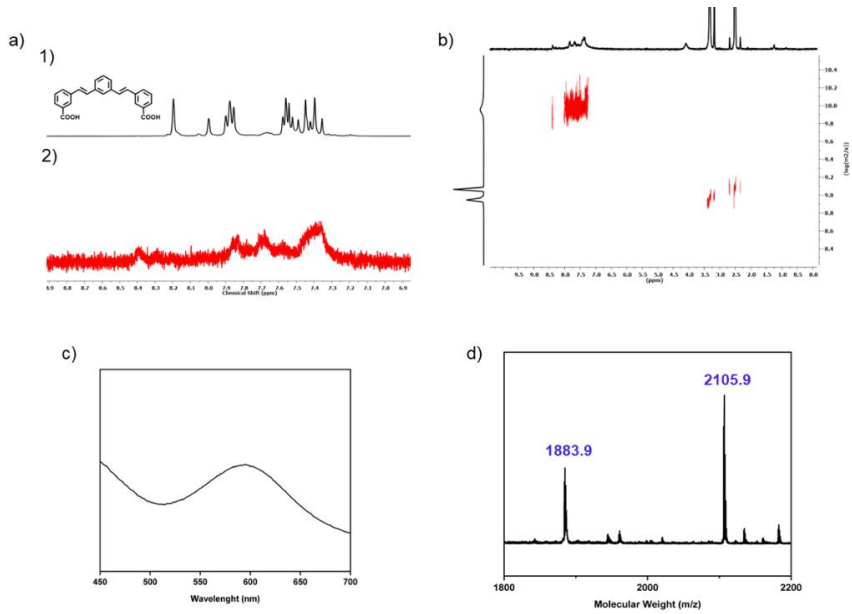

Figure 3.10. (a) ^{1}H-NMR spectra (400 MHz, DMSO-d_6) of (a_1) $\mathbf{L^{3.2}}$; and (a_2) $Rh_4\mathbf{L^{3.2}}_4$. (b) DOSY spectrum (400 MHz, DMSO-d_6) of $Rh_4\mathbf{L^{3.2}}_4$. (c) UV-vis spectrum of a solution of $Rh_4\mathbf{L^{3.2}}_4$ in DMA. The maximum of adsorption band I (λ_{max}) of $Rh_4\mathbf{L^{3.2}}_4$ is centered at 595 nm. (d) MALDI-TOF spectrum of $Rh_4\mathbf{L^{3.2}}_4$. The weight corresponding to the formula $[Rh_4\mathbf{L^{3.2}}_4 + H]^+$ has been highlighted: expected = 1885.0; found = 1883.9. The weight corresponding to the formula $[Rh_4\mathbf{L^{3.2}}_4(DMA)_2(H_2O)(MeOH) + H]^+$ has been highlighted: expected = 2109.2; found = 2105.9.

Finally, diffusion of diethyl ether into a DMA solution of this green powder in the presence of 4-*tert*-butylpyridine yields parallelepiped purple crystals. The single-crystal X-ray diffraction (SCXRD) data was collected at 'Bruker APEX-II CCD' at 150 K (CuK a radiation, λ = 1.54178 Å). SCXRD confirmed the formation of the expected $Rh_4\mathbf{L^{3.2}}_4$, built up from four $\mathbf{L^{3.2}}$ ligands and two Rh_2-clusters (Figure 3.11). The obtained MOP crystalized in the monoclinic $P2_1/c$ space group. The asymmetric unit is formed by two

halves of MOPs: two 4-*tert*-butylpyridine coordinated in the axial external positions of the Rh_2-paddlewheel and two DMA coordinated in the axial internal positions of the Rh_2-paddlewheel. Each half of MOP is built by two Rh atoms, located in different paddlewheel units, and by two $\mathbf{L^{3.2}}$ ligands.

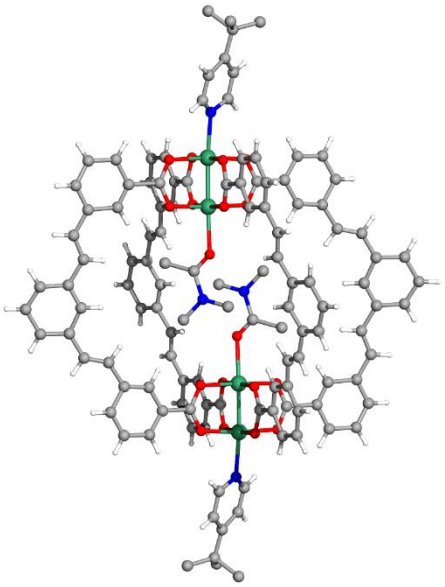

Figure 3.11. Crystal structure of $Rh_4\mathbf{L^{3.2}}_4$ with 4-*tert*-butylpyridine and DMA coordinated to the axial external and internal positions of the Rh_2-paddlewheel, respectively. Only one of the cages has been represented. The other cage has been omitted for clarity.

The formation of the expected $Rh_4\mathbf{L^{3.2}}_4$ was confirmed; however, two different isomers formed by different conformations of $\mathbf{L^{3.2}}$ could be observed by SCXRD. Each double bond of $\mathbf{L^{3.2}}$ can adopt two conformations, allowing the formation of three possible $\mathbf{L^{3.2}}$ conformations where the angles between binding sites are 0°. These possible conformations allow the formation of multiple isomers of the $Rh_4\mathbf{L^{3.2}}_4$ (Figure 3.12). In the crystal that we solved, two of these possible isomers were crystallized. Nevertheless, this fact does not affect the formation of our Rh_2-cluster as all the possible isomers break into the same Rh_2-cluster.

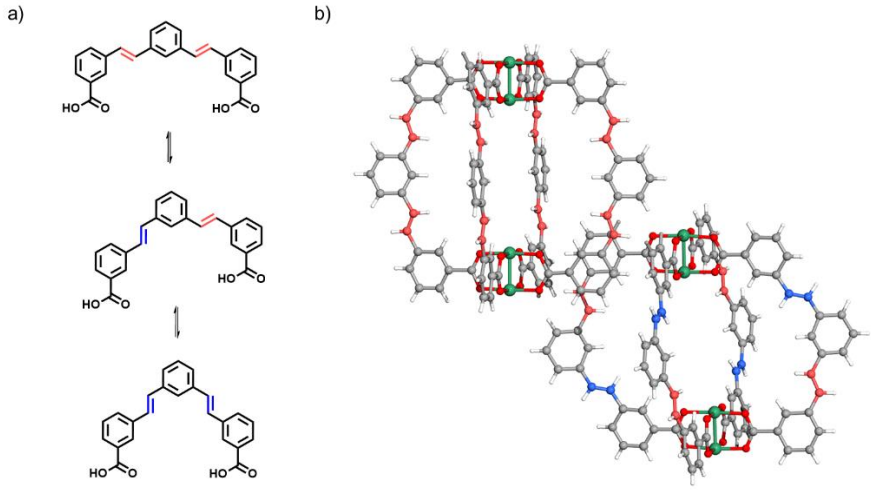

Figure 3.12. (a) Different $\mathbf{L^{3.2}}$ conformations where the angles between binding sites are 0°; and (b) crystal structure of the $Rh_4\mathbf{L^{3.2}}_4$: Two different isomers of the MOP can be detected. 4-*tert*-butylpyridine and DMA have been omitted for clarity.

3.2.5 Cleavage of the lantern MOP, $Rh_4\mathbf{L^{3.2}}_4$: synthesis of an homoleptic Rh_2-cluster functionalized with aldehyde groups

3.2.5.1 Ozonolysis cleavage of $\mathbf{L^{3.2}}$ containing olefinic bonds

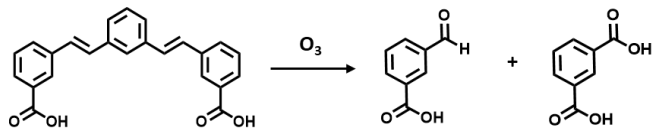

(3.6)

First, we confirmed the cleavage of the olefinic bonds of $\mathbf{L^{3.2}}$ by ozonolysis. To do so, $\mathbf{L^{3.2}}$ was initially dissolved in DMA and, subsequently, ozone was bubbled into this solution for 2 h. The ^{1}H-NMR of the reaction crude confirmed the total cleavage of the olefinic bonds of $\mathbf{L^{3.2}}$, as all the peaks corresponding to the $\mathbf{L^{3.2}}$ ligand completely disappeared (Figure 3.13a and 3.13b). The ^{1}H-NMR further confirmed the formation of 3-

formylbenzoic acid and isophthalic acid in a proportion of 1:0.4 (Figure 3.13b, 3.13c, and 3.13d).

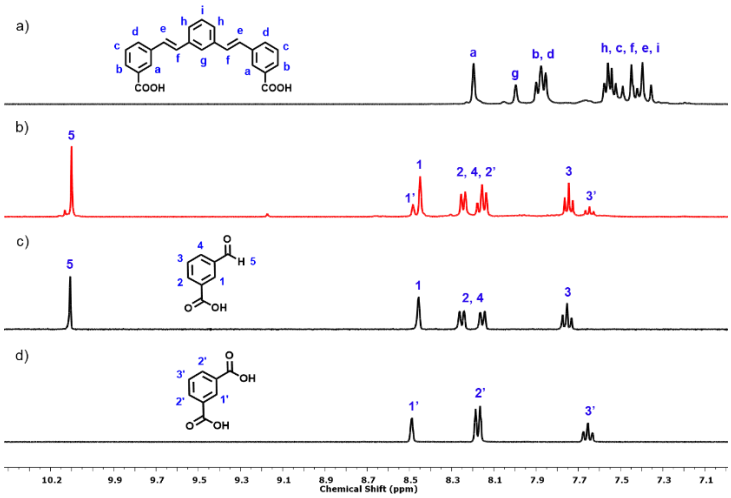

Figure 3.13. ^{1}H-NMR spectra (400 MHz, DMSO-d$_6$) of (a) $\mathbf{L^{3.2}}$; (b) ozonolyzed $\mathbf{L^{3.2}}$; (c) 3-formylbenzoic acid; and (d) isophthalic acid.

3.2.5.2 Ozonolysis cleavage of the lantern $Rh_4L^{3.2}{}_4$ MOP

After confirming that the $\mathbf{L^{3.2}}$ ligand can be easily cleaved by an ozonolysis reaction, we proceeded with the cleavage of $Rh_4\mathbf{L^{3.2}}_4$. First, 10 mg of $Rh_4\mathbf{L^{3.2}}_4$ were solubilized in 2 mL of DMA. Then, ozone was bubbled during 2.5 min. The obtained green solution was precipitated with acidic water and digested to analyse their organic building blocks. The ^{1}H-NMR of the digested sample shows that the starting ligand was completely cleaved and a mixture of 3-formylbenzoic acid and isophthalic acid (1:0.4 relation) was formed. In Figure 3.14, it is shown the comparation between the ^{1}H-NMR of the ozonized sample (Figure 3.14a), that of 3-formylbenzoic acid (Figure 3.14b), and that of isophthalic acid (Figure 3.14c) where we can observe that all the sample is composed by 3-formylbenzoic acid and isophthalic acid with no traces of the initial $\mathbf{L^{3.2}}$ ligand.

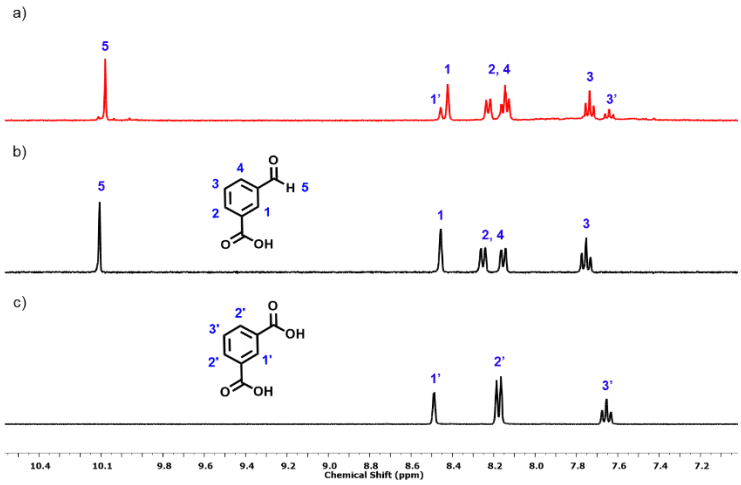

Figure 3.14. ^{1}H-NMR spectra (400 MHz, DMSO-d_6) of (a) digested homoleptic Rh_2-cluster synthesized by the ozonolysis of the $Rh_4\mathbf{L}^{3.2}{}_4$ in DMA; (b) 3-formylbenzoic acid; and (c) isophthalic acid.

In brief, we found that the cleavage reaction of $Rh_4\mathbf{L}^{3.2}{}_4$ had been successfully achieved, and that the initial paddlewheel Rh_2-clusters had survived to this cleavage reaction performed under the above-explained experimental conditions. However, following those experimental conditions, we experienced reproducibility issues. The cleavage reaction was found to be very sensitive to the reaction times since differences of few seconds resulted in incomplete cleavage of the starting MOP or in the formation of a yellow solution and therefore, in rhodium cluster decomposition. To solve this reproducibility issues, we explored the reactive properties of Rh_2-paddlewheel clusters. We found that Rh_2-paddlewheel clusters can coordinate donor ligands in their axial positions; a property that has been exploited to postsynthetically modify them or change their solubility.[18,19,60] In consequence, we hypothesized that blocking axial positions of Rh_2-paddlewheel clusters would prevent other molecules to attack them, thus increasing their stability under the ozonolysis conditions. For that reason, we decided to add a coordinative solvent to the reaction conditions. We added 1

mL of dimethyl sulfoxide, DMSO, to a solution of 1 mL of DMA and 10 mg $Rh_4\mathbf{L}^{3.2}{}_4$. When DMSO was added to a DMA MOP solution, DMSO coordinated to the rhodium clusters changing the solution colour from green to red and occupying the Rh_2-paddlewheel axial positions. The DMSO acted as protecting group increasing the stability of Rh_2 paddlewheels in the presence of ozone and making the reaction less dependent to reaction time. The reaction time could be increased to 7 minutes to ensure the total cleavage of double bonds without appreciating any Rh_2-paddlewheel decomposition. Any reproducibility problem was solved by working under these experimental conditions. Again, the ^{1}H-NMR of the digested ozonized MOP shows that the initial ligand was totally broken and that a mixture of 3-formylbenzoic acid and isophthalic acid with a proportion of 1:0.3 was formed (Figure 3.15).

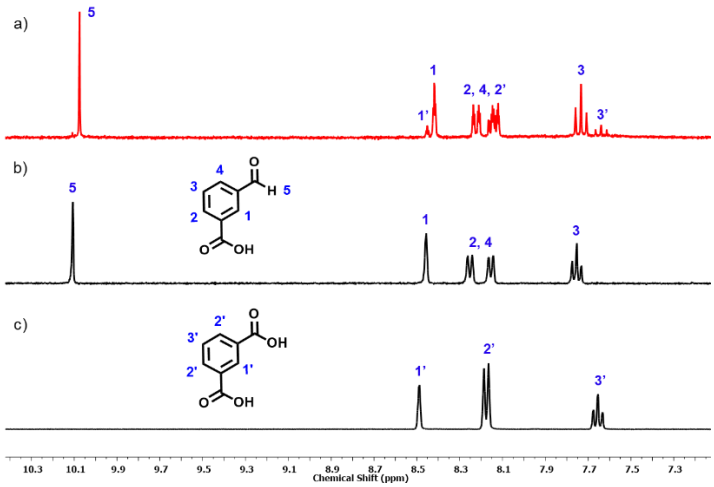

Figure 3.15. ^{1}H-NMR spectra (400 MHz, DMSO-d_6) of (a) digested homoleptic Rh_2-cluster synthesized by the ozonolysis of the $Rh_4\mathbf{L}^{3.2}{}_4$ in DMA: DMSO (1:1); (b) 3-formylbenzoic acid; and (c) isophthalic acid.

The mixture of 3-formylbenzoic acid and isophthalic acid appreciated in the ^{1}H-NMR of the digested sample of the cleaved $Rh_4\mathbf{L}^{3.2}{}_4$ indicates that a mixture of clusters functionalized with different amounts of

aldehydes and carboxylic acid groups was formed. The different functional groups are randomly distributed around the obtained molecules forming all the possible Rh_2-clusters: clusters formed by (1) four 3-formylbenzoic acid; (2) clusters formed by three 3-formylbenzoic acid and one isophthalic acid; (3) clusters formed by two 3-formylbenzoic acid and two isophthalic acid; (4) clusters formed by one 3-formylbenzoic acid and three isophthalic acid; and (5) clusters formed by four isophthalic acid. Since the proportion of 3-formylbenzoic acid and isophthalic acid found in the ^{1}H-NMR is one 3-formylbenzoic acid per 0.3 isophthalic acid, most of the products were probably those clusters fully functionalized with aldehyde groups and that with three 3-formylbenzoic acid and one isophthalic acid. We decided to purify the mixture resulting from the ozonolysis reaction, with the aim to isolate that cluster fully functionalized by four 3-formylbenzoic acid. In organic chemistry, it is common to purify acid or basic compounds changing their solubility by deprotonating or protonating them and then, taking advantage of this solubility change, to separate them from their impurities through an extraction. Inspired by this purification methodology, we decided to take advantage of the acidic character of the Rh_2-clusters functionalized with carboxylic acid groups. We hypothesized that, if a base is added to the reaction media, the clusters formed by at less one isophthalic acid ligand will be deprotonated acquiring negative charge and becoming soluble in water. On the contrary, those clusters fully functionalized with aldehyde groups will remain insoluble in water (Figure 3.16). Thus, we chose Na_2CO_3 as a soft base that does not damage the Rh_2 paddlewheel units.

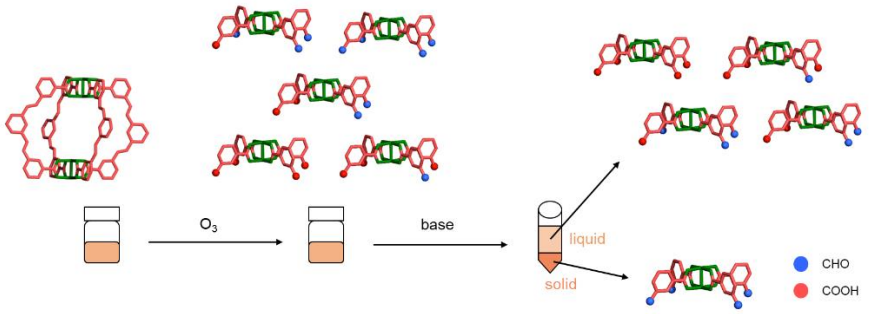

Figure 3.16. Schematic showing the experimental methodology used for the isolation of the aldehyde functionalized Rh_2-cluster.

We confirmed that, when we added a water solution of Na_2CO_3 to the reaction crude, the clusters fully functionalized with aldehydes precipitated forming a red solid, whereas those clusters containing at least one carboxylic acid group remained in the solution. After the precipitation, the obtained solid was first cleaned once with the solution of Na_2CO_3, and later, with a 3M solution of HCl until obtaining a green solid and discoordinating DMSO from the axial positions. ^{1}H-NMR of the digested Rh_2-cluster shows that our clusters were formed exclusively by 3-formylbenzoic acid, and that there were no traces of ligands functionalized with carboxylic acid groups (Figure 3.17).

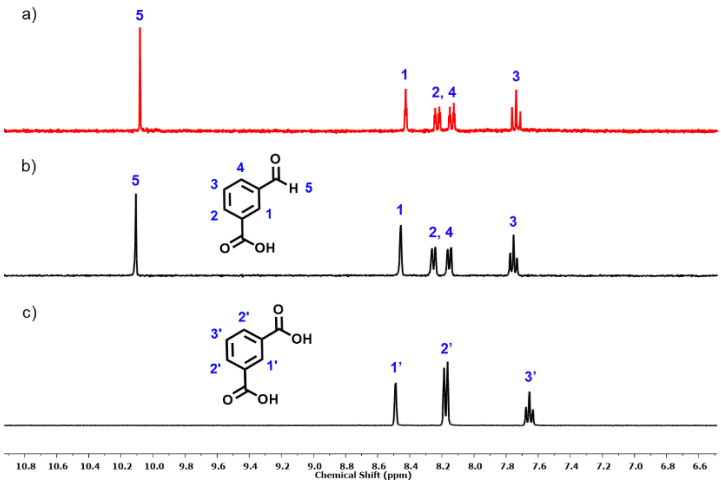

Figure 3.17. ^{1}H-NMR spectra (400 MHz, DMSO-d_6) of (a) digested homoleptic Rh_2-cluster synthesized by the ozonolysis of the $Rh_4\mathbf{L}^{3.2}{}_4$ in DMA : DMSO, (b) 3-formylbenzoic acid, and (c) isophthalic acid.

^{1}H-NMR of the non-digested sample and UV-vis spectrum show that Rh_2-paddlewheels had survived the reaction conditions. In the ^{1}H-NMR, we can observe that all the ligands were coordinated (Figure 3.18a_1), and that there were no traces of free ligands (Figure 3.18a_2). In the UV-vis spectrum of the cluster, we found the characteristic band centered at 597 nm ascribed to the $\pi^* \rightarrow \sigma^*$ transition of Rh^{2+} paddlewheel clusters (Figure 3.18b).

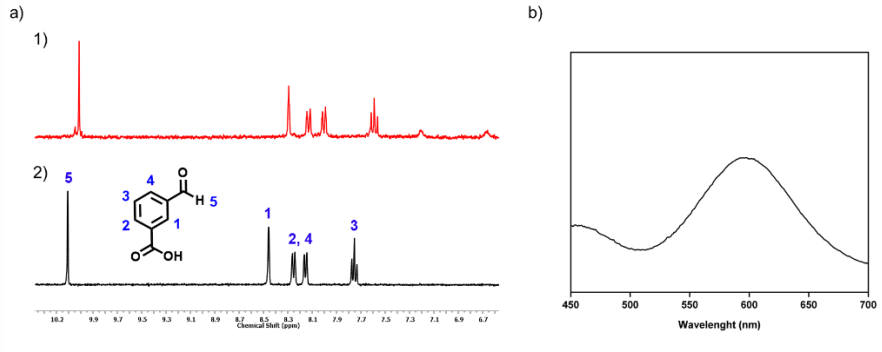

Figure 3.18. (a) ^{1}H-NMR spectra (400 MHz, DMSO-d_6) of (a_1) homoleptic Rh_2-cluster synthesized by the ozonolysis of the $Rh_4\mathbf{L}^{3,2}{}_4$ in DMA:DMSO and (a_2) 3-formylbenzoic acid. (b) UV-vis spectrum of a DMA solution of homoleptic Rh_2-cluster. The maximum of adsorption band I (λ_{max}) of $Rh_4\mathbf{L}^{3,2}{}_4$ is centered at 597 nm.

ESI mass spectroscopy confirms the exact mass of the ion $[Rh_2C_{32}H_{20}O_{12} + Na^+]^+$ (m/z = 824.8953), thus confirming the formation of the desired cluster. Also, the carbon isotopic distribution of the experimental spectrum clearly matches the simulated spectrum (Figure 3.19).

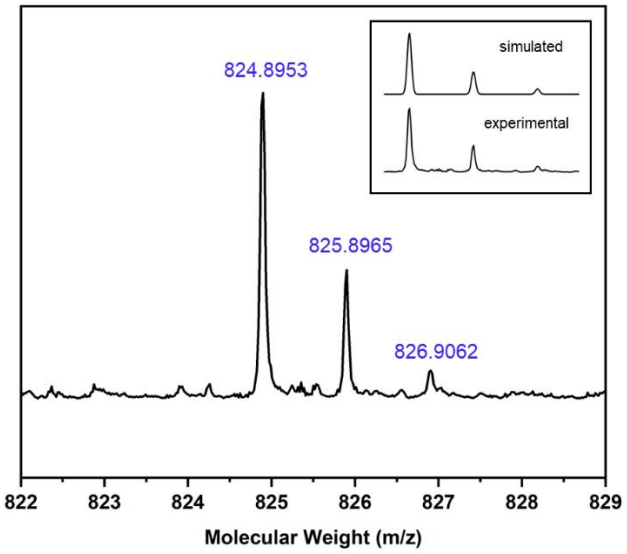

Figure 3.19. ESI mass spectroscopy spectrum of $Rh_2C_{32}H_{20}O_{12}$. The weight corresponding to the formula $[Rh_2C_{32}H_{20}O_{12} + Na^+]^+$ has been highlighted: expected = 824.8957; found = 824.8953.

Finally, we attempted to crystalize this cluster by solubilizing 2 mg of the cluster in 2 mL of MeOH and then adding 0.1 mL of hexane. The vial was left a bit open to let the solvents evaporate and, after one week, green crystals grew. The single crystals obtained were suitable for X-ray diffraction studies. The SCXRD data was collected using synchrotron radiation. SCXRD confirmed the formation of the expected homoleptic Rh_2-cluster but functionalized with two methoxys in each ligand instead of being functionalized with aldehyde groups. The obtained cluster crystalized in the monoclinic $P2_1/n$ space group. The asymmetric unit is formed by half of the cluster: one rhodium atom and two 3-(dimethoxymethyl)benzoic acid ligands. Extensive bonding takes place between the methoxy groups of one cluster and the axial positions of the Rh_2-paddlewheels of other clusters. Each cluster is bonded to four clusters by two methoxy groups of benzene rings located in *para* and the two axial positions of the Rh_2-paddlewheel, affording a 3D architecture.

As already mentioned, the obtained cluster is functionalized with methoxy groups instead of been functionalized with aldehyde groups. It should be mentioned that the high reactivity of the aldehyde groups makes easy to be attacked by nucleophile molecules, like MeOH (Figure 3.20). This reaction is catalysed by acid media, as acid protons can coordinate to aldehydes making them more electrophile (Figure 3.20). Since the crystallization was carried out in excess of MeOH and our cluster was cleaned with HCl 3M, the reaction between MeOH and aldehyde occurred during the crystallisation process forming acetals, which are functional groups formed by two methoxys.

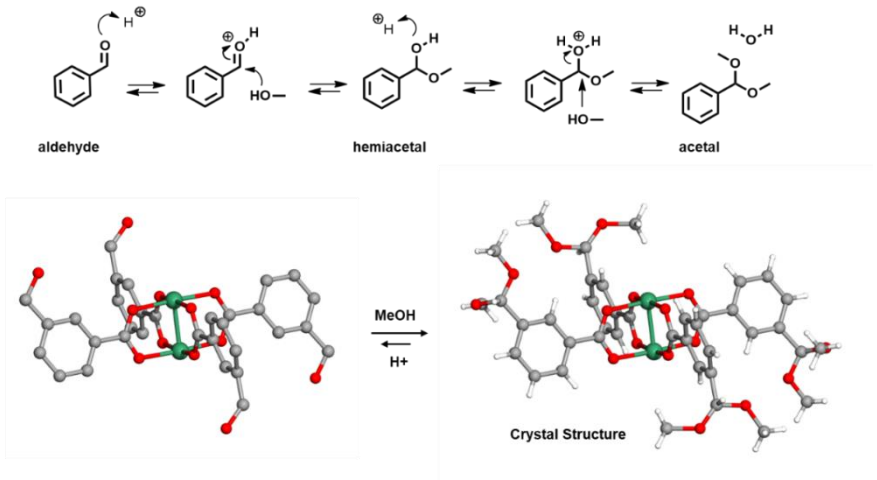

Figure 3.20. Mechanism of the formation of hemiacetals and acetals via the nucleophilic attack of MeOH in acid media (top). Crystal structure of the homoleptic Rh_2-cluster functionalized with acetals (down right).

To avoid the formation of acetals, we modified the crystallization solvent avoiding the use of MeOH or other nucleophilic solvents. We solubilized 2 mg of the aldehyde cluster in 1 mL of acetone, and then added 0.2 mL of water. We did not close the vial and the acetone was slowly evaporated overnight yielding green rod like crystals. The single crystals obtained were also suitable for X-ray diffraction studies. The SCXRD data was collected using synchrotron radiation. SCXRD confirmed the formation of the expected homoleptic Rh_2-cluster built by four 3-formylbenzoic acids and one Rh_2-paddlewheel (Figure 3.21). The obtained cluster crystalized in the monoclinic $P2_1/n$ space group. The asymmetric unit is formed by half of the cluster: one rhodium atom and two 3-formylbenzoic acids ligands. Extensive bonding takes place between the aldehyde groups of one cluster and the axial positions of other clusters. Each cluster is bonded to four clusters by two aldehyde groups of benzene rings located in *para* and the two axial positions of the Rh_2-paddlewheel units, affording a 3D architecture.

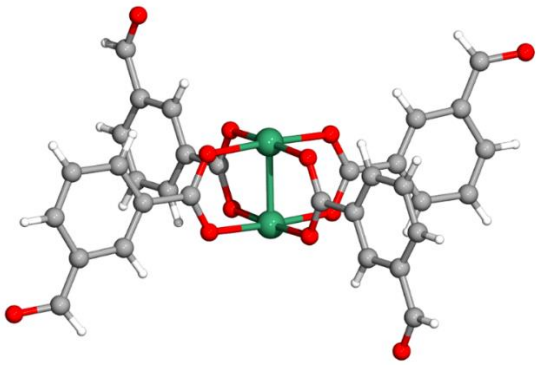

Figure 3.21. Crystal structure of the homoleptic Rh_2-cluster.

3.3 Conclusion

Summarizing, we have successfully synthesized a new homoleptic lantern Rh_2-MOP, $Rh_4\mathbf{L}^{3.2}{}_4$, containing olefinic bonds in known crystallographic positions. In doing so, we have achieved a required MOP towards its subsequent use as the precursor reagent in Clip-off Chemistry, overcoming the limitations of previously reported MOPs. Finally, we have successfully synthesized a new metal complex through the selective ozonolysis cleavage of the olefinic bonds of $Rh_4\mathbf{L}^{3.2}{}_4$ and, thus, we have provided the first example of the synthesis of a metal-organic compound through Clip-off Chemistry. Specifically, we have successfully synthesized an homoleptic Rh_2-cluster fully functionalized with aldehyde groups.

3.4 Experimental Part

3.4.1 Materials and Methods

Rhodium acetate was purchased from Acros Organics. Sodium carbonate (Na_2CO_3), 1,3-diiodobenzene, palladium(II) acetate, 4-*tert*-butylpyridine were purchased from TCI. Triphenylphosphine and hydrochloric acid 37% (HCl) were purchased from Sigma Aldrich. 3-Vinylbenzoic acid was purchased from Alfa Aesar. All deuterated solvents were purchased from Eurisotop. Diethyl ether, tetrahydrofuran (THF), methanol (MeOH) and dimethylacetamide (DMA) were purchased from Fischer Chemicals. All the reagents and solvents were used without further purification.

Ultraviolet-visible (UV−Vis) spectra were measured in an Agilent Cary 4000 at room temperature (ca. 25 °C). **Proton Nuclear Magnetic Resonance (^{1}H-NMR) spectra** were acquired in a Bruker Avance III 250SB NMR, 300SB NMR and a 400SB NMR spectrometer at "Servei d'Análisi Química" from Autonomous University of Barcelona (UAB). **Mass Spectroscopy (MALDI-TOF)** measurements were performed using a 4800 Plus MALDI TOF/TOF (ABSCIEX – 2010). The matrix used in each case was trans-2-[3-(4-*tert*-butylphenyl)-2-methyl-2-propenylidene]malononitrile (DCTB) measured in positive mode. **Acid digestions of Rh_2-MOP** were performed by adding 20 µL of DCl into a solution of 2 mg of Rh_2-MOP in 0.45 mL of DMSO-d_6 and heating the resulting solution at 100 ºC for 6 h.

3.4.2 Synthetic Methodologies

Synthesis of $Rh_4\mathbf{L}^{3.1}{}_4$: $Rh_4\mathbf{L}^{3.1}{}_4$ was synthesized following the previously reported synthetic method.[51] $\mathbf{L}^{3.1}$ (198 mg, 0.48 mmol), rhodium acetate (100 mg, 0.20 mmol), and Na_2CO_3 (53 mg, 0.50 mmol) were suspended in DMA (7 mL), sealed in a vial, and heated at 100 °C for 72 h. After cooling to room temperature, the Na_2CO_3 was separated from the resulting green suspension

by centrifugation. Single crystals were obtained after one week by layering 1 mL aliquot of the supernatant with MeOH (1:1).

Synthesis of 3,3'-((1E,1'E)-1,3-phenylenebis(ethene-2,1-diyl))dibenzoic acid ($\mathbf{L^{3.2}}$*):* 3-vinylbenzoic acid (2.22 g, 15 mmol), 1,3-diiodobenzene (2.22 g, 6.7 mmol), triphenylphosphine (177 mg, 0.67 mmol), triethylamine (10 mL) and palladium (II) acetate (120 mg, 0.53 mmol) were allowed to react in THF (20 ml) at 80 ºC for 24 h. The resulting suspension was filtered, and the obtained solution was evaporated under reduced pressure. The resulting solid was dissolved in a minimum amount of THF and precipitated with concentrated HCl (12 M). The white solid was separated by centrifugation and washed with small amounts of THF, MeOH and water (2.1 g, yield: 85 %).

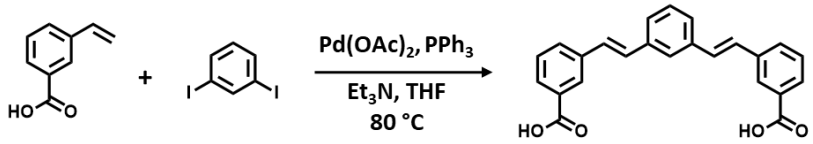

Synthesis of $Rh_4\mathbf{L^{3.2}}_4$*:* 400 mg of $\mathbf{L^{3.2}}$ (5 eq, 1.0 mmol), 115 mg of Na_2CO_3 (5 eq, 1.0 mmol), 100 mg of rhodium acetate (1 eq, 0.2 mmol), and 10 mL of DMA were sonicated for a few minutes and placed into a preheated oven at 100 ºC for 72 h. The obtained dispersion was centrifuged to separate the Na_2CO_3. The solution was precipitated into 30 mL of cold MeOH to obtain a green solid, which was washed three times with MeOH and dried in an oven at 85 ºC (49.8 mg; yield: 70 %).

$Rh_4\mathbf{L^{3.2}}_4$ crystallization: 2 mg of $Rh_4\mathbf{L^{3.2}}_4$ were dissolved in 0.5 mL of DMA and then, 200 µL of a 4-*tert*-butylpyridine solution (3 µL of 4-*tert*-butylpyridine in 1 mL of DMA) were added. Purple parallelepiped crystals were obtained by slow ether vapor diffusion into this solution.

Homoleptic Rh_2-cluster functionalized with aldehydes: 10 mg of $Rh_4\mathbf{L^{3.2}}_4$ were dissolved in 1 mL of DMA. 1 mL of DMSO was added. The obtained solution was centrifuged to removed possible particles that could not be solubilized. Ozone was bubbled for 7 minutes. 2.6 mL of a solution of 5 10^{-5} mol/L Na_2CO_3 were added. The obtained red solid was cleaned with the Na_2CO_3 solution and with HCl 3M to remove the DMSO obtaining a green solid. This green solid was dried under vacuum (2.8 mg; yield: 33%).

Acetal homoleptic Rh_2-cluster crystallization: 2 mg of the cluster were solubilized in 2 mL of MeOH. 0.1 mL of hexane were added. The solution was slowly evaporated forming crystals.

Aldehyde homoleptic Rh_2-cluster crystallization: 2 mg of the cluster were solubilized in 1 mL acetone. 0.2 mL of water were added. Acetone was slowly evaporated overnight forming rod-like crystals.

3.4.3 Crystallography

Crystallographic data for $Rh_4\mathbf{L}^{3.2}{}_4$ was collected at 'Bruker APEX-II CCD' at 100 K. Absorption correction was not applied in the case of $Rh_4\mathbf{L}^{3.2}{}_4$. Semiempirical multi-scan absorption correction was applied $Rh_4\mathbf{L}^{3.2}{}_4$ using SADAbs.[61] Crystallographic data for acetal homoleptic Rh_2-cluster and aldehyde homoleptic Rh_2-cluster were collected at 100 K at XALOC beamline at ALBA synchrotron (0.82653 Å).[62] Data were indexed, integrated and scaled using the XDS program.[63] The structures were solved by direct methods and subsequently refined by correction of F2 against all reflections, using SHELXT2018 within Olex2 package.[64,65] All non-hydrogen atoms were refined with anisotropic thermal parameters by full-matrix least-squares calculations on F2 using the program SHELXL2018.[64] The hydrogen atoms were calculated in their expected positions with the HFIX instruction of SHELXL2018 and refined as riding atoms with Uiso(H) = 1.5 Ueq(C). We treated the presence of solvent molecules in the cavities of all structures running solvent mask using Olex2 solvent mask.[66,67] Thermal motions of some benzene rings and acetal groups of acetal homoleptic Rh_2-cluster were restrained by DELU, SIMU and RIGU. Thermal motions of one of the aldehyde groups of aldehyde homoleptic Rh_2-cluster were restrained with DELU and SIMU. This aldehyde group was also restricted by DFIX. Reflections where I(obs) and I(calc) differ more than 10 times Sigma (W) were omitted, (homoleptic Rh_2-cluster) (-1 0 1) (-3 0 1).

$Rh_4L^{3.2}{}_4$

Formula	$C_{236}H_{144}N_6O_{36}Rh_8$
Formula weight ($g.mol^{-1}$)	4462.84
Temperature (K)	99.96
Wavelength (Å)	1.54184
Crystal system	monoclinic
Space group	$P2_1/c$
Unit cell dimensions	a = 20.755 Å; b = 25.129 Å; c = 27.268 Å
	α = 90°; β = 101.604°; γ = 90°
Volume/$Å^3$	13931
Z	2
Density calculated (g/cm^3)	1.064
Absorption coefficient (mm^{-1})	4.188
F(000)	4500.0
Crystal size (mm)	0.05 × 0.05 × 0.03
2Theta range for data collection (°)	4.346 to 102.042
Index ranges	$-20 \leq h \leq 20$, $-25 \leq k \leq 25$, $-27 \leq l \leq 27$
Reflections collected	133904
Independent reflections	14656 [R_{int} = 0.1075, R_{sigma} = 0.0591]
Refinement method	Full-matrix least-squares on F2
Data / restraints / parameters	14656/48/1229
Goodness-of-fit on F^2	1.081
Final R indices [I>2sigma(I)]	R_1 = 0.1220, wR_2 = 0.3172
R indices (all data)	R_1 = 0.1572, wR_2 = 0.3504
Largest diff. peak and hole	1.82, -1.04e $Å^{-3}$

Acetal homoleptic Rh_2-cluster

Formula	$C_{40}H_{44}O_{16}Rh_2$
Formula weight ($g.mol^{-1}$)	986.57
Temperature (K)	100
Wavelength (Å)	0.82653
Crystal system	monoclinic
Space group	$P2_1/n$
Unit cell dimensions	a = 10.387 Å; b = 12.325 Å; c = 18.309 Å
	$\alpha = 90°$; $\beta = 100.96°$; $\gamma = 90°$
Volume/$Å^3$	2301.2
Z	2
Density calculated (g/cm^3)	1.424
Absorption coefficient (mm^{-1})	0.781
F(000)	1004.0
Crystal size (mm)	0.09 x 0.1 x 0.7
2Theta range for data collection (°)	4.006 to 48.812
Index ranges	$-12 \leq h \leq 11$, $0 \leq k \leq 14$, $0 \leq l \leq 21$
Reflections collected	22158
Independent reflections	3750 [R_{int} = 0.1364, R_{sigma} = 0.1153]
Refinement method	Full-matrix least-squares on F2
Data / restraints / parameters	3750/85/240
Goodness-of-fit on F^2	1.103
Final R indices [I>2sigma(I)]	R_1 = 0.0928, wR_2 = 0.2643
R indices (all data)	R_1 = 0.1152, wR_2 = 0.2764
Largest diff. peak and hole	1.84, -0.61e $Å^{-3}$

Aldehyde homoleptic Rh_2-cluster

Formula	$C_{32}H_{20}O_{12}Rh_2$
Formula weight ($g.mol^{-1}$)	802.30
Temperature (K)	100
Wavelength (Å)	0.82653
Crystal system	monoclinic
Space group	$P2_1/n$
Unit cell dimensions	a = 12.819 Å; b = 10.606 Å; c = 14.344 Å
	α = 90°; β = 97.89°; γ = 90°
Volume/$Å^3$	1931.7
Z	2
Density calculated (g/cm^3)	1.379
Absorption coefficient (mm^{-1})	1.360
F(000)	796.0
Crystal size (mm)	0.23 × 0.08 × 0.08
2Theta range for data collection (°)	5.334 to 54.7
Index ranges	$-14 \leq h \leq 14$, $0 \leq k \leq 11$, $0 \leq l \leq 15$
Reflections collected	16360
Independent reflections	2761 [R_{int} = 0.1560, R_{sigma} = 0.1103]
Refinement method	Full-matrix least-squares on F2
Data / restraints / parameters	2761/10/208
Goodness-of-fit on F^2	1.001
Final R indices [I>2sigma(I)]	R_1 = 0.0570, wR_2 = 0.1506
R indices (all data)	R_1 = 0.0728, wR_2 = 0.1571
Largest diff. peak and hole	1.46, -0.83 e $Å^{-3}$

4.4.4 Characterization

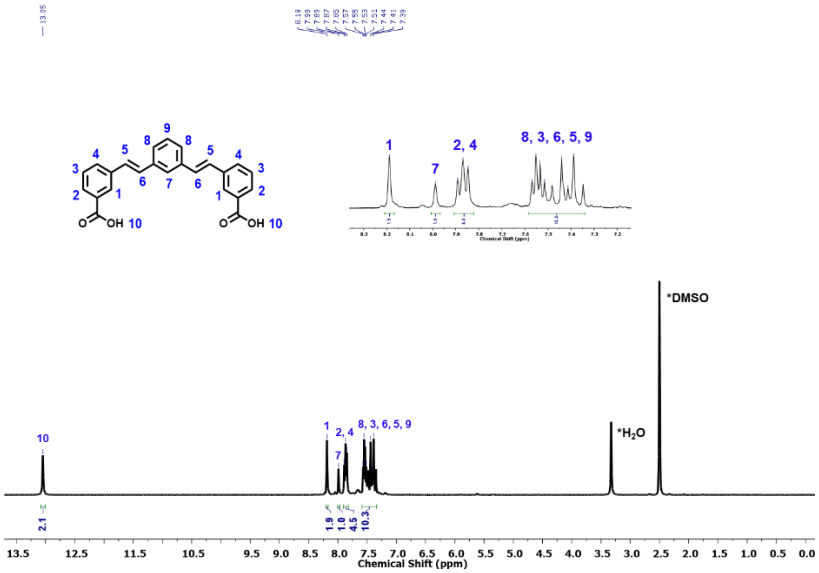

Figure S3.1: ^{1}H-NMR spectrum (400 MHz, DMSO-d_6) of $\mathbf{L^{3.2}}$.

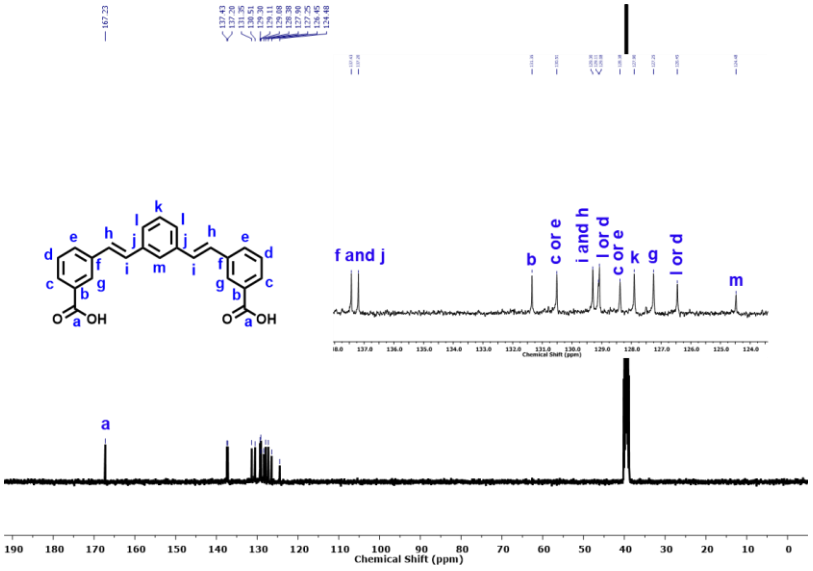

Figure S3.2: ^{13}C-NMR spectrum (400 MHz, DMSO-d_6) of $\mathbf{L^{3.2}}$.

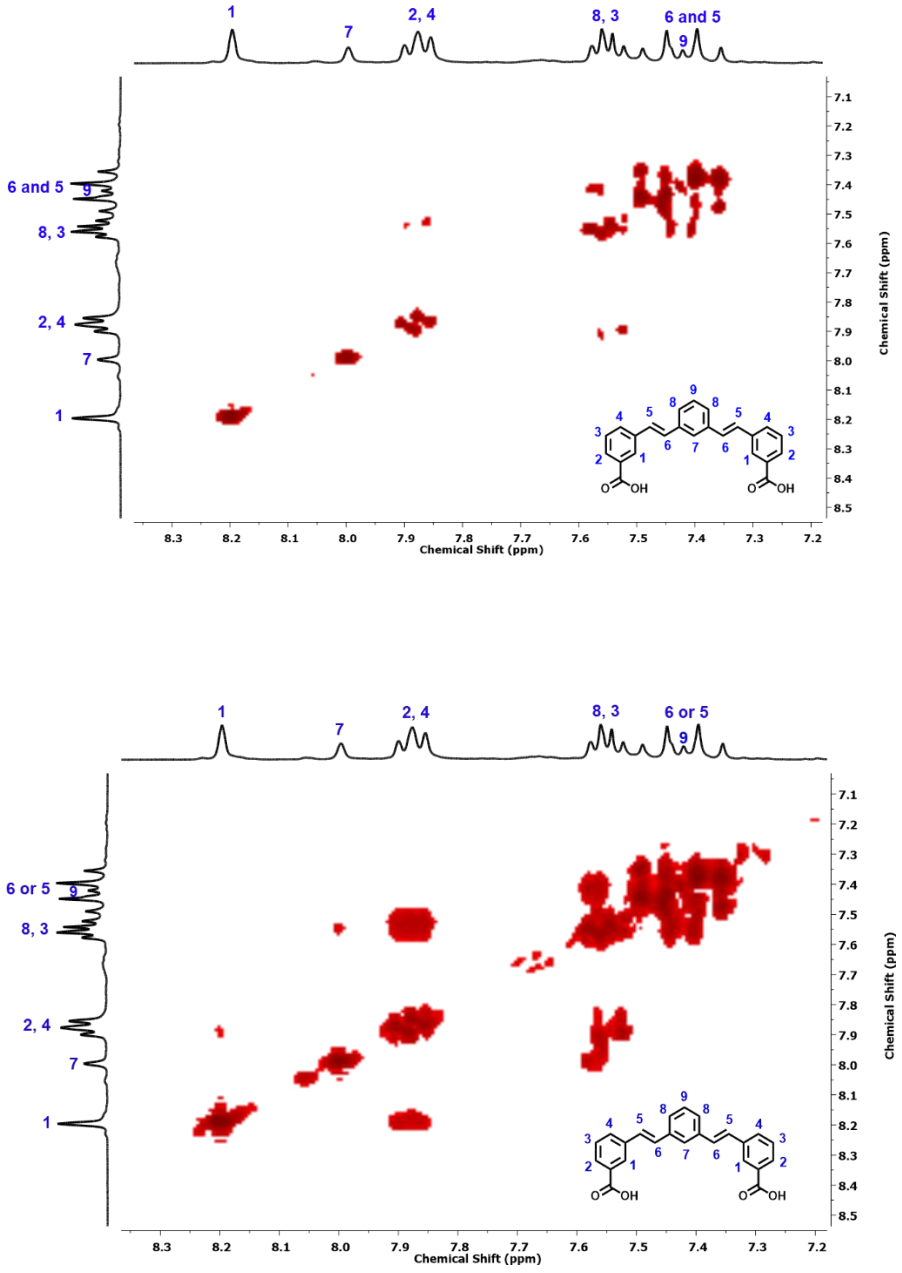

Figure S3.3. COSY spectrum (400 MHz, DMSO-d_6) of $\mathbf{L}^{3.2}$.

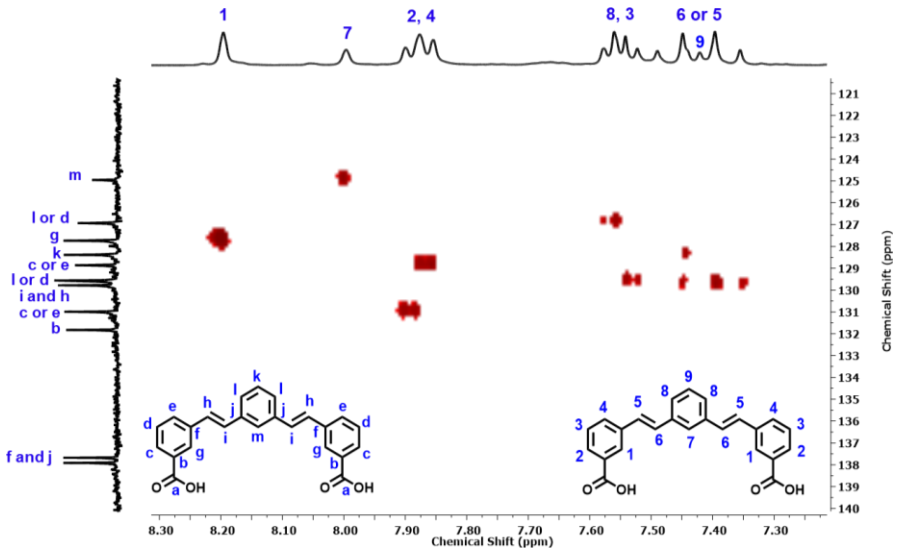

Figure S3.4. HSQC spectrum (400 MHz, DMSO-d_6) of $\mathbf{L}^{3.2}$.

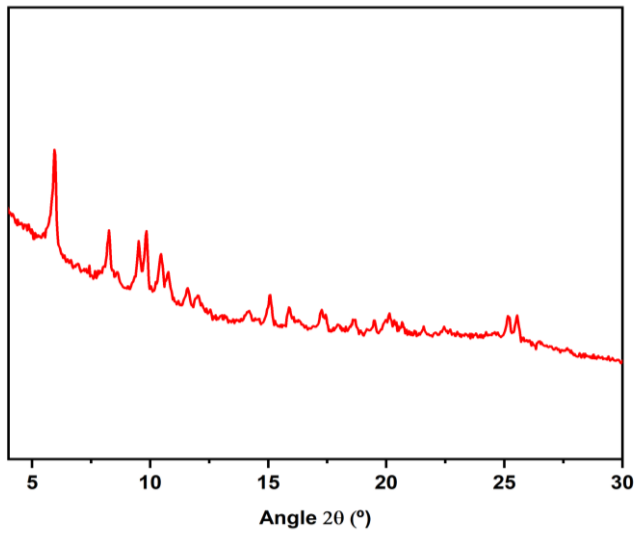

Figure S3.5. Experimental PXRD diffractogram of the previously reported $Rh_4\mathbf{L}^{3.1}{}_4$ MOP.

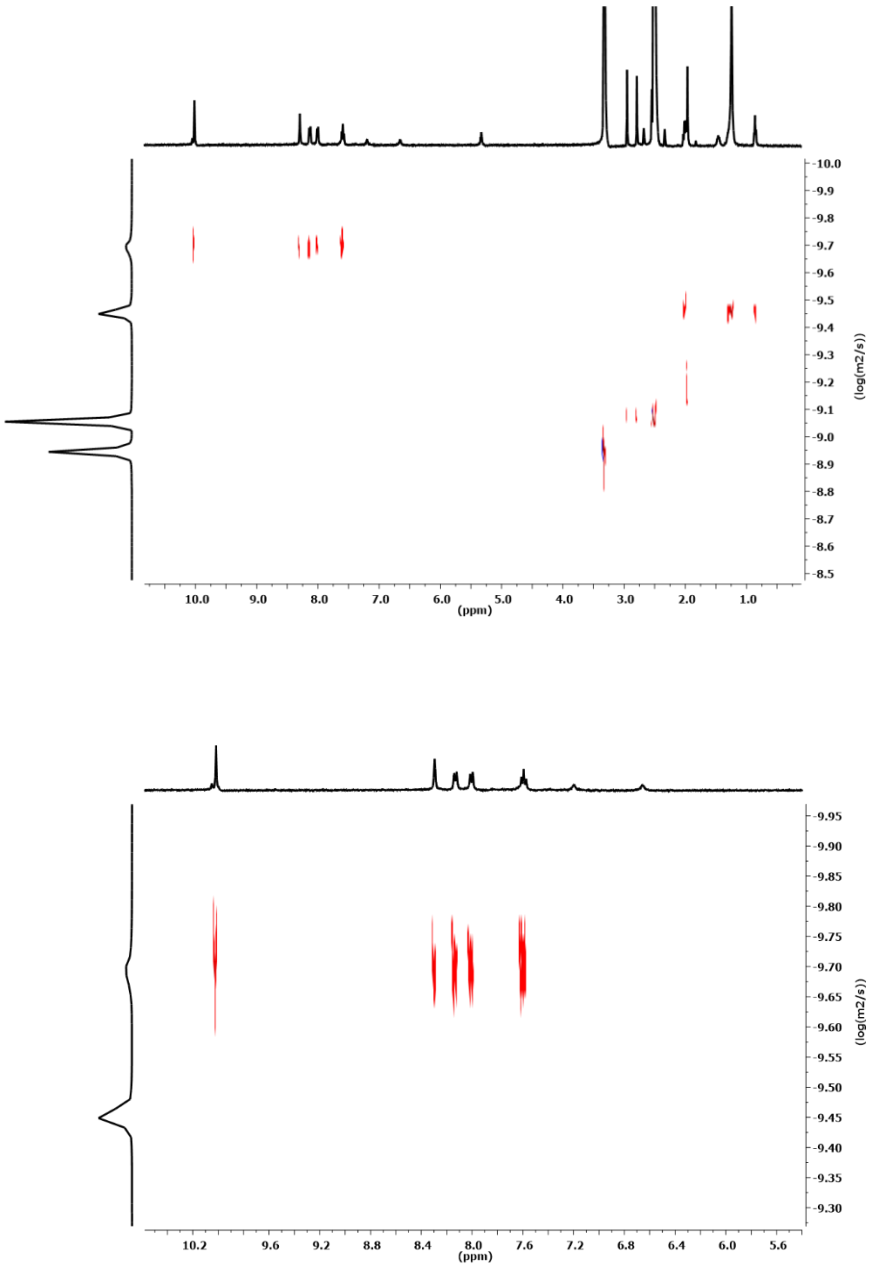

Figure S3.6. DOSY spectrum (400 MHz, DMSO-d_6) of homoleptic Rh_2-cluster.

Chapter 4

Synthesis of a family of trigonal antiprismatic heteroleptic $Rh_{12}L_6L'_6$ MOPs

4.1 Introduction

MOPs are nanoscale, zero-dimensional, discrete molecular cages comprising metal ions and clusters connected via organic ligands.[21,49] Owing to their molecular nature, they are soluble in various solvents, which facilitates their liquid processability, their use in the liquid phase for recognition and transport of molecules,[17,18] and stoichiometric control over their post-synthetic functionalisation.[19,68] Moreover, MOPs are porous in the solid state. However, the initial reports on the permanent porosity of MOPs have revealed only modest Brunauer-Emmett-Teller surface areas (S_{BET}), ranging from 10 m^2/g to 200 m^2/g. These low values have been attributed to the lack of structural stability of MOPs and to their lack of long-range order, which derives from their monomeric nature. However, researchers have recently reported much higher S_{BET} values, ranging from 600 m^2/g to 1300 m^2/g, for certain robust MOPs that contain strong carboxylate-metal ion bonds.[69,70] In particular, the use of Zr(IV),[71] Mo(II),[72] Cr(II),[73] and Rh(II)[55] has provided access to new MOPs that are more porous and structurally more robust. Nevertheless, the reported MOPs that exhibit permanent porosity fall into three main geometric classes: cuboctahedra (most of which are analogous to the archetypical $Cu_{24}(bdc)_{24}$ structure),[21,49] octahedra,[50] or tetrahedra.[71] Less common geometries include cubes,[74] cigars,[75] lanterns,[51] triangular prisms,[76] icosahedra[77] and dodecahedra.[78]

Most of these reported MOPs are built by a single type of ligand or edge linking the clusters or vertices. If we apply Clip-off Chemistry to an homoleptic MOP, cleavable bonds will need to be introduced to all the ligands of the MOP. Thus, when the cleavable reaction is applied, all the ligands are expected to be broken, releasing an homoleptic metal cluster (*Chapter 3*). One way to diversify the catalog of MOPs and increase the possibilities and complexity of the metal complexes obtained through the use of MOPs as precursors in Clip-off Chemistry is to assemble new cages using at least two different ligands. Although the use of mixed ligands has been

widely applied to MOFs and COFs,[79] it remains relatively unexplored for MOPs[80]. It must be noted that multiple ligands can assemble into a single heteroleptic cage structure while leading to undesired concomitant formation of single-component homoleptic cages, mixtures of different multicomponent cages, and/or extended 2D or 3D networks. To face this challenge, researchers have proposed various synthetic methodologies, including the use of guest molecules as structure-directing agents or templates, and steric effects or shape-complementarity of ligands with different geometries.[81]

Few paddlewheel M_2-MOPs made of mixed-ligands have been reported. There are a few more reported examples of mixed-ligand palladium cages. Palladium cages and paddlewheel M_2-MOPs are geometrically analogous as both are constructed from square planar 4-c SBUs built by one metal and four pyridine ligands in the case of palladium cages, and by two metals and four carboxylate ligands in the case of paddlewheel M_2-MOPs. That fact makes that reported palladium cages can be used as source of inspiration to design new paddlewheel M_2-MOPs, and the other way around. Reported mixed ligand MOPs and cages can be classified in three groups depending on the geometric relation between their different kinds of ligands: (1) MOPs and cages built by analogous ligands; (2) MOPs and cages built by ligands with the same angle between binding sites but different length between these sites; and (3) MOPs and cages built by ligands with a different angle between binding sites.

(1) MOPs and cages built by analogous ligands: These cages are constructed using two or more types of analogous ligands. All the ligands used in their construction have the same lengths and angles between their binding sites. The geometry of the mixed-ligand cage is identical to the geometry of two homoleptic cages constructed separately using each type of ligand. Lantern-type cages represent the majority of reported examples of this type of cages, although we have also encountered two cuboctahedral cages constructed with analogous ligands.[53,82] Since the various types of ligands are

geometrically equivalent, each ligand can occupy any of the geometric positions within the cage. Consequently, mixtures of several compounds containing different proportions and locations of each type of ligand are frequently obtained (Figure 4.1a).

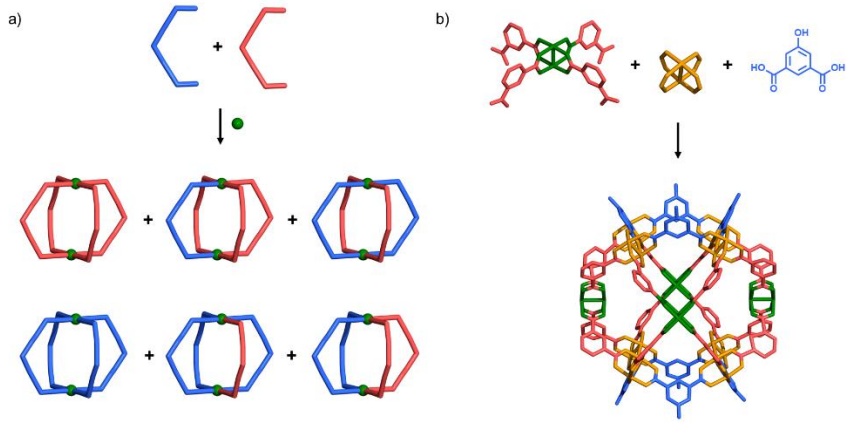

Figure 4.1. (a) Mixture of lantern-type cages which can be obtained by mixing two kinds of analogous ligands. (b) ‘‘Triblock Janus-type’’ MOP built by two types of ligands which are analogous between them in terms of length and connectivity. This ‘‘triblock Janus-type’’ is built by mixing a pre-synthesized rhodium cluster composed of one type of ligand, copper, and another kind of ligand. If the components are in the reported proportions, there is only one possible MOP that can be built using this method. However, if the proportion is different, the fragments can be located in different positions inside the MOP.[53]

Some researchers have been able to control this problem by introducing bulky ligands into key positions of the cages. For example, one of the ligands can be functionalized with a bulky group positioning it at the centre of the cage during its assembly. Thus, only one ligand with a bulky group can fit into the cage, so the other ligands used to construct the cage must be the non-functionalized one (Figure 4.2a).[82,83] There are also reported examples where the inner or the outside part of the cages near the metal SBUs is functionalized, in a way that the bulky groups of different ligands interact each other, favouring, in most cases, the formation of a *cis* lantern (Figure 4.2b).[84–86]

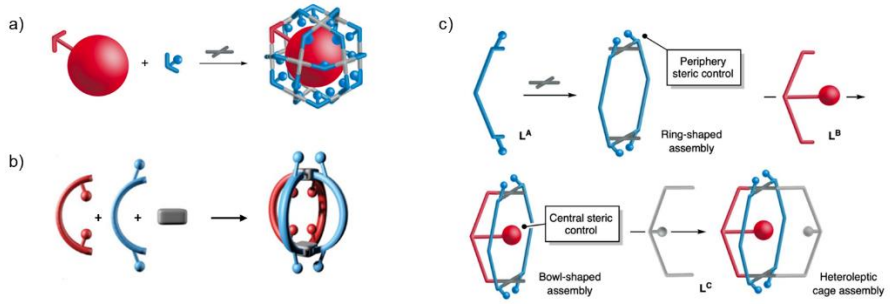

Figure 4.2. (a) Construction of an heteroleptic cuboctahedra coordination cage by utilizing central steric control.[82] (b) Construction of heteroleptic *cis*-lantern coordination cage by utilizing inside and periphery steric control.[86] (c) Construction of a three ligand heteroleptic lantern coordination cage by utilizing central and periphery steric control and a step-by-step strategy.[87] Image reprinted with permission from reference 87. Copyright 2023 John Wiley and Sons.

(2) MOPs and cages built by ligands with the same angle between binding sites but different length: These cages are built by ligands which have the same angle between binding sites but different distance between these sites. In this case, the geometry of the mixed-ligand cage is similar to the geometry of the two homoleptic cages built by each ligand separately. As a result, the geometry of the cage made of different ligands will be distorted because of the different length of the ligands or it may vary between geometries of the same family, such as between cuboctahedra/anticuboctahedra. In Figure 4.3, it is shown a mixed-ligand anticuboctahedra cage (Figure 4.3a) and a mixed-ligand cuboctahedra MOP (Figure 4.3b) built by two ligands with an angle of 120° between binding sites but with different distance between binding sites.[88,89]

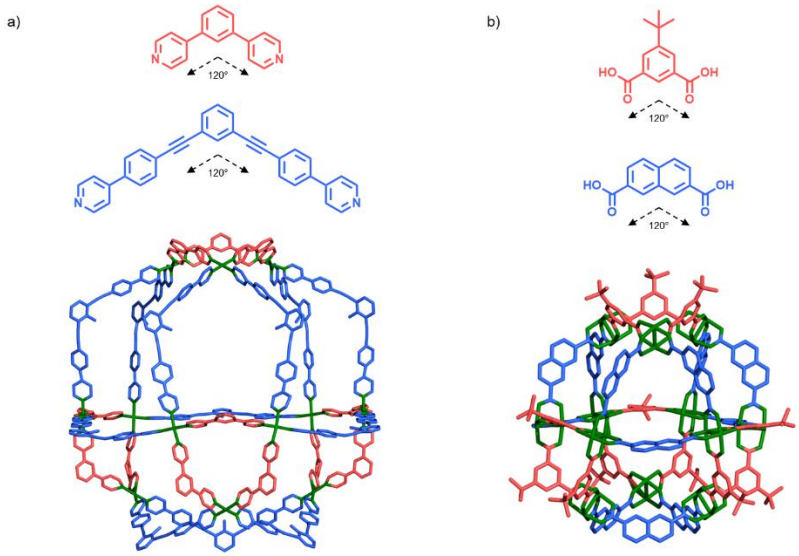

Figure 4.3. (a) Distorted anticuboctahedra or pseudocantellated tetrahedron cage built by two ligands with a bridging angle of 120°.[88] (b) Distorted cuboctahedra MOP built by two ligands with a bridging angle of 120°.[89]

(3) MOPs and cages built by ligands with different angle between binding sites: These cages are built with ligands that have different angle between binding sites. The shapes of the two types of ligands should be geometrically complementary to each other as a closed cage must be assembled. In most of the cases, the geometry of the mixed-ligand cage is different to the geometry of the two homoleptic cages built by each ligand separately. The most commonly reported cages of this type of cages are lantern-type cages, where frequently the binding sites of one ligand point outside while the binding sites of the other ligand point inside (Figure 4.4).[90–98] Ligands that exhibit an angle equal to zero between binding sites or an angle close to zero can form homoleptic lantern-type cages. On the other hand, ligands with higher angles will form other types of homoleptic structures when combined individually with the metal.

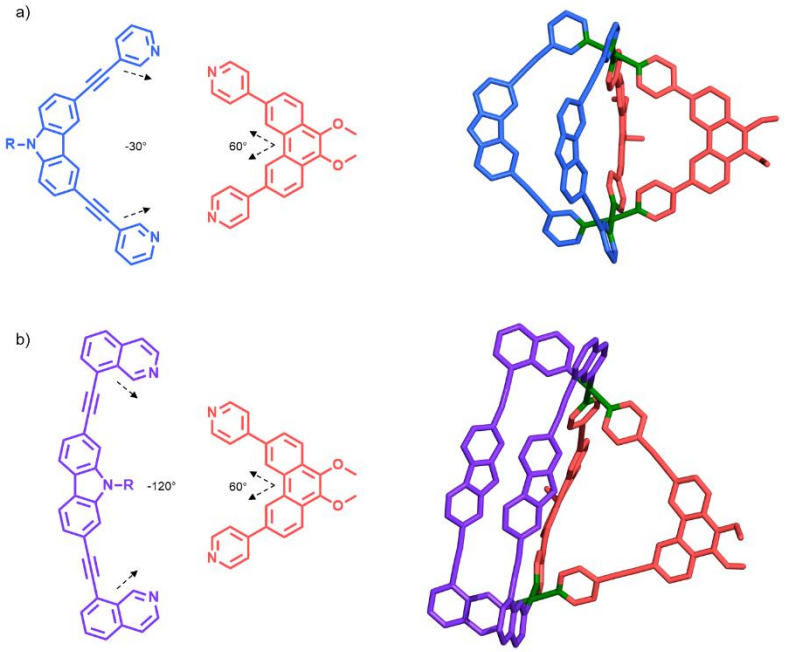

Figure 4.4. Formation of a lantern with two ligands with different angle between binding sites. One of the ligands have the binding sites pointing outside, whereas the other ligand has the binding sites pointing inside (one could consider that one ligand has negative angle and the other ligand has positive angle).[96,98]

There is also the case of trigonal antiprismatic, or distorted octahedral cages[99] or MOPs,[89,100–102] which are assembled from connecting six metal ions/paddlewheel clusters through six ligands with a 60° angle between binding sites and six ligands with a 120° bent angle between binding sites. Note that the average of the angles is 90°, which is the angle of a non-distorted octahedral cage. These cages are composed by two trigonal macrocycles, each one built up from connecting three metal ions/clusters through three ligands of the same type. Both trigonal macrocycles, which form the top and bottom facets of the antiprism, are connected through six ligands of the other type, which are in the equatorial positions of the antiprism (Figure 4.5). In the case of the cage, the 60° and 120° ligands are located in axial and

equatorial positions, respectively, whereas in the case of the reported MOPs, the positions are inverted. The ligand with a bridging angle of 120° gives an homoleptic MOP with cuboctahedra geometry, whereas the ligand with a bridging angle of 60° can give various types of homoleptic structures such as triangles, squares, or tetrahedra.

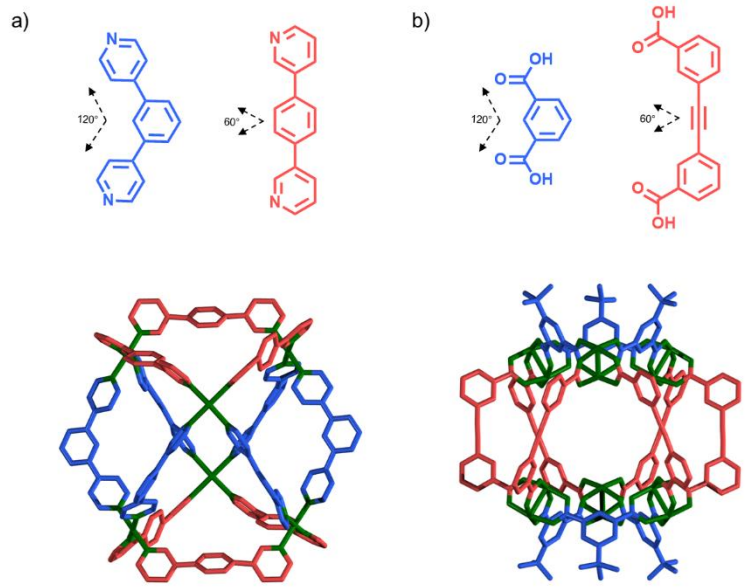

Figure 4.5. (a) Palladium trigonal antiprismatic cage.[99] (b) Copper trigonal antiprismatic MOP.[89]

Additionally, it exists the hendecahedra MOPs that are formed by the connection of nine clusters through six ligands with a bridging angle of 90° and twelve ligands with a bridging angle of 120°. The six ligands with a bridging angle of 90° form two triangular windows at the top and bottom positions of the MOP, which are linked by twelve ligands exhibiting a bridging angle of 120° and three clusters located in the equatorial positions of the MOP forming six triangular windows and three distorted square windows (Figure 4.6).[103] This hendecahedra MOP geometry can be formed by symmetrical and asymmetrical ligands with a 120° angle between binding

sites. It should be noticed that using only the symmetric ligand with a bridging angle of 120° gives an homoleptic MOP with a cuboctahedra geometry, whereas using only the ligand with a bridging angle of 90° can give an octahedral MOP.

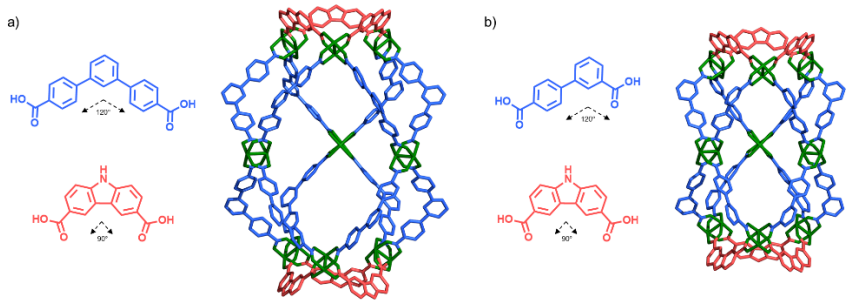

Figure 4.6. Hendecahedra MOPs built by ligands with 90° and 120° angles between binding sites. The 120° ligand can be symmetric (a) or asymmetric (b).

Various cages resulting from the combination of a ligand with a bridging angle of 0° and a ligand with bridging angles of 120°, 149°, or 180° have also been reported. In these cages, two ligands with a bridging angle of 0° are coordinated to each metal in a *cis* configuration. These ligands act as corners and prevent the growth of the cage in blocked directions, thereby hindering the formation of a cuboctahedron (bridging angle of 120°), a rhombicuboctahedron ($M_{24}L_{48}$), a $M_{30}L_{60}$ cage (bridging angle of 149°), or a network (bridging angle of 149°). Alternatively, the heteroleptic cages shown in Figures 4.7 are formed.[104]

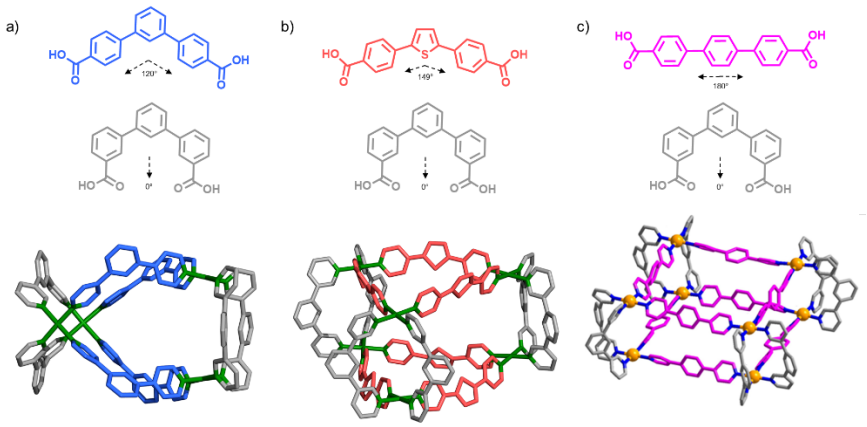

Figure 4.7. Heteroleptic cages (a) $[Pd_4(\mathbf{L}^{\mathbf{0}^\circ})_4(\mathbf{L}^{\mathbf{120}^\circ})_4]^{8+}$, b) $[Pd_6(\mathbf{L}^{\mathbf{0}^\circ})_6(\mathbf{L}^{\mathbf{149}^\circ})_6]^{12+}$ and c) $[Pd_8(\mathbf{L}^{\mathbf{0}^\circ})_8(\mathbf{L}^{\mathbf{180}^\circ})_8]^{16+}$. Image adapted with permission from reference 104. Copyright 2021 John Wiley and Sons.

Among all the analysed reported examples, there are only four types of mixed-ligand paddlewheel-MOPs. Interestingly, only two of these types of MOPs are constructed using non-analogous ligands: the trigonal antiprismatic MOP and the hendecahedral MOP. Both MOPs are built using Cu_2 paddlewheel clusters. To apply our Clip-off Chemistry to a mixed-ligand MOP, we first need to expand the library of available Rh_2-MOPs as robust mixed-ligand MOPs that can stand typical ozonolysis conditions are needed. With this objective in mind, we have decided to choose the trigonal antiprismatic MOP because it should be feasible to assemble this particular MOP using ligands that contain olefinic bonds through Reticular Chemistry. The trigonal antiprismatic MOP consists of two trigonal macrocycles positioned axially within the MOP, connected to each other by six ligands in the equatorial positions (Figure 4.8).

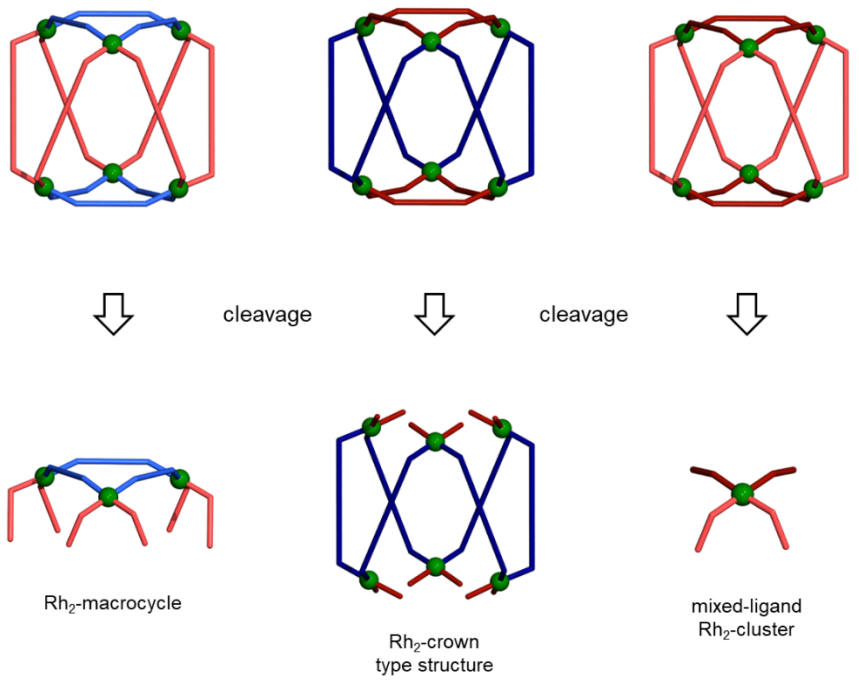

Figure 4.8. Different trigonal antiprismatic Rh_2-MOP that can be built by locating cleavable (red) and non-cleavable (blue) bonds in known positions of the Rh_2-MOP (top). Different types of coordination complex that can be synthesized by breaking the cleavable bonds (bottom).

If we apply Clip-off Chemistry to this type of trigonal antiprismatic MOP, we can synthesize three different types of M_2-complex depending on the positions of the cleavable bonds: (1) a M_2-macrocycle by locating the cleavable bonds in the equatorial positions of the MOP (*Chapter 5*); (2) a M_2-crown type structure by locating the cleavable bonds in the axial positions; and finally, (3) a mixed-ligand M_2-cluster locating the cleavable bonds in both axial and equatorial positions (*Chapter 6*). Direct synthesis of these M_2-complexes would be exceedingly challenging or even impossible, as the spontaneous assembly of the building blocks in this precise manner, without the formation of mixtures of other M_2-complexes, MOPs, or extended structures, is highly unlikely. Moreover, the synthesized M_2-complexes will

be functionalized with aldehyde or carboxylic acid groups, further intensifying the difficulty of their direct synthesis.

In this Chapter, we report the synthesis of a family of 12 new heteroleptic trigonal antiprismatic MOPs, expanding the catalog of available porous MOPs and the amount of possible precursors to be used in our Clip-off Chemistry strategy. We have chosen Rh as the metal because paddlewheel Rh(II) clusters have been demonstrated to form strong carboxylate-metal ion bonds that lead to the formation of structurally robust porous MOPs.

4.2 Results and Discussion

4.2.1 Synthesis of the first mixed-ligand Rh_2-MOP: A trigonal antiprismatic Rh_2-MOP

Initially, inspired by the previously published trigonal antiprismatic Cu_2-MOP, we designed the simplest analogous MOP, the one with no functionalization; formed by six 3,3'-(ethene-1,2-diyl)dibenzoic acid (**$L^{4.1}$,** angle of 60º) and six isophthalic acid (**$L^{4.1'}$,** angle of 120º) ligands. Both **$L^{4.1}$** and **$L^{4.1'}$** were mixed with $Rh_2(acetate)_4$ under solvothermal conditions in dimethylacetamide in the presence of Na_2CO_3 at 100 ºC for 72 h with a 5 : 5 : 5 : 1 ratio (**$L^{4.1}$**: **$L^{4.1'}$**: Na_2CO_3: $Rh_2(acetate)_4$). An excess of ligands was added to ensure the substitution of acetates by these ligands. This reaction yielded a brown-green solution, which was centrifuged to eliminate the Na_2CO_3. The supernatant was then added drop by drop to cold methanol inducing the precipitation of a green powder, which was cleaned with more methanol and isolated. ^{1}H-NMR spectrum of the digested green powder shows a ratio of 1:2 (**$L^{4.1}$**: **$L^{4.1'}$**) between ligands. The expected ratio between ligands in the MOP is, however, 1:1. This means that there is an excess of the ligand **$L^{4.1'}$**, which probably indicates that a mixture of the antiprismatic Rh_2-MOP and the cuboctahedra Rh_2-MOP has been formed. To avoid the formation of lateral products, we adjusted the ratio between ligands to 7:5 trying to favour the formation of the mixed-ligand antiprismatic Rh_2-MOP. Under these new conditions, analysis of the ^{1}H-NMR spectrum of digested green powder confirmed the expected 1:1 ratio between both **$L^{4.1}$** and **$L^{4.1'}$** ligands (Figure 4.9). This fact and the rest of the spectroscopic characterization of the obtained solid were consistent with the formation of the expected heteroleptic antiprismatic MOP, hereafter named as $Rh_{12}\mathbf{L^{4.1}}_6\mathbf{L^{4.1'}}_6$.

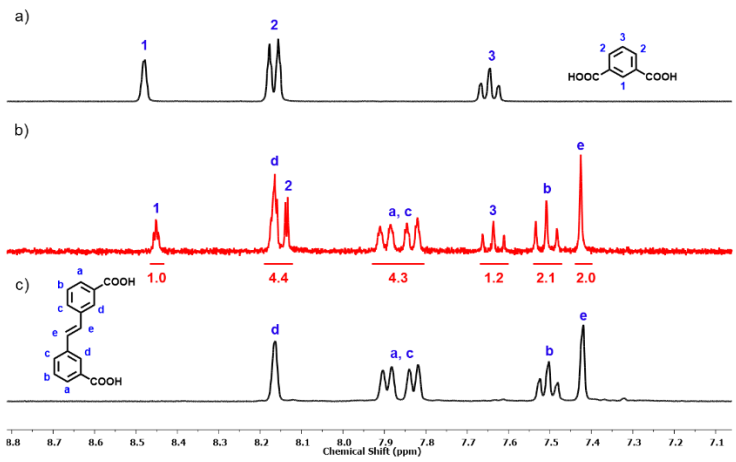

Figure 4.9. ^{1}H-NMR spectra (400 MHz, DMSO-d$_6$) of digested $Rh_{12}\mathbf{L^{4.1}}_6\mathbf{L^{4.1'}}_6$. The integrals of the assigned protons revealed that the relation between the two ligands is the expected 1:1. (a) $\mathbf{L^{4.1'}}$, (b) digested $Rh_{12}\mathbf{L^{4.1}}_6\mathbf{L^{4.1'}}_6$, and (c) $\mathbf{L^{4.1}}$.

The UV-vis spectrum of $Rh_{12}\mathbf{L^{4.1}}_6\mathbf{L^{4.1'}}_6$ in DMA shows the characteristic band centred at 590 nm ascribed to the $\pi^* \rightarrow \sigma^*$ transition of Rh(II) paddlewheel clusters (λ_{max}) (Figure 4.10).

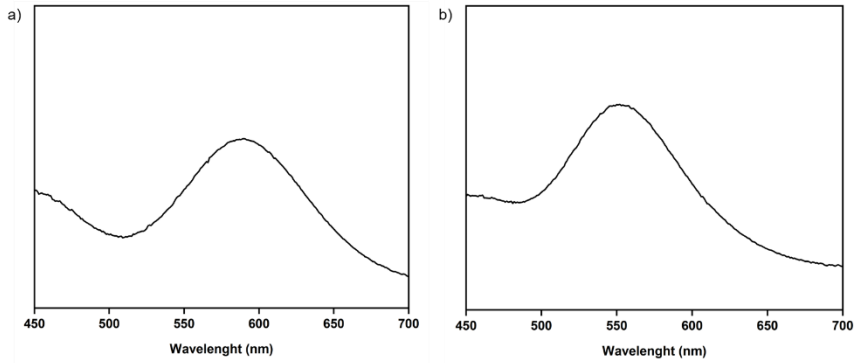

Figure 4.10. (a) UV-vis spectrum of a DMF solution of $Rh_{12}\mathbf{L^{4.1}}_6\mathbf{L^{4.1'}}_6$. The maximum of adsorption band I (λmax) of $Rh_{12}\mathbf{L^{4.1}}_6\mathbf{L^{4.1'}}_6$ is centered at 590 nm. (b) UV-vis spectrum of a DMF solution of $Rh_{12}\mathbf{L^{4.1}}_6\mathbf{L^{4.1'}}_6$ and six equivalents of 4-hydroxypyridine. The maximum of adsorption band I (λmax) of $Rh_{12}\mathbf{L^{4.1}}_6\mathbf{L^{4.1'}}_6$ is centered at 552 nm.

Finally, the MALDI-TOF spectrum of this green powder contains a peak that concurs with the expected molecular mass for a MOP made from the assembly of six Rh(II) paddlewheel SBUs, six $\mathbf{L^{4.1}}$ ligands and six $\mathbf{L^{4.1'}}$ ligands, of formula $[Rh_{12}(\mathbf{L^{4.1}})_6(\mathbf{L^{4.1'}})_6 + H]^+$ (expected = 3816.3 g/mol ; found = 3817.9 g/mol) (Figures 4.11).

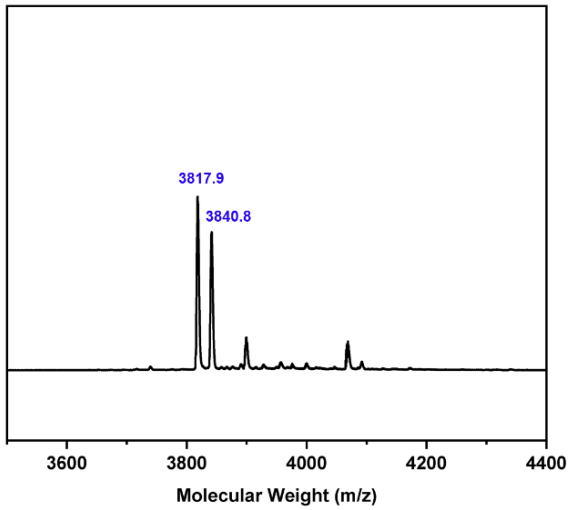

Figure 4.11. MALDI-TOF spectrum of $Rh_{12}\mathbf{L^{4.1}}_6\mathbf{L^{4.1'}}_6$. The weight corresponding to the formula $[(Rh_{12}(\mathbf{L^{4.1}})_6\ \mathbf{L^{4.1'}})_6) + H]^+$ has been highlighted: expected = 3816.3 g/mol; found = 3817.9 g/mol.

Having acquired a convincing body of spectroscopic evidence to corroborate the formation of $Rh_{12}\mathbf{L^{4.1}}_6\mathbf{L^{4.1'}}_6$, we next unambiguously confirmed its synthesis by crystallography. Initially, all our attempts to crystalize $Rh_{12}\mathbf{L^{4.1}}_6\mathbf{L^{4.1'}}_6$ were unsuccessful. We attributed these difficulties to the limited solubility of the sample in organic solvents. Thus, we envisaged coordinating an additional ligand to the Rh(II) sites of the polyhedral cage to change the surface chemistry of the MOP and increase its solubility. Accordingly, six molar equivalents of 4-hydroxypyridine were added to a solution of $Rh_{12}\mathbf{L^{4.1}}_6\mathbf{L^{4.1'}}_6$ in DMA. Immediately afterwards, the green suspension of $Rh_{12}\mathbf{L^{4.1}}_6\mathbf{L^{4.1'}}_6$ became a purple solution. The UV-vis spectrum

of this solution revealed a λ_{max} centered at 552 nm, which corresponds to one 4-hydroxypyridine ligand coordinated to one Rh(II) paddlewheel through its axial site (Figure 4.10b).[105] Single big purple parallelepiped crystals of $Rh_{12}\mathbf{L^{4.1}}_6\mathbf{L^{4.1'}}_6$ coordinated to 4-hydroxypyridine were obtained by slow diffusion of ether vapors into the DMA solution. The SCXRD data was collected using synchrotron radiation. SCXRD data revealed the formation of the expected heteroleptic Rh_2-MOP with trigonal antiprismatic geometry, in which the top and bottom triangular windows are formed by the connection of three paddlewheel Rh(II) SBUs through three $\mathbf{L^{4.1'}}$ ligands (Figure 4.12). These two triangular windows are connected by six $\mathbf{L^{4.1}}$ ligands, thereby forming six larger triangular windows, which are delineated by two $\mathbf{L^{4.1}}$ and one $\mathbf{L^{4.1'}}$ ligands. The obtained cage crystalized in triclinic P-1 space group. The asymmetric unit is formed by half MOP; three Rh_2-paddlewheel units, three $\mathbf{L^{4.1'}}$ ligands, three $\mathbf{L^{4.1}}$ ligands, three 4-hydroxypyridine ligands coordinated to the external axial positions of the Rh_2-paddlewheels, and four solvent DMA molecules.

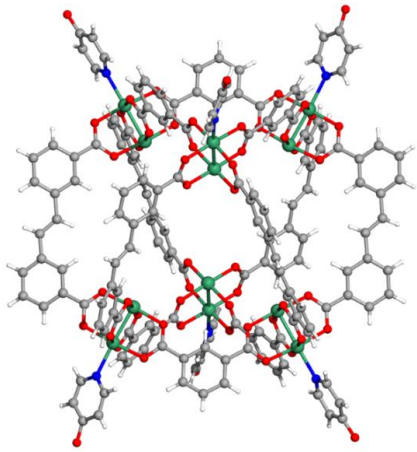

Figure 4.12. Crystal structure of $Rh_{12}\mathbf{L^{4.1}}_6\mathbf{L^{4.1'}}_6$ with 4-hydroxypyridine coordinated to the Rh_2-clusters.

Interestingly, it should be noted that the obtained trigonal antiprismatic structure of $Rh_{12}\mathbf{L}^{4.1}{}_6\mathbf{L}^{4.1'}{}_6$ can be conceptually obtained from the archetypical cuboctahedral MOP architecture (formed by 24 isophthalate ligands and 18 paddlewheel units). The fusion of the square windows with one of the adjacent triangular windows of cuboctahedral MOPs while the two triangular windows remain unalterated at the poles of the MOP renders a distorted octahedral with the same structure as $Rh_{12}\mathbf{L}^{4.1}{}_6\mathbf{L}^{4.1'}{}_6$ (Figure 4.13). The fusion of adjacent square and triangular windows of cuboctahedral MOPs is possible because the angle described by the carboxylic acid groups of the unit formed by two $\mathbf{L}^{4.1'}$ ligands and a paddlewheel is of 60º and therefore, can be replaced by reticular chemistry by a single $\mathbf{L}^{4.1}$ ligand having the same angle.

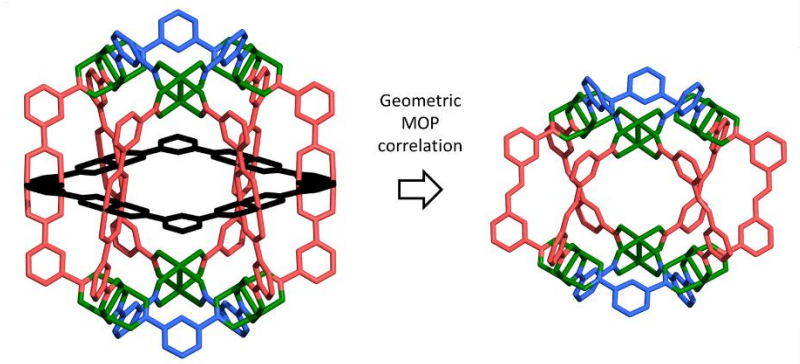

Figure 4.13. Geometric MOP correlation between the cuboctahedral MOP and the trigonal antiprismatic MOP.

The experimental powder of $Rh_{12}\mathbf{L}^{4.1}{}_6\mathbf{L}^{4.1'}{}_6$ crystals matched with the simulated powder for $Rh_{12}\mathbf{L}^{4.1}{}_6\mathbf{L}^{4.1'}{}_6$, confirming that our crystalline sample is pure (Figure 4.14).

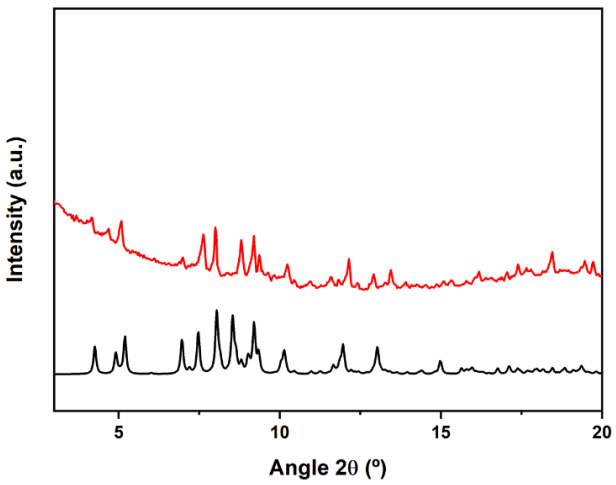

Figure 4.14. Simulated PXRD diffractogram of $Rh_{12}\mathbf{L}^{4.1}{}_6\mathbf{L}^{4.1'}{}_6$ from crystal structure (black) and experimental PXRD diffractogram of $Rh_{12}\mathbf{L}^{4.1}{}_6\mathbf{L}^{4.1'}{}_6$ crystals (red).

4.2.2 Functionalization of the ligand with a bridging angle of 120°

To extend the number of accessible heteroleptic trigonal antiprismatic Rh(II)-MOPs and tune their solubility and processability, we envisaged modulation of the MOP surface chemistry through isoreticular design, for which we used four derivatives of the $\mathbf{L}^{4.1'}$ ligand: 5-*tert*-butylisophthalic acid ($\mathbf{L}^{4.2'}$) to form $Rh_{12}\mathbf{L}^{4.1}{}_6\mathbf{L}^{4.2'}{}_6$; 5-butoxyisophthalic acid ($\mathbf{L}^{4.3'}$) to form $Rh_{12}\mathbf{L}^{4.1}{}_6\mathbf{L}^{4.3'}{}_6$; 5-(hexyloxy)isophthalic acid ($\mathbf{L}^{4.4'}$) to form $Rh_{12}\mathbf{L}^{4.1}{}_6\mathbf{L}^{4.4'}{}_6$; and 5-(dodecyloxy)isophthalic acid ($\mathbf{L}^{4.5'}$) to form $Rh_{12}\mathbf{L}^{4.1}{}_6\mathbf{L}^{4.5'}{}_6$. We separately combined each ligand, $\mathbf{L}^{4.2'\text{-}4.5'}$, with the $\mathbf{L}^{4.1}$ ligand and $Rh_2(acetate)_4$ under solvothermal conditions like those we used to synthesize $Rh_{12}\mathbf{L}^{4.1}{}_6\mathbf{L}^{4.1'}{}_6$. Spectroscopic characterisation was consistent with formation of the expected heteroleptic MOPs of formula $Rh_{12}\mathbf{L}^{4.1}{}_6\mathbf{L}^{4.2\text{-}4.5'}{}_6$. Specifically, analysis of the ^{1}H-NMR spectra of digested $Rh_{12}\mathbf{L}^{4.1}{}_6\mathbf{L}^{4.2'\text{-}4.5'}{}_6$ confirmed the expected 1:1 ratio between $\mathbf{L}^{4.1}$ and each of $\mathbf{L}^{4.2'\text{-}4.5'}$ (Figure S4.6-S4.9). Moreover, the UV-vis spectra of $Rh_{12}\mathbf{L}^{4.1}{}_6\mathbf{L}^{4.2'\text{-}4.5'}{}_6$ showed the characteristic band centred at 589-593 nm, which we ascribed to the $\pi^* \rightarrow \sigma^*$

transition of Rh(II) paddlewheel clusters (λ_{max}) (Figure S4.17-S4.20). Finally, the MALDI-TOF spectra contained a peak that evidences the expected molecular mass for the MOPs made from the assembly of six paddlewheel Rh(II) clusters, six $\mathbf{L^{4.1}}$ and six ligands $\mathbf{L^{4.2'\text{-}4.5'}}$, of formula $[Rh_{12}(\mathbf{L^{4.1}})_6(\mathbf{L^{4.2'}})_6(DMA)(H_2O)_2(MeOH)_4 + H]^+$ (m/z = 4405.3 g/mol); $[(Rh_{12}(\mathbf{L^{4.1}})_6(\mathbf{L^{4.3'}})_6(DMA)_2(H_2O)_2(MeOH)+H]^+$(m/z = 4491.7 g/mol); $[Rh_{12}(\mathbf{L^{4.1}})_6(\mathbf{L^{4.4'}})_6(DMA)_2(H_2O)_4 + H]^+$ (m/z = 4669.6 g/mol); $[(Rh_{12}(\mathbf{L^{4.1}})_6(\mathbf{L^{4.5'}})_6) + H]^+$ (m/z = 4925.1 g/mol) (Figure S4.28-S4.31).

Having acquired a convincing body of spectroscopic evidence to corroborate the formation of heteroleptic $Rh_{12}\mathbf{L^{4.1}}_6\mathbf{L^{4.2'\text{-}4.5'}}_6$, we next unambiguously determined their structure through SCXRD. Note that, for the formation of single crystals suitable for SCXRD, $Rh_{12}\mathbf{L^{4.1}}_6\mathbf{L^{4.2'\text{-}4.5'}}_6$ were all crystallised by first pre-coordinating a functionalised pyridine to the Rh(II) sites of the polyhedral cage. Accordingly, a DMA or dimethylformamide (DMF) solution of 4-hydroxypyridine, 4-*tert*-butylpyridine or isonicotinic acid was added to a solution of $Rh_{12}\mathbf{L^{4.1}}_6\mathbf{L^{4.2'\text{-}4.5'}}_6$ in either DMA or DMF. Immediately afterwards, all the green suspensions of $Rh_{12}\mathbf{L^{4.1}}_6\mathbf{L^{4.2'\text{-}4.5'}}_6$ became purple solutions. The UV-vis spectra of these solutions revealed a λ_{max} centred at 552-559 nm, which corresponds to one 4-hydroxypyridine, 4-*tert*-butylpyridine or isonicotinic acid ligand coordinated to one Rh(II) paddlewheel through its axial site (Figure S4.17-S4.20).[19] Single purple parallelepiped crystals of $Rh_{12}\mathbf{L^{4.1}}_6\mathbf{L^{4.1'}}_6$, $Rh_{12}\mathbf{L^{4.1}}_6\mathbf{L^{4.2'}}_6$ and $Rh_{12}\mathbf{L^{4.1}}_6\mathbf{L^{4.3'}}_6$, and cubic crystals of $Rh_{12}\mathbf{L^{4.1}}_6\mathbf{L^{4.4'}}_6$ and $Rh_{12}\mathbf{L^{4.1}}_6\mathbf{L^{4.5'}}_6$ were obtained by slow diffusion of ether vapours into the DMA or DMA/DMF solutions. SCXRD data revealed the formation of heteroleptic, trigonal, antiprismatic $Rh_{12}\mathbf{L}_6\mathbf{L'}_6$ MOPs analogous to $Rh_{12}\mathbf{L^{4.1}}_6\mathbf{L^{4.1'}}_6$ (Figure 4.15). In these cages, the top and bottom trigonal facets (diameter: 3.8 Å) are formed by the connection of three paddlewheel Rh(II) clusters through three $\mathbf{L^{4.2\text{-}4.5'}}$ ligands. These two triangular facets are connected by six $\mathbf{L^{4.1}}$ ligands to form six larger triangular

windows (diameter: 6.6 Å), which are delineated by two $\mathbf{L^{4.1}}$ ligands and one $\mathbf{L^{4.2'\text{-}4.5'}}$ ligand. In these isostructural cages, the functional groups placed in the isophthalate-based ligand **L'** define the functionalisation of the top and bottom triangular facets of the antiprism (Figure 4.15). For all these MOPs, experimental PXRD patterns matched the corresponding simulated patterns from the crystal structures (Figure S4.39-S4.42), thereby confirming their phase purity.

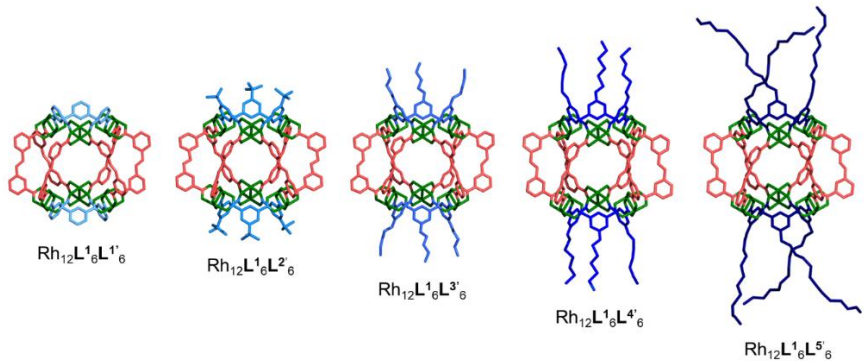

Figure 4.15. Crystal structures (removing coordinated pyridines for clarification) of $Rh_{12}\mathbf{L^{4.1}}_6\mathbf{L^{4.1'}}_6$, $Rh_{12}\mathbf{L^{4.1}}_6\mathbf{L^{4.2'}}_6$, $Rh_{12}\mathbf{L^{4.1}}_6\mathbf{L^{4.3'}}_6$, $Rh_{12}\mathbf{L^{4.1}}_6\mathbf{L^{4.4'}}_6$, and $Rh_{12}\mathbf{L^{4.1}}_6\mathbf{L^{4.5'}}_6$.

4.2.3 Increase of the size of the axial triangular windows: discovery of a new isomer

To increase the size of the windows and the accessibility to the confined space, we increased the length of the ligand exhibiting a bridging angle of 120° substituting the $\mathbf{L^{4.1\text{-}4.5'}}$ ligands for a naphthalene ligand, $\mathbf{L^{4.6'}}$, which contains one more phenyl ring. Reaction of $Rh_2(acetate)_4$ with the ligands $\mathbf{L^{4.1}}$ and $\mathbf{L^{4.6'}}$, and Na_2CO_3 in DMA under similar solvothermal conditions produced a green powder, which we identified as the expected heteroleptic $Rh_{12}\mathbf{L^{4.1}}_6\mathbf{L^{4.6'}}_6$ MOP by ^{1}H-NMR, UV-vis, and MALDI-TOF (Figure S4.10, S4.21, S4.32). Single-crystals suitable for SCXRD were obtained by dissolving the powder in DMF in the presence of isonicotinic acid, and then exposing the resulting solution to ether vapours. Unexpectedly,

SCXRD data revealed the formation a trigonal antiprismatic MOP that was not analogous with respect to the structures of $Rh_{12}\mathbf{L^{4.1}}_6\mathbf{L^{4.1'\text{-}4.5'}}_6$. In this case, the top and bottom trigonal facets (diameter: 8.6 Å) are formed by the connection of three paddlewheel Rh(II) clusters through three $\mathbf{L^{4.1}}$ ligands. These two trigonal facets are connected by six $\mathbf{L^{4.6'}}$ ligands, thereby forming six larger triangular windows (diameter: 6.6 Å) that are delineated by two naphthalene moieties and one $\mathbf{L^{4.1}}$ ligand. That structure is an isomeric structure of the antiprismatic $Rh_{12}\mathbf{L^{4.1}}_6\mathbf{L^{4.1'\text{-}4.5'}}_6$, as the ligands with a bridging angle of 120° occupy the positions of the ligands with a bridging angle of 60° in the $Rh_{12}\mathbf{L^{4.1}}_6\mathbf{L^{4.1'\text{-}4.5'}}_6$, and the ligands with a bridging angle of 60° occupy the positions of the ligands with a bridging angle of 120° in the $Rh_{12}\mathbf{L^{4.1}}_6\mathbf{L^{4.1'\text{-}4.5'}}_6$. Both isomers are composed by two top and bottom trigonal macrocycles connected through the other six complementary ligands. Both isomeric antiprismatic cages were named as: **Isomer A**, the one formed by two trigonal macrocycles assembled using **L'** ligands interconnected through **L** ligands; and **Isomer B**, the one formed by two trigonal macrocycles assembled using **L** ligands and interconnected through **L'** ligands (Figure 4.16). The experimental PXRD pattern of these $Rh_{12}\mathbf{L^{4.1}}_6\mathbf{L^{4.6'}}_6$ crystals matched the simulated pattern from the crystal structure, thus confirming its phase purity (Figure S4.43).

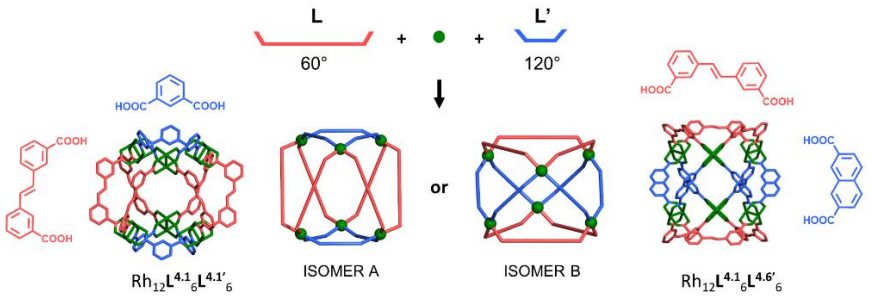

Figure 4.16. Schematic representation of $Rh_{12}\mathbf{L^{4.1}}_6\mathbf{L^{4.1'}}_6$ and $Rh_{12}\mathbf{L^{4.1}}_6\mathbf{L^{4.6'}}_6$ MOPs, where it can be clearly appreciated that the ligands exhibiting an angle between binding sites of 60° (in red) and the ligands having an angle of 120° degrees (in blue) occupy complementary positions in both trigonal antiprismatic MOPs, forming isomers A and B.

As it has been previously commented, **Isomer A** has previously been obtained by connecting Cu(II) paddlewheel clusters with two complementary dicarboxylate ligands.[89,100–102] Alternatively, **isomer B** has been synthesized by the assembly of Pd(II) ions with two complementary ligands based on pyridine moieties.[99] However, to our knowledge, that isomer B has never been formed before using polycarboxylate ligands. Overall, this isomerization, in which two non-analogous ligands can be located in complementary positions of a cage maintaining its topology and varying its dimensions, is rare in molecular cages. In the following section, several cases of isomerization of molecular cages are described.

4.2.3.1 Isomerization in M_2-MOPs and Pd-cages

The known metal coordination environments and the defined geometry binding sites of the organic ligand allow the prediction and rational design of the resulting geometry of the MOP. However, in some cases, there is not a unique way to link specific building blocks, allowing for the assembly of different cages. If these different cages contain the same number of ligands and clusters, we can consider that they are isomers. This is the case of the cuboctahedra-anticuboctahedra Rh_2-MOP topological isomers, which differ in how their two halves are aligned.[106] If we orientate the MOP with two triangular windows at the top and bottom, the cuboctahedra is the one that have the triangular windows of one half matching with the square windows of the other half. On the other hand, the anticuboctahedra is the one that have the triangular windows of one half matching with the triangular windows of the other half and the square windows of one half matching with the square windows of the other half (Figure 4.17). The formation of cuboctahedral or anticuboctahedral structures is determined by the synthetic experimental conditions, specifically by the reaction solvent.[106] Additionally, there have been reports of a Mo_2-cuboctahedral-MOP and a Mo_2-anticuboctahedral-MOP. However, their synthesis depends not only on the reaction conditions

but also on the functionalization of their ligands. In this case, the two reported structures are not strictly isomers. The cuboctahedra is formed with 5-*tert*-butylisophthalic acid whereas anticuboctahedra is formed with isophthalic acid.[107]

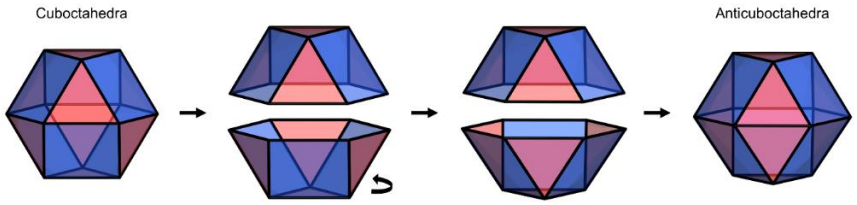

Figure 4.17. Schematic representation of a cuboctahedra (left) and an anticuboctahedra (right).

The number of possible isomers that can be formed grows as the complexity of the system increases. The reported cases of isomerization in M_2-paddlewheel-MOPs and Pd-cages can be classified in four groups, based on the factor that contributes to the system's complexity: (1) use of an asymmetric ligand; (2) use of a ligand with more than one conformer; (3) use of several ligands that are geometrically analogous; and (4) use of ligands that are not geometrically analogous.

(1) Use of an asymmetric ligand. In this case, the cage is built by a unique type of ligand that is not symmetric. As a result, this ligand can adopt two possible orientations in each position of the cage (Figure 4.18). The most common examples of these type of cages are lantern-type cages,[108–114] but a cuboctahedra cage[115] and a tetrahedron cage[116] can also be found.

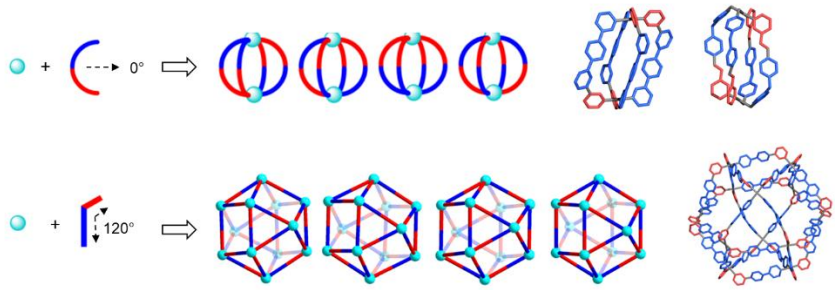

Figure 4.18. Schematic representation of different possible lantern-type cages built by an asymmetric ligand with a bridging angle of 0° (top) and four of the 350 696 potential cuboctahedra isomers, which can be formed by an asymmetric ligand with a bridging angle of 120°(bottom). In the right, there are some examples of an specific formation of one concrete isomer by "orientational self-sorting": lantern-type cage [108,111] (top) and cuboctahedra type cage (bottom).[115] Image reprinted with permission from reference 115. Open Access CC BY 3.0.

(2) Use of a ligand with more than one conformer. In this case, the cage is built by a unique type of ligands, which can have more than one conformer. This induces that each position can be occupied by any of the possible conformers.[117,118,119] In the lantern-type MOPs built by ligands which contains imine bonds (Figure 4.19), it can be observed how each imine bond can adopt two possible *trans* conformations, giving different isomers. In this case, the use of different crystallization conditions for the same reaction crude results in the crystallization of different isomers.[119]

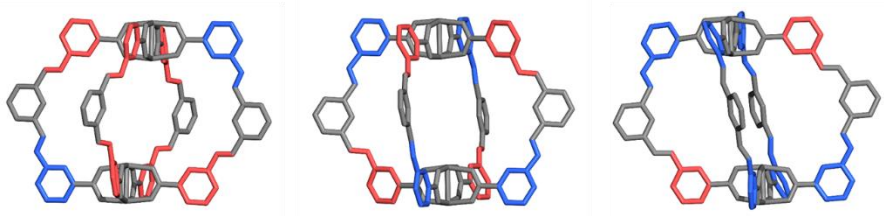

Figure 4.19. Schematic representation of three possible isomers of a lantern-type MOP formed thanks to the different conformations that can adopt the ligand.[119]

(3) Use of several ligands geometrically analogous between them. Here, the cage is built by two or more types of geometrically analogous ligands; that is, ligands that have the same length and angle between binding sites.[86,85,84] For a lantern M_2-MOP built by two kinds of ligands, the only way to form isomers is to have two molecules of the two types of ligands allowing the formation of the *cis* or *trans* isomers (Figure 4.20).

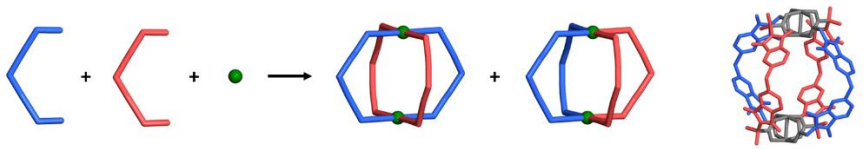

Figure 4.20. Schematic representation of *cis* and *trans* isomers of a lantern cage built by two geometrically analogous ligands. Example of a lantern-type MOP (right). [85]

(4) Use of ligands that are not geometrically analogous. In this case, the cage is formed by two or more types of ligands that are not geometrically analogous in terms of length or connectivity. That fact made that the positions that occupy each ligand are not equivalent, making the ligands not interchangeable between them. In the literature, we have only found a mixed ligand palladium cage of this type and it presents a topologic isomerization analogous to the cuboctahedra-anticuboctahedra case. In this case, two possible isomers were postulated but only the anticuboctahedra cage was crystalized (Figure 4.21).[88]

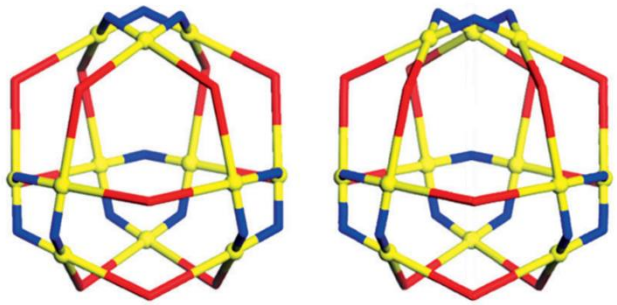

Figure 4.21. Representation of the two isomers which can be formed by mixing two types of ligands with a bridging angle of 120°.[88] Isomerization analogous to the cuboctahedra-anticuboctahedra topologic isomerization typical from the homoleptic cuboctahedra cages. Image reprinted with permission from reference 88. Copyright 2014 John Wiley and Sons.

4.2.4 Change of the double bond of the ligand with a bridging angle of 60° by an azo bond

Having observed that both isomeric trigonal antiprismatic MOPs could be assembled depending on the complementary dicarboxylate ligands, we sought to validate our observations by creating six additional heteroleptic MOPs combining $\mathbf{L}^{\mathbf{4.1\text{-}4.6'}}$ with $\mathbf{L}^{\mathbf{4.2}}$, which contains an azo group in place of the olefinic group in $\mathbf{L}^{\mathbf{4.1}}$ (Figure 4.22). We began by mixing rhodium acetate with $\mathbf{L}^{\mathbf{4.2}}$ and the naphthalene-based $\mathbf{L}^{\mathbf{4.6'}}$, from which **isomer B** was again assembled. We then combined rhodium acetate with $\mathbf{L}^{\mathbf{4.2}}$ and the other, isophtalate-based, $\mathbf{L}^{\mathbf{4.1\text{-}4.5'}}$. These reactions led to formation of either **isomer A**, when $\mathbf{L}^{\mathbf{4.2}}$ was combined with $\mathbf{L}^{\mathbf{4.1'}}$, $\mathbf{L}^{\mathbf{4.2'}}$ and $\mathbf{L}^{\mathbf{4.5'}}$, or **isomer B**, when $\mathbf{L}^{\mathbf{4.2}}$ was combined with $\mathbf{L}^{\mathbf{4.3'}}$ or $\mathbf{L}^{\mathbf{4.4'}}$. Altogether, our results suggest that both isomers of trigonal antiprismatic MOPs are accessible, and that minor variations in the length and functionalities of the complementary ligands can tip the balance in favour of one isomer or the other.

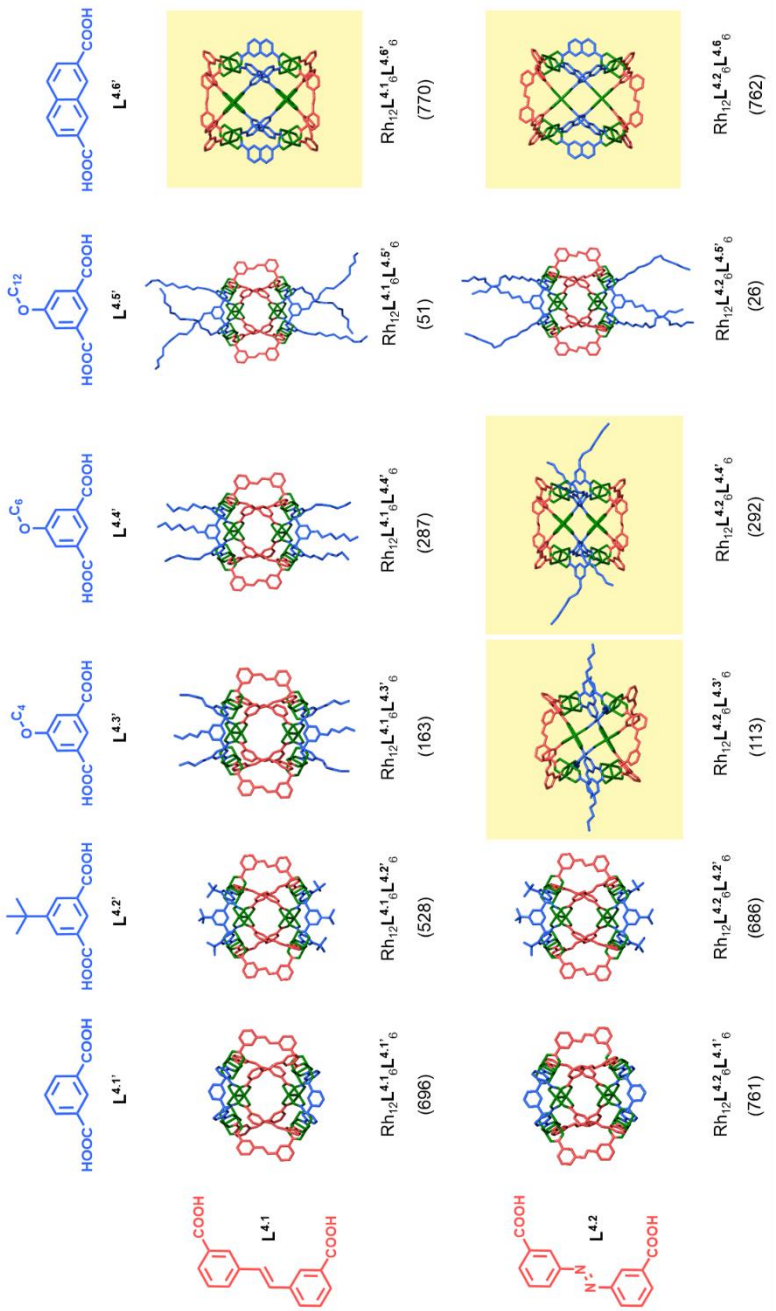

Figure 4.22. Representation of the complementary ligands $\mathbf{L^{4.1\text{-}4.2}}$ and $\mathbf{L^{4.1\text{-}4.6'}}$, and the crystal structures of the corresponding isomeric trigonal antiprismatic cages assembled with Rh(II), as either isomer A (white background) or isomer B (yellow boxes). The corresponding S_{BET} values (in m^2/g) are shown below each formula.[120]

4.3.5 Solid-state porosity of our family of trigonal antiprismatic Rh_2-MOPs

Once we had synthesized the library of the 12 new heteroleptic trigonal antiprismatic Rh_2-MOPs, we assessed their solid-state porosity by subjecting them to N_2 adsorption experiments at 77 K (Figure 4.23a, Figure 4.24). All $Rh_{12}\mathbf{L}_6\mathbf{L'}_6$ MOPs were microporous in the solid state, as evidenced by their corresponding type I isotherms, from which we determined the corresponding S_{BET} values. Remarkably, these values further support the premise that use of Rh(II) ions tends to form stable and highly porous MOPs in the solid state, whereby steric hindrance around the MOP core remains the principal hurdle to porosity, as commonly observed in archetypical cuboctahedral Rh_2-MOPs.[19] Accordingly, regardless of the isomer, the four heteroleptic MOPs assembled by combining either $\mathbf{L}^{4.1}$ or $\mathbf{L}^{4.2}$ with either $\mathbf{L}^{4.1'}$ or $\mathbf{L}^{4.6'}$ exhibited the highest S_{BET} values (range: 696 to 770 m^2/g). Similarly, the two heteroleptic MOPs built up either from $\mathbf{L}^{4.1}$ or $\mathbf{L}^{4.2}$ with (the *tert*-butyl-functionalised) $\mathbf{L}^{4.2'}$ exhibited S_{BET} values of 528 and 686 m^2/g, respectively. Finally, encouraged by the robustness, porosity and accessible metal sites of our heteroleptic Rh(II) MOPs, we also evaluated their capacity for CO_2 adsorption at 298 K (Figure 4.23b, Figure 4.24), observing CO_2 uptake values from 2.56 to 10.95 mol CO_2/ mol MOP.

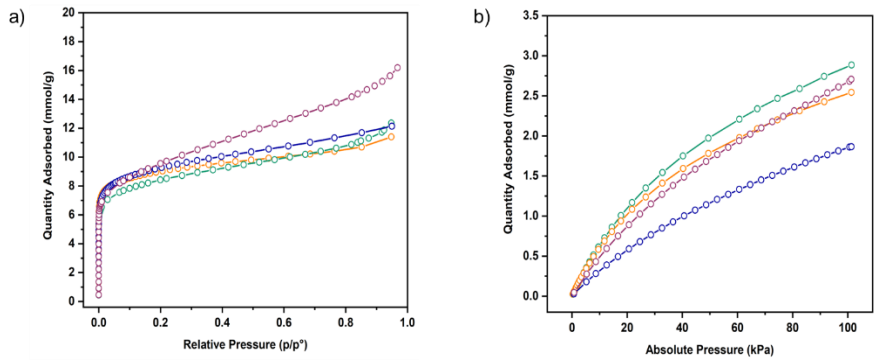

Figure 4.23. N_2 (a) and CO_2 (b) sorption isotherm for $Rh_{12}\mathbf{L}^{4.1}{}_6\mathbf{L}^{4.1'}{}_6$ (green), $Rh_{12}\mathbf{L}^{4.2}{}_6\mathbf{L}^{4.1'}{}_6$ (orange), $Rh_{12}\mathbf{L}^{4.1}{}_6\mathbf{L}^{4.6'}{}_6$ (red) and $Rh_{12}\mathbf{L}^{4.2}{}_6\mathbf{L}^{4.6'}{}_6$ (blue).

	S_{BET} (m^2/g)	CO_2 uptake (mmol/g)	CO_2 uptake (mol CO_2/mol MOP)
$Rh_{12}L^{4.1}{}_6L^{4.1'}{}_6$	696	2.87	10.95
$Rh_{12}L^{4.2}{}_6L^{4.1'}{}_6$	761	2.55	9.76
$Rh_{12}L^{4.1}{}_6L^{4.2'}{}_6$	528	1.77	7.35
$Rh_{12}L^{4.2}{}_6L^{4.2'}{}_6$	686	2.15	8.96
$Rh_{12}L^{4.1}{}_6L^{4.3'}{}_6$	163	1.29	5.48
$Rh_{12}L^{4.2}{}_6L^{4.3'}{}_6$	113	1.33	5.67
$Rh_{12}L^{4.1}{}_6L^{4.4'}{}_6$	287	1.28	5.66
$Rh_{12}L^{4.2}{}_6L^{4.4'}{}_6$	292	0.94	4.16
$Rh_{12}L^{4.1}{}_6L^{4.5'}{}_6$	51	0.52	2.56
$Rh_{12}L^{4.2}{}_6L^{4.5'}{}_6$	26	0.57	2.81
$Rh_{12}L^{4.1}{}_6L^{4.6'}{}_6$	770	2.69	11.08
$Rh_{12}L^{4.2}{}_6L^{4.6'}{}_6$	762	1.86	7.66

Figure 4.24. S_{BET} area, CO_2 uptake and CO_2 uptake/mol of MOP for the trigonal antiprismatic Rh_2-MOPs.

4.3 Conclusion

To conclude, we have synthesized and characterised a family of 12 new heteroleptic trigonal antiprismatic porous MOPs. We discovered that, depending on the combination of complementary ligands, the two possible heteroleptic cage isomers could be assembled. We have also demonstrated that the external functionality of these MOPs can be tailored by means of isoreticular chemistry. Moreover, all these MOPs are microporous in the solid state, enlarging the still short-list of porous cages.

4.4 Experimental Part

4.4.1 Materials and Methods

Rhodium acetate was purchased from Acros Organics. 1,3-benzenedicarboxylate (**L**$^{4.1'}$), sodium carbonate (Na_2CO_3), potassium hydroxide (KOH), potassium carbonate (K_2CO_3), sodium carbonate (Na_2CO_3), hydrochloric acid 37% (HCl). 3-iodobenzoic acid, palladium(II) acetate, (E)-3,3'-(diazene-1,2-diyl)dibenzoic acid (**L**$^{4.2}$), 4-*tert*-butylpyridine, 5-*tert*-butylbenzene-1,3-dicarboxylic acid (**L**$^{4.2'}$), dimethyl 5-hydroxyisophthalate and 1-bromobutane, 1-bromohexane, 1-bromododecane, dimethyl naphthalene-2,7-dicarboxylate were purchased from TCI. Triphenylphosphine and HCl 37 % were purchased from Sigma Aldrich. 3-Vinylbenzoic acid was purchased from Alfa Aesar. All deuterated solvents were purchased from Eurisotop. Dimethylformamide (DMF), tetrahydrofuran (THF), methanol (MeOH) and dimethylacetamide (DMA) were purchased from Fischer Chemicals. All the reagents and solvents were used without further purification unless otherwise specified.

Ultraviolet-visible (UV−Vis) spectra were measured in an Agilent Cary 4000 at room temperature (ca. 25 °C). ***Proton Nuclear Magnetic Resonance (^{1}H-NMR) spectra*** were acquired in a Bruker Avance III 250SB NMR and a 360 250SB NMR spectrometer at "Servei d'Análisi Química" from Autonomous University of Barcelona (UAB). ***Powder X-ray diffraction (PXRD) diagrams*** were collected on a Panalytical X'pert diffractometer with monochromatic Cu-Ka radiation (λ_{Cu} = 1.5406 Å). Diffractograms were collected in capillary to keep the samples solvated during the measurement. ***Mass Spectroscopy (MALDI-TOF)*** measurements were performed using a 4800 Plus MALDI TOF/TOF (ABSCIEX – 2010). The matrix used in each case was trans-2-[3-(4-*tert*-butylphenyl)-2-methyl-2-propenylidene]malononitrile (DCTB) measured in positive mode. ***Volumetric N_2 and CO_2 isotherms*** were collected at 77 K (N_2) and at 298 K (CO_2) using an ASAP 2020 (Micromeritics). Before sorption measurements,

MOP samples were activated by acetone exchange for 5 days and heating at vacuum at 85 ºC overnight. ***Acid digestion of Rh_2-MOP*** were performed by adding 20 µL of DCl into a solution of 2 mg of Rh_2-MOP in 0.45 mL of DMSO-d_6 and heating the resulting solution at 100 ºC for 6 h.

4.4.2 Synthetic Methodologies

*Synthesis of (E)-3,3'-(ethene-1,2-diyl)dibenzoic acid (**$L^{4.1}$**)*: 3-vinylbenzoic acid (2.0 g, 13.5 mmol), 3-iodobenzoic acid (3.3 g, 13.5 mmol), triphenylphosphine (118 mg, 0.45 mmol), triethylamine (20 mL) and palladium(II) acetate (80 mg, 0.36 mmol) were allowed to react in THF (40 ml) at 80 ºC for 24 h. The resulting suspension was filtered, and the obtained solution was evaporated under reduced pressure. The resulting solid was then dissolved in a minimum amount of THF and precipitated with concentrated HCl (12 M). The white solid was separated by centrifugation and washed with small amounts of THF, MeOH and water (2.2 g; yield: 61 %). ^{1}H-NMR (250 MHz, DMSO-d_6): δ 13.05 (s, 1H), 8.21 (s, 1H), 7.91 (d, J = 8.0 Hz, 1H), 7.86 (d, J = 7.9 Hz, 1H), 7.52 (t, J = 7.7 Hz, 1H), 7.45 (s, 1H). ^{13}C-NMR (250 MHz, DMSO-d_6): δ 168.05, 138.10, 132.17, 131.54, 129.87, 129.47, 129.41, 128.33.

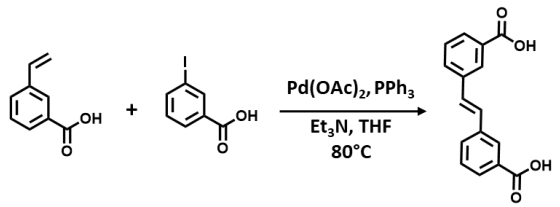

*Synthesis of 5-butoxyisophthalic acid (**$L^{4.3'}$**):* 2.0 g of dimethyl 5-hydroxyisophthalate (9.5 mmol) and 3.9 g of K_2CO_3 (28.5 mmol) were mixed in 50 mL of DMF. Then, 1.15 mL of 1-bromobutane (10.6 mmol) was added, and the resulting reaction mixture was heated at 100 ºC overnight. Afterwards, DMF was evaporated under reduced pressure, H_2O was added and the resulting dispersion was centrifugated. The resulting solid was

washed several times with H_2O, and dried at 85ºC vacuum oven obtaining an oil. This oil was dissolved into 40 mL of THF, in which 40 mL of MeOH and 30 mL of 2 M aqueous of KOH solution were added. This mixture was heated at 80 ºC overnight. MeOH and THF were evaporated under reduced pressure. The obtained aqueous solution was acidified with HCl forming a white precipitate, which was filtrated, washed several times with H_2O and dried at 85ºC vacuum oven (1.3 g; 55%). ^{1}H-NMR (360 MHz, DMSO-d_6) δ 13.28 (s, 1H), 8.07 (s, 1H) 7.64 (s, 2H), 4.09 (t, J = 6.0 Hz, 2H), 1.73 (p, J = 6.5 Hz, 2H), 1.53 – 1.38 (m, 2H), 0.95 (t, J = 6.8 Hz, 3H).

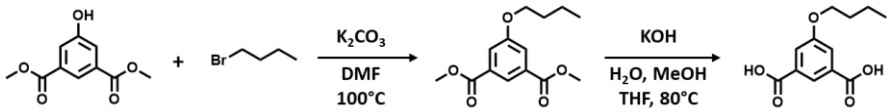

*Synthesis of 5-(hexyloxy)isophthalic acid (**L**$^{4,4'}$):* 2.0 g of dimethyl 5-hydroxyisophthalate (9.5 mmol) and 3.9 g of K_2CO_3 (28.5 mmol) were mixed in 50 mL of DMF. Then, 1.5 mL of 1-bromohexa (10.6 mmol) was added, and the resulting reaction mixture was heated at 100 ºC overnight. Afterwards, DMF was evaporated under reduced pressure, H_2O was added, and the resulting dispersion was centrifugated. The obtained solid was washed several times with H_2O and dried at 85ºC vacuum oven to obtain an oil. This oil was dissolved into 40 mL of THF, in which 40 mL of MeOH and 30 mL of 2 M aqueous of KOH solution were added. The resulting mixture was heated at 80 ºC overnight. MeOH and THF were evaporated under reduced pressure. The obtained aqueous solution was acidified with HCl forming a white precipitate, which was filtrated, washed several times with H_2O and dried at 85ºC vacuum oven (2.2 g; 86%). ^{1}H-NMR (360 MHz, DMSO-d_6) δ 13.30 (s, 1H), 8.07 (s, 1H), 7.63 (s, 2H), 4.08 (t, J = 6.4 Hz, 2H), 1.74 (p, J = 6.6 Hz, 2H), 1.51 – 1.38 (m, 2H), 1.32 (m, 4H), 0.89 (t, 3H).

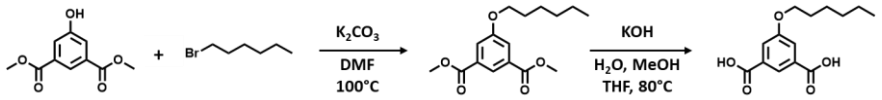

*Synthesis of 5-(dodecyloxy)isophthalic acid (**L**$^{4.5'}$)*: 2.6 mL of 1-bromododecane (10.6 mmol) were added into a mixture of 2.0 g of dimethyl 5-hydroxyisophthalate (9.5 mmol) and 3.94 g of K_2CO_3 (28.5 mmol) in 50 mL of DMF. The reaction mixture was then heated at 100 ºC overnight. Afterwards, DMF was evaporated under reduced pressure and H_2O was added to the solid residue to obtain a white dispersion, which was centrifugated and washed three times with H_2O. The resulting solid was dried at 85 ºC in vacuum oven overnight to finally obtain a transparent oil. This oil was dissolved into 40 mL of THF, in which 40 mL of MeOH and 30 mL of 2 M aqueous of KOH solution were added. Afterwards, MeOH and THF were evaporated under reduced pressure. The obtained aqueous solution was acidified with HCl forming a white precipitate, which was filtrated and washed several times with H_2O, and finally dried at 85 ºC vacuum oven (1.5 g; 45 %). ^{1}H-NMR (360 MHz, DMSO-d_6): δ 13.26, 8.06 (s, 1H), 7.62 (s 2H), 4.06 (t, J = 6.4 Hz, 2H), 1.81 – 1.66 (m, 2H), 1.47 – 1.35 (m, 2H), 1.24 (s, 16H), 0.85 (t, J = 6.6 Hz, 3H).

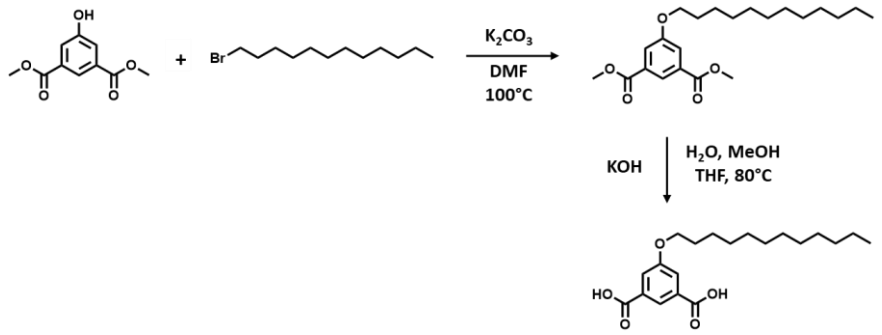

*Synthesis of naphthalene-2,7-dicarboxylic acid (**L**$^{4.6'}$):* 0.5 g of dimethyl naphthalene-2,7-dicarboxylate (2.0 mmol), 1.2 g of KOH (20.5 mmol), 9 mL of MeOH and 1 mL of H_2O were heated at 65 ºC overnight. Afterwards, MeOH was evaporated under reduced pressure obtaining a water solution. HCl 12M was added, forming a white precipitate, which was filtrated and washed with water (0.40 g; yield: 91%). ^{1}H-NMR (360 MHz, DMSO-d_6): δ 13.24 (s, 2H), 8.80 (s, 2H), 8.12 (s, 4H).

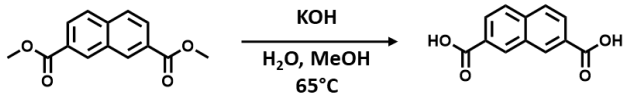

*Synthesis of Rh$_{12}$**L**$^{4.1\text{-}4.2}{}_6$**L**$^{4.1\text{-}4.6'}{}_6$:* A mixture of 7 eq of **L**$^{4.1\text{-}4.2}$, 5 eq of **L**$^{4.1\text{-}4.6'}$, 5 eq of Na_2CO_3 and 1 eq (20 mg) of rhodium acetate in 2 mL of DMA were sonicated for a few minutes and then, heated at 100 º C for 72 h. The resulting dispersion was centrifugated to separate the Na_2CO_3. The brown-green (for Rh$_{12}$**L**$^{4.1}{}_6$**L**$^{4.1\text{-}4.6'}{}_6$) and brown (Rh$_{12}$**L**$^{4.2}{}_6$**L**$^{4.1\text{-}4.6'}{}_6$) solution was precipitated into 10 mL of cold MeOH yielding a green solid which was washed three times with MeOH and dried at vacuum (8 mg; 28 % for Rh$_{12}$**L**$^{4.1}{}_6$**L**$^{4.1'}{}_6$; 9 mg; 29 % for Rh$_{12}$**L**$^{4.1}{}_6$**L**$^{4.2'}{}_6$; 4 mg; 12 % for Rh$_{12}$**L**$^{4.1}{}_6$**L**$^{4.3'}{}_6$, 10 mg; 30 % for Rh$_{12}$**L**$^{4.1}{}_6$**L**$^{4.4'}{}_6$; 20 mg; 54 % for Rh$_{12}$**L**$^{4.1}{}_6$**L**$^{4.5'}{}_6$; 2 mg; 7 % for Rh$_{12}$**L**$^{4.1}{}_6$**L**$^{4.6'}{}_6$; 0.5 mg; 2 % for Rh$_{12}$**L**$^{4.2}{}_6$**L**$^{4.6'}{}_6$; 6 mg; 21% for Rh$_{12}$**L**$^{4.2}{}_6$**L**$^{4.1'}{}_6$; 4 mg; 13 % for Rh$_{12}$**L**$^{4.2}{}_6$**L**$^{4.2'}{}_6$; 2.5 mg; 8 % for Rh$_{12}$**L**$^{4.2}{}_6$**L**$^{4.3'}{}_6$; 4.5 mg; 14 % for Rh$_{12}$**L**$^{4.2}{}_6$**L**$^{4.4'}{}_6$; 10 mg; 27% for Rh$_{12}$**L**$^{4.2}{}_6$**L**$^{4.5'}{}_6$).

*Crystallization of Rh$_{12}$**L**$^{4.1}{}_6$**L**$^{4.1'}{}_6$*: 2 mg of Rh$_{12}$**L**$^{4.1}{}_6$**L**$^{4.1}$'$_6$ were dissolved in 0.5 mL of DMA and then, 150 µL of a 4-hydroxypyridine solution (3 mg of 4-hydroxypyridine in 1 mL of DMA) were added. Purple parallelepiped crystals were obtained by slow ether vapor diffusion into this solution.

Crystallization of $Rh_{12}L^{4.1}{}_6L^{4.2'}{}_6$*:* 2 mg of $Rh_{12}L^{4.1}{}_6L^{4.2'}{}_6$ were dissolved in 0.5 mL of DMF and then, 120 µL of a isonicotinic acid solution (3.6 mg of isonicotinic acid in 1 mL of DMF) were added. Purple parallelepiped crystals were obtained by slow ether vapor diffusion into this solution.

Crystallization of $Rh_{12}L^{4.1}{}_6L^{4.3'}{}_6$*:* 2 mg of $Rh_{12}L^{4.1}{}_6L^{4.3'}{}_6$ were dissolved in 0.5 mL of DMA and then, 200 µL of an isonicotinic acid solution (3.5 mg of isonicotinic acid in 1 mL of DMA) were added. Purple parallelepiped crystals were obtained by slow ether vapor diffusion into this solution.

Crystallization of $Rh_{12}L^{4.1}{}_6L^{4.4'}{}_6$: 2 mg of $Rh_{12}L^{4.1}{}_6L^{4.4'}{}_6$ were dissolved in 0.5 mL of DMF and then, 200 µL of an isonicotinic acid solution (3.3 mg of isonicotinic acid in 1 mL of DMA) were added. Purple cubic crystals were obtained by slow ether vapor diffusion into this solution.

Crystallization of $Rh_{12}L^{4.1}{}_6L^{4.5'}{}_6$*:* 2 mg of $Rh_{12}L^{4.1}{}_6L^{4.5'}{}_6$ were dissolved in 0.5 mL of DMA and then, 120 µL of an isonicotinic acid solution (3.9 mg of isonicotinic acid in 1 mL of DMF) were added. Purple cubic crystals were obtained by slow ether vapor diffusion into this solution.

Crystallization of $Rh_{12}L^{4.1}{}_6L^{4.6'}{}_6$*:* 2 mg of $Rh_{12}L^{4.1}{}_6L^{4.6'}{}_6$ were dissolved in 0.5 mL of DMF and then, 120 µL of an isonicotinic acid solution (3.9 mg of isonicotinic acid in 1 mL of DMF) were added. Purple parallelepiped crystals were obtained by slow ether vapor diffusion into this solution.

Crystallization of $Rh_{12}L^{4.2}{}_6L^{4.6'}{}_6$: 1 mg of $Rh_{12}L^{4.2}{}_6L^{4.6'}{}_6$ were dissolved in 0.5 mL of DMF and then, 120 µL of isonicotinic acid solution (3.6 mg isonicotinic acid/1 mL DMA) were added. Purple parallelepiped crystals were obtained by slow ether vapor diffusion into this solution.

Crystallization of $Rh_{12}\mathbf{L^{4.2}}_6\mathbf{L^{4.1'}}_6$: 2 mg of $Rh_{12}\mathbf{L^{4.2}}_6\mathbf{L^{4.1}}'_6$ were dissolved in 0.5 mL of DMA and then, 200 µL 4-*tert*-butylpyridine solution (3.5 µL 4-*tert*-butylpyridine/1 mL DMA) were added. Purple parallelepiped crystals were obtained by slow ether vapor diffusion into this solution.

Crystallization of $Rh_{12}\mathbf{L^{4.2}}_6\mathbf{L^{4.2'}}_6$*:* 2 mg of $Rh_{12}\mathbf{L^{4.2}}_6\mathbf{L^{4.2}}'_6$ were first dissolved in 20 mL of DMF. Green parallelepiped crystals were obtained by slow ether vapor diffusion into this solution.

Crystallization of $Rh_{12}\mathbf{L^{4.2}}_6\mathbf{L^{4.3'}}_6$*:* 2 mg of $Rh_{12}\mathbf{L^{4.2}}_6\mathbf{L^{4.3}}'_6$ were dissolved in 0.5 mL of DMA and then, 200 µL 4-*tert*-butylpyridine solution (4.1 µL 4-*tert*-butylpyridine /1 mL DMA) were added. Purple parallelepiped crystals were obtained by slow ether vapor diffusion into this solution.

Crystallization of $Rh_{12}\mathbf{L^{4.2}}_6\mathbf{L^{4.4'}}_6$: 2 mg of $Rh_{12}\mathbf{L^{4.2}}_6\mathbf{L^{4.4}}'_6$ were dissolved in 0.5 mL of DMF and then, 120 µL of isonicotinic acid solution (3.8 mg isonicotinic acid/1 mL DMF) were added. Purple rhombic crystals were obtained by slow ether vapor diffusion into this solution.

Crystallization of $Rh_{12}\mathbf{L^{4.2}}_6\mathbf{L^{4.5'}}_6$*:* Hexagonal crystals of $Rh_{12}\mathbf{L^{4.2}}_6\mathbf{L^{4.5}}'_6$ were obtained by slow evaporation of a solution of 50 mg of $Rh_{12}\mathbf{L^{4.2}}_6\mathbf{L^{4.5}}'_6$ in 25 mL THF.

4.4.3 Crystallography

Crystallographic data for $Rh_{12}\mathbf{L^{4.1}}_6\mathbf{L^{4.1\text{-}4.6'}}_6$ MOPs and $Rh_{12}\mathbf{L^{4.2}}_6\mathbf{L^{4.1,4.3\text{-}4.6'}}_6$ MOPs were collected at 100 K at XALOC beamline at ALBA synchrotron (0.82653 Å).[62] Data were indexed, integrated and scaled using the XDS program.[63] Crystallographic data for $Rh_{12}\mathbf{L^{4.2}}_6\mathbf{L^{4.2'}}_6$ was collected at 'Bruker APEX-II CCD' at 150 K. Absorption correction was not applied in the case of $Rh_{12}\mathbf{L^{4.1}}_6\mathbf{L^{4.1\text{-}4.6'}}_6$ MOPs and $Rh_{12}\mathbf{L^{4.2}}_6\mathbf{L^{4.1,4.3\text{-}4.6'}}_6$ MOPs. Semiempirical multi-scan absorption correction was applied to $Rh_{12}\mathbf{L^{4.2}}_6\mathbf{L^{4.2'}}_6$ using SADAbs.[61] The structures were solved by direct methods and subsequently refined by correction of F2 against all reflections, using SHELXT2018 within Olex2 package.[64,65] All non-hydrogen atoms were refined with anisotropic thermal parameters by full-matrix least-squares calculations on F2 using the program SHELXL2018.[64] The hydrogen atoms were calculated in their expected positions with the HFIX instruction of SHELXL2018 and refined as riding atoms with Uiso(H) = 1.5 Ueq(C). We treated the presence of solvent molecules in the cavities of all structures running solvent mask using Olex2 solvent mask.[66,67] Thermal motion of some benzene rings and some coordinated solvents and pyridines of $Rh_{12}\mathbf{L}_6\mathbf{L'}_6$ MOPs was restrained by FLAT, DELU and SIMU. Thermal motion of $Rh_{12}\mathbf{L^{4.1}}_6\mathbf{L^{4.1'}}_6$, $Rh_{12}\mathbf{L^{4.2}}_6\mathbf{L^{4.2'}}_6$ and $Rh_{12}\mathbf{L^{4.2}}_6\mathbf{L^{4.6'}}_6$ was also restrained with EADPs restraints on the DMF or DMA moieties and in some positions of the benzene rings and ^{t}But groups of $Rh_{12}\mathbf{L^{4.2}}_6\mathbf{L^{4.2'}}_6$. The rotation of the three ^{t}But groups of $\mathbf{L^{4.2'}}$ of $Rh_{12}\mathbf{L^{4.2}}_6\mathbf{L^{4.2'}}_6$ and the coordinated pyridines of $Rh_{12}\mathbf{L^{4.2}}_6\mathbf{L^{4.3'}}_6$ was modeled splitting them in two parts. Due to their high mobility the positions corresponding to the four, six and twelve carbons of the OC_4, OC_6 and OC_{12} carbon chains of $Rh_{12}\mathbf{L^{4.1\text{-}4.2}}_6\mathbf{L^{4.3,4.4,4.5'}}_6$ were not well defined; constraints as EADP, DELU, RIGU and DFIX have been applied in the proposed model. Hydrogen atoms were inserted at calculated positions in the three structures. Reflections where I(obs) and I(calc) differ more than 10 times Sigma (W) were omitted, ($Rh_{12}\mathbf{L^{4.1}}_6\mathbf{L^{4.1'}}_6$) (-1 -1 4); ($Rh_{12}\mathbf{L^{4.1}}_6\mathbf{L^{4.3'}}_6$) (0 2 10) (-3 4 14) (-4 4 16) (-3 12

18) (-1 10 1); (Rh_{12}**L**$^{4.1}_{6}$**L**$^{4.4'}_{6}$) (0 5 10) (-3 6 12) (-5 6 7) (-2 3 7) (-7 7 4); (Rh_{12}**L**$^{4.1}_{6}$**L**$^{4.6'}_{6}$) (0 6 9) (-4 5 15) (-3 6 3) (-2 3 7); (Rh_{12}**L**$^{4.2}_{6}$**L**$^{4.6'}_{6}$) (2 -3 3) (-1 10 0) (-1 0 4) (2 0 5) (0 -5 8) (-3 -4 3) (-1 -2 7) (-2 -6 6) (3 -1 12); (Rh_{12}**L**$^{4.2}_{6}$**L**$^{4.1'}_{6}$) (-3 6 9) (-5 5 2); (Rh_{12}**L**$^{4.2}_{6}$**L**$^{4.2'}_{6}$) (-1 0 1) (2 0 0) (0 -1 1); (Rh_{12}**L**$^{4.2}_{6}$**L**$^{4.3'}_{6}$) (0 5 1); (Rh_{12}**L**$^{4.2}_{6}$**L**$^{4.5'}_{6}$) (-4 4 1) (-1 5 3) (-4 7 1).

$Rh_{12}\mathbf{L}^{\mathbf{4.1}}{}_6\mathbf{L}^{\mathbf{4.1'}}{}_6$

Identification code	2176188
Formula	$C_{206}H_{180}N_{14}O_{68}Rh_{12}$
Formula weight ($g.mol^{-1}$)	5174.55
Temperature (K)	100
Wavelength (Å)	0.82656
Crystal system	triclinic
Space group	P-1
Unit cell dimensions	a = 20.10034(7); b = 21.47025(6); c = 23.37885(8) α = 99.5536(3); β = 109.2065(3); γ = 113.9476(7)
Volume ($Å^3$)	8166.45(6)
Z	1
Density calculated (g/cm^{-3})	1.052
Absorption coefficient (mm^{-1})	0.971
F(000)	2598.0
Crystal size (mm)	0.18 × 0.18 × 0.16
2Theta range for data collection (º)	2.574 to 67.602
Index ranges	$-27 \leq h \leq 23$, $-28 \leq k \leq 28$, $0 \leq l \leq 31$
Reflection collected	103894
Independent reflections	31293 [R_{int} = 0.0951, R_{sigma} = 0.0958]
Refinement method	Full-matrix least-squares on F2
Data / restraints / parameters	31293/126/1268
Goodness-of-fit on F^2	1.043
Final R indices [I>2sigma(I)]	R_1 = 0.0796, wR_2 = 0.2431
R indices (all data)	R_1 = 0.0823, wR_2 = 0.2478
Largest diff. peak and hole	2.49, -2.02 e $Å^{-3}$

$Rh_{12}\mathbf{L}^{4.1}{}_6\mathbf{L}^{4.2'}{}_6$

Identification code	2176191
Formula	$C_{204}\ H_{168}\ N_6\ O_{66}\ Rh_{12}$
Formula weight ($g.mol^{-1}$)	4927.83
Temperature (K)	293(2)
Wavelength (Å)	0.82653
Crystal system	trigonal
Space group	R-3c
Unit cell dimensions	a = 31.480; b = 31.480; c = 72.390 α = 90; β =90; γ =120
Volume ($Å^3$)	62126.7
Z	6
Density calculated (g/cm^{-3})	0.790
Absorption coefficient (mm^{-1})	0.508
F(000)	14616.0
Crystal size (mm)	0.09 x 0.09 x 0.04
2Theta range for data collection (º)	1.87 to 57.568
Index ranges	$-41 \leq h \leq 41$, $-42 \leq k \leq 42$, $-89 \leq l \leq 89$
Reflection collected	235704
Independent reflections	15183 [Rint = 0.1119, Rsigma = 0.0495]
Refinement method	Full-matrix least-squares on F2
Data / restraints / parameters	15183/39/409
Goodness-of-fit on F^2	1.318
Final R indices [I>2sigma(I)]	R_1 = 0.1492, wR_2 = 0.3991
R indices (all data)	R_1 = 0.2037, wR_2 = 0.4526
Largest diff. peak and hole	2.12/-0.70

$Rh_{12}\mathbf{L}^{\mathbf{4.1}}{}_6\mathbf{L}^{\mathbf{4.3'}}{}_6$

Identification code	2176185
Formula	$C_{204}H_{144}N_6O_{72}Rh_{12}$
Formula weight ($g.mol^{-1}$)	5066.16
Temperature (K)	100
Wavelength (Å)	0.82656
Crystal system	trigonal
Space group	R-3c
Unit cell dimensions	a = 31.4131(2); b = 31.4131(2); c = 72.4411(2) α = 90; β = 90; γ = 120
Volume ($Å^3$)	61906.6(8)
Z	6
Density calculated (g/cm^{-3})	0.815
Absorption coefficient (mm^{-1})	0.768
F(000)	15156.0
Crystal size (mm)	0.12 × 0.11 × 0.09
2Theta range for data collection (º)	2.178 to 49.842
Index ranges	$0 \leq h \leq 27$, $0 \leq k \leq 16$, $-73 \leq l \leq 73$
Reflection collected	142271
Independent reflections	7642 [R_{int} = 0.0648, R_{sigma} = 0.0268]
Refinement method	Full-matrix least-squares on F2
Data / restraints / parameters	7642/62/406
Goodness-of-fit on F^2	1.343
Final R indices [I>2sigma(I)]	R_1 = 0.1098, wR_2 = 0.3219
R indices (all data)	R_1 = 0.1240, wR_2 = 0.3447
Largest diff. peak and hole	1.45, -0.46 e $Å^{-3}$

$Rh_{12}\mathbf{L}^{4.1}{}_6\mathbf{L}^{4.4'}{}_6$

Identification code	2176186
Formula	$C_{216}H_{180}N_6O_{72}Rh_{12}$
Formula weight ($g.mol^{-1}$)	5246.57
Temperature (K)	100
Wavelength (Å)	0.82656
Crystal system	trigonal
Space group	R-3c
Unit cell dimensions	a = 31.2593(3); b = 31.2593(3); c = 73.3075(10) α = 90; β = 90; γ = 120
Volume ($Å^3$)	62035.1(15)
Z	6
Density calculated (g/cm^{-3})	0.843
Absorption coefficient (mm^{-1})	0.768
F(000)	15804.0
Crystal size (mm)	0.12 × 0.11 × 0.09
2Theta range for data collection (º)	3.03 to 58.18
Index ranges	$0 \leq h \leq 31$, $0 \leq k \leq 18$, $-86 \leq l \leq 86$
Reflection collected	213203
Independent reflections	11763 [R_{int} = 0.0930, R_{sigma} = 0.0361]
Refinement method	Full-matrix least-squares on F2
Data / restraints / parameters	11763/29/436
Goodness-of-fit on F^2	1.057
Final R indices [I>2sigma(I)]	R_1 = 0.0695, wR_2 = 0.2399
R indices (all data)	R_1 = 0.0846, wR_2 = 0.2525
Largest diff. peak and hole	1.01, -0.61 e $Å^{-3}$

$Rh_{12}\mathbf{L}^{\mathbf{4.1}}{}_6\mathbf{L}^{\mathbf{4.5'}}{}_6$

Identification code	2176187
Formula	$C_{252}H_{252}N_6O_{72}Rh_{12}$
Formula weight ($g.mol^{-1}$)	5751.50
Temperature (K)	100
Wavelength (Å)	0.82656
Crystal system	trigonal
Space group	R-3c
Unit cell dimensions	a = 31.6843(5); b = 31.6843(5); c = 72.349(2) α = 90; β = 90; γ = 120
Volume ($Å^3$)	62900(3)
Z	6
Density calculated (g/cm^{-3})	0.911
Absorption coefficient (mm^{-1})	0.763
F(000)	17532.0
Crystal size (mm)	0.09 × 0.07 × 0.06
2Theta range for data collection (º)	2.99 to 48.814
Index ranges	$0 \leq h \leq 27$, $0 \leq k \leq 15$, $-71 \leq l \leq 72$
Reflection collected	134519
Independent reflections	7315 [R_{int} = 0.1340, Rsigma = 0.0505]
Refinement method	Full-matrix least-squares on F2
Data / restraints / parameters	7315/101/394
Goodness-of-fit on F^2	1.245
Final R indices [I>2sigma(I)]	R_1 = 0.1105, wR_2 = 0.3237
R indices (all data)	R_1 = 0.1354, wR_2 = 0.3509
Largest diff. peak and hole	1.46, -0.48 e $Å^{-3}$

$Rh_{12}\mathbf{L}^{4.1}{}_6\mathbf{L}^{4.6'}{}_6$

Identification code	2176189
Formula	$C_{204}H_{120}N_6O_{66}Rh_{12}$
Formula weight ($g.mol^{-1}$)	4945.97
Temperature (K)	100
Wavelength (Å)	0.82656
Crystal system	trigonal
Space group	R-3
Unit cell dimensions	a = 29.1065(5); b = 29.1065(5); c = 56.2463(9) α = 90; β = 90; γ = 120
Volume ($Å^3$)	41267.1(16)
Z	3
Density calculated (g/cm^{-3})	0.597
Absorption coefficient (mm^{-1})	0.574
F(000)	7362.0
Crystal size (mm)	0.07 × 0.07 × 0.04
2Theta range for data collection (º)	2.526 to 50.966
Index ranges	$0 \le h \le 25$, $0 \le k \le 26$, $-58 \le l \le 58$
Reflection collected	100303
Independent reflections	10826 [R_{int} = 0.0810, R_{sigma} = 0.0503]
Refinement method	Full-matrix least-squares on F2
Data / restraints / parameters	10826/88/385
Goodness-of-fit on F^2	1.029
Final R indices [I>2sigma(I)]	R_1 = 0.0648, wR_2 = 0.2102
R indices (all data)	R_1 = 0.0864, wR_2 = 0.2286
Largest diff. peak and hole	0.72, -0.36 e $Å^{-3}$

$Rh_{12}\mathbf{L}^{\mathbf{4.2}}{}_6\mathbf{L}^{\mathbf{4.6'}}{}_6$

Identification code	2176190
Formula	$C_{195}H_{115}N_{19}O_{67}Rh_{12}$
Formula weight ($g.mol^{-1}$)	5030.97
Temperature (K)	100
Wavelength (Å)	0.82656
Crystal system	triclinic
Space group	P-1
Unit cell dimensions	a = 22.9616(5); b = 27.9645(4); c = 29.9154(4) α = 87.892(2); β = 68.779(2); γ = 77.069(2)
Volume ($Å^3$)	17431.7(6)
Z	2
Density calculated (g/cm^{-3})	0.959
Absorption coefficient (mm^{-1})	0.908
F(000)	4988.0
Crystal size (mm)	0.16 × 0.14 × 0.07
2Theta range for data collection (º)	1.7 to 59.768
Index ranges	$-25 \leq h \leq 27$, $-33 \leq k \leq 33$, $0 \leq l \leq 35$
Reflection collected	188103
Independent reflections	57778 [R_{int} = 0.0481, R_{sigma} = 0.0526]
Refinement method	Full-matrix least-squares on F2
Data / restraints / parameters	57778/451/2464
Goodness-of-fit on F^2	1.170
Final R indices [I>2sigma(I)]	R_1 = 0.1123, wR_2 = 0.3103
R indices (all data)	R_1 = 0.1379, wR_2 = 0.3414
Largest diff. peak and hole	2.70, -0.98 e $Å^{-3}$

$Rh_{12}\mathbf{L}^{4.2}{}_6\mathbf{L}^{4.1'}{}_6$

Identification code	2095292
Formula	$C_{186}H_{150}N_{18}O_{54}Rh_{12}$
Formula weight ($g.mol^{-1}$)	4736.15
Temperature (K)	100
Wavelength (Å)	0.82653
Crystal system	trigonal
Space group	R-3c
Unit cell dimensions	a = 31.163; b = 31.163; c = 69.154 α = 90º; β = 90º; γ =120º
Volume/Å3	58160.2
Z	6
Density calculated (g/cm-3)	0.811
Absorption coefficient (mm^{-1})	0.809
F(000)	14184.0
Crystal size (mm)	0.11 x 0.095 x 0.088
2Theta range for data collection (º)	3.04 to 49.344
Index ranges	$0 \leq h \leq 27$, $0 \leq k \leq 15$, $-69 \leq l \leq 69$
Reflections collected	131593
Independent reflections	6990 [Rint = 0.0673, Rsigma = 0.0272]
Refinement method	Full-matrix least-squares on F2
Data / restraints / parameters	6990/233/374
Goodness-of-fit on F^2	1.366
Final R indices [I>2sigma(I)]	R_1 = 0.1002, wR_2 = 0.3216
R indices (all data)	R_1 = 0.1108, wR_2 = 0.3418
Largest diff. peak and hole	1.07, -0.36 e $Å^{-3}$

$Rh_{12}\mathbf{L}^{4.2}{}_6\mathbf{L}^{4.2'}{}_6$

Identification code	2095294
Formula	$C_{180}H_{176}N_{20}O_{62}Rh_{12}$
Formula weight ($g.mol^{-1}$)	4846.32
Temperature (K)	150
Wavelength (Å)	1.54178
Crystal system	Triclinic
Space group	P-1
Unit cell dimensions	a = 19.1839(14); b = 19.3591(14); c = 21.9788(17) α = 98.356(5); β = 109.317(5); γ = 109.104(4)
Volume ($Å^3$)	6978.3(9)
Z	1
Density calculated (g/cm^{-3})	1.153
Absorption coefficient (mm^{-1})	6.108
F(000)	2432.0
Crystal size (mm)	0.08 × 0.08 × 0.04
2Theta range for data collection (º)	4.444 to 101.764
Index ranges	$-19 \leq h \leq 19$, $-19 \leq k \leq 19$, $-22 \leq l \leq 22$
Reflection collected	45605
Independent reflections	14581 [R_{int} = 0.1814, R_{sigma} = 0.2072]
Refinement method	Full-matrix least-squares on F2
Data / restraints / parameters	14581/470/1190
Goodness-of-fit on F^2	0.923
Final R indices [I>2sigma(I)]	R_1 = 0.0805, wR_2 = 0.1989
R indices (all data)	R_1 = 0.1575, wR_2 = 0.2416
Largest diff. peak and hole	1.46, -1.07 e $Å^{-3}$

$Rh_{12}\mathbf{L}^{4.2}{}_6\mathbf{L}^{4.3'}{}_6$

Identification code	2176184
Formula	$C_{234}H_{252}N_{24}O_{60}Rh_{12}$
Formula weight ($g.mol^{-1}$)	5595.50
Temperature (K)	100
Wavelength (Å)	0.82656
Crystal system	trigonal
Space group	R-3
Unit cell dimensions	a = 33.9017(2); b = 33.9017(2); c = 23.6843(7) α = 90; β = 90; γ = 120
Volume ($Å^3$)	23574.0(8)
Z	3
Density calculated (g/cm^{-3})	1.182
Absorption coefficient (mm^{-1})	1.014
F(000)	8532.0
Crystal size (mm)	0.11 × 0.09 × 0.03
2Theta range for data collection (º)	3.796 to 66.798
Index ranges	$0 \leq h \leq 38$, $0 \leq k \leq 38$, $-31 \leq l \leq 31$
Reflection collected	99905
Independent reflections	12006 [R_{int} = 0.0791, R_{sigma} = 0.0517]
Refinement method	Full-matrix least-squares on F2
Data / restraints / parameters	12006/100/524
Goodness-of-fit on F^2	0.985
Final R indices [I>2sigma(I)]	R_1 = 0.0806, wR_2 = 0.2342
R indices (all data)	R_1 = 0.1094, wR_2 = 0.2602
Largest diff. peak and hole	2.32, -0.45 e $Å^{-3}$

$Rh_{12}\mathbf{L}^{4.2}{}_6\mathbf{L}^{4.4'}{}_6$

Identification code	2176183
Formula	$C_{204}H_{168}N_{18}O_{72}Rh_{12}$
Formula weight ($g.mol^{-1}$)	5258.47
Temperature (K)	100
Wavelength (Å)	0.82656
Crystal system	trigonal
Space group	R-3
Unit cell dimensions	a = 28.4941(2); b = 28.4941(2); c = 46.4950(5) α = 90; β = 90; γ = 120
Volume ($Å^3$)	32692.4(6)
Z	3
Density calculated (g/cm^{-3})	0.801
Absorption coefficient (mm^{-1})	0.730
F(000)	7902.0
Crystal size (mm)	0.11 × 0.07 × 0.06
2Theta range for data collection (º)	5.18 to 44.134
Index ranges	$0 \leq h \leq 21$, $0 \leq k \leq 22$, $-42 \leq l \leq 42$
Reflection collected	55567
Independent reflections	5693 [R_{int} = 0.0300, R_{sigma} = 0.0178]
Refinement method	Full-matrix least-squares on F2
Data / restraints / parameters	5693/398/370
Goodness-of-fit on F^2	2.486
Final R indices [I>2sigma(I)]	R_1 = 0.1742, wR_2 = 0.4732
R indices (all data)	R_1 = 0.1821, wR_2 = 0.5059
Largest diff. peak and hole	2.27, -0.69 e $Å^{-3}$

$Rh_{12}\mathbf{L}^{4.2}{}_6\mathbf{L}^{4.5'}{}_6$

Identification code	2095293
Formula	$C_{228}H_{264}N_{12}O_{66}Rh_{12}$
Formula weight ($g.mol^{-1}$)	5463.42
Temperature (K)	100
Wavelength (Å)	0.82653
Crystal system	Trigonal
Space group	R-3
Unit cell dimensions	a = 26.590; b = 26.590; c = 43.610 α = 90º; β = 90º; γ =120º
Volume ($Å^3$)	26702.6
Z	3
Density calculated (g/cm^{-3})	1.019
Absorption coefficient (mm^{-1})	0.894
F(000)	8352.0
Crystal size (mm)	0.34 × 0.18 × 0.04
2Theta range for data collection (º)	2.992 to 49.866
Index ranges	$0 \le h \le 22$, $0 \le k \le 23$, $-44 \le l \le 44$
Reflections collected	64408
Independent reflections	6603 [R_{int} = 0.0718, R_{sigma} = 0.0802]
Refinement method	Full-matrix least-squares on F2
Data / restraints / parameters	6603/194/412
Goodness-of-fit on F^2	1.060
Final R indices [I>2sigma(I)]	R_1 = 0.0808, wR_2 = 0.2689
R indices (all data)	R_1 = 0.1044, wR_2 = 0.2975
Largest diff. peak and hole	0.60, -0.47 e $Å^{-3}$

4.4.4 Characterization

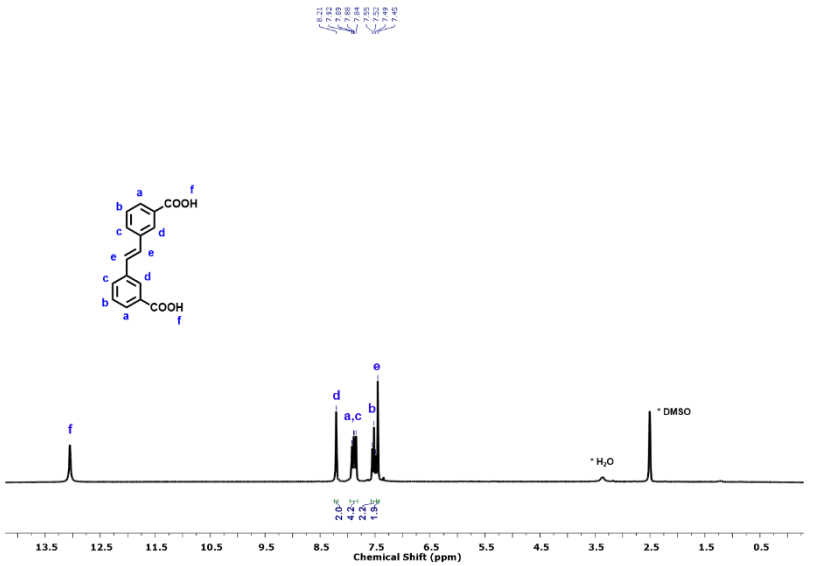

Figure S4.1. [1]H-NMR spectrum (250 MHz, DMSO-d_6) of (E)-3,3'-(ethene-1,2-diyl)dibenzoic acid.

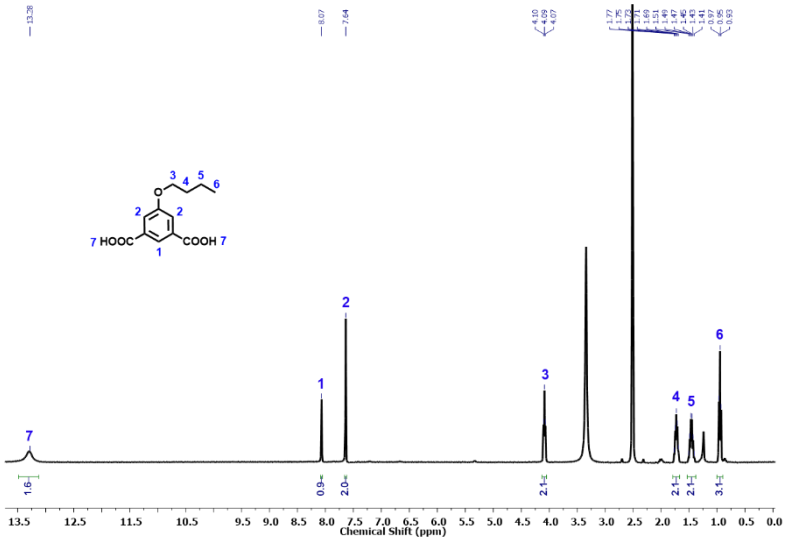

Figure S4.2. [1]H-NMR spectrum (400 MHz, DMSO-d_6) of 5-butoxyisophthalic acid.

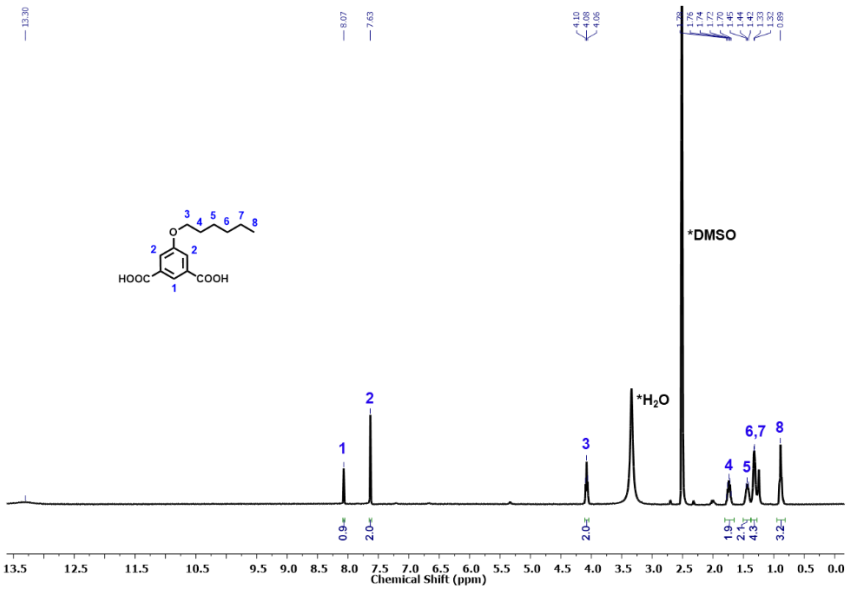

Figure S4.3. ^{1}H-NMR spectrum (400 MHz, DMSO-d_6) of 5-(hexyloxy)isophthalic acid.

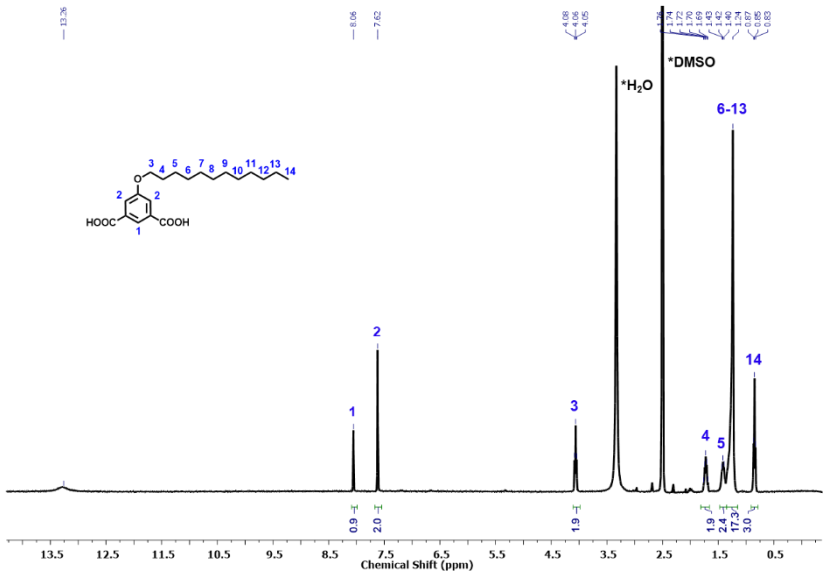

Figure S4.4. ^{1}H-NMR spectrum (400 MHz, DMSO-d_6) of 5-(dodecyloxy)isophthalic acid.

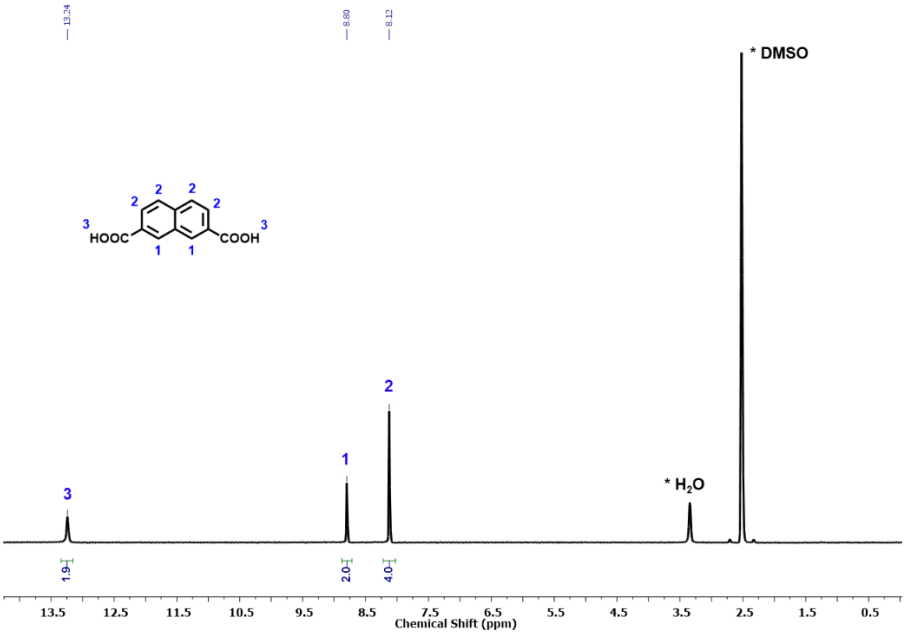

Figure S4.5. [1]H-NMR spectrum (400 MHz, DMSO-d_6) of naphthalene-2,7-dicarboxylic acid.

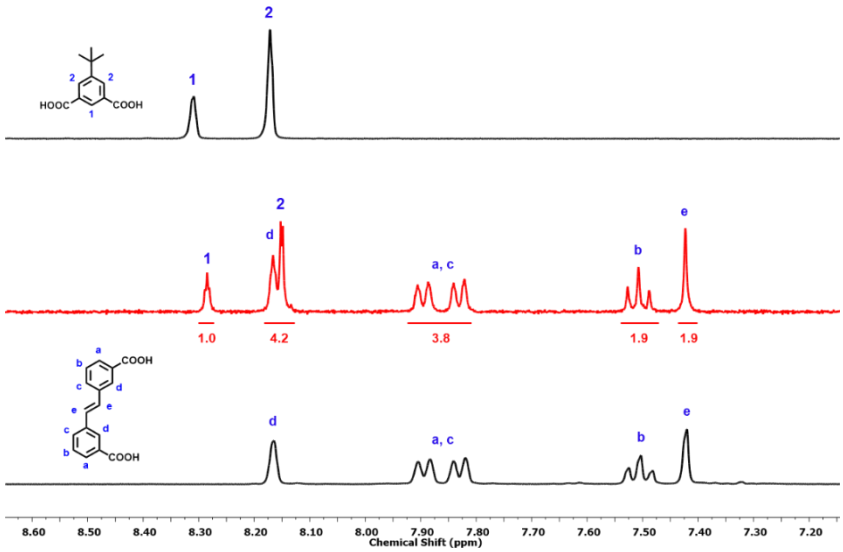

Figure S4.6. [1]H-NMR spectra (400 MHz, DMSO-d_6) of digested $Rh_{12}\mathbf{L^{4.1}}_6\mathbf{L^{4.2'}}_6$. The integrals of the assigned protons revealed that the relation between the two ligands is the expected 1:1. (a) $\mathbf{L^{4.2'}}$; (b) digested $Rh_{12}\mathbf{L^{4.1}}_6\mathbf{L^{4.2'}}_6$; and (c) $\mathbf{L^{4.1}}$.

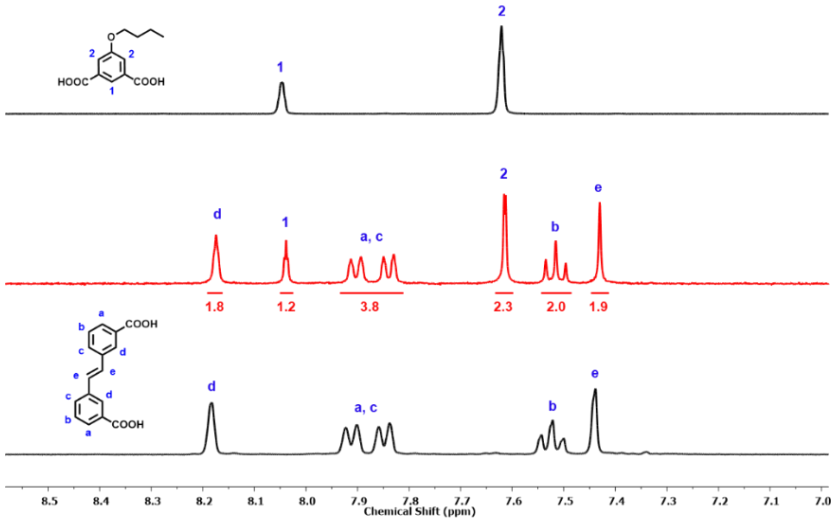

Figure S4.7. ^{1}H-NMR spectra (400 MHz, DMSO-d$_6$) of digested $Rh_{12}\mathbf{L^{4.1}}_6\mathbf{L^{4.3'}}_6$. The integrals of the assigned protons revealed that the relation between the two ligands is the expected 1:1. (a) $\mathbf{L^{4.3'}}$; (b) digested $Rh_{12}\mathbf{L^{4.1}}_6\mathbf{L^{4.3'}}_6$; and (c) $\mathbf{L^{4.1}}$.

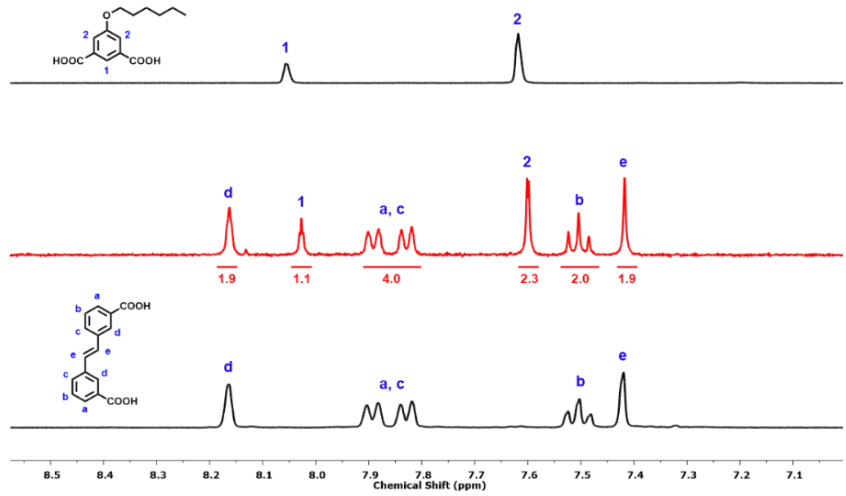

Figure S4.8. ^{1}H-NMR spectra (400 MHz, DMSO-d$_6$) of digested $Rh_{12}\mathbf{L^{4.1}}_6\mathbf{L^{4.4'}}_6$. The integrals of the assigned protons revealed that the relation between the two ligands is the expected 1:1. (a) $\mathbf{L^{4.4'}}$; (b) digested $Rh_{12}\mathbf{L^{4.1}}_6\mathbf{L^{4.4'}}_6$; and (c) $\mathbf{L^{4.1}}$.

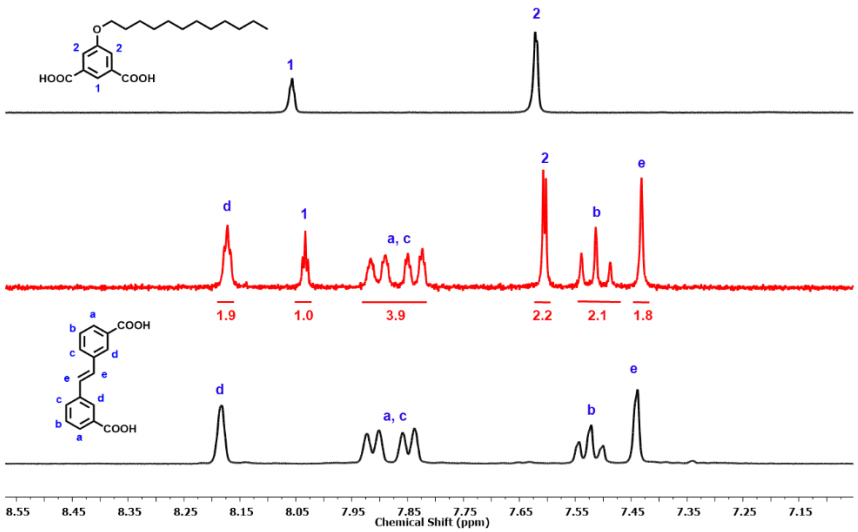

Figure S4.9. ^{1}H-NMR spectra (400 MHz, DMSO-d$_6$) of digested $Rh_{12}\mathbf{L^{4.1}}_6\mathbf{L^{4.5'}}_6$. The integrals of the assigned protons revealed that the relation between the two ligands is the expected 1:1. (a) $\mathbf{L^{4.5'}}$; (b) digested $Rh_{12}\mathbf{L^{4.1}}_6\mathbf{L^{4.5'}}_6$; and (c) $\mathbf{L^{4.1}}$.

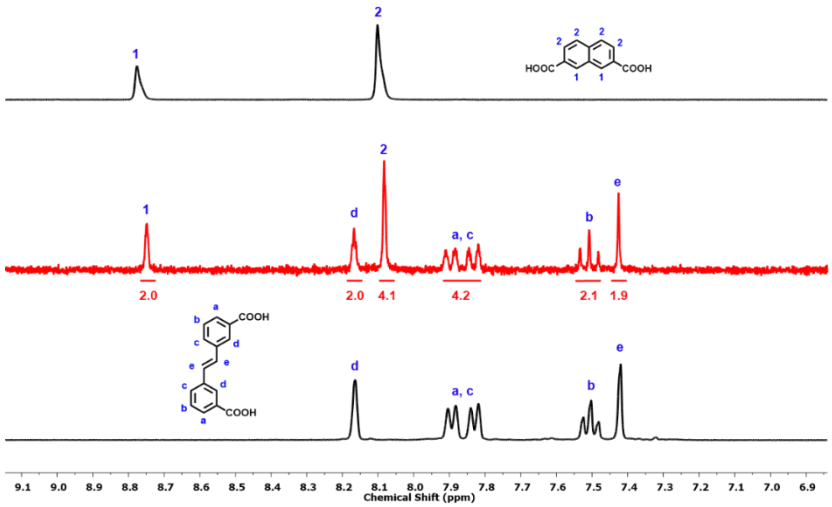

Figure S4.10. ^{1}H-NMR spectra (400 MHz, DMSO-d$_6$) of digested $Rh_{12}\mathbf{L^{4.1}}_6\mathbf{L^{4.6'}}_6$. The integrals of the assigned protons revealed that the relation between the two ligands is the expected 1:1. (a) $\mathbf{L^{4.6'}}$; (b) digested $Rh_{12}\mathbf{L^{4.1}}_6\mathbf{L^{4.6'}}_6$; and (c) $\mathbf{L^{4.1}}$.

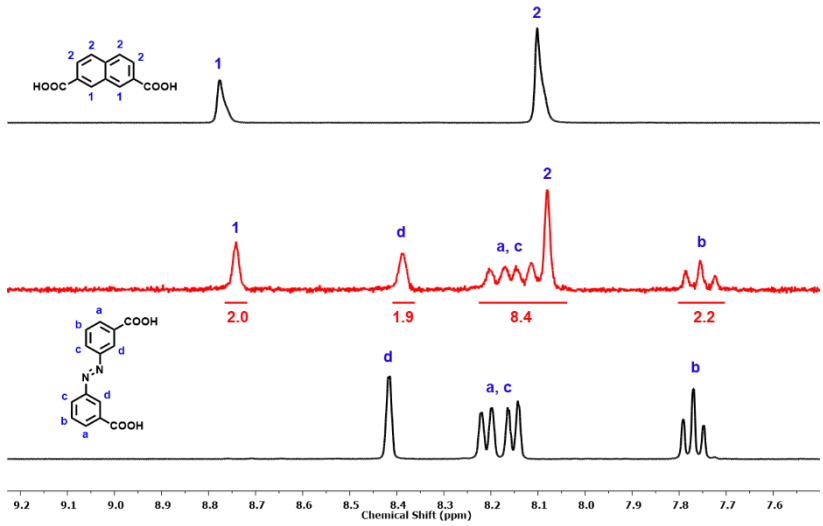

Figure S4.11. ^{1}H-NMR spectra (400 MHz, DMSO-d_6) of digested $Rh_{12}\mathbf{L^{4.2}}_6\mathbf{L^{4.6'}}_6$. The integrals of the assigned protons revealed that the relation between the two ligands is the expected 1:1. (a) $\mathbf{L^{4.6'}}$; (b) digested $Rh_{12}\mathbf{L^{4.2}}_6\mathbf{L^{4.6'}}_6$; and (c) $\mathbf{L^{4.2}}$.

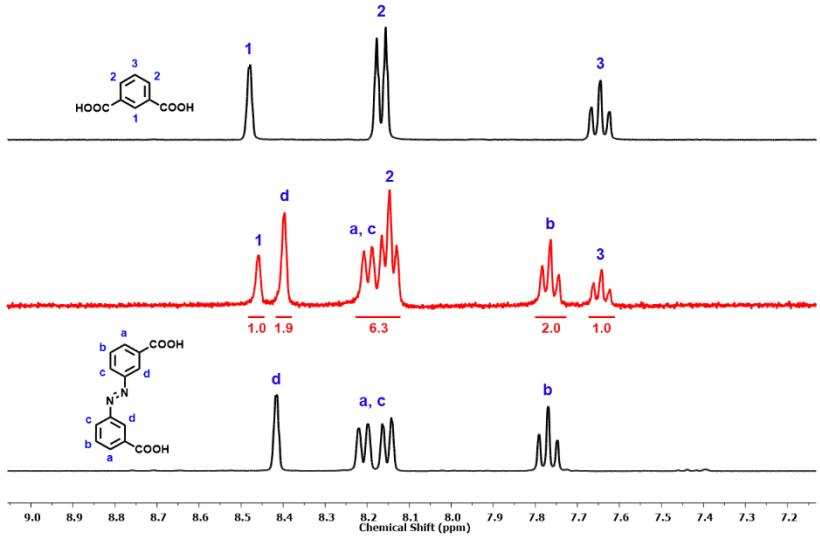

Figure S4.12. ^{1}H-NMR spectra (400 MHz, DMSO-d_6) of digested $Rh_{12}\mathbf{L^{4.2}}_6\mathbf{L^{4.1'}}_6$. The integrals of the assigned protons revealed that the relation between the two ligands is the expected 1:1. (a) $\mathbf{L^{4.1'}}$; (b) digested $Rh_{12}\mathbf{L^{4.2}}_6\mathbf{L^{4.1'}}_6$; and (c) $\mathbf{L^{4.2}}$.

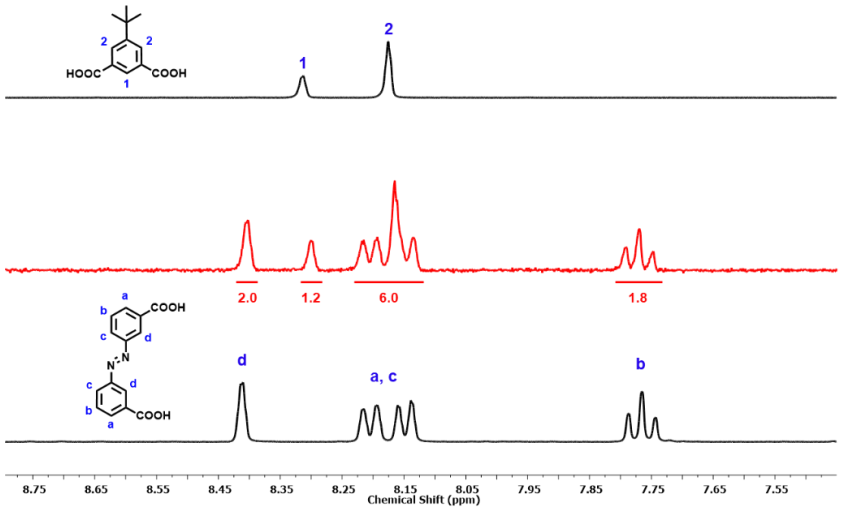

Figure S4.13. ^{1}H-NMR spectra (400 MHz, DMSO-d$_6$) of digested $Rh_{12}\mathbf{L}^{\mathbf{4.2}}{}_6\mathbf{L}^{\mathbf{4.2'}}{}_6$. The integrals of the assigned protons revealed that the relation between the two ligands is the expected 1:1. (a) $\mathbf{L}^{\mathbf{4.2'}}$; (b) digested $Rh_{12}\mathbf{L}^{\mathbf{4.2}}{}_6\mathbf{L}^{\mathbf{4.2'}}{}_6$; and (c) $\mathbf{L}^{\mathbf{4.2}}$.

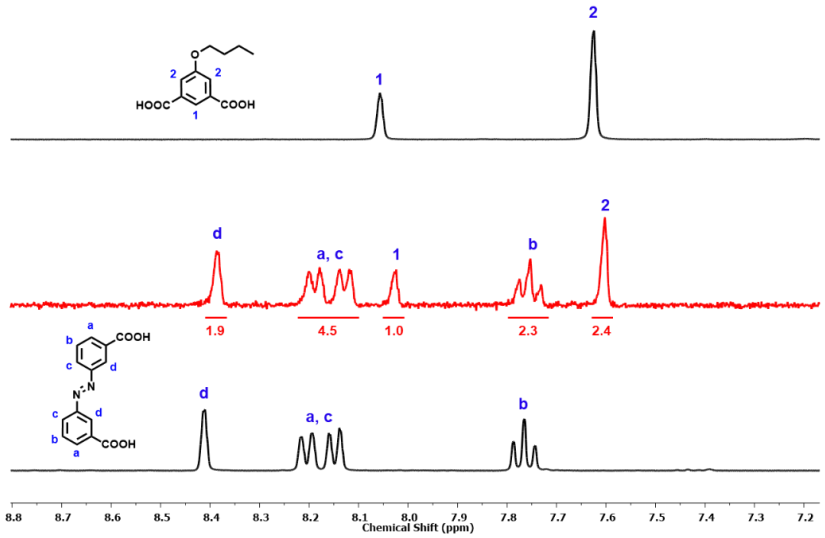

Figure S4.14. ^{1}H-NMR spectra (400 MHz, DMSO-d$_6$) of digested $Rh_{12}\mathbf{L}^{\mathbf{4.2}}{}_6\mathbf{L}^{\mathbf{4.3'}}{}_6$. The integrals of the assigned protons revealed that the relation between the two ligands is the expected 1:1. (a) $\mathbf{L}^{\mathbf{4.3'}}$; (b) digested $Rh_{12}\mathbf{L}^{\mathbf{4.2}}{}_6\mathbf{L}^{\mathbf{4.3'}}{}_6$; and (c) $\mathbf{L}^{\mathbf{4.2}}$.

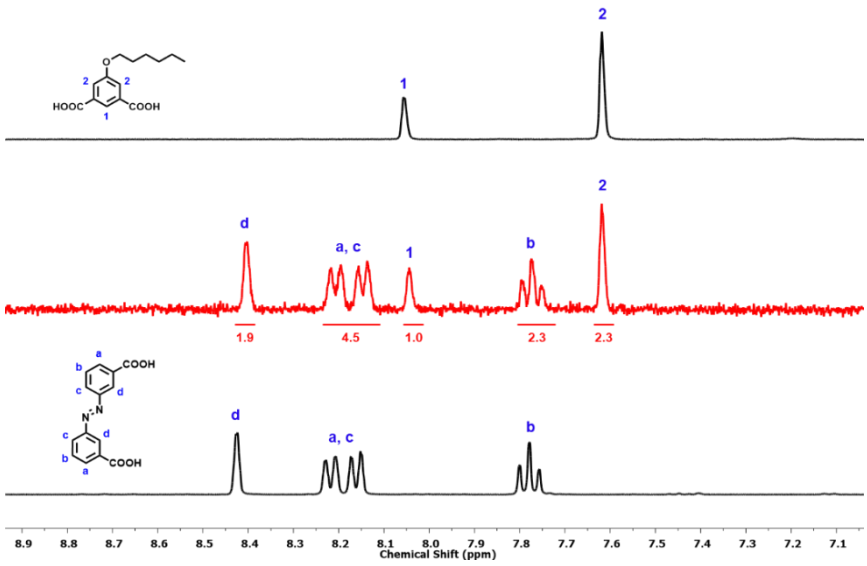

Figure S4.15. ^{1}H-NMR spectra (400 MHz, DMSO-d$_6$) of digested $Rh_{12}\mathbf{L^{4.2}}_6\mathbf{L^{4.4'}}_6$. The integrals of the assigned protons revealed that the relation between the two ligands is the expected 1:1. (a) $\mathbf{L^{4.4'}}$; (b) digested $Rh_{12}\mathbf{L^{4.2}}_6\mathbf{L^{4.4'}}_6$; and (c) $\mathbf{L^{4.2}}$.

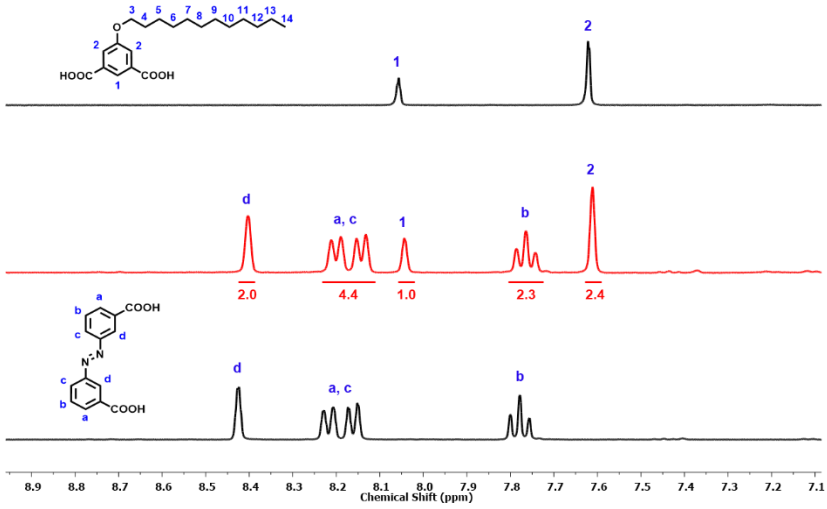

Figure S4.16. ^{1}H-NMR spectra (400 MHz, DMSO-d$_6$) of digested $Rh_{12}\mathbf{L^{4.2}}_6\mathbf{L^{4.5'}}_6$. The integrals of the assigned protons revealed that the relation between the two ligands is the expected 1:1. (a) $\mathbf{L^{4.5'}}$; (b) digested $Rh_{12}\mathbf{L^{4.2}}_6\mathbf{L^{4.5'}}_6$; and (c) $\mathbf{L^{4.2}}$.

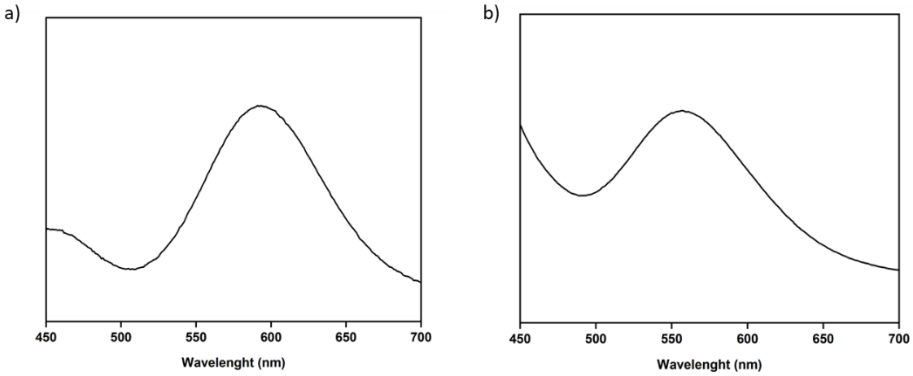

Figure S4.17. (a) UV-vis spectrum of a DMF solution of $Rh_{12}\mathbf{L^{4.1}}_6\mathbf{L^{4.2'}}_6$. The maximum of adsorption band I (λ_{max}) of $Rh_{12}\mathbf{L^{4.1}}_6\mathbf{L^{4.2'}}_6$ is centered at 593 nm. (b) UV-vis spectrum of a DMF solution of $Rh_{12}\mathbf{L^{4.1}}_6\mathbf{L^{4.2'}}_6$ and six equivalents of isonicotinic acid. The maximum of adsorption band I (λ_{max}) of $Rh_{12}\mathbf{L^{4.1}}_6\mathbf{L^{4.2'}}_6$ is centered at 557 nm.

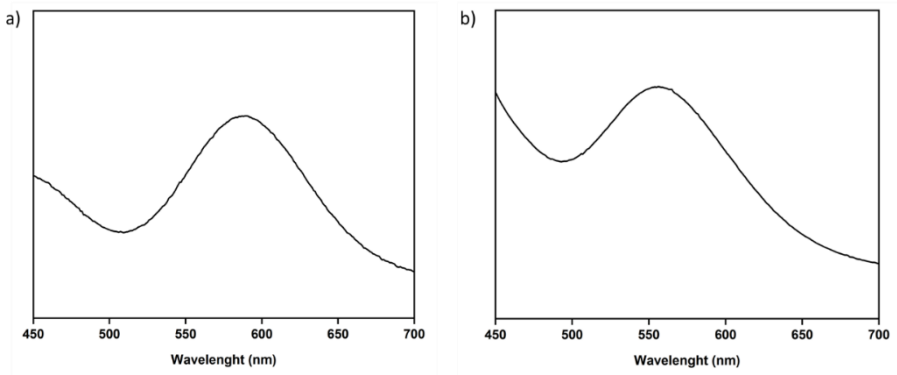

Figure S4.18. (a) UV-vis spectrum of a DMF solution of $Rh_{12}\mathbf{L^{4.1}}_6\mathbf{L^{4.3'}}_6$. The maximum of adsorption band I (λ_{max}) of $Rh_{12}\mathbf{L^{4.1}}_6\mathbf{L^{4.3'}}_6$ is centered at 589 nm. (b) UV-vis spectrum of a DMF solution of $Rh_{12}\mathbf{L^{4.1}}_6\mathbf{L^{4.3'}}_6$ and six equivalents of isonicotinic acid. The maximum of adsorption band I (λ_{max}) of $Rh_{12}\mathbf{L^{4.1}}_6\mathbf{L^{4.3'}}_6$ is centered at 556 nm.

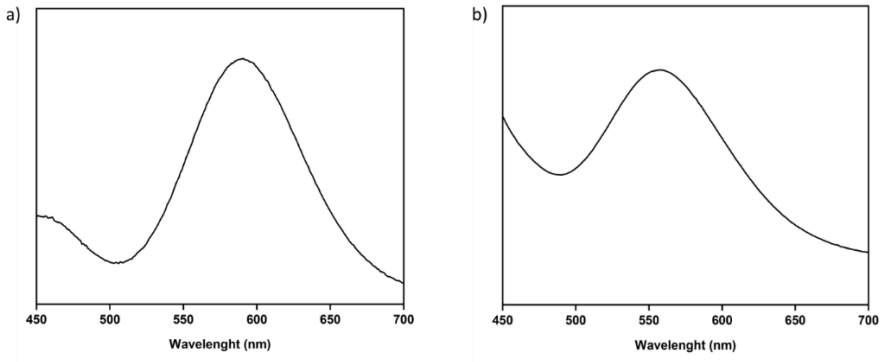

Figure S4.19: (a) UV-vis spectrum of a DMF solution of $Rh_{12}\mathbf{L^{4.1}}_6\mathbf{L^{4.4'}}_6$. The maximum of adsorption band I (λ_{max}) of $Rh_{12}\mathbf{L^{4.1}}_6\mathbf{L^{4.4'}}_6$ is centered at 591 nm. (b) UV-vis spectrum of a DMF solution of $Rh_{12}\mathbf{L^{4.1}}_6\mathbf{L^{4.4'}}_6$ and six equivalents of isonicotinic acid. The maximum of adsorption band I (λ_{max}) of $Rh_{12}\mathbf{L^{4.1}}_6\mathbf{L^{4.4'}}_6$ is centered at 558 nm.

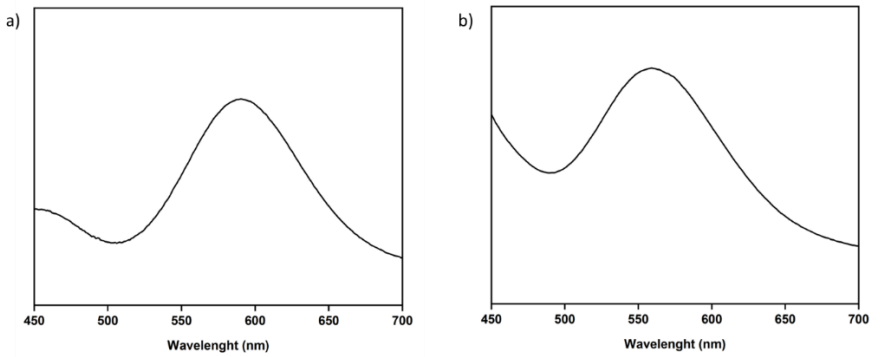

Figure S4.20. (a) UV-vis spectrum of a DMF solution of $Rh_{12}\mathbf{L^{4.1}}_6\mathbf{L^{4.5'}}_6$. The maximum of adsorption band I (λ_{max}) of $Rh_{12}\mathbf{L^{4.1}}_6\mathbf{L^{4.5'}}_6$ is centered at 591 nm. (b) UV-vis spectrum of a DMF solution of $Rh_{12}\mathbf{L^{4.1}}_6\mathbf{L^{4.5'}}_6$ and six equivalents of isonicotinic acid. The maximum of adsorption band I (λ_{max}) of $Rh_{12}\mathbf{L^{4.1}}_6\mathbf{L^{4.5'}}_6$ is centered at 559 nm.

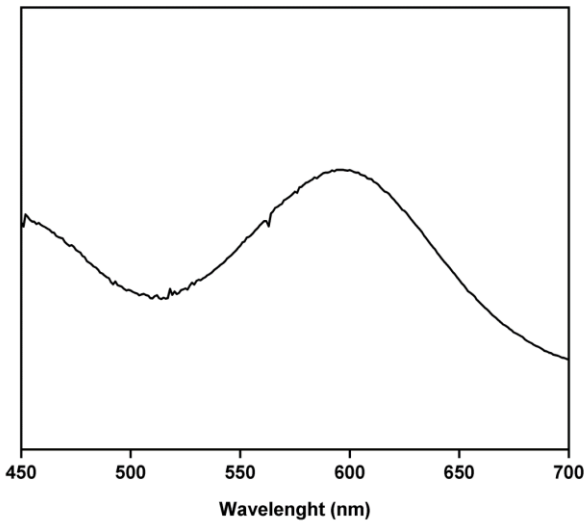

Figure S4.21. UV-vis spectrum of a DMA solution of $Rh_{12}\mathbf{L^{4.1}}_6\mathbf{L^{4.6'}}_6$. The maximum of adsorption band I (λ_{max}) of $Rh_{12}\mathbf{L^{4.1}}_6\mathbf{L^{4.6'}}_6$ is centered at 597 nm.

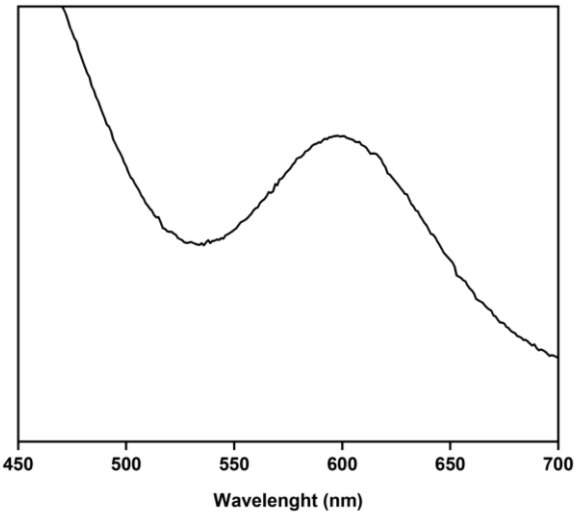

Figure S4.22. UV-vis spectrum of a DMF solution of $Rh_{12}\mathbf{L^{4.2}}_6\mathbf{L^{4.6'}}_6$. The maximum of adsorption band I (λ_{max}) of $Rh_{12}\mathbf{L^{4.2}}_6\mathbf{L^{4.6'}}_6$ is centered at 599 nm.

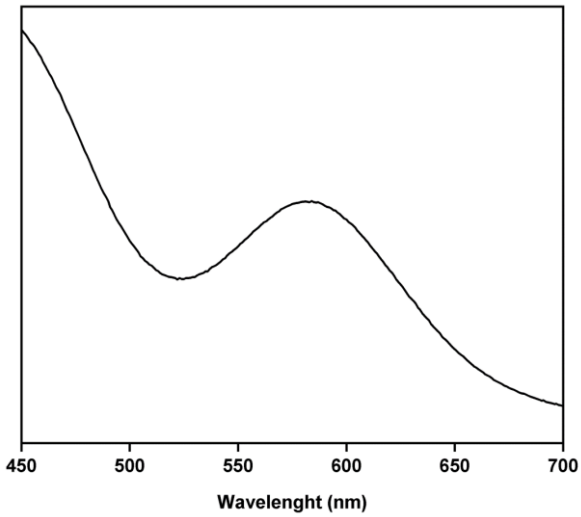

Figure S4.23. UV-vis spectrum of a DMF solution of $Rh_{12}\mathbf{L}^{4.2}{}_6\mathbf{L}^{4.1'}{}_6$. The maximum of adsorption band I (λ_{max}) of $Rh_{12}\mathbf{L}^{4.2}{}_6\mathbf{L}^{4.1'}{}_6$ is centered at 583 nm.

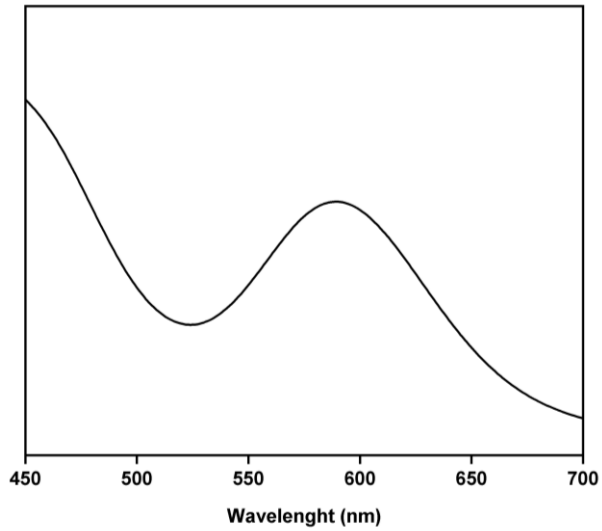

Figure S4.24. UV-vis spectrum of a DMF solution of $Rh_{12}\mathbf{L}^{4.2}{}_6\mathbf{L}^{4.2'}{}_6$. The maximum of adsorption band I (λ_{max}) of $Rh_{12}\mathbf{L}^{4.2}{}_6\mathbf{L}^{4.2'}{}_6$ is centered at 590 nm.

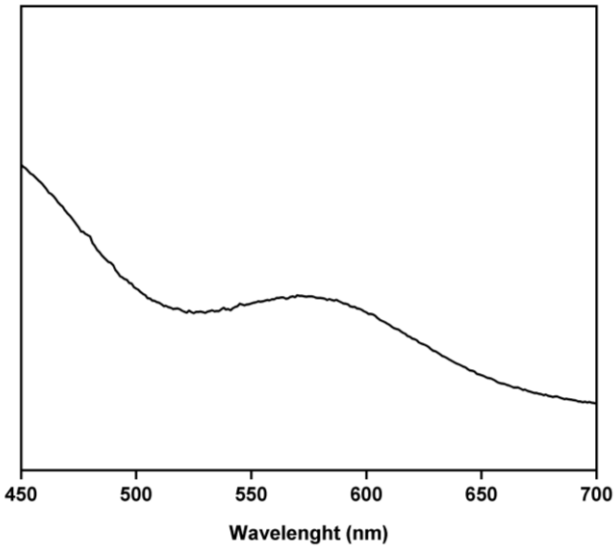

Figure S4.25: UV-vis spectrum of a DMF solution of $Rh_{12}\mathbf{L}^{4.2}{}_6\mathbf{L}^{4.3'}{}_6$. The maximum of adsorption band I (λ_{max}) of $Rh_{12}\mathbf{L}^{4.2}{}_6\mathbf{L}^{4.3'}{}_6$ is centered at 573 nm.

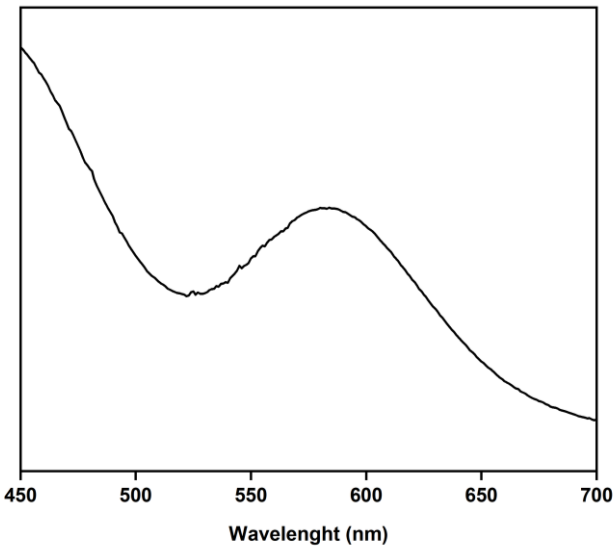

Figure S4.26. UV-vis spectrum of a $Rh_{12}\mathbf{L}^{4.2}{}_6\mathbf{L}^{4.4'}{}_6$ solution of DMF. The maximum of adsorption band I (λ_{max}) of $Rh_{12}\mathbf{L}^{4.2}{}_6\mathbf{L}^{4.4'}{}_6$ is centered at 591 nm.

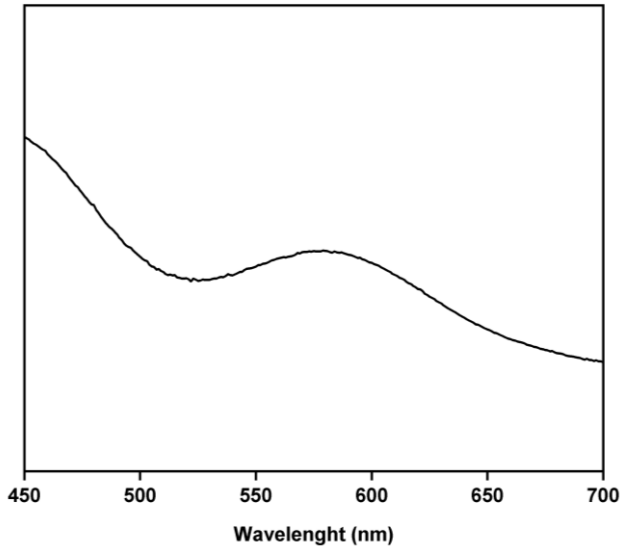

Figure S4.27. UV-vis spectrum of a DMF solution of $Rh_{12}\mathbf{L}^{4.2}{}_6\mathbf{L}^{4.5'}{}_6$. The maximum of adsorption band I (λ_{max}) of $Rh_{12}\mathbf{L}^{4.2}{}_6\mathbf{L}^{4.5'}{}_6$ is centered at 579 nm.

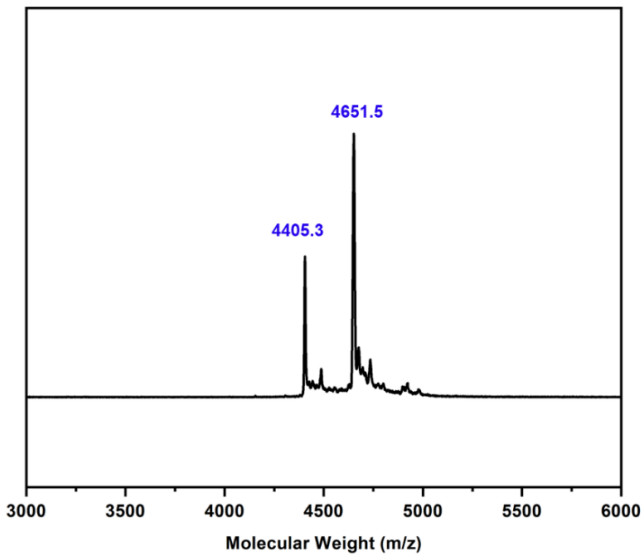

Figure S4.28. MALDI-TOF spectrum of $Rh_{12}\mathbf{L}^{4.1}{}_6\mathbf{L}^{4.2'}{}_6$. The weight corresponding to the formula $[Rh_{12}(\mathbf{L}^{4.1})_6(\mathbf{L}^{4.2'})_6(DMA)(H_2O)_2(MeOH)_4 + H]^+$ has been highlighted: expected = 4403.8 g/mol ; found = 4405.3 g/mol. The weight corresponding to the formula $[Rh_{12}(\mathbf{L}^{4.1})_6(\mathbf{L}^{4.2'})_6(H_2O)_2(DMA)_2(CH_3CN)_7 + H]^+$ has been highlighted: expected = 4650.0 g/mol ; found = 4651.5 g/mol.

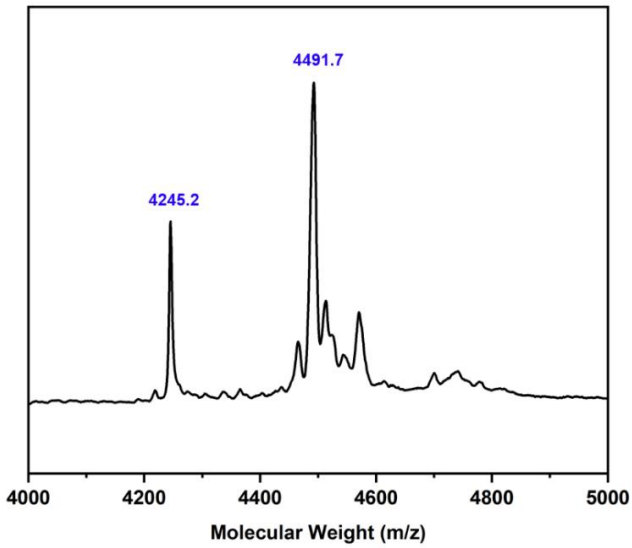

Figure S4.29. MALDI-TOF spectrum of $Rh_{12}\mathbf{L}^{4.1}{}_6\mathbf{L}^{4.3'}{}_6$. The weight corresponding to the formula $[(Rh_{12}(\mathbf{L}^{4.1})_6(\mathbf{L}^{4.3'})_6 + H]^+$ has been highlighted: expected = 4248.6 g/mol ; found = 4245.2 g/mol. The weight corresponding to the formula $[(Rh_{12}(\mathbf{L}^{4.1})_6(\mathbf{L}^{4.3'})_6(DMA)_2(H_2O)_2(MeOH) + H]^+$ has been highlighted: expected = 4490.8 g/mol ; found = 4491.7 g/mol.

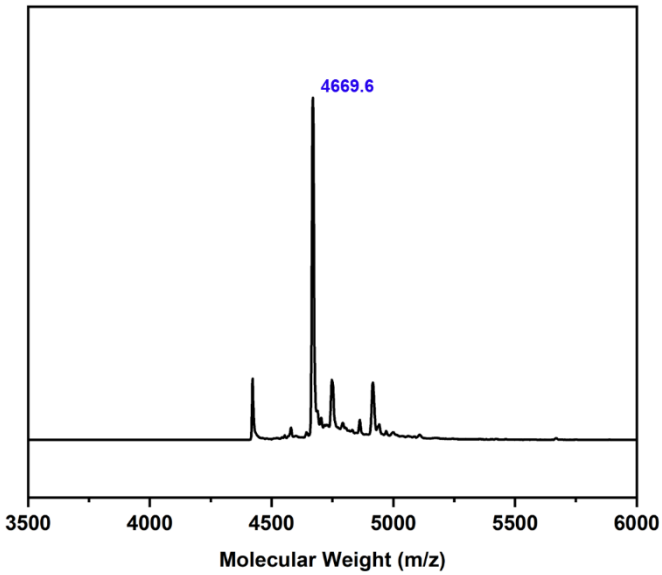

Figure S4.30: MALDI-TOF spectrum of $Rh_{12}\mathbf{L}^{4.1}{}_6\mathbf{L}^{4.4'}{}_6$. The weight corresponding to the formula $[Rh_{12}(\mathbf{L}^{4.1})_6(\mathbf{L}^{4.4'})_6(DMA)_2(H_2O)_4 + H]^+$ has been highlighted: expected = 4664.0; found = 4669.6.

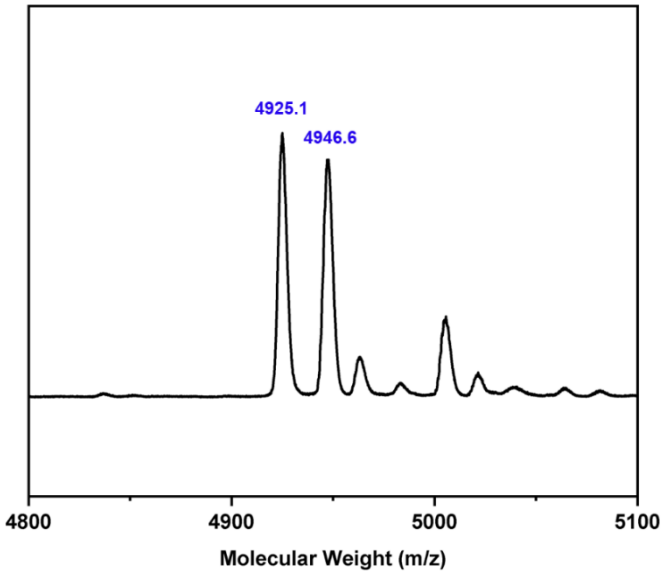

Figure S4.31. MALDI-TOF spectrum of $Rh_{12}\mathbf{L^{4.1}}_6\mathbf{L^{4.5'}}_6$. The weight corresponding to the formula $[(Rh_{12}(\mathbf{L^{4.1}})_6(\mathbf{L^{4.5'}})_6 + H]^+$ has been highlighted: expected = 4921.4 g/mol ; found = 4925.1 g/mol.

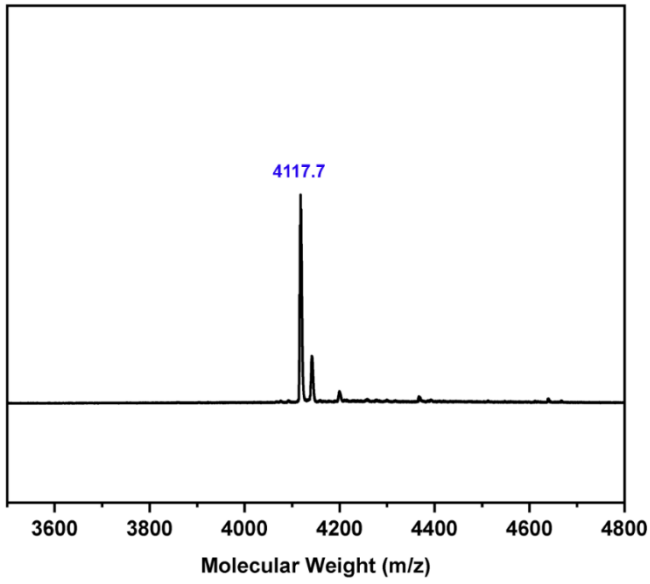

Figure S4.32. MALDI-TOF spectrum of $Rh_{12}\mathbf{L^{4.1}}_6\mathbf{L^{4.6'}}_6$. The weight corresponding to the formula $[(Rh_{12}(\mathbf{L^{4.1}})_6(\mathbf{L^{4.6'}})_6 + H]^+$ has been highlighted: expected = 4116.4 g/mol ; found = 4117.7 g/mol.

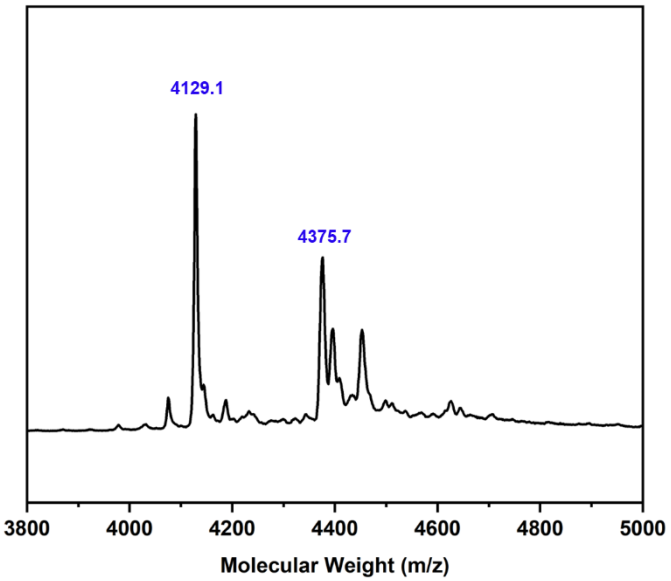

Figure S4.33. MALDI-TOF spectrum of $Rh_{12}\mathbf{L^{4.2}}_6\mathbf{L^{4.6'}}_6$. The weight corresponding to the formula $[Rh_{12}(\mathbf{L^{4.2}})_6(\mathbf{L^{4.6'}})_6 + H]^+$ has been highlighted: expected = 4128.3; found = 4129.1.

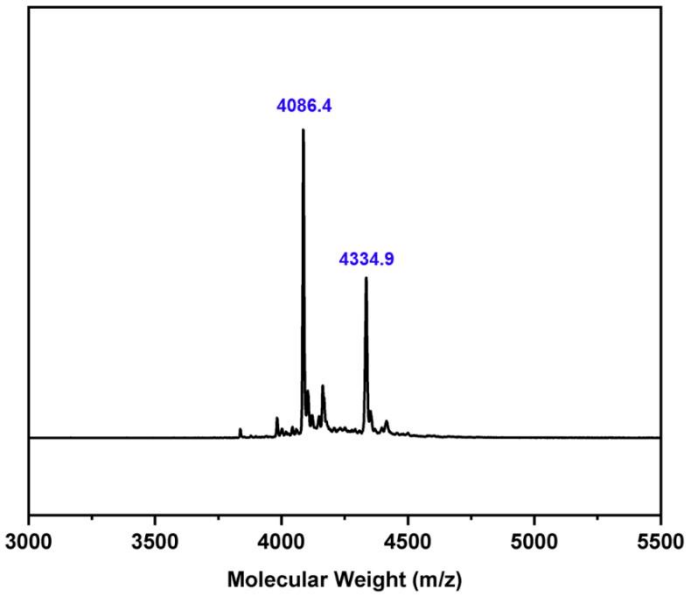

Figure S4.34. MALDI-TOF spectrum of $Rh_{12}\mathbf{L^{4.2}}_6\mathbf{L^{4.1'}}_6$. The weight corresponding to the formula $[Rh_{12}(\mathbf{L^{4.2}})_6(\mathbf{L^{4.1'}})_6(H_2O)_3(DMA)_2(MeOH) + H]^+$ has been highlighted: expected = 4088.4; found = 4086.4. The weight corresponding to the formula $[Rh_{12}(\mathbf{L^{4.2}})_6(\mathbf{L^{4.1'}})_6(H_2O)_4(DMA)_5 + H]^+$ has also been highlighted: expected = 4335.6; found = 4334.9.

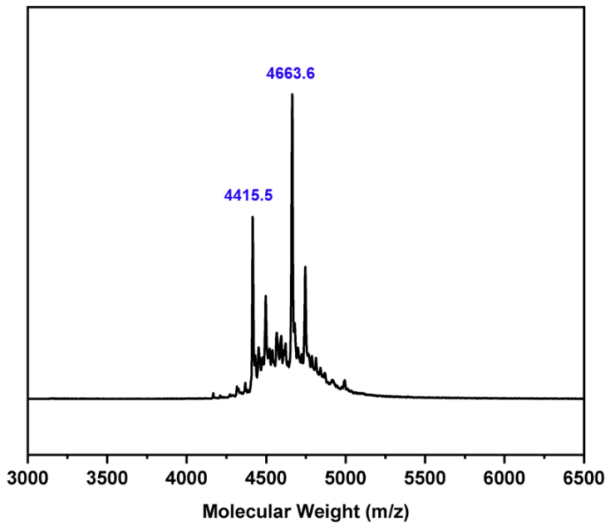

Figure S4.35. MALDI-TOF spectrum of $Rh_{12}\mathbf{L^{4.2}}_6\mathbf{L^{4.2'}}_6$. The weight corresponding to the formula $[Rh_{12}(\mathbf{L^{4.2}})_6(\mathbf{L^{4.2'}})_6(MeOH)(DMF)_3 + H]^+$ has been highlighted: expected = 4415.8; found = 4415.5. The weight corresponding to the formula $[Rh_{12}(\mathbf{L^{4.2}})_6(\mathbf{L^{4.2'}})_6(H_2O)_4(DMF)_5(MeOH)_2 + H]^+$ has also been highlighted: expected = 4665.9; found = 4663.6.

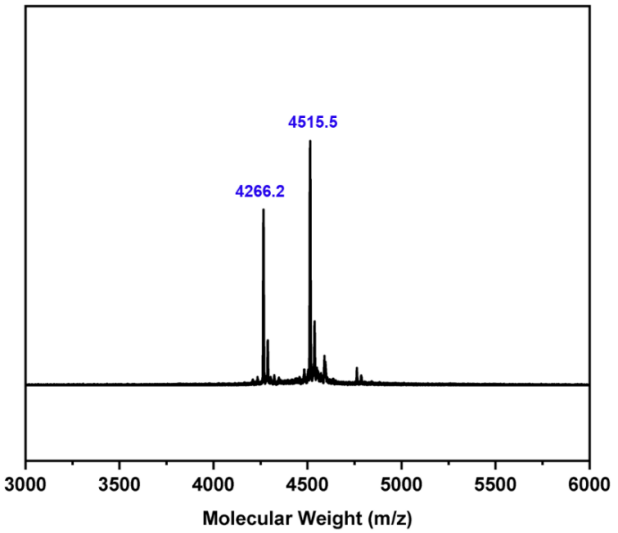

Figure S4.36: MALDI-TOF spectrum of $Rh_{12}\mathbf{L^{4.2}}_6\mathbf{L^{4.3'}}_6$. The weight corresponding to the formula $[Rh_{12}(\mathbf{L^{4.2}})_6(\mathbf{L^{4.3'}})_6 + H]^+$ has been highlighted: expected = 4260.6; found = 4266.2. The weight corresponding to the formula $[Rh_{12}(\mathbf{L^{4.2}})_6(\mathbf{L^{4.3'}})_6(H_2O)_2(DMF)_3 + H]^+$ has been highlighted: expected = 4515.7; found = 4515.5.

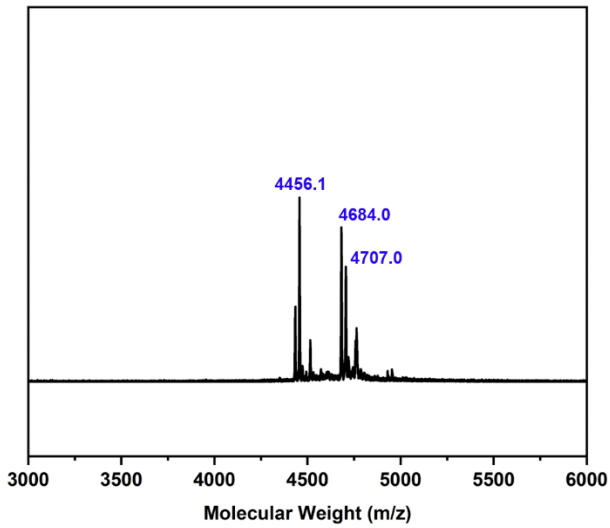

Figure S4.37. MALDI-TOF spectrum of $Rh_{12}\mathbf{L}^{4.2}{}_6\mathbf{L}^{4.4'}{}_6$. The weight corresponding to the formula $[Rh_{12}(\mathbf{L}^{4.2})_6(\mathbf{L}^{4.4'})_6(MeOH) + H]^+$ has been highlighted: expected = 4460.8; found = 4456.1. The weight corresponding to the formula $[Rh_{12}(\mathbf{L}^{4.2})_6(\mathbf{L}^{4.4'})_6(MeOH)_4(H_2O)_3(DMF) + H]^+$ has been highlighted: expected = 4683.9; found = 4684.0.

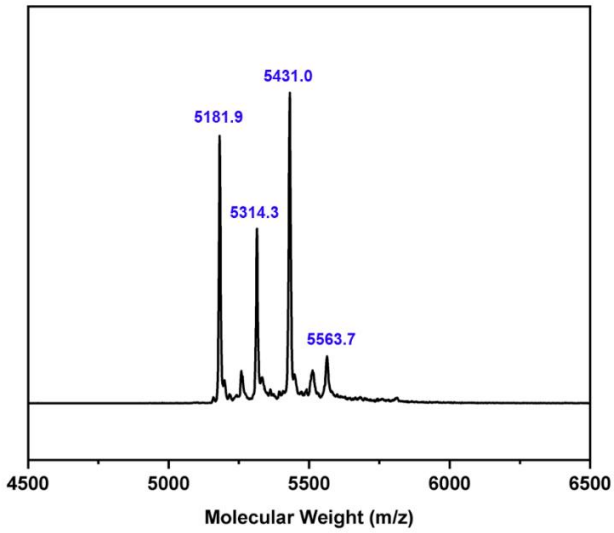

Figure S4.38. MALDI-TOF spectrum of $Rh_{12}\mathbf{L}^{4.2}{}_6\mathbf{L}^{4.5'}{}_6$. The weight corresponding to the formula $[Rh_{12}(\mathbf{L}^{4.2})_6(\mathbf{L}^{4.5'})_6(H_2O)_4(DMF)_2(MeOH) + H]^+$ has been highlighted: expected = 5183.5; found = 5181.9. The weight corresponding to the formula $[Rh_{12}(\mathbf{L}^{4.2})_6(\mathbf{L}^{4.5'})_6(H_2O)_2(DMF)_5(MeOH)_3 + H]+$ has also been highlighted: expected = 5430.7; found = 5431.0.

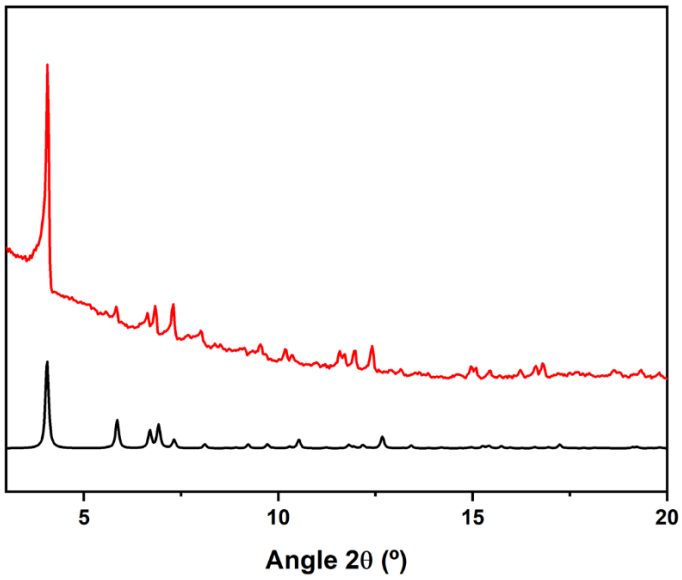

Figure S4.39. Simulated PXRD diffractogram of $Rh_{12}\mathbf{L}^{4.1}{}_6\mathbf{L}^{4.2'}{}_6$ from crystal structure (black) and experimental PXRD diffractogram of $Rh_{12}\mathbf{L}^{4.1}{}_6\mathbf{L}^{4.2'}{}_6$ crystals (red).

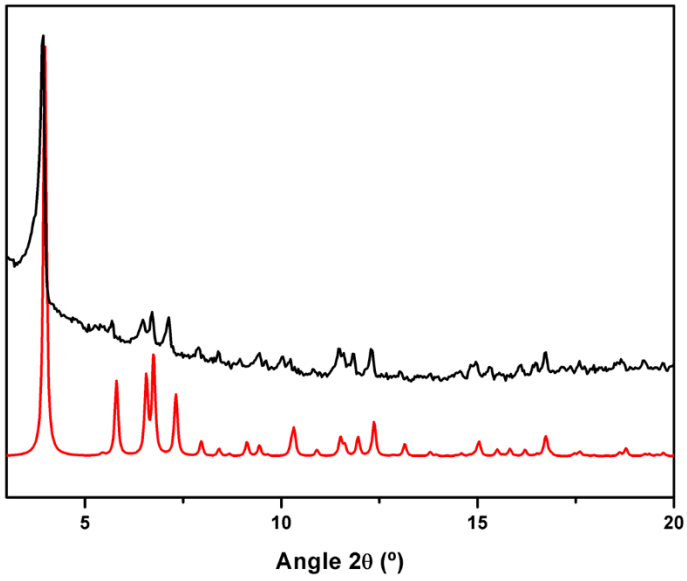

Figure S4.40. Simulated PXRD diffractogram of $Rh_{12}\mathbf{L}^{4.1}{}_6\mathbf{L}^{4.3'}{}_6$ from crystal structure (black) and experimental PXRD diffractogram of $Rh_{12}\mathbf{L}^{4.1}{}_6\mathbf{L}^{4.3'}{}_6$ crystals (red).

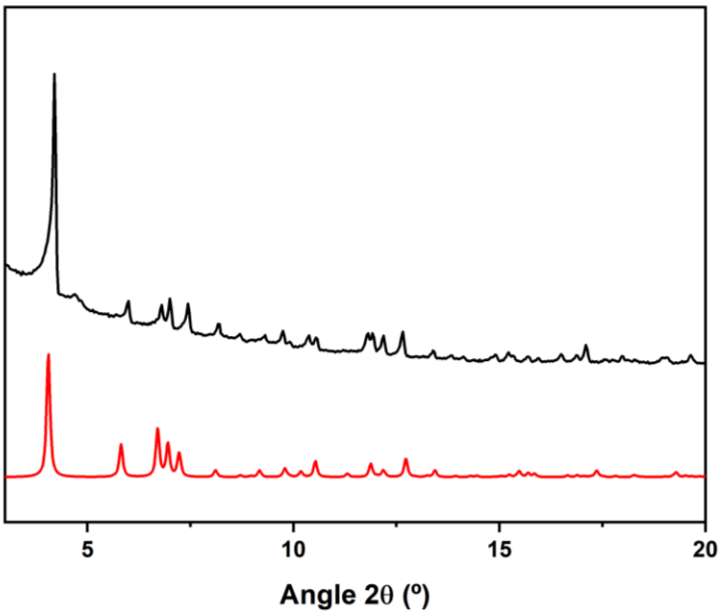

Figure S4.41. Simulated PXRD diffractogram of $Rh_{12}\mathbf{L}^{4.1}{}_6\mathbf{L}^{4.4'}{}_6$ from crystal structure (black) and experimental PXRD diffractogram of $Rh_{12}\mathbf{L}^{4.1}{}_6\mathbf{L}^{4.4'}{}_6$ crystals (red).

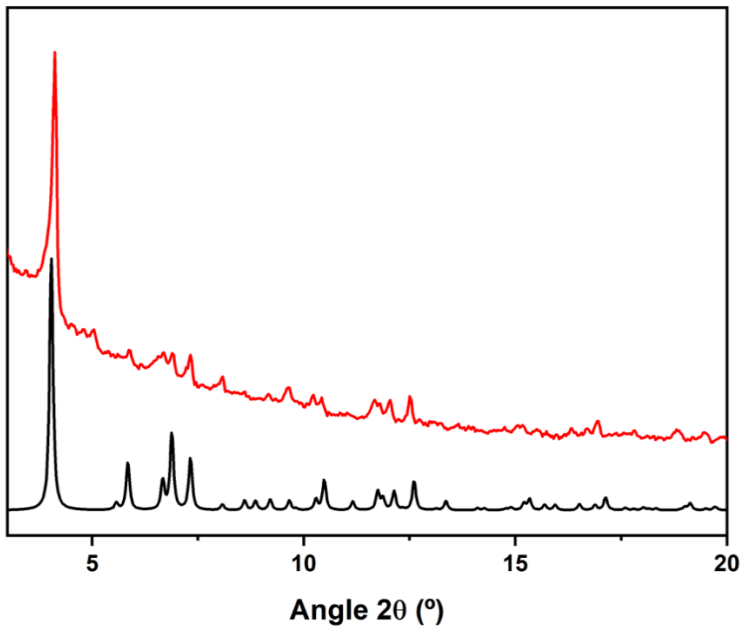

Figure S4.42. Simulated PXRD diffractogram of $Rh_{12}\mathbf{L}^{4.1}{}_6\mathbf{L}^{4.5'}{}_6$ from crystal structure (black) and experimental PXRD diffractogram of $Rh_{12}\mathbf{L}^{4.1}{}_6\mathbf{L}^{4.5'}{}_6$ crystals (red).

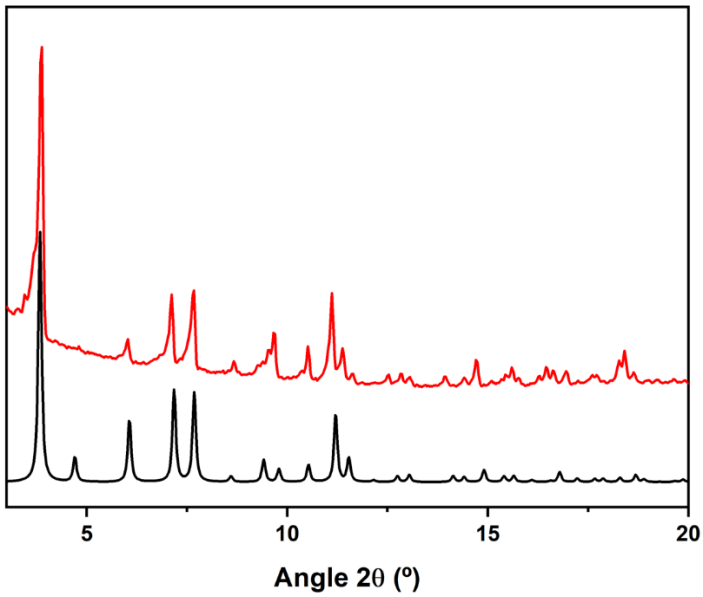

Figure S4.43. Simulated PXRD diffractogram of $Rh_{12}\mathbf{L}^{4.1}{}_6\mathbf{L}^{4.6'}{}_6$ from crystal structure (black) and experimental PXRD diffractogram of $Rh_{12}\mathbf{L}^{4.1}{}_6\mathbf{L}^{4.6'}{}_6$ crystals (red).

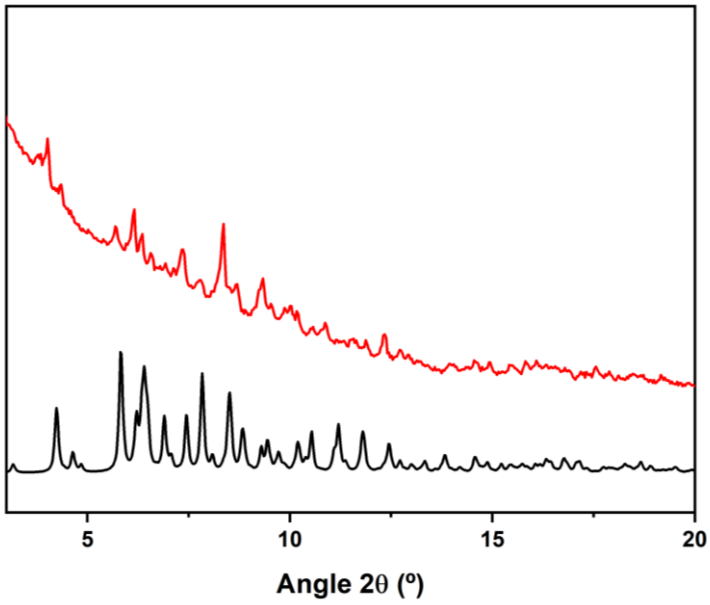

Figure S4.44. Simulated PXRD diffractogram of $Rh_{12}\mathbf{L}^{4.2}{}_6\mathbf{L}^{4.6'}{}_6$ from crystal structure (black) and experimental PXRD diffractogram of $Rh_{12}\mathbf{L}^{4.2}{}_6\mathbf{L}^{4.6'}{}_6$ crystals (red).

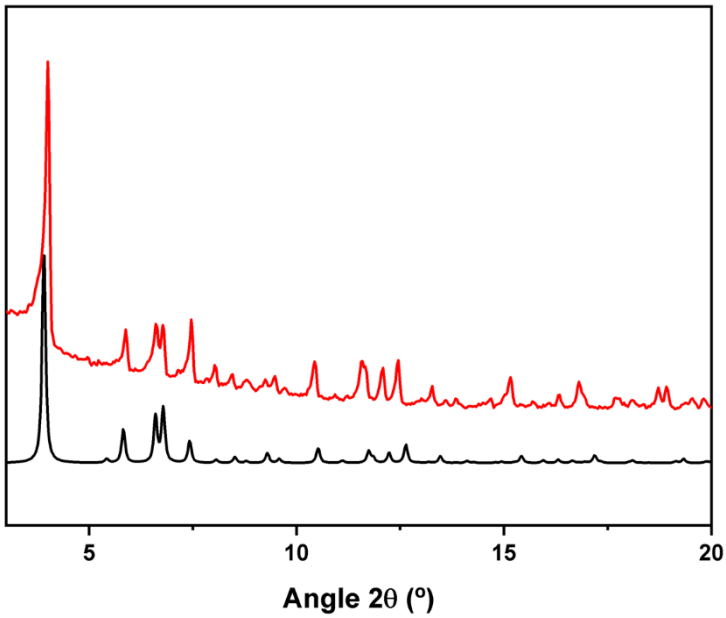

Figure S4.45. Simulated PXRD diffractogram of $Rh_{12}\mathbf{L}^{4.2}{}_6\mathbf{L}^{4.1'}{}_6$ from crystal structure (black) and experimental PXRD diffractogram of $Rh_{12}\mathbf{L}^{4.2}{}_6\mathbf{L}^{4.1'}{}_6$ crystals (red).

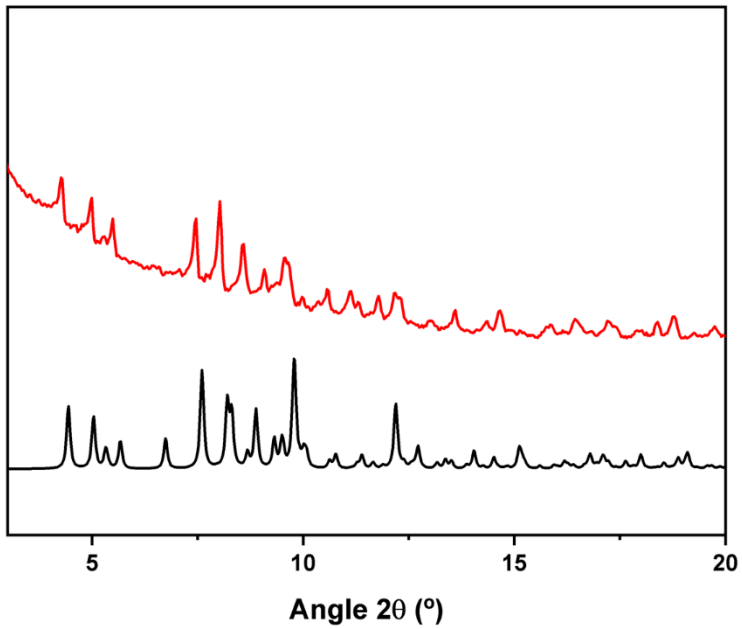

Figure S4.46. Simulated PXRD diffractogram of $Rh_{12}\mathbf{L}^{4.2}{}_6\mathbf{L}^{4.2'}{}_6$ from crystal structure (black) and experimental PXRD diffractogram of $Rh_{12}\mathbf{L}^{4.2}{}_6\mathbf{L}^{4.2'}{}_6$ crystals (red).

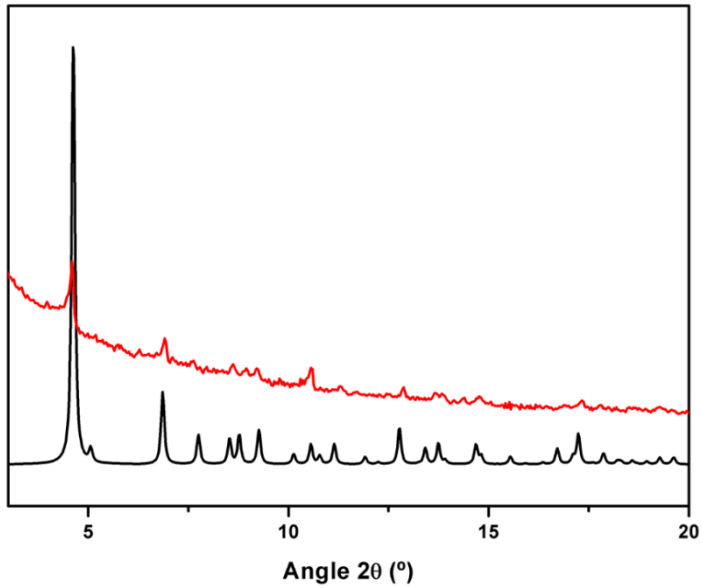

Figure S4.47. Simulated PXRD diffractogram of $Rh_{12}\mathbf{L}^{4.2}{}_6\mathbf{L}^{4.3'}{}_6$ from crystal structure (black) and experimental PXRD diffractogram of $Rh_{12}\mathbf{L}^{4.2}{}_6\mathbf{L}^{4.3'}{}_6$ crystals (red).

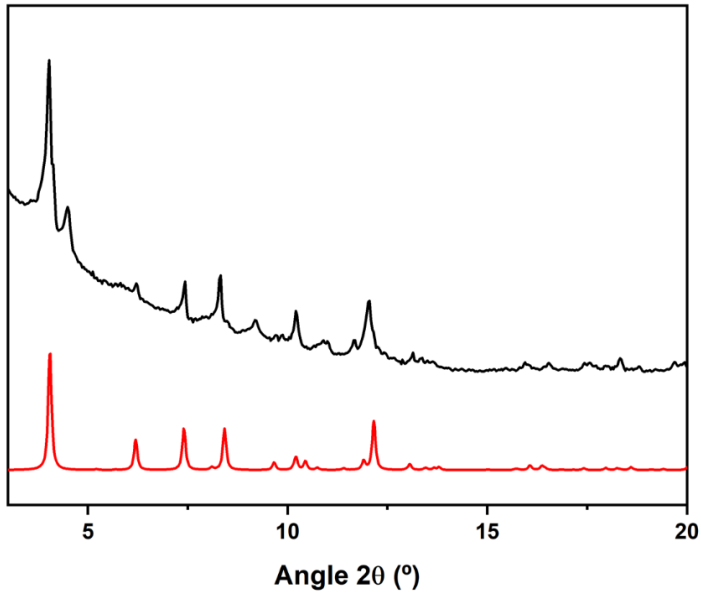

Figure S4.48. Simulated PXRD diffractogram of $Rh_{12}\mathbf{L}^{4.2}{}_6\mathbf{L}^{4.4'}{}_6$ from crystal structure (black) and experimental PXRD diffractogram of $Rh_{12}\mathbf{L}^{4.2}{}_6\mathbf{L}^{4.4'}{}_6$ crystals (red).

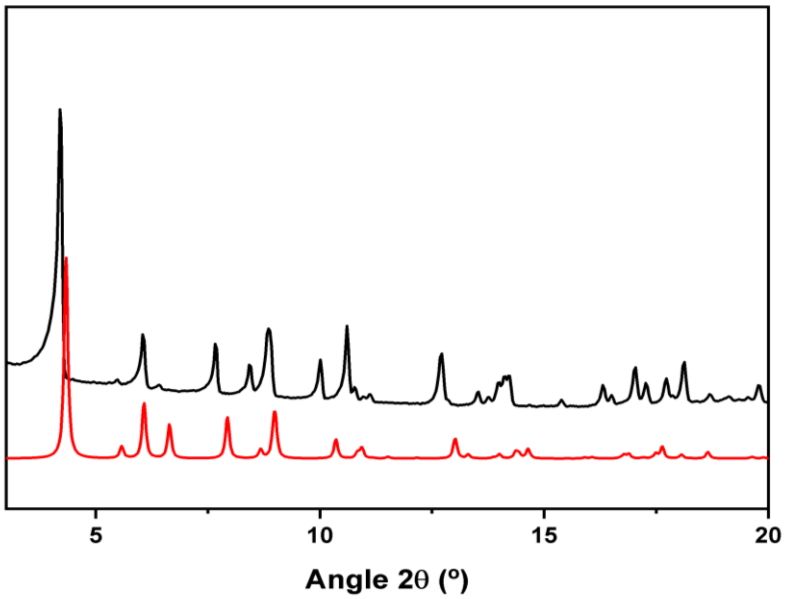

Figure S4.49. Simulated PXRD diffractogram of $Rh_{12}\mathbf{L}^{4.2}{}_6\mathbf{L}^{4.5'}{}_6$ from crystal structure (black) and experimental PXRD diffractogram of $Rh_{12}\mathbf{L}^{4.2}{}_6\mathbf{L}^{4.5'}{}_6$ crystals (red).

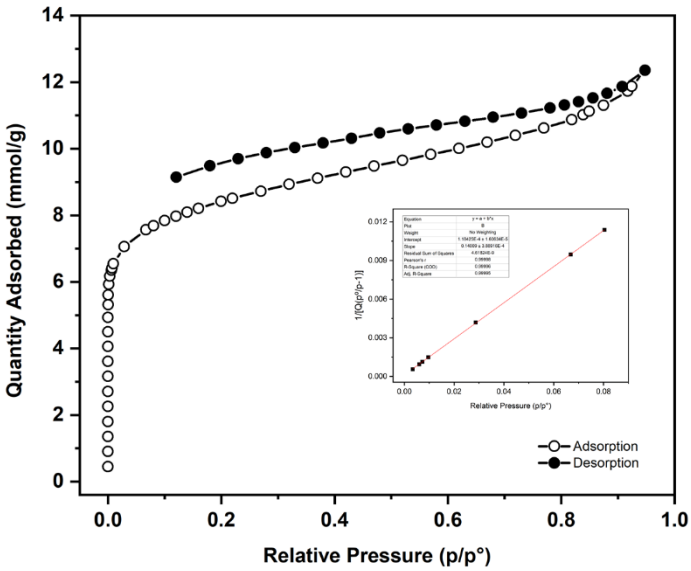

Figure S4.50. N_2 adsorption-desorption isotherm for $Rh_{12}\mathbf{L}^{4.1}{}_6\mathbf{L}^{4.1'}{}_6$ at 77 K (S_{BET} = 696 m^2/g).

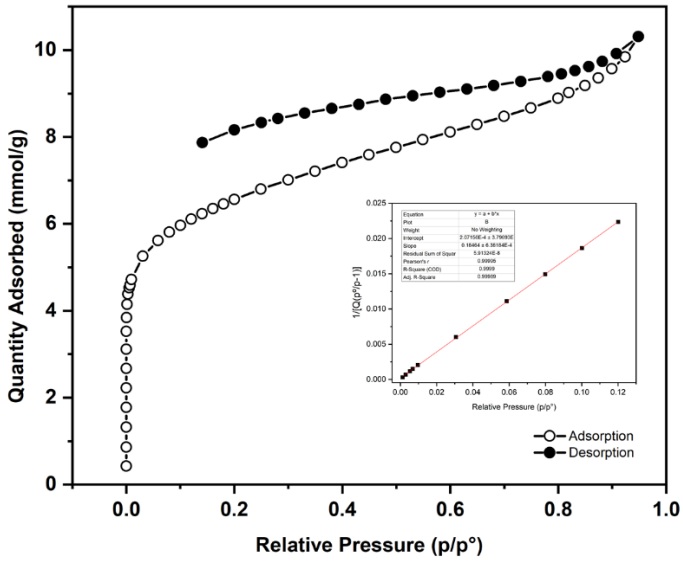

Figure S4.51. N_2 adsorption-desorption isotherm for $Rh_{12}\mathbf{L^{4.1}}_6\mathbf{L^{4.2'}}_6$ at 77 K (S_{BET} = 528 m^2/g).

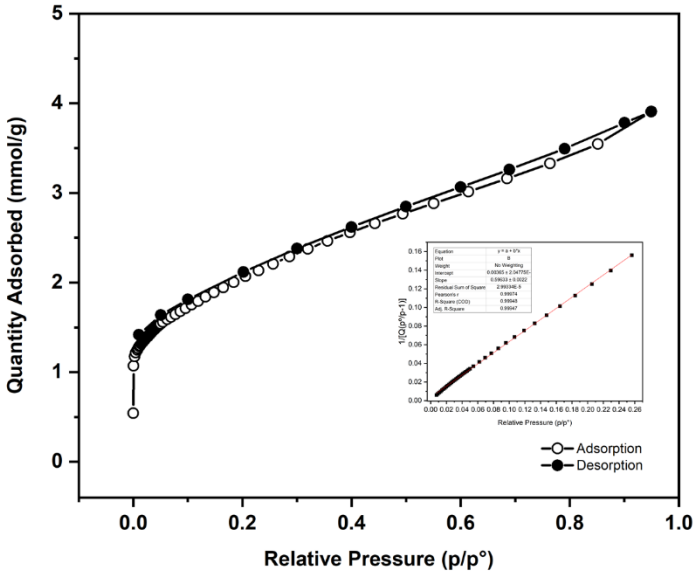

Figure S4.52. N_2 adsorption-desorption isotherm for $Rh_{12}\mathbf{L^{4.1}}_6\mathbf{L^{4.3'}}_6$ at 77 K (S_{BET} = 163 m^2/g).

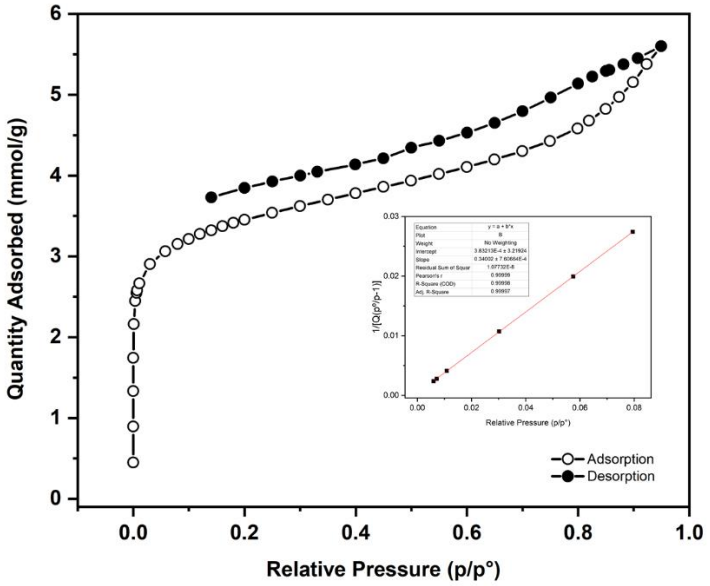

Figure S4.53. N_2 adsorption-desorption isotherm for $Rh_{12}\mathbf{L^{4.1}}_6\mathbf{L^{4.4'}}_6$ at 77 K (S_{BET} = 287 m^2/g).

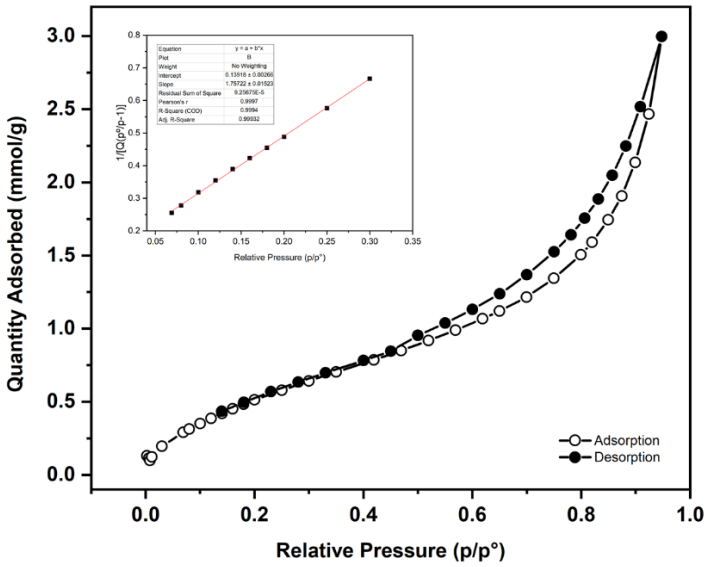

Figure S4.54. N_2 adsorption-desorption isotherm for $Rh_{12}\mathbf{L^{4.1}}_6\mathbf{L^{4.5'}}_6$ at 77 K (S_{BET} = 51 m^2/g).

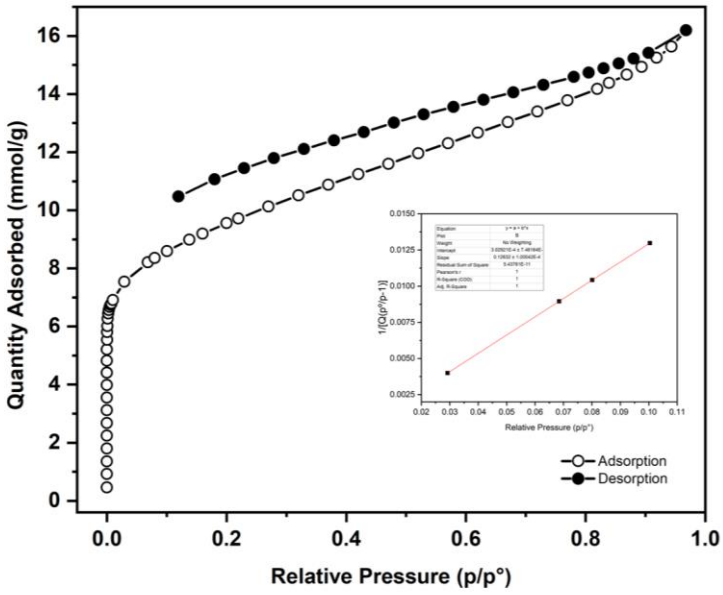

Figure S4.55. N_2 adsorption-desorption isotherm for $Rh_{12}\mathbf{L^{4.1}}_6\mathbf{L^{4.6'}}_6$ at 77 K (S_{BET} = 770 m^2/g).

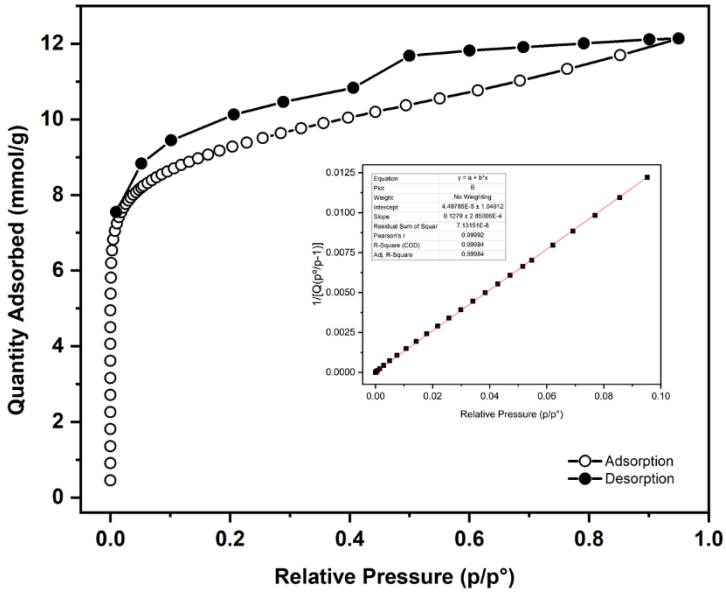

Figure S4.56. N_2 adsorption-desorption isotherm for $Rh_{12}\mathbf{L^{4.2}}_6\mathbf{L^{4.6'}}_6$ at 77 K (S_{BET} = 762 m^2/g).

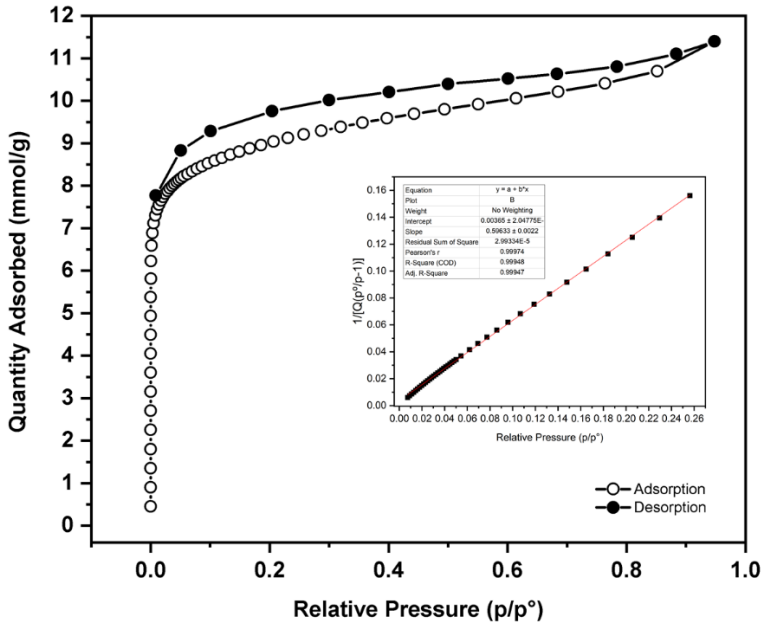

Figure S4.57. N_2 adsorption-desorption isotherm for $Rh_{12}\mathbf{L^{4.2}}_6\mathbf{L^{4.1}}'_6$ at 77 K (S_{BET}= 761 m^2/g).

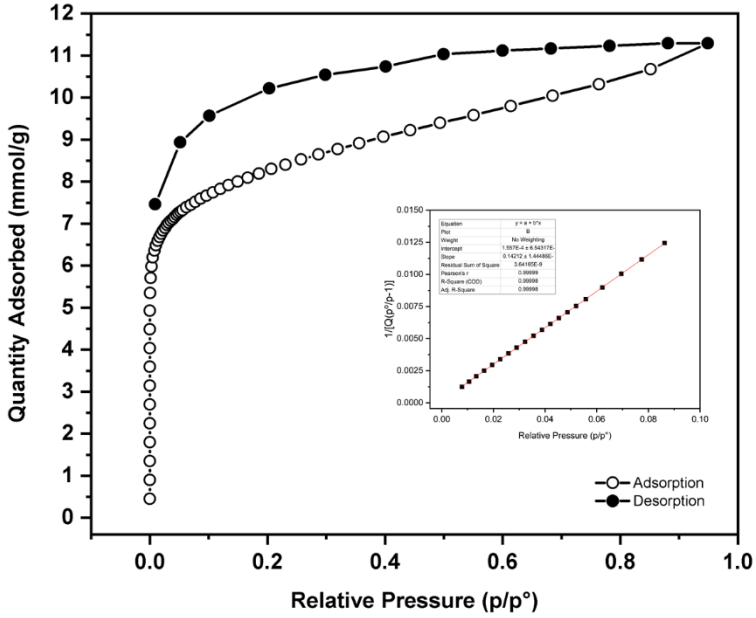

Figure S4.58. N_2 adsorption-desorption isotherm for $Rh_{12}\mathbf{L^{4.2}}_6\mathbf{L^{4.2}}'_6$ at 77 K (S_{BET}= 686 m^2/g).

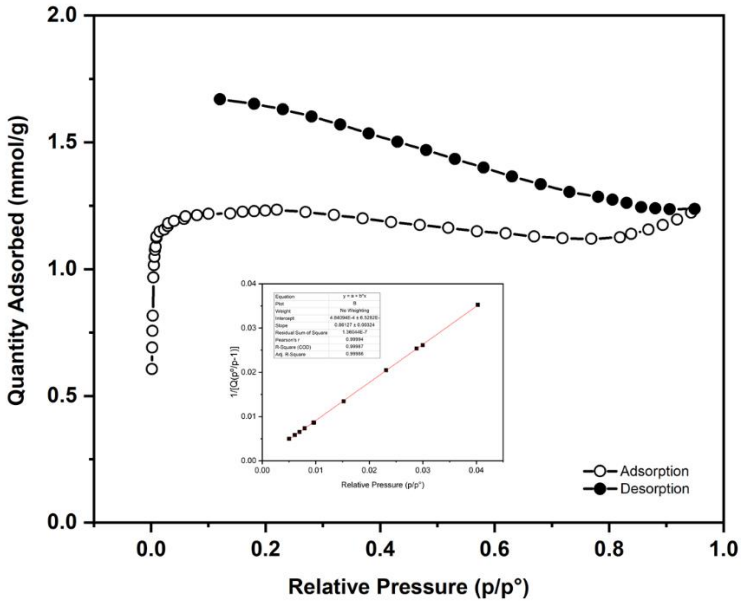

Figure S4.59. N_2 adsorption-desorption isotherm for $Rh_{12}\mathbf{L^{4.2}}_6\mathbf{L^{4.3'}}_6$ at 77 K (S_{BET}= 113 m^2/g).

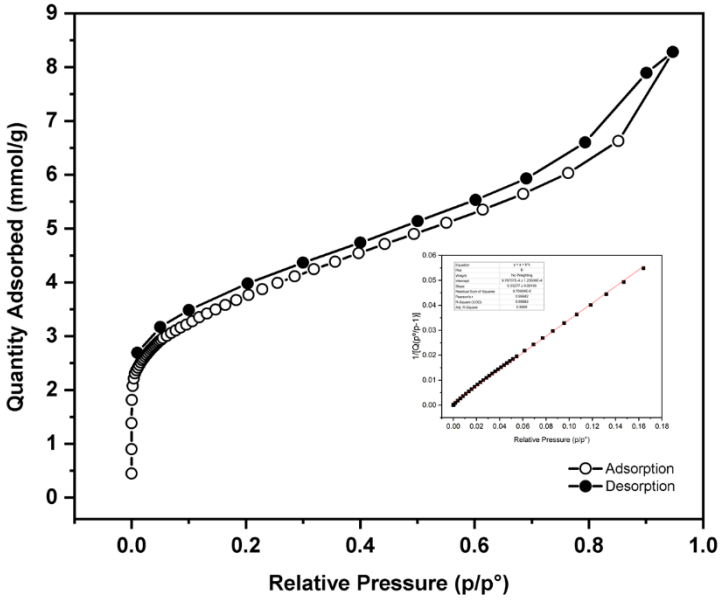

Figure S4.60. N_2 adsorption-desorption isotherm for $Rh_{12}\mathbf{L^{4.2}}_6\mathbf{L^{4.4'}}_6$ at 77 K (S_{BET}= 292 m^2/g).

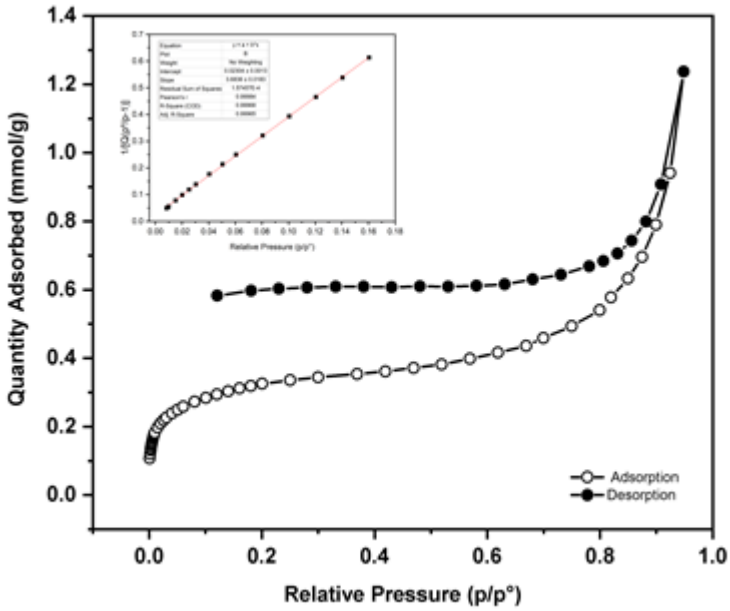

Figure S4.61. N_2 adsorption-desorption isotherm for $Rh_{12}\mathbf{L^{4.2}}_6\mathbf{L^{4.5'}}_6$ at 77 K (S_{BET}= 26 m^2/g).

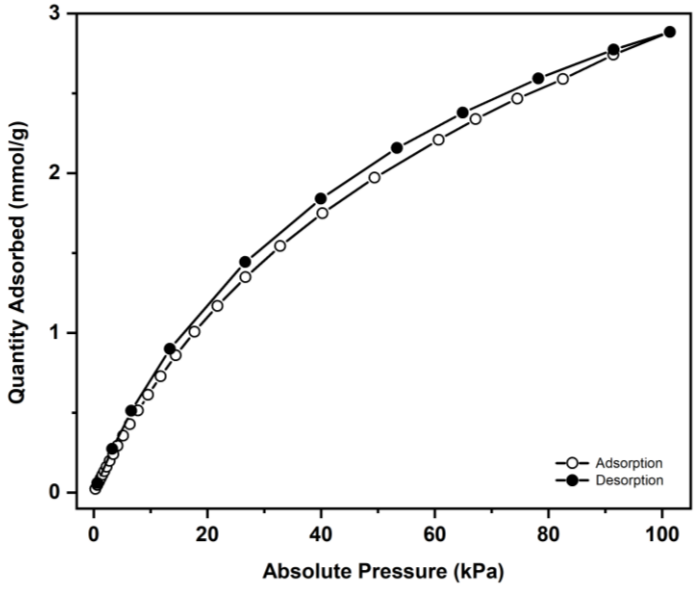

Figure S4.62. CO_2 adsorption-desorption isotherm for $Rh_{12}\mathbf{L^{4.1}}_6\mathbf{L^{4.1'}}_6$ at 298 K.

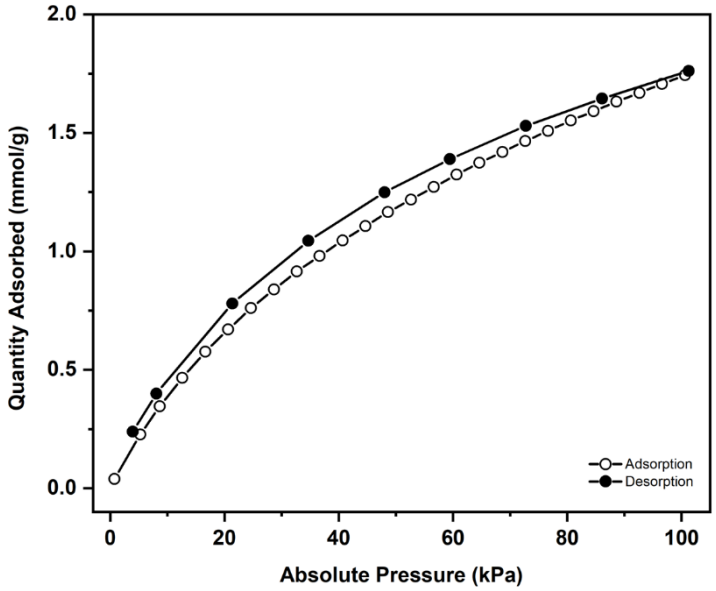

Figure S4.63. CO_2 adsorption-desorption isotherm for $Rh_{12}\mathbf{L^{4.1}}_6\mathbf{L^{4.2'}}_6$ at 298 K.

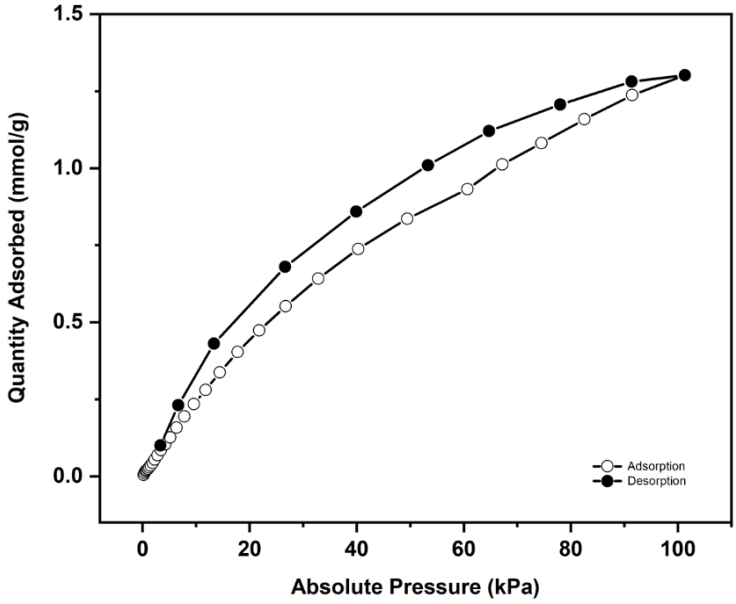

Figure S4.64. CO_2 adsorption-desorption isotherm for $Rh_{12}\mathbf{L^{4.1}}_6\mathbf{L^{4.3'}}_6$ at 298 K.

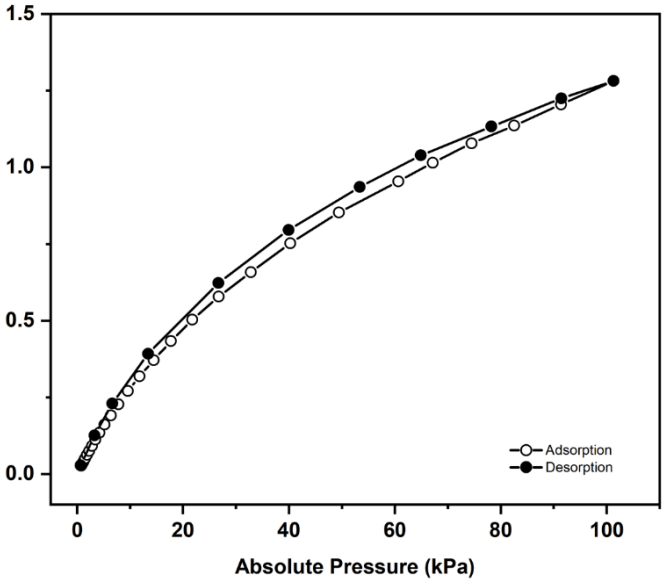

Figure S4.65. CO_2 adsorption-desorption isotherm for $Rh_{12}\mathbf{L^{4.1}}_6\mathbf{L^{4.4'}}_6$ at 298 K.

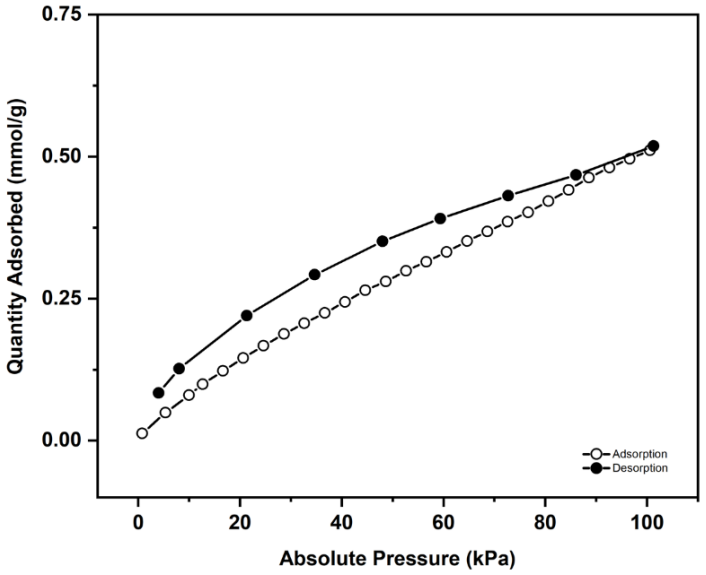

Figure S4.66. CO_2 adsorption-desorption isotherm for $Rh_{12}\mathbf{L^{4.1}}_6\mathbf{L^{4.5'}}_6$ at 298 K.

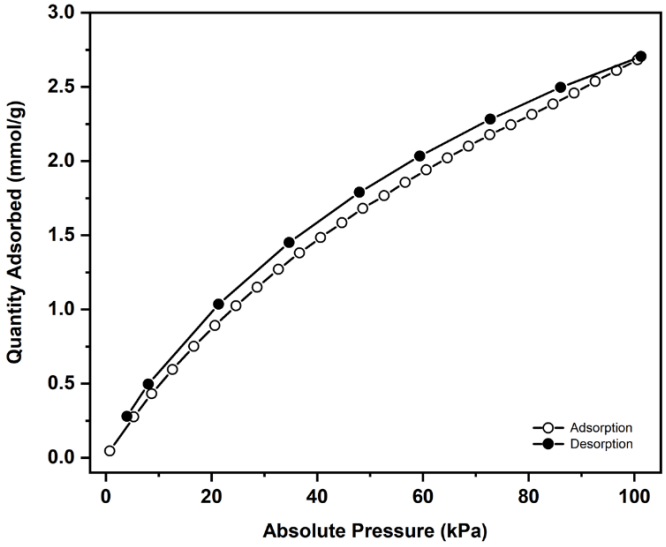

Figure S4.67. CO_2 adsorption-desorption isotherm for $Rh_{12}\mathbf{L}^{4.1}{}_6\mathbf{L}^{4.6'}{}_6$ at 298 K.

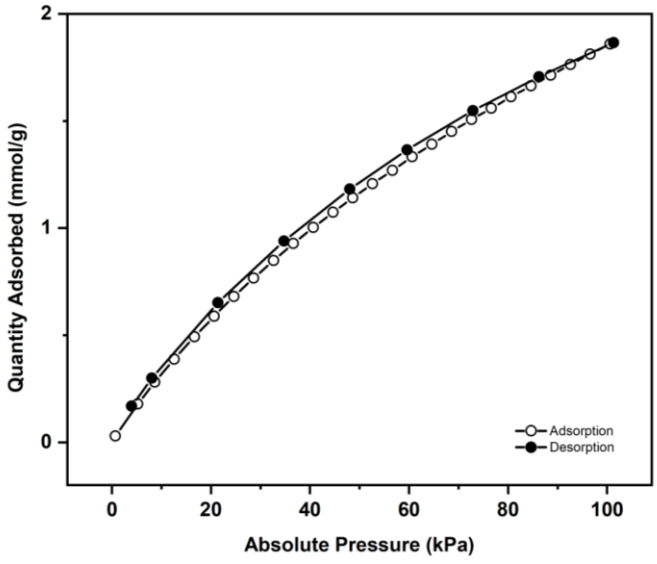

Figure S4.68. CO_2 adsorption-desorption isotherm for $Rh_{12}\mathbf{L}^{4.2}{}_6\mathbf{L}^{4.6'}{}_6$ at 298 K.

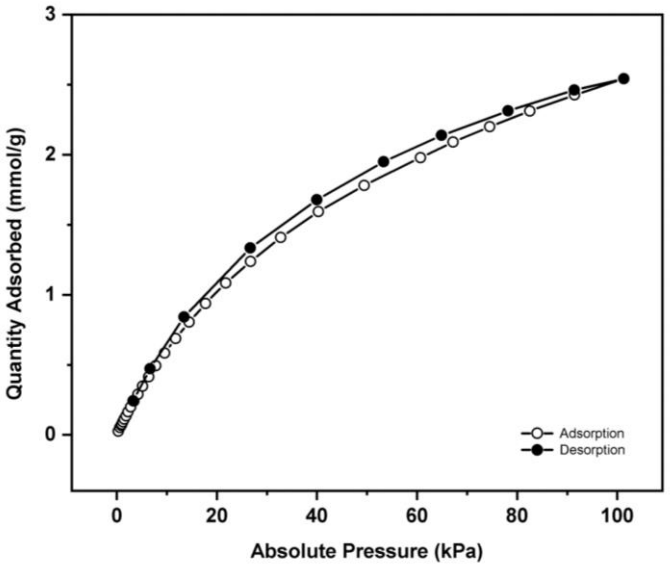

Figure S4.69. CO_2 adsorption-desorption isotherm for $Rh_{12}\mathbf{L^{4.2}}_6\mathbf{L^{4.1'}}_6$ at 298 K.

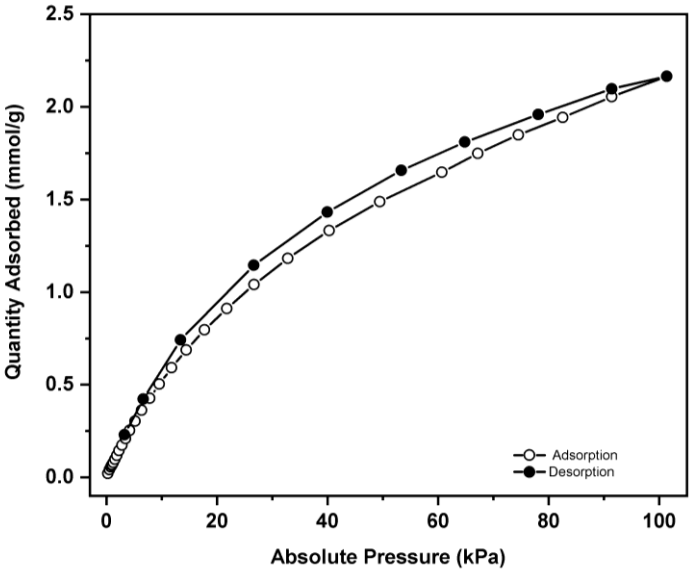

Figure S4.70. CO_2 adsorption-desorption isotherm for $Rh_{12}\mathbf{L^{4.2}}_6\mathbf{L^{4.2'}}_6$ at 298 K.

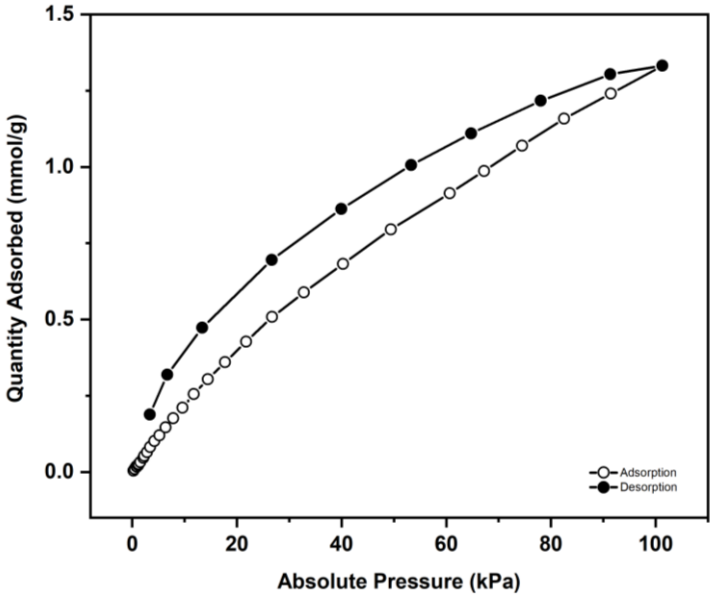

Figure S4.71. CO_2 adsorption-desorption isotherm for $Rh_{12}\mathbf{L}^{4.2}{}_6\mathbf{L}^{4.3'}{}_6$ at 298 K.

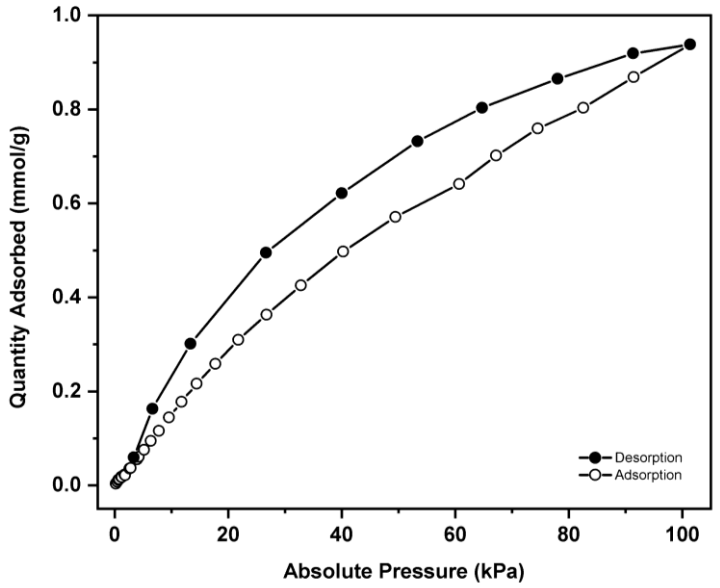

Figure S4.72. CO_2 adsorption-desorption isotherm for $Rh_{12}\mathbf{L}^{4.2}{}_6\mathbf{L}^{4.4'}{}_6$ at 298 K.

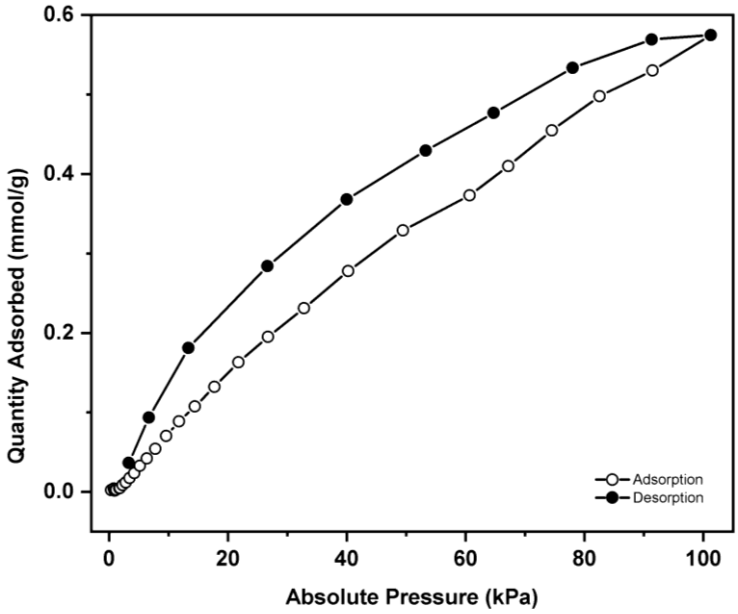

Figure S4.73. CO_2 adsorption-desorption isotherm for $Rh_{12}\mathbf{L}^{4.2}{}_6\mathbf{L}^{4.5'}{}_6$ at 298 K.

Chapter 5

Synthesis a triangular Rh_2-macrocycle from the cleavage of a heteroleptic MOP

5.1 Introduction

Numerous supramolecular structures have been built by the coordination of metal ions with polydentate organic donors. When metals and ligands with more than one binding site are combined, they start coordinating with each other forming supramolecular units that keep growing in the directions determined by the angles of the building blocks. If this growth is allowed to go on indefinitely, infinite extended materials, such as MOFs and polymers, will be formed (Figure 5.1a). One the other hand, closed structures, such as MOPs and cages, are formed if the growing structure finds itself while growing (Figure 5.1b).

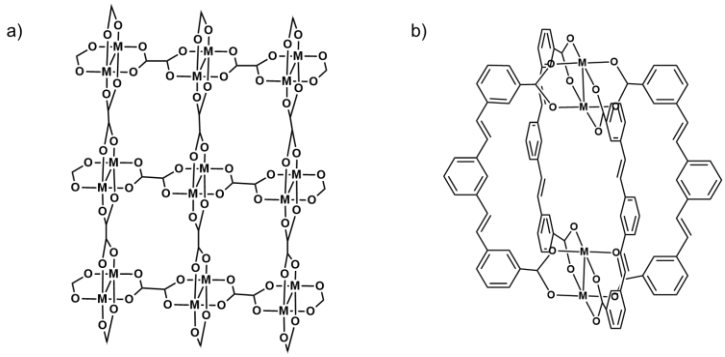

Figure 5.1. (a) Extended two-dimensional structure formed by the coordination of paddlewheel metal clusters and linear dicarboxylic ligands (180° between binding sites). (b) Closed zero-dimensional structure formed by the coordination of metal paddlewheels and a bend ligand with an angle of 0° between binding sites.

To obtain discrete supramolecular structures by direct synthesis, the structure growth cannot be infinite. One possible strategy is to use capping ligands, which are nonlabile ligands, to block some of the growing directions of the coordination compounds. In this approach, metal SBUs formed by metals, labile ligands and nonlabile ligands are usually previously synthesized. The labile ligands of these SBUs are later replaced with polydentate ligands, which connect different SBUs to each other creating

poly-cluster structures. In this manner, the structure only expands in the directions occupied by the labile ligands, whereas the nonlabile ligands block preselected metal coordination sites acting as the structure's corners and preventing the expansion in those directions. Many discrete supramolecular structures, such as triangles, squares, and other polygons, were created using mononuclear coordination units, such as the corner species *cis*-ML_2 (M = Pd, Pt, or Zn, L = bidentate ligand) (Figure 5.2a).[121] One of the biggest drawbacks of this strategy is the fact that the metal centres are usually coordinatively saturated, which rules out using them for metal-based catalysis or to create more complex structures through additional coordination chemistry.

In 1999, Cotton *et al.* introduced the use of dimetal paddlewheel units, M^{2n+} (M = Mo, Rh, W, Ir, and other metals) as building blocks. Carboxylates can connect paddlewheel dimetal units through their equatorial positions while leaving the axial positions free. These axially free paddlewheel locations may be employed to grow more complex structures or as metal centers with catalytic activity. In addition, the use of appropriate paddlewheel dimetal units can introduce magnetic or electrochemical properties. Imitating the capping ligands used for building superstructures with mononuclear coordination centers, Cotton *et al.* designed a nonlabile formamidinate bridge to be used for metal paddlewheels, M_2. Formamidinate ligands are formed by two aromatic rings connected by a $[-N-CH-N-]^-$ group (Figure 5.2b).[122] The two nitrogen atoms in this group serve as binding sites and are positioned in a way that they can coordinate with both metals of a paddlewheel SBU to block one of the SBU's growing directions. The number of formamidinate ligands coordinated to the metal SBU can be changed to create SBUs with one, two, three, or four obstructed growing directions.[123–126] Other types of capping ligands for metal paddlewheels have been designed and synthesized. These include 2,2'-bipyridine, which has two

nitrogen donor atoms precisely positioned to coordinate to one metal of a paddlewheel cluster in a way that another 2,2'-bipyridine is required to occupy the other metal of the paddlewheel, blocking two adjacent growing directions of the SBU with two ligands (Figure 5.2c).[127] Another example of a capping ligand is bis(tetramethyl-1,3-benzenedipropionate), which has a flexible structure that can be adjusted to the required distance for the coordination of the two carboxylates to a metal paddlewheel in *cis* conformation blocking two adjacent growing directions of the SBU with only one ligand (Figure 5.2d).[54,127]

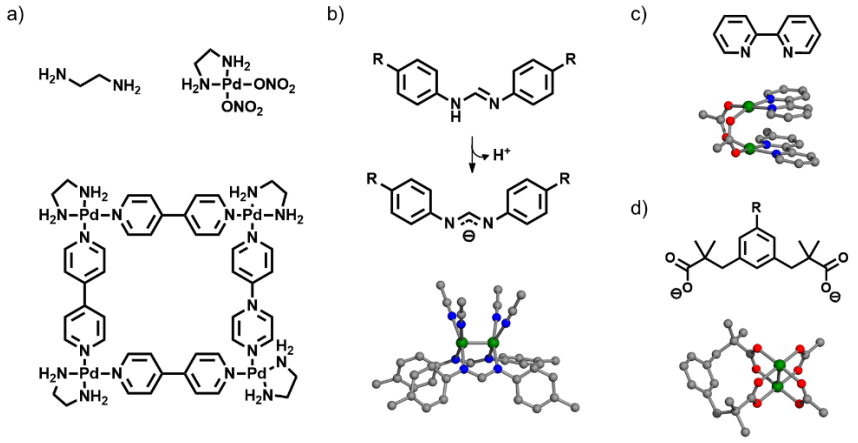

Figure 5.2. (a) Tree-component Pd-macrocycle capped with ethane-1,2-diamine.[121] Capping ligands for metal paddlewheels and examples of paddlewheels SBUs synthesized with them: (b) N,N-diarylformamidine[122]; (c) 2,2'-bipyridine[127]; and (d) bis(tetramethyl-1,3-benzenedipropionate).[54,127]

Different types of supramolecular structures can be constructed depending on the number and the position of the blocked directions obstructed by the capping ligands. Paddlewheel metal SBUs with three blocked growing positions can only grow in one direction, giving rise to dimetal complexes formed by two paddlewheel SBUs linked together by just one ligand (Figure 5.3a), whereas paddlewheel SBUs with two blocked

positions in *cis* can grow in two directions, forming various types of macromolecules, such as loops, triangles, squares and MOPs, depending on the geometry of the linking ligands and on the experimental conditions. More specifically, the reaction between *cis* SBUs with ligands with two binding sites can produce loops, triangles or squares. The formation of MOPs requires ligands with at least three binding sites (Figure 5.3e).[123,124] Loops are bimetallic complex linked each other by two dicarboxylate ligands.[128] These dicarboxylate ligands must have low angles between binding sites, which is frequently achieved using flexible ligands (Figure 5.3b). Triangle and square molecules are structures formed by three or four *cis* paddlewheel SBUs linked each other by three or four dicarboxylate ligands, respectively (Figure 5.3c and 5.3d). The synthesis of square molecules is only possible when the ligand is linear and has an angle of 180° between binding sites. Note that, with these type of ligands, triangles can also be formed (Figure 5.3d).[129] The formation of triangles depends on the experimental conditions and on the flexibility of the ligand.

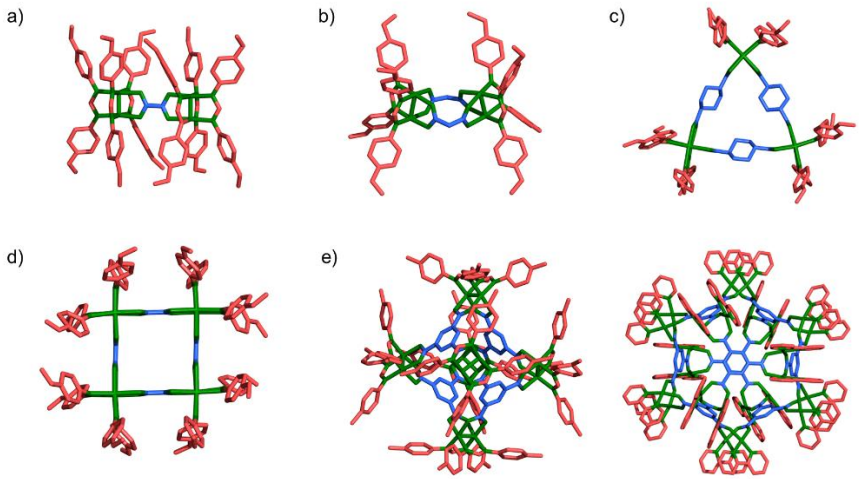

Figure 5.3. Discrete superstructures limited by capped ligands: (a) Mo-dimers[123,124]**;** (b) loop[128,130]**;** (c) Mo_2 and Rh_2 triangles[125,126]**;** (d) Mo_2 and Rh_2 squares[54,125]**;** and (e) MOPs.[127,131]

In this Chapter, we describe a new method for synthesizing a discrete Rh_2-marcrocycle without the use of capping ligands. Rather than using a capping ligand to block some of the cluster growing directions, our method consists of cutting a previously synthesized material to release fragments that already exist within the initial structure. A functionalized triangular Rh_2-macrocycle has been obtained from the selectively cleavage of a previously synthesized Rh_2-MOP. The carboxylic functionalization of the acquired Rh_2-macrocycle made the direct synthesis of this Rh_2-macrocycle even more challenging, opening the door for using it as a building block for obtaining more complex structures.

5.2 Results and Discussion

5.2.1 Selection of the precursor material for the synthesis of a Rh_2-macrocycle ($Rh_{12}L^{5.1}{}_6L^{5.1'}{}_6$) via Clip-off Chemistry

Triangular Rh_2-macrocycles can be obtained by the cleavage of the **isomer A** of heteroleptic MOPs reported in *Chapter 4*. Ideally, the cleavage of the olefinic bonds of **isomer A** will split the MOP by half releasing two triangular Rh_2-macrocycles. To this end, we chose $Rh_{12}L^{4.1}{}_6L^{4.2'}{}_6$ (which in this Chapter will be named $Rh_{12}L^{5.1}{}_6L^{5.1'}$) for carrying out the synthesis of the targeted macrocycles. These macrocycles will be built by three paddlewheel clusters linked to each other by three 5-*tert*-butylisophthalic acid ligands, and they will be functionalized with six pendant isophthalic ligands (Figure 5.4).

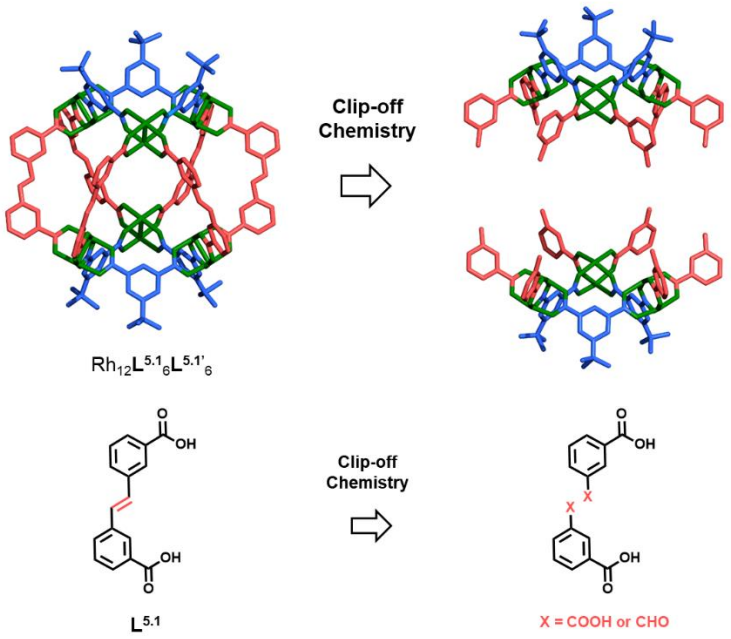

Figure 5.4. Schematic representation of the selective cleavage of the olefinic bonds in $Rh_{12}L^{5.1}{}_6L^{5.1'}{}_6$ to form a triangular Rh_2-macrocycle.

5.2.2 Ozonolysis cleavage of the olefinic bond of ligand $L^{5.1}$

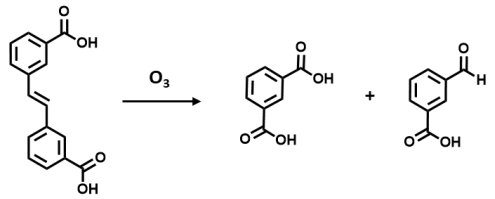

(5.1)

Initially, we confirmed the cleavage of the olefinic bond of $\mathbf{L}^{5.1}$ by ozonolysis. 10 mg of $\mathbf{L}^{5.1}$ was dissolved in DMA and ozone was bubbled into the solution for 2 h. ^{1}H-NMR spectrum of the resulting solution lacks of all the characteristic peaks of $\mathbf{L}^{5.1}$ (olefinic protons at δ = 7.43 ppm; and phenyl protons at δ = 8.18 ppm, 7.92 ppm, 7.85 ppm and 7.51 ppm) confirming its total cleavage. The formation of 3-formylbenzoic acid (aldehyde proton at δ = 10.10; and phenyl protons at δ = 8.45 ppm, 8.24 ppm, 8.14 ppm, and 7.74 ppm) and isophthalic acid (phenyl protons at δ = 8.47 ppm, 8.17 ppm and 7.65 ppm) is confirmed by the appearance of their characteristic signals. This integrated spectrum indicates a 3-formylbenzoic acid/isophthalic acid ratio of 1:0.2 (Figure 5.5).

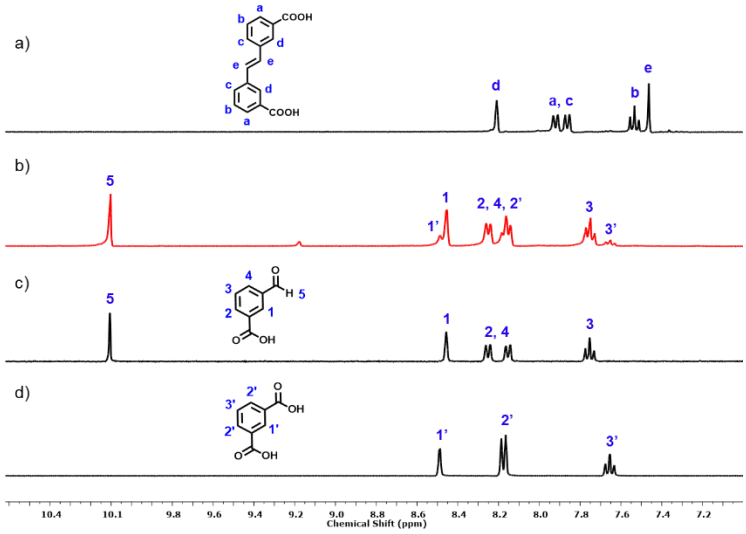

Figure 5.5. ^{1}H-NMR spectra (360 MHz, DMSO-d_6) of (a) $\mathbf{L}^{5.1}$; (b) ozonolyzed $\mathbf{L}^{5.1}$ in DMA; (c) 3-formylbenzoic acid; and (d) isophthalic acid.

5.2.3 Ozonolysis cleavage of trigonal antiprismatic Rh_2-MOP, $Rh_{12}L^{5.1}{}_6L^{5.1'}{}_6$

After confirming that the $\mathbf{L^{5.1}}$ ligand can be broken by an ozonolysis reaction, we proceeded with the ozonolysis cleavage of $Rh_{12}\mathbf{L^{5.1}}_6\mathbf{L^{5.1'}}_6$ to cut the MOP into two. First, we dissolved 10 mg of $Rh_{12}\mathbf{L^{5.1}}_6\mathbf{L^{5.1'}}_6$ in 1 mL of DMA. Ozone was bubbled into the solution for 20 minutes obtaining a complete yellow solution. This colour change of the solution suggested the oxidation of Rh from Rh^{2+} to Rh^{3+} together with the discoordination of the ligands from the metals. However, after low-pressure evaporation, ^{1}H-NMR of the digested obtained sample confirmed that $\mathbf{L^{5.1}}$ ligands had been totally broken. To avoid oxidation of Rh^{2+} ions, we decreased the reaction time to two minutes. Under these conditions, a green solution was obtained but $\mathbf{L^{5.1}}$ was not completely broken, as confirmed by ^{1}H-NMR. The reaction time was finally optimized to 4 minutes of ozonolysis, which ensured complete cleavage of all $\mathbf{L^{5.1}}$ ligands. After bubbling ozone for 4 min, a green solution was obtained indicating the presence of rhodium paddlewheels. ^{1}H-NMR spectrum of the digested sample confirmed the total cleavage of all $\mathbf{L^{5.1}}$ ligands, leading to the formation of 3-formylbenzoic acid and isophthalic acid with a ratio around 1:0.16. In this spectrum, we could not detect $\mathbf{L^{5.1}}$ ligand, concluding that the ozonolysis conversion was 100 % (Figure 5.6).

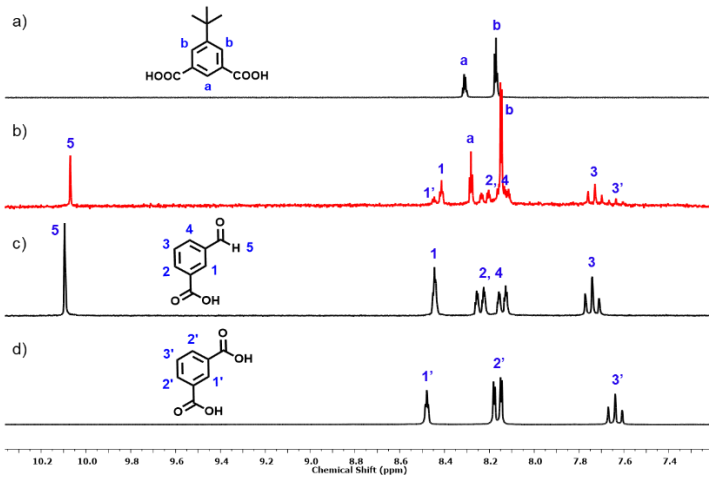

Figure 5.6. ^{1}H-NMR spectra (400 MHz, DMSO-d_6) of (a) 5-*tert*-butylisophthalic acid; (b) digested ^{1}H-NMR of the Rh_2-macrocycle obtained by the cleavage of $Rh_{12}\mathbf{L}^{5.1}{}_6\mathbf{L}^{5.1}{}'_6$ in DMA; (c) 3-formylbenzoic acid; and (d) isophthalic acid.

In the MALDI-TOF spectrum of the obtained sample, we could observe how the peak of $Rh_{12}\mathbf{L}^{5.1}{}_6\mathbf{L}^{5.1}{}'_6$ (4651.5 g/mol) disappeared while several new peaks between 2100 g/mol and 2300 g/mol appeared. Those new peaks correspond to the expected triangular Rh_2-macrocycle with different amounts of aldehyde (3-formylbenzoic acid) and carboxylate (isophthalic acid) ligands (Figure 5.7). The difference of mass between ligands corresponds to one oxygen (16 g/mol), which is attributed to the substitution of one aldehyde by one carboxylic acid group. The following peaks were assigned as follows: 2171.9 g/mol, which corresponds to the Rh_2-macrocycle functionalized with 6 aldehydes groups (Figure 5.7a; expected peak (M+1) at 2172.8 g/mol); 2187.9 g/mol, which corresponds to the Rh_2-macrocycle functionalized with 5 aldehydes and 1 carboxylic acid group (Figure 5.7b; expected peak(M+1) at 2188.8 g/mol); 2203.9 g/mol, which corresponds to the Rh_2-macrocycle functionalized with 4 aldehydes and 2 carboxylic acid groups (Figure 5.7c; expected peak(M+1) at 2204.8 g/mol); 2219.9 g/mol, which corresponds to the Rh_2-macrocycle functionalized with 3 aldehydes

and 3 carboxylic acid groups (Figure 5.7d; expected peak(M+1) at 2220.8 g/mol), and 2235.9 g/mol, which corresponds to the Rh_2-macrocycle functionalized with 2 aldehydes and 4 carboxylic acid groups (Figure 5.7e; expected peak(M+1) at 2236.8 g/mol). The presence of these five peaks in the MALDI-TOF spectrum shows that, as expected, the few COOH ligands formed during the ozonolysis process (CHO 1: COOH 0.16 according to digested ^{1}H-NMR) were randomly distributed around the synthesized triangular Rh_2-macrocycle molecules.

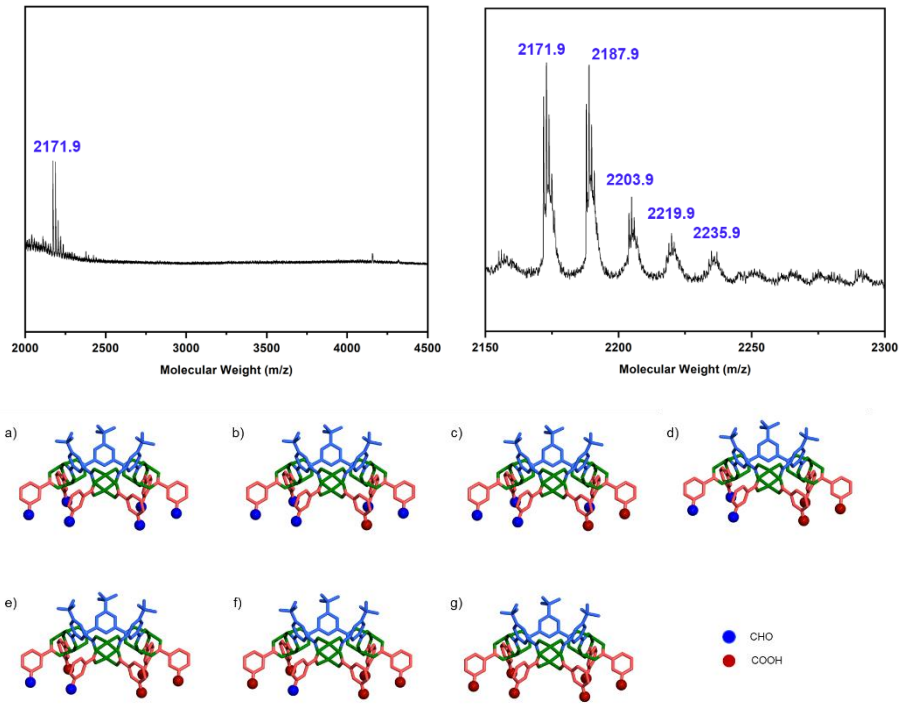

Figure 5.7. MALDI-TOF spectrum of the synthesized triangular Rh_2-macrocycle (top). Representation of all the possible macrocycles that can be formed with different amounts of aldehyde and carboxylic acid groups (bottom).

Because of the presence of this mixture of functionalized Rh_2-macrocycle, we decided to add a purification step to isolate at least one of them. For this, we added a base to the mixture to try to precipitate only the aldehyde functionalized macrocycle using a similar method to that used for the cluster

(*Chapter 3*). However, we failed as the macrocycles functionalized with few carboxylic acid groups were also insoluble on this basic media. We also tried to separate them by column chromatography, but the interactions between the different macrocycles and the silica were too similar. We also tried different reaction solvents or the addition of reducing agents but, although we found conditions (e.g. making the reaction in DMSO or adding Me_2S to the DMA solution) where we had low amounts of carboxylic acid groups, we could not significantly improve our initial aldehyde carboxylic relation of 1:0.16 obtained in pure DMA.

For that reason, we finally decided to try to obtain the triangular Rh_2-macrocycle fully functionalized with carboxylic acid groups carrying out the reaction in oxidative conditions. For this, we solubilized 10 mg of MOP in 4 mL of DMA and, after adding 2.4 mL of H_2O_2, a green suspension was formed. Then, ozone was bubbled into this green suspension for 15 min. Afterwards, we centrifuged the suspension obtaining a green solution containing the triangular Rh_2-macrocycle and a green solid that corresponded to non-cleaved MOP. To decrease the amount of unreacted MOP and increase the yield of the synthesized Rh_2-macrocycle, we increased the reaction time to 30 min. Under these new conditions, the amount of non-cleaved MOP recovered by centrifugation drastically decreased, increasing the yield of the synthesized Rh_2-macrocycle, from 10 % to 32 %.

After ozonolysis the Rh_2-macrocycle functionalized with carboxylic acid groups was separated by precipitation, using 3M HCl. ^{1}H-NMR spectrum of the digested sample confirmed the total cleavage of all $\mathbf{L^{5.1}}$ ligands leading to the formation of isophthalic acid. ^{1}H-NMR spectrum of Figure 5.8 lacks all the characteristic peaks of $\mathbf{L^{5.1}}$ (olefinic protons at δ = 7.43 ppm; and phenyl protons at δ = 8.18 ppm, 7.92 ppm, 7.85 ppm and 7.51 ppm). Yet, it reveals the characteristic signals of $\mathbf{L^{5.1'}}$(phenyl protons at δ = 8.30 ppm and 8.16 ppm; and *tert*-butyl protons at δ = 1.33 ppm) and those of isophthalic acid (phenyl protons at δ = 8.47 ppm, 8.17 ppm and 7.65 ppm).

This integrated spectrum indicates a $\mathbf{L^{5.1'}}$/isophthalic acid ratio of 1:2, as depicted in Figure 5.8, consistent with the formula expected for the Rh_2-macrocycle. Moreover, the absence of any proton signal corresponding to 3-formylbenzoic corroborates the successful isolation of the Rh_2-macrocycles fully functionalized with carboxylic acid groups groups.

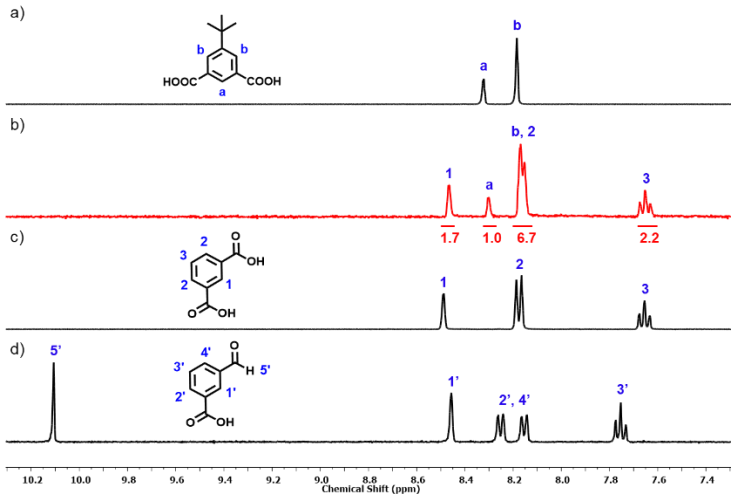

Figure 5.8. ^{1}H-NMR spectra (400 MHz, DMSO-d_6) of (a) 5-*tert*-butylisophthalic acid; (b) digested ^{1}H-NMR of the Rh_2-macrocycle obtained by the cleavage of $Rh_{12}\mathbf{L^{5.1}}_6\mathbf{L^{5.1'}}_6$ in DMA/H_2O_2; (c) isophthalic acid; and (d) 3-formylbenzoic acid.

Furthermore, the broad peaks of the non-digested ^{1}H-NMR and the characteristic rhodium paddlewheel band in the UV-vis spectrum gave us evidence that all the ligands were still coordinated to rhodium and that the rhodium paddlewheel clusters had survived the reaction conditions (Figure 5.9).

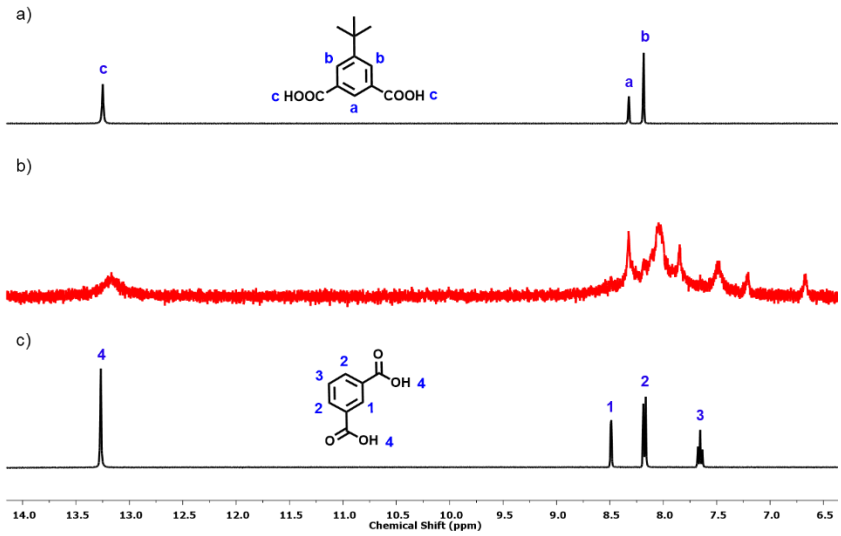

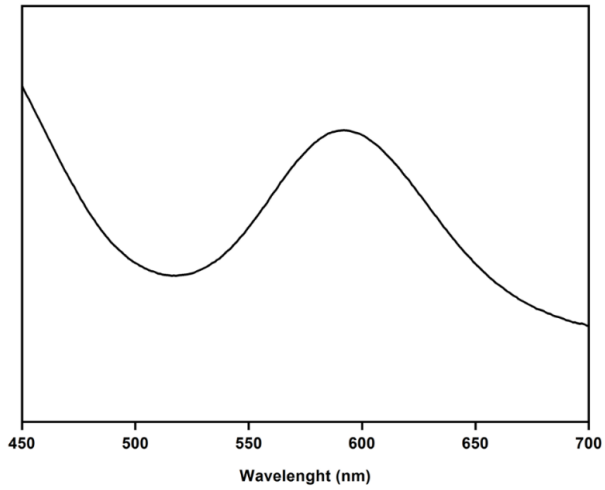

Figure 5.9. ^{1}H-NMR spectra (400 MHz, DMSO-d_6) of (a) 5-*tert*-butylisophthalic acid; (b) ^{1}H-NMR of the Rh_2-macrocycle obtained by the cleavage of $Rh_{12}\mathbf{L}^{5.1}{}_6\mathbf{L}^{5.1'}{}_6$ in DMA/H_2O_2; and (c) isophthalic acid (top). UV-vis spectrum of a THF solution of $Rh_{12}\mathbf{L}^{5.1}{}_6\mathbf{L}^{5.1'}{}_6$. The maximum of adsorption band I (λ_{max}) of $Rh_{12}\mathbf{L}^{5.1}{}_6\mathbf{L}^{5.1'}{}_6$ is centred at 592 nm (bottom).

Finally, formation of the triangular Rh_2-macrocycle funcionalized with carboxylic acid groups was fully corroborated by MALDI-TOF. Indeed, MALDI-TOF spectrum showed how the peak of $Rh_{12}\mathbf{L}^{5.1}{}_6\mathbf{L}^{5.1'}{}_6$ (4651.5 g/mol) disappears and a new peak at 2267.7 g/mol appears. This peak corresponds to the expected Rh_2-macrocycle fully functionalized by carboxylic acid groups (expected mass $[Rh_6(\mathbf{L}^{5.1'})_3(\mathbf{isophthalic\ acid\ ligand})_6 +1]^+$: 2268.8 g/mol) (Figure 5.10).

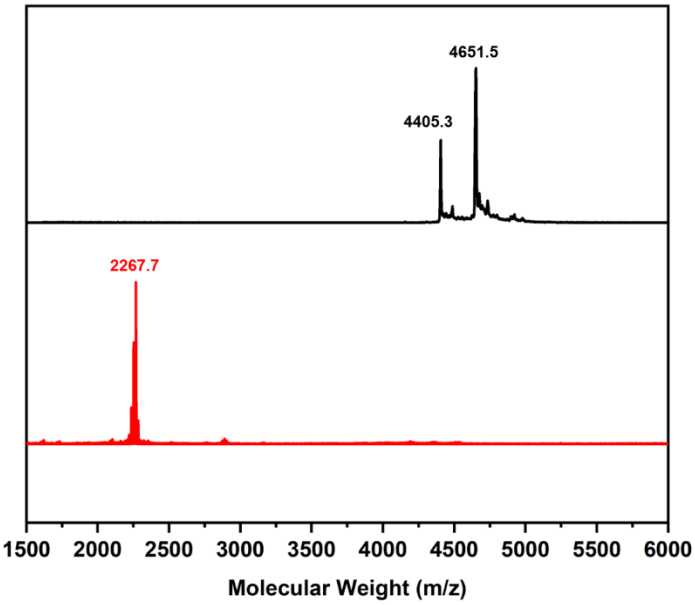

Figure 5.10. MALDI-TOF spectra of $Rh_{12}\mathbf{L}^{5.1}{}_6\mathbf{L}^{5.1'}{}_6$ (black) and of the Rh_2-macrocycle fully functionalized with COOH groups (red).

5.3 Conclusions

We have successfully synthesized a triangular Rh_2-macrocycle without using the capping ligand synthetic strategy. Instead, we have used the Clip-off-Chemistry strategy. To this end, we have cut a previously synthesized antiprismatic Rh_2-MOP, releasing two identical triangular Rh_2-macrocycles. In addition, the synthesized Rh_2-macrocycle was fully functionalized with carboxylic acid groups, opening new avenues for using it as a potential building block for obtaining more complex structures.

5.4. Experimental Part

5.4.1 Materials and Methods

Rhodium acetate was purchased from Acros Organics. Hydrochloric acid 37% (HCl) and hydrogen peroxide 50 wt. % in H_2O were purchased from Sigma-Aldrich. All deuterated solvents were purchased from Eurisotop. Diethyl ether and dimethylacetamide (DMA) were purchased from Fischer Chemicals. All the reagents and solvents were used without further purification.

Ultraviolet-visible (UV−Vis) spectra were measured in an Agilent Cary 4000 at room temperature (ca. 25 °C). **Proton Nuclear Magnetic Resonance (^{1}H-NMR) spectra** were acquired in a Bruker Avance III 250SB NMR, 300SB NMR and a 400SB NMR spectrometer at the "Servei d'Análisi Química" from Autonomous University of Barcelona (UAB). **Mass Spectroscopy (MALDI-TOF)** measurements were performed using a 4800 Plus MALDI TOF/TOF (ABSCIEX – 2010). The matrix used in each case was trans-2-[3-(4-*tert*-butylphenyl)-2-methyl-2-propenylidene]malononitrile (DCTB) measured in positive mode. **Acid digestions of Rh_2-macrocycle** were performed by adding 20 µL of DCl into a solution of 2 mg of Rh_2-MOP in 0.45 mL of DMSO-d_6 and heating the resulting solution at 100 ºC for 6 h.

5.4.2 Synthetic Methodologies

$Rh_{12}L^{5.1}{}_6L^{5.1'}{}_6$ synthesis scale-up: $\mathbf{L^{5.1}}$ (250 mg, 5 eq, 1.1 mmol), $\mathbf{L^{5.1'}}$ (422 mg, 7 eq, 1.6 mmol), Na_2CO_3 (120 mg, 5 eq, 1.1 mmol), rhodium(II) acetate dimer (100 mg, 1 eq, 0.23 mmol) and 10 mL of DMA were sonicated for 5 minutes and placed into an oven at 100 ºC for 72 h. After cooling down to room temperature, the resulting mixture was centrifuged to remove the Na_2CO_3. Then, the obtained solution was added drop by drop to 25 mL of cold MeOH to precipitate the Rh_2-MOP, which was washed three times with MeOH. The obtained green solid was dried at room temperature (40 mg; yield: 18.3%).

Triangular Rh_2-macrocycle functionalized with a mixture of aldehyde and carboxylic acid groups: 10 mg of the $Rh_{12}\mathbf{L}^{5.1}{}_6\mathbf{L}^{5.1'}{}_6$ were dissolved in 1 mL DMA and ozone was bubbled into the solution for 4 minutes. The obtained solution was precipitated into 8 mL of cold ether. After centrifugation, the obtained green solid was dried under vacuum.

Triangular Rh_2-macrocycle fully functionalized with carboxylic acid groups: 10 mg of the $Rh_{12}\mathbf{L}^{5.1}{}_6\mathbf{L}^{5.1'}{}_6$ were dissolved in 4 mL DMA. 2.4 mL of H_2O_2 solution were added and ozone was bubbled into the solution for 30 minutes. After ozonolysis, the obtained suspension was centrifuged, and 8 mL of 3M HCl solution were added forming a green precipitate. The precipitate was separated by centrifugation and washed with water three times (3.5 mg; 32%).

5.4.3. Characterization

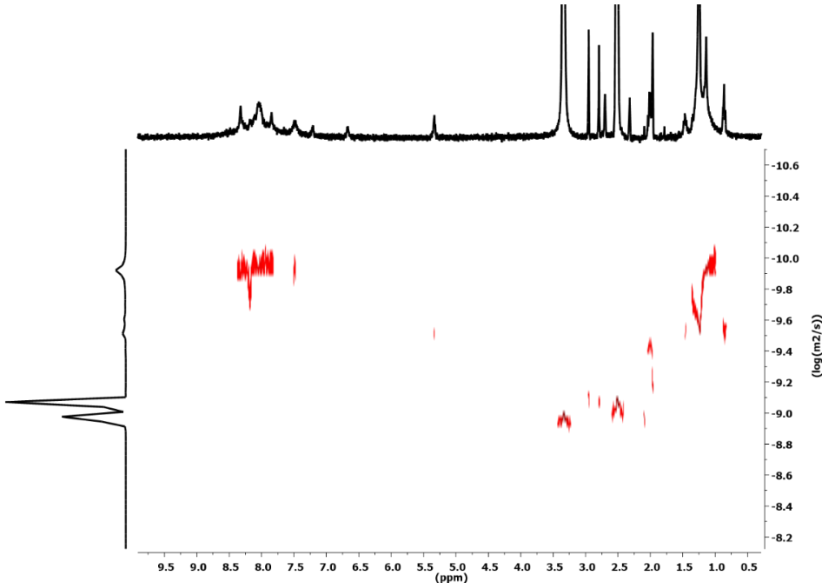

Figure S5.1: DOSY spectrum (400 MHz, DMSO-d_6) of the Rh_2-macrocycle functionalized with carboxylic acid groups.

Chapter 6

Synthesis of a *cis*-Rh_2-cluster by the cleavage of a heteroleptic MOP

6.1 Introduction

In recent decades, carboxylate-bridged paddlewheel-type metal clusters containing metal-metal bonds, with the general formula $[M_2(RCO_2)_4]^{n+}$, have been extensively studied due to their potential applications as building blocks[132–134] or catalysts.[135–137] Because of the many existing combinations of metal ions with carboxylate ligands, a huge library of paddlewheel clusters has been synthesized. Mixed ligand M_2-paddlewheel clusters can be used as terminal or corner building blocks, if one of their ligands is more labile than the other(s),[132–134] or, as enantioselective catalysts, depending on the metal forming them.[135] The direct synthesis of mixed ligand paddlewheel M_2-clusters is challenging as it usually results in complicated mixtures of clusters containing different amounts of ligands of each type. For example, for a cluster built by two types of ligands, A and B, a mixture of $M_2(A)_4$, $M_2(B)_4$, $M_2(A)_3(B)$, $M_2(A)_2(B)_2$, $M_2(A)(B)_3$ and/or $M_2(B)_4$ can be formed. In addition, for $M_2(A)_2(B)_2$, two possible geometric isomers can be formed; *cis*-$M_2(A)_2(B)_2$ or *trans*-$M_2(A)_2(B)_2$ (Figure 6.1). These mixtures must be further purified, making the isolation of a unique mixed ligand M_2-cluster very challenging.

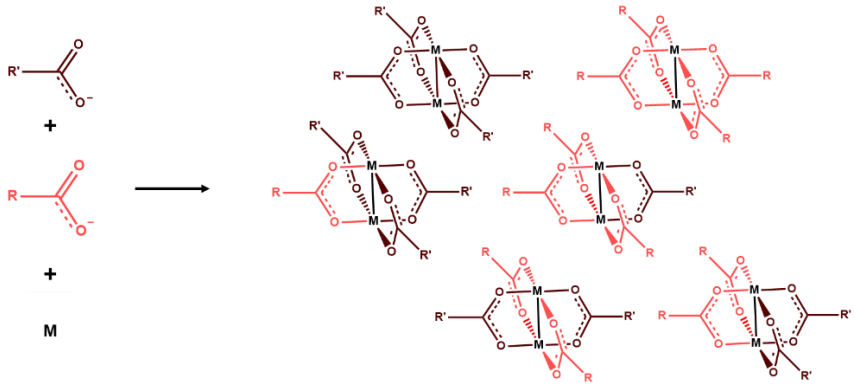

Figure 6.1. Mixture of all the possible M_2-clusters that can be formed when trying to synthesize a mixed ligand paddlewheel M_2-cluster by direct synthesis.

To have an idea of how common the successful isolation and crystallization of mixed ligand M_2-clusters is, we carried out an exhaustive search in the Cambridge Crystallographic Data Centre (CCDC). Note that the length and geometry of the bonds are not important for the search but that the connection between atoms and the type of bonds is crucial. To avoid confusions in the carboxylate ligands exhibiting O-C bonds between single and double bond (bond order 1.5) due to their resonance structures, we draw the structure with discontinuous bonds, (Figure 6.2) meaning that atoms can be linked by any type of bond.

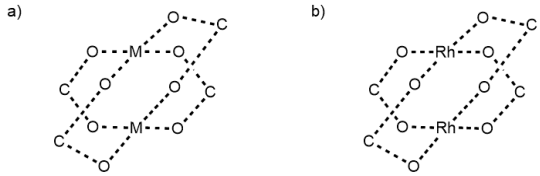

Figure 6.2. Search at the Cambridge Crystallographic Data Centre (CCDC) of the reported (a) paddlewheel M_2-cluster and (b) paddlewheel M_2-cluster crystal structures.

After discarding M_2-paddlewheel superstructures that are not clusters, such as extended structures or MOPs, we count 5236 structures of homoleptic paddlewheel M_2-clusters, with the formula $[M_2(RCO_2)_4]^{n+}$, and 223 mixed ligand paddlewheel M_2-clusters, with the formula $[M_2(RCO_2)_x(RCO_2)_{4-x}]^{n+}$. Therefore, the amount of reported mixed-ligand paddlewheel M_2-clusters represents just 4 % of the total amount of reported paddlewheel M_2-clusters. The 223 mixed-ligand paddlewheel M_2-clusters can be divided in two groups, depending on if they have three ligands of one type and one ligand of the other type, or if they have two ligands of each type. We found 23 with the formula $[M_2(RCO_2)_3(\text{'}RCO_2)]^{n+}$ and 100 with the formula $[M_2(RCO_2)_2(\text{'}RCO_2)_2]^{n+}$, of which 93 were *trans* and only 7 were *cis*. When we ran the search again, but only looking for Rh_2-clusters, we found 627 homoleptic Rh_2-clusters, with the formula $[Rh_2(RCO_2)_4]$, and 47 mixed-

ligand Rh_2-clusters, with the formula $[Rh_2(RCO_2)_x(RCO_2)_{4-x}]^{n+}$. In this case, the amount of the reported mixed-ligand paddlewheel M_2-clusters represents 7 % of the total amount of reported paddlewheel Rh_2-clusters. When we divided these heteroleptic Rh_2-clusters in groups depending on the number and location of ligands, we found that 11 had the formula $[Rh_2(RCO_2)_3(`RCO_2)]$ and, 18 the formula $[Rh_2(RCO_2)_2(`RCO_2)_2]$, of which 14 had a *trans* configuration while only 4 had a *cis* configuration (Figure 6.3).[135,138,139]

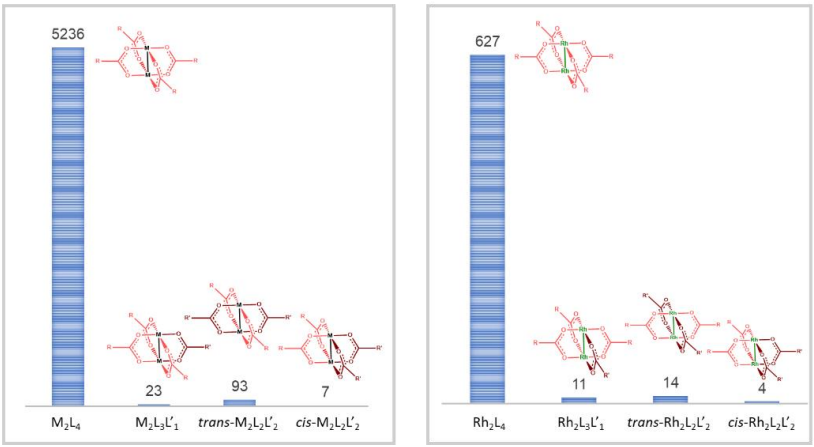

Figure 6.3. Representation of the number of crystal structures of homoleptic and mixed-ligand M_2-paddlewheel clusters (left) and Rh_2-paddlewheel clusters (right) found in the literature.

Accordingly, *cis*-M_2-clusters are the less reported paddlewheel clusters representing only 0.1% of the total amount of reported M_2-clusters, and the 0.6% of the 627 reported Rh_2-clusters. Moreover, one should note that the synthesis of these *cis*-M_2-clusters usually implies difficult separation steps. For example, in one of these *cis*-Rh_2-clusters, a mixture of $Rh_2(A)_3(B)$ and $Rh_2(A)_2(B)_2$ clusters was formed and separated by silica-gel column chromatography. Then, the fraction containing $Rh_2(A)_2(B)_2$ was afterwards recrystallized yielding two kinds of crystals which corresponded to the *cis* and *trans* isomers.[138] In another case, a mixture of $Rh_2(A)_3(B)$ and $Rh_2(A)_2(B)_2$ was first separated by silica-gel column chromatography and

then, further purified by gel permeation chromatography (GPC).[139] In one last example, the authors tried to control *cis*/*trans* geometric isomerism by the *trans* effect, which is based on the fact that the different electronic effects of the ligands encourage the replacement of the ligand in *trans* to one or to the other kind of ligand, favoring the formation of the *cis* or the *trans* cluster. They managed to synthesize and crystalize two types of *cis* clusters. However, the reaction was not fully selective and further purification by column chromatography and recrystallization was necessary.[135]

In this Chapter, we reported the use of Clip-off Chemistry to unequivocally synthesize a functionalized mixed-ligand Rh_2-cluster exhibiting a *cis*-$Rh_2(A)_2(B)_2$ configuration. A new mixed-ligand Rh_2-MOP precursor was successfully designed, synthesized, and cleaved giving an aldehyde functionalized *cis*-mixed-ligand Rh_2-cluster.

6.2 Results and Discussion

6.2.1 Design of the precursor material: a new trigonal antiprismatic Rh_2-MOP

To synthesize a mixed-ligand Rh_2-cluster through Clip-off Chemistry, we require a mixed-ligand Rh_2-MOP as the initial material. This Rh_2-MOP should possess olefinic bonds in all its ligand components, ensuring that upon the cleavage reaction, all the ligands are broken, resulting in the formation of Rh_2-clusters. Thus, if instead of initiating the ozonolysis reaction using a trigonal antiprismatic MOP that only contains olefinic bonds in the equatorial positions (as described in *Chapter 5*), we opt for a trigonal antiprismatic MOP that contains olefinic bonds in both axial and equatorial positions, the ozonolysis reaction should yield a *cis*-mixed-ligand Rh_2-cluster rather than a triangular Rh_2-macrocycle (as discussed in *Chapter 5*) (Figure 6.4).

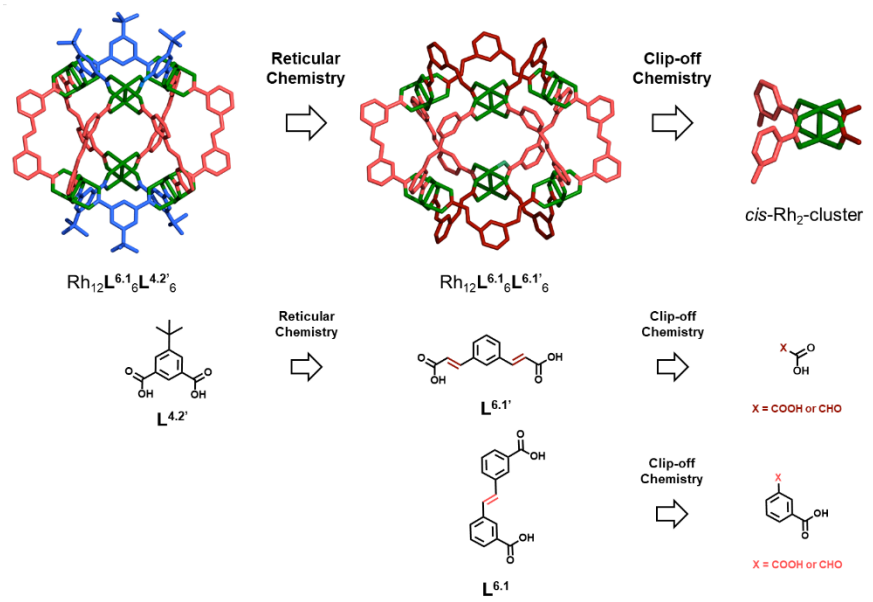

Figure 6.4. Design of the new MOP precursor by reticular chemistry substitution of the 5-*tert*-butylisophtalic acid ligand by a ligand that has the same angle between binding sites but contains olefinic bonds.

According to this, we designed a mixed-ligand antiprismatic Rh_2-MOP analog to the antiprismatic MOP used in *Chapter 5*, but with olefinic bonds in all its ligands. First, we designed a new ligand with a bridging angle of 120°, $\mathbf{L^{6.1'}}$, and two olefinic bonds. This ligand is analogous to the 5-*tert*-butylisophthalic acid of $Rh_{12}\mathbf{L^{4.1}}_6\mathbf{L^{4.1'}}_6$ MOP of *Chapter 5* in terms of geometry as it has the same angle between binding sites. That fact allows its substitution by reticular chemistry obtaining a new mixed-ligand antiprismatic Rh_2-MOP, $Rh_{12}\mathbf{L^{6.1}}_6\mathbf{L^{6.1'}}_6$. When this new MOP is cleaved, all the ligands of the MOP break, resulting in the formation of the targeted mixed-ligand Rh_2-cluster. This cluster consists of two benzene rings functionalized in the *meta* position, along with two other ligands, either oxalic acid or 2-oxoacetic acids. The two different ligands of the initial MOPs are linked to each paddlewheel in the *cis* configuration, which make that the formed mixed-ligand Rh_2-cluster has also a *cis* configuration (Figure 6.4).

6.2.2 Synthesis of the trigonal antiprismatic Rh_2-MOP, $Rh_{12}\mathbf{L^{6.1}}_6\mathbf{L^{6.1'}}_6$, precursor

Initially, we synthesized the ligands $\mathbf{L^{6.1}}$ (which is the same as $\mathbf{L^{4.1}}$) and $\mathbf{L^{6.1'}}$. The $\mathbf{L^{6.1}}$ synthesis is explained in *Chapter 4*. $\mathbf{L^{6.1'}}$ was synthesized by the reaction between methyl acrylate and 1,3-diiodobenzene at 70 ºC for 48 h. The obtained solution was extracted by ethyl acetate and the organic phase was evaporated under reduced pressure. Finally, the carboxylic acids of the obtained product were deprotected in basic media. The synthesis of this ligand was confirmed by ^{1}H-NMR (Figure 6.5).

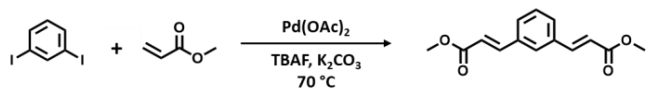

(6.1)

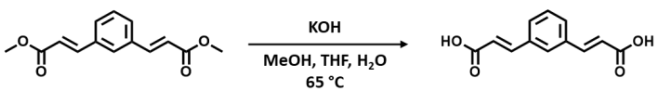

(6.2)

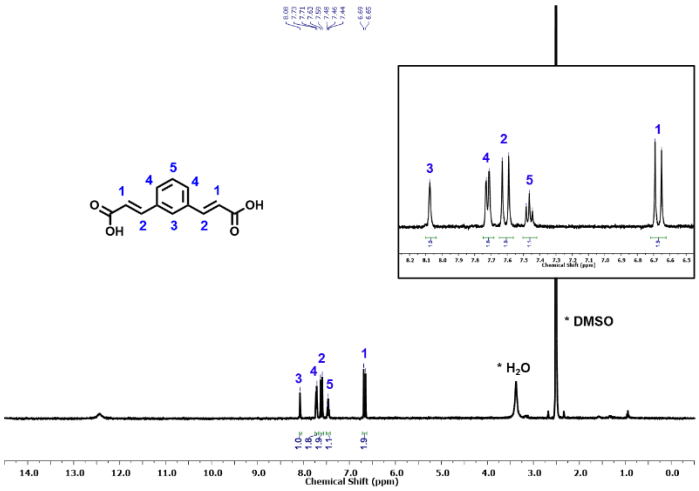

Figure 6.5. ^{1}H-NMR spectrum (400 MHz, DMSO-d_6) of $\mathbf{L^{6.1'}}$.

Once the ligands $\mathbf{L^{6.1}}$ and $\mathbf{L^{6.1'}}$ (*Chapter 4*) had been synthesized, we proceeded with the synthesis of the MOP. We reacted 5 equivalents of $\mathbf{L^{6.1}}$ and 5 equivalents of $\mathbf{L^{6.1'}}$ with rhodium acetate under solvothermal conditions, in the presence of Na_2CO_3, in DMA at 100 ºC for 72 h. This reaction yielded a brown solution, which was centrifuged to eliminate the Na_2CO_3. The supernatant was added drop by drop to cold MeOH inducing green powder precipitation. This green powder was cleaned three times with MeOH and characterized by ^{1}H-NMR, ^{1}H-NMR of the digested sample, UV-vis and MALDI-TOF (Figure 6.6). The ^{1}H-NMR spectrum indicates that both ligands are coordinated, as evidenced by the broadening and slight displacement of the peaks compared to the positions of the free ligands. The DOSY shows that all the peaks correspond to the same molecule, or to molecules with similar size. The UV-vis spectrum in DMA shows the characteristic band centered at 587 nm ascribed to the $\pi^* \rightarrow \sigma^*$ transition of Rh(II) paddlewheel clusters (λ_{max}). The ^{1}H-NMR of the digested MOP shows a relation between ligands of 1:1, which is consistent with the fact that there are six ligands of each kind in each MOP. MALDI-TOF spectrum of the product shows a peak that concurs with the expected molecular mass for a

MOP made from the assembly of six Rh(II) paddlewheel SBUs and six ligands of each type $[(Rh_{12}(\mathbf{L^{6.1}})_6(\mathbf{L^{6.1'}})_6) + H]^+$ (expected = 4128.5; found = 4127.2).

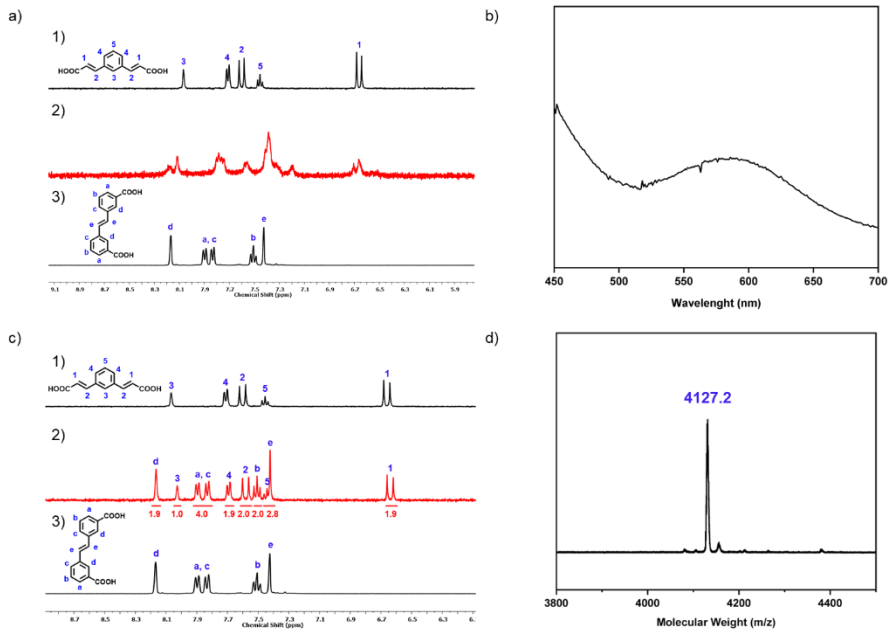

Figure 6.6. (a) ^{1}H-NMR spectra (400 MHz, DMSO-d_6) of (a_1) $\mathbf{L^{6.1'}}$; (a_2) $Rh_{12}\mathbf{L^{6.1}}_6\mathbf{L^{6.1'}}_6$; and ($a_3$) $\mathbf{L^{6.1}}$. (a_c) UV-vis spectrum of a DMA solution of $Rh_{12}\mathbf{L^{6.1}}_6\mathbf{L^{6.1'}}_6$. The maximum of adsorption band I (λ_{max}) of $Rh_{12}\mathbf{L^{6.1}}_6\mathbf{L^{6.1'}}_6$ is centered at 592 nm. (c) ^{1}H-NMR spectra (400 MHz, DMSO-d_6) of (c_1) $\mathbf{L^{6.1'}}$; (c_2) digested $Rh_{12}\mathbf{L^{6.1}}_6\mathbf{L^{6.1'}}_6$; and ($c_3$) $\mathbf{L^{6.1}}$. (d) MALDI-TOF spectrum of $Rh_{12}\mathbf{L^{6.1}}_6\mathbf{L^{6.1'}}_6$. The weight corresponding to the formula $[Rh_{12}\mathbf{L^{6.1}}_6\mathbf{L^{6.1'}}_6 + H]^+$ has been highlighted: expected = 4128.5; found = 4127.2.

Finally, diffusion of diethyl ether into a DMF solution of this green powder in the presence of 4-*tert*-butylpyridine yielded parallelepiped purple crystals. The SCXRD data was collected using synchrotron radiation at XALOC beamline of the ALBA synchrotron. SCXRD confirmed the formation of the expected $Rh_{12}\mathbf{L^{6.1}}_6\mathbf{L^{6.1'}}_6$, built up from six ligands of each type and six Rh_2-clusters (Figure 6.7). The obtained MOP crystalized in the trigonal R-3c space group. The asymmetric unit consists of one-sixth of the MOP and one 4-*tert*-butylpyridine ligand coordinated in the external axial position of the Rh_2-paddlewheel. Each one-sixth portion of the MOP

comprises two Rh atoms and one ligand of each type. The resulting MOP exhibited the geometry of **isomer A**, as described in *Chapter 4*. In this geometry, the top and bottom triangular windows are formed by connecting three paddlewheel Rh(II) SBUs through three ligands with a bridging angle of 120°, $\mathbf{L^{6.1'}}$. These two triangular windows are interconnected by six ligands with a bridging angle of 60°, $\mathbf{L^{6.1}}_6$, forming six larger triangular windows. These larger windows are defined by two ligands with a bridging angle of 60° and one ligand with a bridging angle of 120° (Figure 6.7).

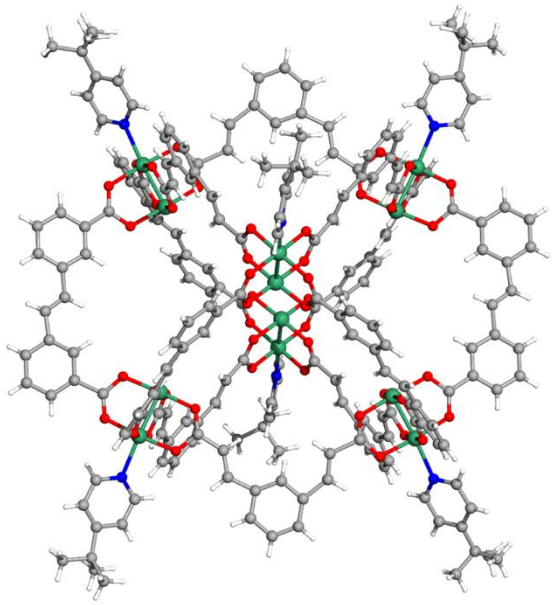

Figure 6.7. Crystal structure of $Rh_{12}\mathbf{L^{6.1}}_6\mathbf{L^{6.1'}}_6$ with 4-*tert*-butylpyridine coordinated to the rhodium paddlewheels.

6.2.3 Ozonolysis cleavage of the olefinic bonds in ligand $L^{6.1'}$

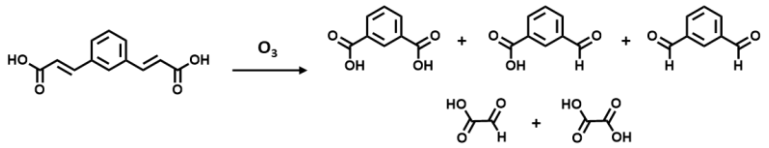

(6.3)

First, we confirmed the ozonolysis cleavage of the olefinic bonds of both ligands $\mathbf{L^{6.1}}$ and $\mathbf{L^{6.1'}}$. The cleavage of $\mathbf{L^{6.1}}$ can be found in *Chapter 5*. To investigate the cleavage process in $\mathbf{L^{6.1'}}$, we solubilized 10 mg of $\mathbf{L^{6.1'}}$ in 2 mL of DMA, and ozone was bubbled into this solution for 2 h. The ^{1}H-NMR analysis of the ozonated solution revealed the cleavage of the ligand $\mathbf{L^{6.1'}}$ after 2 h, as the peaks corresponding to the initial ligand disappeared. The cleavage predominantly resulted in the formation of 3-formylbenzoic acid and isophthalic acid in a 1:1 ratio (Figure 6.8). However, it was not possible to identify oxalic acid and 2-oxoacetic acids by ^{1}H-NMR. This is attributed to the fact that oxalic acid only possesses acidic protons, and that 2-oxoacetic acids have one acidic proton and an aldehyde proton that overlaps with the other aldehyde groups of the ligands.

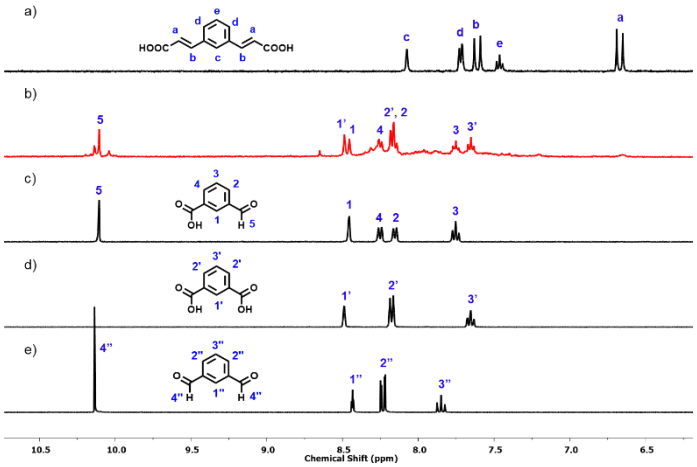

Figure 6.8. ^{1}H-NMR spectra (400 MHz, DMSO-d_6) of (a) $\mathbf{L^{6.1'}}$; (b) ozonolysis of the $Rh_{12}\mathbf{L^{6.1}}_{6}\mathbf{L^{6.1'}}_{6}$ in DMA for 2h; (c) 3-formylbenzoic acid; (d) isophthalic acid; and (e) isophthalaldehyde.

6.2.4 Ozonolysis cleavage of $Rh_{12}L^{6.1}{}_6L^{6.1'}{}_6$ MOP

After confirming that both ligands $\mathbf{L^{6.1}}$ and $\mathbf{L^{6.1'}}$ can be easily cleaved by an ozonolysis reaction, we proceeded with the cleavage of the MOP. To this end, we dissolved 10 mg of the MOP in DMA or in DMA/DMSO and we bubbled ozone for 3 minutes or 10 minutes, respectively. In both experiments, we observed that the ligand with 60° angle between binding sites, $\mathbf{L^{6.1}}$, was easily cleaved, but the ligand with 120° angle between binding sites, $\mathbf{L^{6.1'}}$, remained uncleaved. The ^{1}H-NMR spectrum lacks all the characteristic peaks of $\mathbf{L^{6.1}}$ (olefinic protons at δ = 7.43 ppm; and phenyl protons at δ = 8.18 ppm, 7.92 ppm, 7.85 ppm and 7.51 ppm), yet it still reveals the characteristic signals of $\mathbf{L^{6.1'}}$(olefinic protons at δ = 7.61 ppm and 6.67 ppm; and phenyl protons at δ = 8.08 ppm, 7.72 ppm and 7.46 ppm) (Figure 6.9).

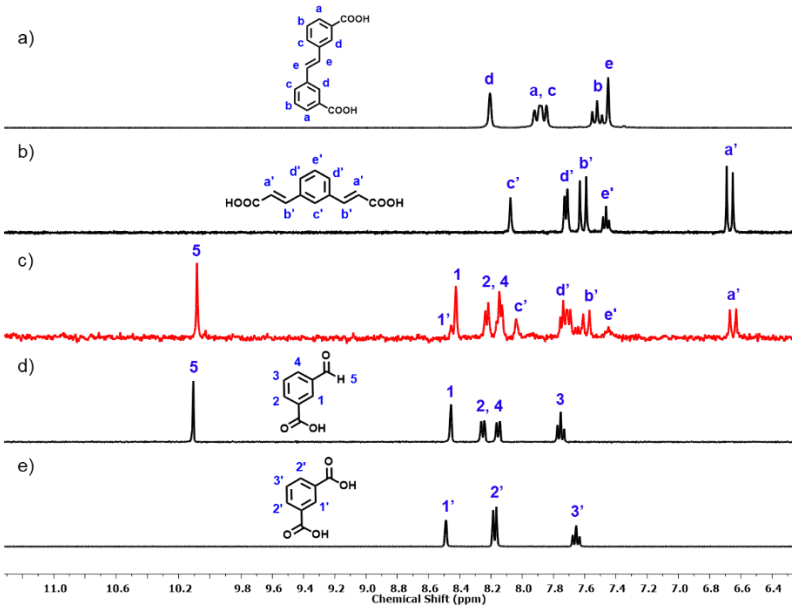

Figure 6.9. ^{1}H-NMR spectra (400 MHz, DMSO-d_6) of (a) $\mathbf{L^{6.1}}$; (b) $\mathbf{L^{6.1'}}$; (c) digested sample of the ozonolysis of the $Rh_{12}L^{6.1}{}_6L^{6.1'}{}_6$ in DMA: DMSO (1:1) for 10 min; (d) 3-formylbenzoic acid; and (e) isophthalic acid.

To overcome this problem, we increased the reaction time to 15 minutes. However, we noticed that the reaction crude turned yellow, due to the oxidation of Rh^{2+} to Rh^{3+}, while $\mathbf{L^{6.1'}}$ was not completely cleaved yet. Therefore, we concluded that, under the studied experimental conditions, the rhodium clusters were less stable than the olefinic bonds of the ligand $\mathbf{L^{6.1'}}$.

We attempted various experimental conditions, including different reaction solvents, to identify a condition in which all the olefinic bonds of $Rh_{12}\mathbf{L^{6.1}}_6\mathbf{L^{6.1'}}_6$ MOP would cleave, whereas the Rh_2-clusters remained unaffected. Unfortunately, we were unsuccessful in finding such condition. Consequently, we decided to alter the precursor material for our Clip-off synthesis. To design a new mixed-ligand antiprismatic M_2-MOP suitable as the precursor material, we considered two strategies: (1) creating a MOP with metal-ligand bonds that are more stable against the cleavage reaction than Rh-carboxylic bonds; or (2) constructing a MOP composed of ligands that contain olefinic bonds, which are more susceptible to ozonolysis than those of $\mathbf{L^{6.1'}}$. We chose to pursue the second strategy by modifying the ligand $\mathbf{L^{6.1'}}$ while retaining the Rh-carboxylic bonds in our new MOP design.

3.2.5 Design and synthesis of a new trigonal antiprismatic Rh_2-MOP, $Rh_{12}\mathbf{L^{6.1}}_6\mathbf{L^{6.2'}}_6$

We decided to design an analogous $\mathbf{L^{6.1'}}$ ligand with a benzene ring positioned between the olefinic bonds and the carboxylic acid groups, $\mathbf{L^{6.2'}}$ (Figure 6.10). This design choice aims to create a chemical environment around the olefinic bonds that closely resembles the ligands $\mathbf{L^{3.2}}$ and $\mathbf{L^{6.1}}$, which undergo cleavage more readily than $\mathbf{L^{6.1'}}$. As $\mathbf{L^{6.1}}$ and $\mathbf{L^{6.1'}}$ are geometrically analogous (both have an angle between binding sites of 120°), they can be exchanged by reticular chemistry obtaining a new trigonal antiprismatic MOP, $Rh_{12}\mathbf{L^{6.1}}_6\mathbf{L^{6.2'}}_6$ (Figure 6.10).

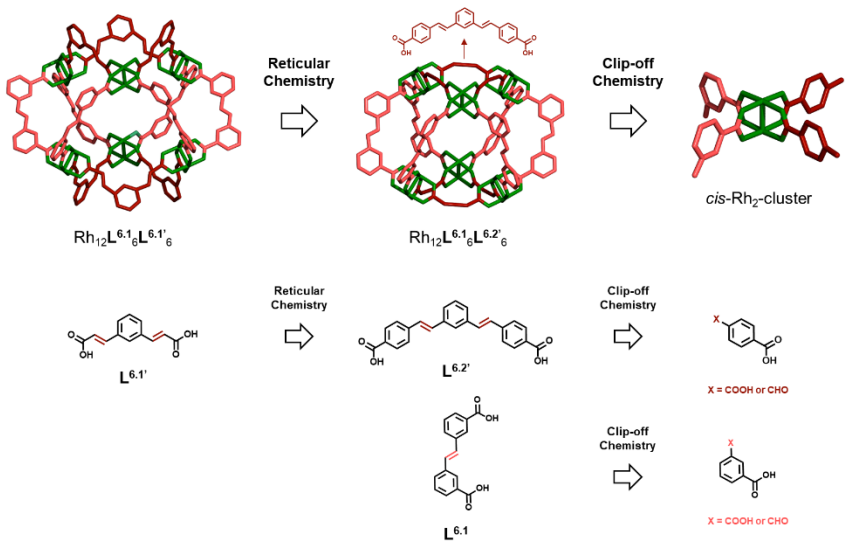

Figure 6.10. Synthesis of a new MOP by reticular synthesis and the expected outcome after cleaving it.

First, we synthesized $\mathbf{L^{6.2'}}$ via the Heck reaction of 4-vinylbenzoic acid and 1,3-diiodobenzene in the presence of triphenylphosphine, triethylamine, and palladium (II) acetate in THF at 80 ºC (Reaction 6.4). The resulting product was purified by acid precipitation from THF and washed with MeOH. Finally, the solid was characterized by ^{1}H-NMR (Figure 6.11).

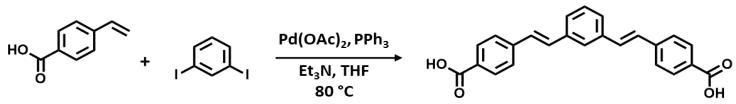

(6.4)

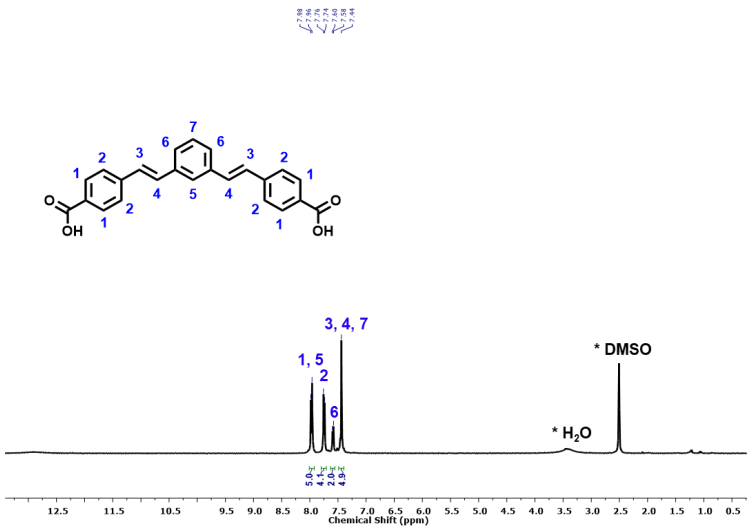

Figure 6.11. ^{1}H-NMR spectrum (400 MHz, DMSO-d_6) of $\mathbf{L^{6.2'}}$.

Once we had synthesized the $\mathbf{L^{6.2'}}$ ligand, we proceeded with the synthesis of the new trigonal antiprismatic Rh_2-MOP. We reacted 5 equivalents of $\mathbf{L^{6.1}}$ and 5 equivalents of $\mathbf{L^{6.2'}}$ with rhodium acetate under solvothermal conditions, in the presence of Na_2CO_3, in DMA at 100 ºC for 72 h. This reaction yielded a brown solution, which was centrifuged to eliminate the Na_2CO_3. The supernatant was added drop by drop to cold MeOH inducing the precipitation of a green powder. This green powder was cleaned three times with MeOH and characterized by ^{1}H-NMR, ^{1}H-NMR of the digested sample, and UV-vis (Figure 6.12). The ^{1}H-NMR spectrum indicates that the ligands are coordinated, as observed from the broadening and slight displacement of the peaks compared to the positions of the free ligands. The DOSY shows that all the peaks correspond to the same molecule, or to molecules with similar size. The UV-vis spectrum of $Rh_{12}\mathbf{L^{6.1}}_6\mathbf{L^{6.2'}}_6$ in THF displays a characteristic band centered at 592 nm ascribed to the $\pi^* \rightarrow \sigma^*$ transition of Rh(II) paddlewheel clusters (λ_{max}). The ^{1}H-NMR of the digested $Rh_{12}\mathbf{L^{6.1}}_6\mathbf{L^{6.2'}}_6$ shows a relation between ligands of 1:1, which is consistent with the fact that six ligands of each kind in each MOP are present.

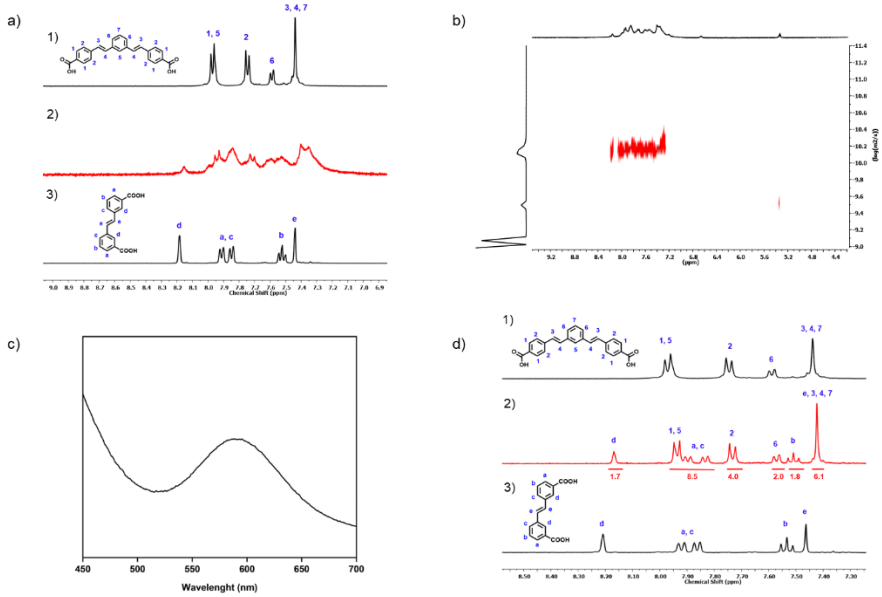

Figure 6.12. (a) ^{1}H-NMR spectra (400 MHz, DMSO-d_6) of (a_1) $\mathbf{L^{6.2'}}$; (a_2) $Rh_{12}\mathbf{L^{6.1}}_6\mathbf{L^{6.2'}}_6$; and ($a_3$) $\mathbf{L^{6.2}}$. (b) DOSY spectrum (400 MHz, DMSO-d_6) of $Rh_{12}\mathbf{L^{6.1}}_6\mathbf{L^{6.2'}}_6$. (c) UV-vis spectrum of a THF solution of $Rh_{12}\mathbf{L^{6.1}}_6\mathbf{L^{6.2'}}_6$. The maximum of adsorption band I (λ_{max}) of $Rh_{12}\mathbf{L^{6.1}}_6\mathbf{L^{6.2'}}_6$ is centered at 592 nm. (d) ^{1}H-NMR spectra (400 MHz, DMSO-d_6) of (d_1) $\mathbf{L^{6.2'}}$; (d_2) digested $Rh_{12}\mathbf{L^{6.1}}_6\mathbf{L^{6.2'}}_6$; and ($d_3$) $\mathbf{L^{6.1}}$.

MALDI-TOF spectrum of the product shows a peak that concurs with the expected molecular mass for a MOP made from the assembly of six Rh(II) paddlewheel SBUs and six ligands of each type $Rh_{12}(\mathbf{L^{6.1}})_6(\mathbf{L^{6.2'}})_6$ and different amounts of DMSO and H_2O coordinated to the rhodium clusters (Figure 6.13).

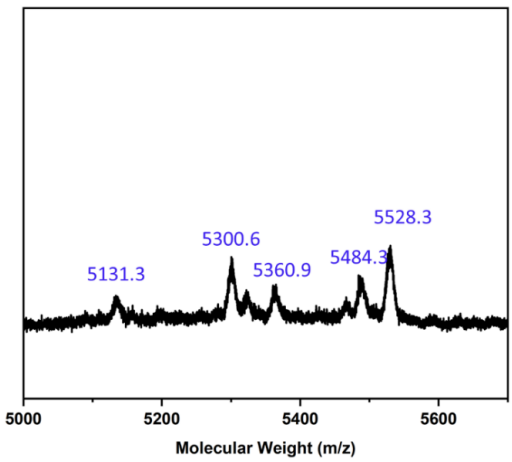

Figure 6.13. MALDI-TOF spectrum of $Rh_{12}\mathbf{L}^{6.1}{}_6\mathbf{L}^{6.2'}{}_6$. The weight corresponding to the formula $[Rh_{12}\mathbf{L}^{6.1}{}_6\mathbf{L}^{6.2'}{}_6(DMSO)_7(H_2O)_3 + H]^+$ has been highlighted: expected = 5529.0; found = 5528.3. The weight corresponding to the formula $[Rh_{12}\mathbf{L}^{6.1}{}_6\mathbf{L}^{6.2'}{}_6(DMSO)_6(H_2O)_4 + H]^+$ has been highlighted: expected = 5585.0; found = 5584.3. The weight corresponding to the formula $[Rh_{12}\mathbf{L}^{6.1}{}_6\mathbf{L}^{6.2'}{}_6(DMSO)_4(H_2O)_4 + H]^+$ has been highlighted: expected = 5561.0; found = 5560.9. The weight corresponding to the formula $[Rh_{12}\mathbf{L}^{6.1}{}_6\mathbf{L}^{6.2'}{}_6(DMSO)_3(H_2O)_5 + H]^+$ has been highlighted: expected = 5298.9; found = 5300.6. The weight corresponding to the formula $[Rh_{12}\mathbf{L}^{6.1}{}_6\mathbf{L}^{6.2'}{}_6(H_2O)_5 + H]^+$ has been highlighted: expected = 5130.9; found = 5131.3.

6.2.6 Ozonolysis cleavage of the olefinic bond ligand, $\mathbf{L}^{6.2'}$

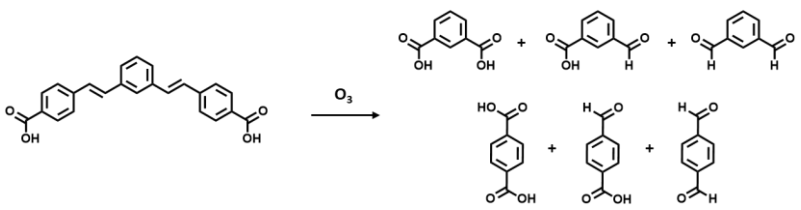

(6.5)

Next, we confirmed the ozonolysis cleavage of the olefinic bond of the ligand $\mathbf{L}^{6.2'}$. For doing so, we solubilized 10 mg of $\mathbf{L}^{6.2'}$ in 2 mL of DMA and we bubbled ozone to the solution during 2 h. ^{1}H-NMR spectrum of the resulting solution lacks of all the characteristic peaks of $\mathbf{L}^{6.2'}$(olefinic protons

at δ = 7.44 ppm; and phenyl protons at δ = 7.97 ppm, 7.75 ppm and 7.59) confirming its total cleavage. It clearly reveals the characteristic signals of 4-formylbenzoic acid (aldehyde proton at δ = 10.11; phenyl protons at δ = 8.14 ppm and 8.02 ppm), those of terephthalic acid (phenyl protons at δ = 8.04 ppm), and those of 3-formylbenzoic acid (aldehyde proton at δ = 10.10; and phenyl protons at δ = 8.45 ppm, 8.24 ppm, 8.14 ppm, and 7.74 ppm). These three compounds are the majority products of the ozonolysis reaction. However, traces of isophthalic acid and isophthalaldehyde can also be appreciated (Figure 6.14).

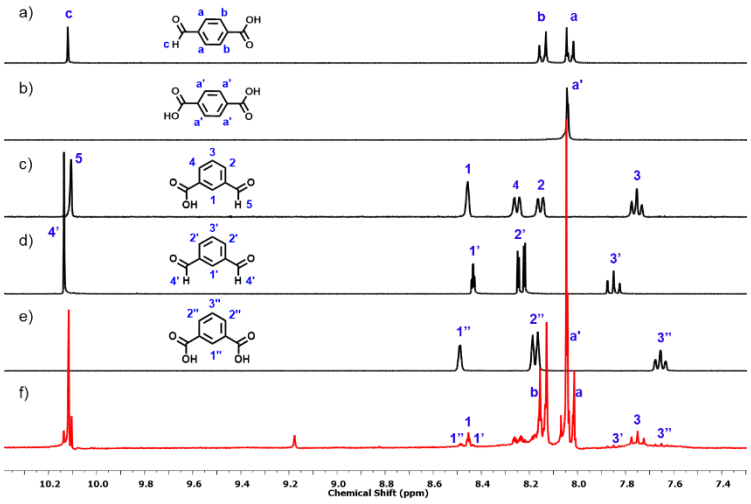

Figure 6.14. ^{1}H-NMR spectra (400 MHz, DMSO-d_6) of (a) 4-formylbenzoic acid; (b) terephthalic acid; (c) 3-formylbenzoic acid; (d) isophthalaldehyde; (e) isophthalic acid; and (f) ozonolysis of the $\mathbf{L^{6.2'}}$ in DMA for 2h.

6.2.7 Clip-off cleavage of Rh_2-MOP, $Rh_{12}\mathbf{L^{6.1}}_6\mathbf{L^{6.2'}}_6$: Formation of a *cis*-$Rh_2$-cluster

After confirming that ligand $\mathbf{L^{6.2'}}$ can be readily cleaved by ozonolysis, we proceeded with the ozonolysis of $Rh_{12}\mathbf{L^{6.1}}_6\mathbf{L^{6.2'}}_6$ using a similar procedure to the one described in *Chapter 3* for the synthesis of the homoleptic Rh_2-cluster. Following previous procedures, 10 mg of

$Rh_{12}\mathbf{L^{6.1}}_6\mathbf{L^{6.2'}}_6$ were dissolved in 1 mL of DMA and 1 mL of DMSO was added. Then, ozone was bubbled through the solution at room temperature for 10 min. Afterwards, 2.6 mL of a solution of $5 \cdot 10^{-5}$ mol/L Na_2CO_3 and 1 mL of HCl 3M were added to the resulting red solution. This addition resulted in the precipitation of clusters that were fully functionalized with aldehydes. The obtained solid was cleaned once with the aqueous solution of Na_2CO_3 and then, with water to remove the coordinated DMSO until the obtention of a green solid. ^{1}H-NMR analysis of the digested Rh_2-cluster reveals that all the initial Rh_2-MOP was successfully cleaved, as it lacks all the characteristic peaks of the initial ligands $\mathbf{L^{6.1}}$ or $\mathbf{L^{6.2'}}$ (olefinic protons at δ = 7.44 and 7.43 ppm; and phenyl protons at δ = 8.18 ppm, 7.97 ppm, 7.92 ppm, 7.85 ppm, 7.75 ppm, 7.59 ppm and 7.51 ppm). Yet, it reveals the characteristic signals of 3-formylbenzoic acid (aldehyde proton at δ = 10.10; and phenyl protons at δ = 8.45 ppm, 8.24 ppm, 8.14 ppm, and 7.74 ppm) and those of 4-formylbenzoic acid (aldehyde proton at δ = 10.11; phenyl protons at δ = 8.14 ppm and 8.02 ppm). This integrated spectrum indicates a 3-formylbenzoic acid/4-formylbenzoic acid ratio of 2:2, as depicted in Figure 6.16, consistent with the formula expected for the *cis*-Rh_2-cluster. Moreover, the absence of any proton signal corresponding to terephthalic acid or isophthalic acid corroborates the successful isolation of the clusters fully functionalized with aldehyde groups (Figure 6.15).

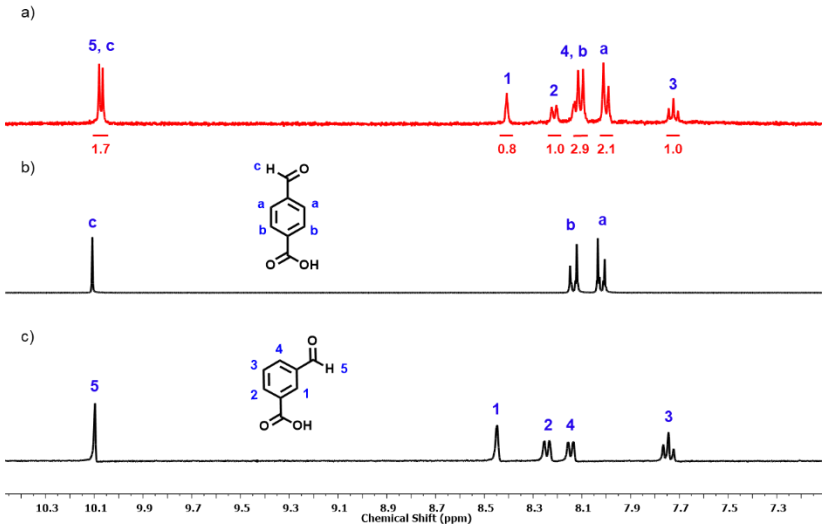

Figure 6.15. ^{1}H-NMR spectra (400 MHz, DMSO-d_6) of (a) digested *cis*-Rh_2-cluster synthesized by the ozonolysis of the $Rh_{12}\mathbf{L}^{6.1}{}_6\mathbf{L}^{6.2'}{}_6$ in DMA : DMSO (1:1); (b) 4-formaldehyde; and (c) 3-formylbenzoic acid.

The ^{1}H-NMR and UV-vis analyses demonstrate that the Rh_2-paddlewheels have remained intact under the reaction conditions. In the ^{1}H-NMR spectrum, it is evident that all the ligands are coordinated, indicating the absence of free ligands. Furthermore, in the UV-vis spectrum of the cluster, a distinct band centered at 600 nm is observed. This band is attributed to the $\pi^* \rightarrow \sigma^*$ transition of Rh(II) paddlewheel clusters, providing additional confirmation of the presence and stability of the Rh_2-paddlewheel structure (Figure 6.16).

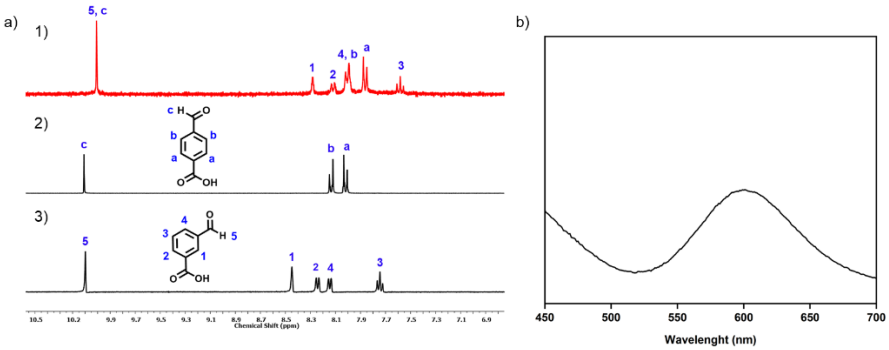

Figure 6.16. (a) ^{1}H-NMR spectra (400 MHz, DMSO-d_6) of (a_1) *cis*-Rh_2-cluster synthesized by the ozonolysis of the $Rh_{12}\mathbf{L}^{6.1}{}_6\mathbf{L}^{6.2'}{}_6$; ($a_2$) 4-formaldehyde; and ($a_3$) 3-formylbenzoic acid. (b) UV-vis spectrum of a DMA solution of *cis*-Rh_2-cluster. The maximum of adsorption band I (λ_{max}) of $Rh_{12}\mathbf{L}^{6.1}{}_6\mathbf{L}^{6.2'}{}_6$ is centered at 600 nm.

Finally, ESI mass spectroscopy confirmed the formation of the desired cluster. The peak at 836.8755 matches perfectly with the expected mass of the ion $[Rh_2C_{32}H_{20}O_{12} + Cl]^-$, 836.8759. The exact mass of the ion $[Rh_2C_{32}H_{20}O_{12}(CH_3OH) + Cl]^-$ (expected: 868.9021, found: 868.9040) and the exact mass of the ion $[Rh_2C_{32}H_{20}O_{12}(CH_3OH)_2 + Cl]^-$ (expected: 900.9283, found: 900.9286), which corresponds to the mass of the cluster coordinated to one or two methanol molecules, can also be appreciated. The isotopic distribution of these peaks concurs with the simulated ones (Figure 6.17).

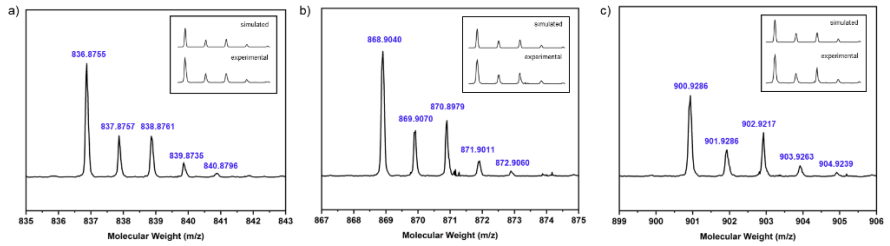

Figure 6.17. ESI mass spectroscopy spectrum of the *cis*-Rh_2-cluster. (a) The weight corresponding to the formula $[Rh_2C_{32}H_{20}O_{12} + Cl]^-$ has been highlighted: expected = 836.8759; found = 836.8755. (b) The weight corresponding to the formula $[Rh_2C_{32}H_{20}O_{12}(CH_3OH) + Cl]^-$ has been highlighted: expected = 868.9021; found = 868.9040. (c) The weight corresponding to the formula $[Rh_2C_{32}H_{20}O_{12}(CH_3OH)_2 + Cl]^-$ has been highlighted: expected = 900.9283; found = 900.9286.

Finally, we successfully crystallized this cluster by dissolving 2 mg of the cluster in 0.5 mL of acetonitrile, adding 0.1 mL of water, and allowing the acetonitrile to evaporate for two days. Once rod-like crystals were formed, the vial was sealed to prevent the evaporation of coordinated CH_3CN molecules within the crystals, as it would decrease their quality. SCXRD data was collected using synchrotron radiation at the XALOC beamline of the ALBA synchrotron. SCXRD confirmed the formation of the expected Rh_2-cluster. The obtained cluster crystallized in the monoclinic P2/n space group. The asymmetric unit consisted of half of the cluster, one rhodium atom, and two 3-formylbenzoic acid ligands (Figure 6.20). Additionally, one acetonitrile molecule was coordinated to the Rh atom.

Upon closer examination of the SCXRD results, it was initially observed that the cluster appeared as an homoleptic Rh_2-paddlewheel functionalized with aldehyde groups in the *meta* and *para* positions. However, this observation contradicts the findings from the digested ^{1}H-NMR analysis, where we observed 3-formylbenzoic acid and 4-formylbenzoic acid, but not 3,4-diformylbenzoic acid. Furthermore, it would not make chemical sense to have an homoleptic cluster composed of 3,4-diformylbenzoic acid. Upon further analysis, it was discovered that each aldehyde group had an occupancy of 0.5. This finding aligns with the expected *cis*-Rh_2-cluster from ozonolysis reaction, and it is consistent with the 1:1 ratio of 3-formylbenzoic acid and 4-formylbenzoic acid observed in the ^{1}H-NMR spectrum. Therefore, we can conclude that our Rh_2-paddlewheel sample is composed of 3-formylbenzoic acid and 4-formylbenzoic acid in a 1:1 ratio. The presence of ligands with two aldehyde groups can be explained by the similarity in geometry between 3-formylbenzoic acid and 4-formylbenzoic acid, allowing different orientations of the clusters within the crystal. In fact, what we observe is an average of the several possible orientations of the cluster (Figure 6.18). Three possible scenarios were

considered to explain the obtained crystal structure: (1) a mixture of two homoleptic Rh_2-clusters, one fully functionalized in *cis* and the other fully functionalized in *trans*, in a 1:1 proportion; (2) a *trans*-mixed-ligand Rh_2-cluster; and (3) a *cis*-mixed-ligand Rh_2-cluster. The first hypothesis was discarded, as we did not observe the formation of two different MOPs in the DOSY analysis, and the MALDI-TOF results indicated the presence of a mass consistent with the expected mixed ligand MOP. Additionally, it would be highly unlikely to obtain two clusters in a 1:1 proportion during the synthesis and purification processes. The formation of a *trans*-mixed-ligand cluster is also implausible, as it would require a MOP where the two types of ligands are in a *trans* configuration around the M_2-paddlewheel, which, as far of our knowledge, is not geometrically possible for these ligands. Therefore, the most plausible hypothesis is that we have the expected *cis*-Rh_2-cluster (Figure 6.19). The obtained crystal exhibits spatial disorder, with the *cis*-Rh_2-cluster oriented in different directions within the crystal (Figure 6.18).

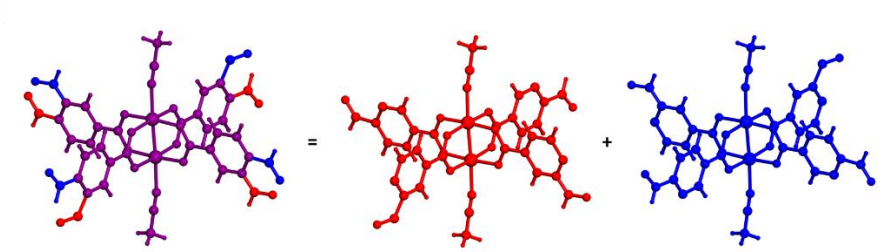

Figure 6.18. Superposition of the *cis*-Rh_2-cluster in the crystal structure.

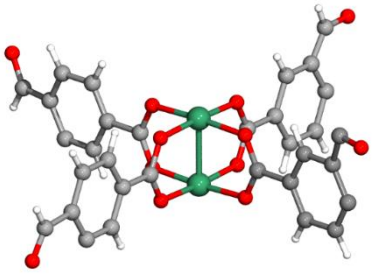

Figure 6.19. Crystal structure of the *cis*-Rh_2-cluster.

6.3 Conclusions

Summarizing, we have proved that our Clip-off synthetic strategy can be used for unequivocally synthesizing mixed-ligand M_2-clusters by the cleaving of a previously existing material releasing fragments that already exist inside the initial compound. First, we have successfully synthesized a new trigonal antiprismatic Rh_2-MOP, $Rh_{12}\mathbf{L^{6.1}}_6\mathbf{L^{6.1'}}_6$, with olefinic bonds in knowing crystallographic positions. In doing so, we have achieved a required MOP towards its subsequent use as initial reagent in Clip-off Chemistry. Finally, we have successfully synthesized a *cis*-Rh_2-cluster fully functionalized with aldehydes by ozonolysis cleavage of $Rh_{12}\mathbf{L^{6.1}}_6\mathbf{L^{6.1'}}_6$.

6.4 Experimental Part

6.4.1 Materials and Methods

Rhodium acetate was purchased from Acros Organics. Sodium carbonate (Na_2CO_3), 1,3-diodobenzene, palladium(II) acetate, methyl acrylate, tetrabutylammonium fluoride solution (TBAF), 4-*tert*-butylpyridine and 4-vinylbenzoic acid were purchased from TCI. Triphenylphosphine, potassium carbonate (K_2CO_3), potassium hydroxide (KOH) and hydrochloric acid 37% (HCl) were purchased from Sigma Aldrich. All deuterated solvents were purchased from Eurisotop. Diethyl ether, tetrahydrofuran (THF), methanol (MeOH), acetonitrile (MeCN) and dimethylacetamide (DMA) were purchased from Fischer Chemicals. All the reagents and solvents were used without further purification.

Ultraviolet-visible (UV−Vis) spectra were measured in an Agilent Cary 4000 at room temperature (ca. 25 °C). **Proton Nuclear Magnetic Resonance (^{1}H-NMR) spectra** were acquired in a Bruker Avance III 250SB NMR, 300SB NMR and a 400SB NMR spectrometer at "Servei d'Análisi Química" from Autonomous University of Barcelona (UAB). **Mass Spectroscopy (MALDI-TOF)** measurements were performed using a 4800 Plus MALDI TOF/TOF (ABSCIEX – 2010). The matrix used in each case was trans-2-[3-(4-*tert*-butylphenyl)-2-methyl-2-propenylidene]malononitrile (DCTB) measured in positive mode. **Acid digestions of Rh_2-MOP** were performed by adding 20 µL of DCl into a solution of 2 mg of Rh_2-MOP in 0.45 mL of DMSO-d_6 and heating the resulting solution at 100 ºC for 6 h.

6.4.2 Synthetic Methodologies

*Synthesis of (2E,2'E)-3,3'-(1,3-phenylene)diacrylic acid (**L**$^{6.1'}$):* Methyl acrylate (2.2 µL, 24 mmol), 1,3-diiodobenzene (1.3 g, 4 mmol), TBAF (17 mL, 57 mmol), K_2CO_3 (1.1 g, 8 mmol) and palladium (II) acetate (160 mg, 0.7 mmol) were allowed to react at 70 ºC for 48 h. The obtained suspension was filtrated. The obtained solution was extracted by ethyl acetate. The organic phase was evaporated under reduced pressure. 80 mL of THF, 80 mL of MeOH and 60 mL of a water solution containing 5g of KOH were added and heated at 65 ºC for 24 h. THF and MeOH were evaporated under reduced pressure. HCl was added and a white solid was formed, which was filtrated and washed with water (0.6 g; yield: 70%). ^{1}H-NMR (400 MHz, DMSO) δ 8.08 (s, 1H), 7.72 (d, J = 7.7 Hz, 2H), 7.61 (d, J = 16.0 Hz, 2H), 7.46 (t, J = 7.6 Hz, 1H), 6.67 (d, J = 16.0 Hz, 2H).

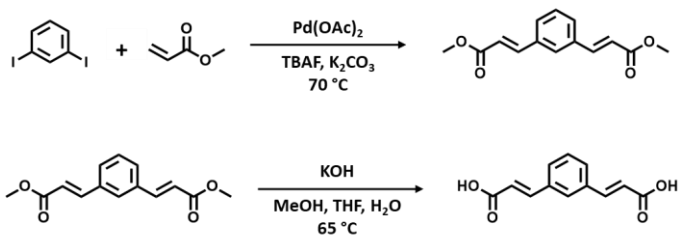

*Synthesis of 4,4'-((1E,1'E)-1,3-phenylenebis(ethene-2,1-diyl))dibenzoic acid, (**L**$^{6.2'}$):* 4-vinylbenzoic acid (0.74 g, 5 mmol), 1,3-diiodobenzene (0.74 g, 2.2 mmol), triphenylphosphine (59 mg, 0.2 mmol), 10 mL of triethylamine and palladium (II) acetate (40 mg, 0.2 mmol) were allowed to react in 20 mL THF at 80 ºC for 24 h. The obtained suspension was filtrated, and the resulting solution was evaporated under reduced pressure. The obtained solid was dissolved in 20 mL of THF and some drops of concentrated HCl (12 M) were added forming a brown suspension. The solid was recovered by centrifugation and washed with MeOH obtaining a white solid

(0.7 g; yield: 85%). ^{1}H-NMR (400 MHz, DMSO) δ 7.97 (d, J = 8.3 Hz, 5H), 7.75 (d, J = 8.3 Hz, 4H), 7.59 (d, J = 7.5 Hz, 2H), 7.44 (s, 5H).

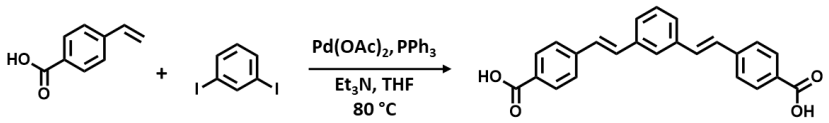

Synthesis of $Rh_{12}\mathbf{L^{6.1}}_6\mathbf{L^{6.1'}}_6$: 47 mg of $\mathbf{L^{6.1}}$ (5 eq, 0.22 mmol), 58 mg of $\mathbf{L^{6.1'}}$ (5 eq, 0.22 mmol), 23 mg of Na_2CO_3 (5 eq, 0.22 mmol), 20 mg of rhodium acetate (1 eq, 0.045 mmol) and 3.5 mL of DMA were sonicated for a few minutes and placed into a preheated oven at 100 º C for 72 h. The obtained dispersion was centrifuged to separate the Na_2CO_3. The brown solution was precipitated into 10 mL of cold MeOH. The resulting green solid was washed three times with MeOH (2 mg; yield: 6 %).

Crystallization $Rh_{12}\mathbf{L^{6.1}}_6\mathbf{L^{6.1'}}_6$: Square crystals plaques were grown under slow ether diffusion of a solution of 2 mg $Rh_{12}\mathbf{L^{6.1}}_6\mathbf{L^{6.1'}}_6$ in 0.5 mL of DMF and 120 µL of 4-*tert*-butylpyridine solution (4.9 µL 4-*tert*-butylpyridine in 1 mL DMF).

Synthesis of $Rh_{12}\mathbf{L^{6.1}}_6\mathbf{L^{6.2'}}_6$: 400 mg of $\mathbf{L^{6.2'}}$ (5 eq, 1.0 mmol), 300 mg of $\mathbf{L^{6.1}}$ (5 eq, 1.0 mmol), 115 mg of Na_2CO_3 (5 eq, 1.0 mmol), 100 mg of rhodium acetate (1 eq, 0.23 mmol) and 10 mL of DMA were sonicated for a few seconds and placed into a pre-heated oven at 100 ºC for 72 h. The obtained dispersion was centrifuged to separate the Na_2CO_3. The solution was precipitated into 60 mL of cold MeOH to obtain a green solid, which was washed three times with MeOH and one time with dichloromethane and dried in an oven at 85 ºC (62 mg; yield: 33%).

cis-Rh_2-cluster functionalized with aldehydes: 10 mg of $Rh_{12}\mathbf{L^{6.1}}_6\mathbf{L^{6.2'}}_6$ were dissolved in 1 mL of DMA. 1 mL of DMSO was then added. The resulting solution was centrifuged to remove possible particles that could not be solubilized. The ozone was bubbled for 10 min. 2.6 mL of a solution of $5 \cdot 10^{-5}$ mol/L Na_2CO_3 and 1 mL of HCl 3M were added. The obtained red solid was cleaned with the Na_2CO_3 solution and with H_2O to remove the DMSO obtaining a green solid. This green solid was dried under vacuum (2.7 mg; yield: 28 %).

Crystallization of cis-Rh_2-cluster: 2 mg of the cluster was solubilized in 0.5 mL of acetonitrile obtaining a red solution. 0.1 mL of H_2O were added. The solution was centrifuged and slowly evaporated for 32 h.

6.4.3 Crystallography

Crystallographic data for $Rh_{12}\mathbf{L^{6.1}}_6\mathbf{L^{6.1'}}_6$ and *cis*-Rh_2-cluster were collected at 100 K at XALOC beamline at ALBA synchrotron (0.82653 Å).[62] Data were indexed, integrated and scaled using the XDS program.[63] Absorption correction was not applied. The structures were solved by direct methods and subsequently refined by correction of F2 against all reflections, using SHELXT2018 within Olex2 package.[64,65] All non-hydrogen atoms were refined with anisotropic thermal parameters by full-matrix least-squares calculations on F2 using the program SHELXL2018.[64] The hydrogen atoms were calculated in their expected positions with the HFIX instruction of SHELXL2018 and refined as riding atoms with Uiso(H) = 1.5 Ueq(C). We treated the presence of solvent molecules in the cavities of all structures running solvent mask using Olex2 solvent mask.[66,67] Thermal motions of some benzene rings and pyridines coordinated to $Rh_{12}\mathbf{L^{6.1}}_6\mathbf{L^{6.1'}}_6$ were restrained by DELU, SIMU and EADP. *tert*-butyl functional group of the pyridine were disordered due to their mobility. This disorder was modeled using parts. SADI and RIGU was used to restrict the *tert*-butyl functional group of the pyridine and SADI to restrict one of the double bonds of $\mathbf{L^{6.1'}}$. DFIX was used to restrict one of the carboxylates of $\mathbf{L^{6.1'}}$. Thermal motions of one of the aldehyde groups of *cis*-Rh_2-cluster were restrained with DELU and SIMU this aldehyde group was also restricted by DFIX. Reflections where I(obs) and I(calc) differ more than 10 times Sigma (W) were omitted, (*cis*-Rh_2-cluster) (-1 0 1) (-1 1 1) (0 0 2) (0 1 2) (-2 1 2) (1 0 1) (-2 0 0) (0 2 0) (-1 2 2) (-3 1 1) (-3 0 3) (1 1 2).

$Rh_{12}\mathbf{L^{6.1}}_6\mathbf{L^{6.1'}}_6$

Formula	$C_{222}H_{186}N_6O_{48}Rh_{12}$
Formula weight ($g.mol^{-1}$)	4940.68
Temperature (K)	100
Wavelength (Å)	0.82653
Crystal system	trigonal
Space group	R-3c
Unit cell dimensions	a = 37.139; b = 37.139; c = 66.729
	α = 90°; β = 90°; γ =120°
Volume/$Å^3$	79710.8
Z	6
Density calculated (g/cm^3)	0.608
Absorption coefficient (mm^{-1})	0.394
F(000)	14904.0
Crystal size (mm)	0.08 x 0.08 x 0.06
2Theta range for data collection (°)	2.194 to 35.362
Index ranges	$0 \leq h \leq 27$, $0 \leq k \leq 15$, $-56 \leq l \leq 57$
Reflections collected	108545
Independent reflections	5801 [R_{int} = 0.1410, R_{sigma} = 0.0554]
Refinement method	Full-matrix least-squares on F2
Data / restraints / parameters	5801/80/413
Goodness-of-fit on F^2	0.935
Final R indices [I>2sigma(I)]	R_1 = 0.0833 , wR_2 = 0.2477
R indices (all data)	R_1 = 0.1057 , wR_2 = 0.2732
Largest diff. peak and hole	0.70, -0.29e $Å^{-3}$

cis-Rh_2-cluster

Formula	$C_{36}H_{21}N_2O_{12}Rh_2$
Formula weight (g.mol^{-1})	879.37
Temperature (K)	100
Wavelength (Å)	0.82653
Crystal system	monoclinic
Space group	P2/n
Unit cell dimensions	a = 12.490; b = 10.130; c = 16.270
	α = 90°; β = 110.48°; γ =90°
Volume/Å^3	1928.4
Z	2
Density calculated (g/cm^3)	1.514
Absorption coefficient (mm^{-1})	1.375
F(000)	874.0
Crystal size (mm)	0.1 x 0.1 x 0.07
2Theta range for data collection (°)	5.616 to 67.88
Index ranges	$-16 \leq h \leq 16$, $-12 \leq k \leq 12$, $-21 \leq l \leq 21$
Reflections collected	23977
Independent reflections	4287 [R_{int} = 0.0360, R_{sigma} = 0.0241]
Refinement method	Full-matrix least-squares on F2
Data / restraints / parameters	4287/14/272
Goodness-of-fit on F^2	1.095
Final R indices [I>2sigma(I)]	R_1 = 0.0459, wR_2 = 0.1437
R indices (all data)	R_1 = 0.0470, wR_2 = 0.1454
Largest diff. peak and hole	0.74, -0.89 e Å^{-3}

6.4.3 Characterization

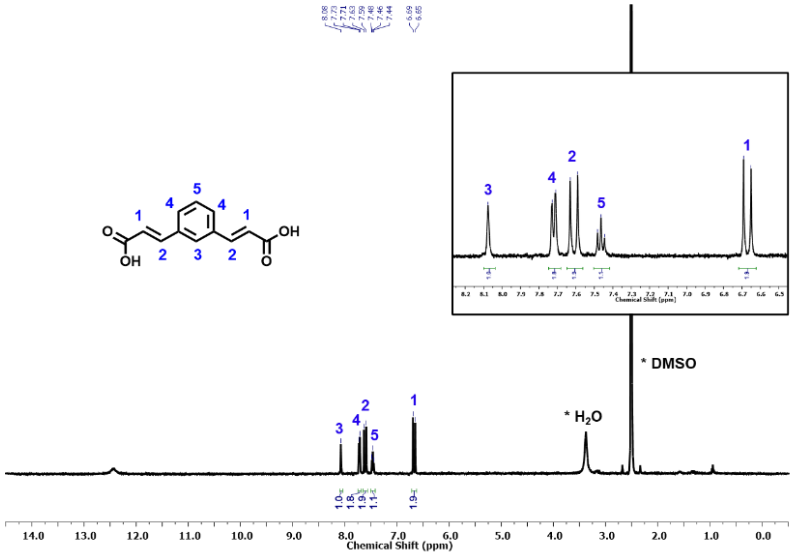

Figure S6.1. ^{1}H-NMR spectrum (400 MHz, DMSO-d_6) of **L$^{6.1}$'**.

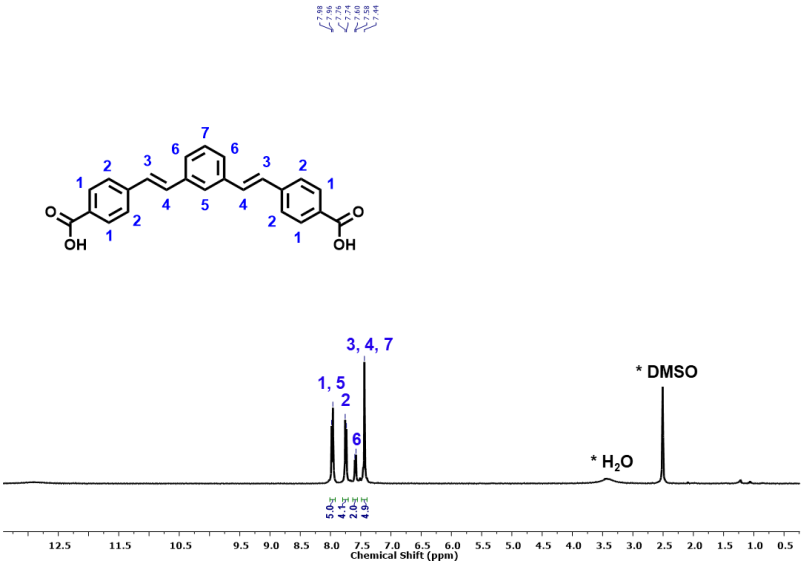

Figure S6.2. ^{1}H-NMR spectrum (400 MHz, DMSO-d_6) of **L$^{6.2}$'**.

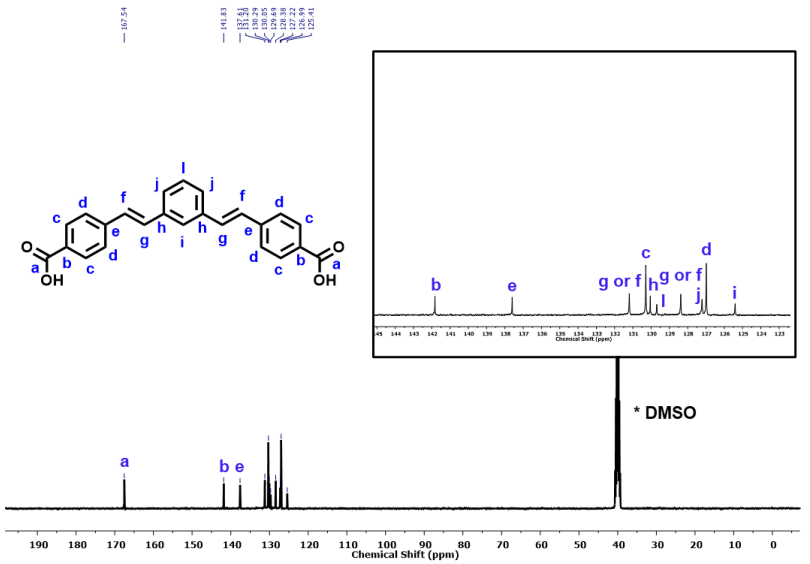

Figure S6.3. ^{13}C-NMR spectrum (400 MHz, DMSO-d_6) of **L$^{6.2'}$**.

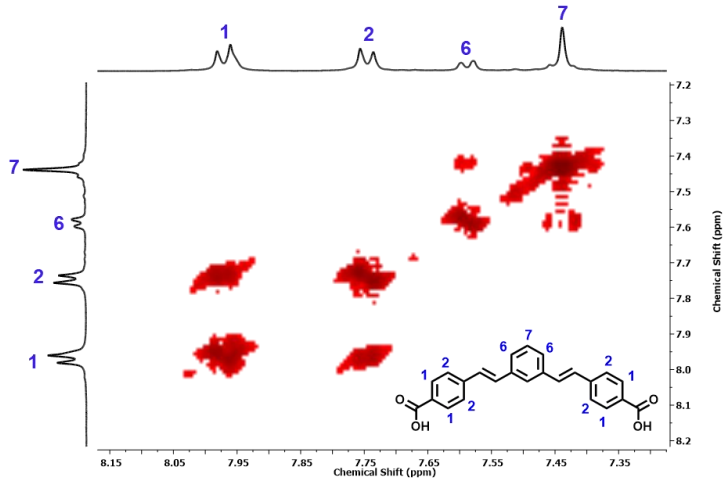

Figure S6.4. COSY spectrum (400 MHz, DMSO-d_6) of $\mathbf{L}^{6.2'}$.

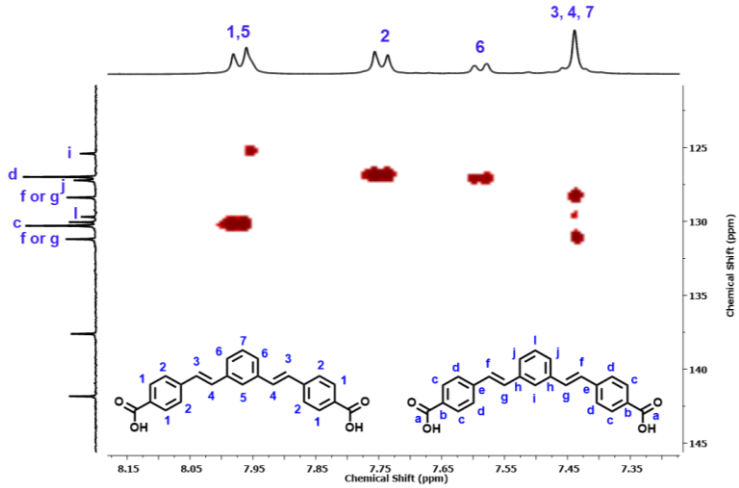

Figure S6.4. HSQC spectrum (400 MHz, DMSO-d_6) of $\mathbf{L}^{6.2'}$.

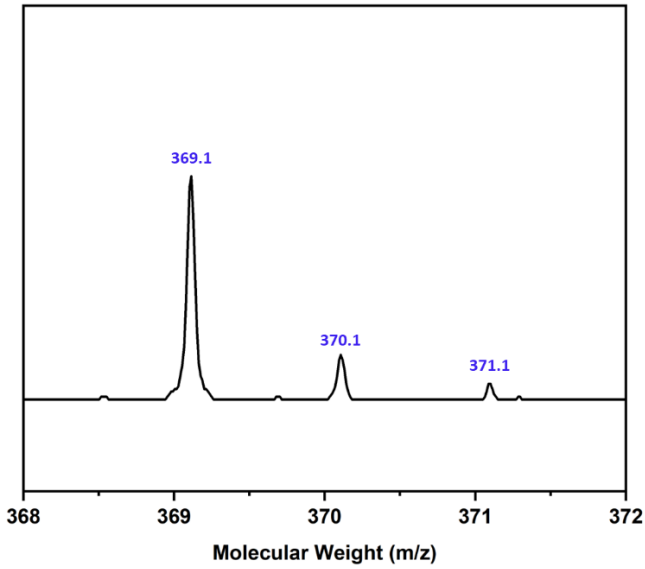

Figure S6.5. Low-resolution ESI-MS spectrometry of $\mathbf{L^{6.2'}}$. The molecular weight corresponding to $\mathbf{L^{6.2'}}$ has been highlighted. The peak at m/z = 369.1 is assigned to $[C_{24}H_{18}O_4 - H]^-$: expected = 369.1.

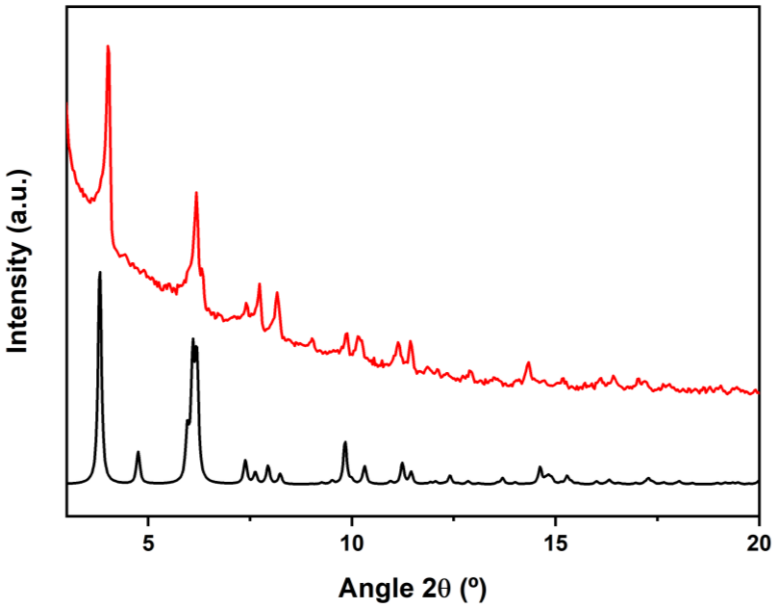

Figure S6.6. Simulated PXRD diffractogram from $Rh_{12}\mathbf{L^{6.1}}_6\mathbf{L^{6.1'}}_6$ crystal structure (black) and experimental PXRD diffractogram of $Rh_{12}\mathbf{L^{6.1}}_6\mathbf{L^{6.1'}}_6$ (red).

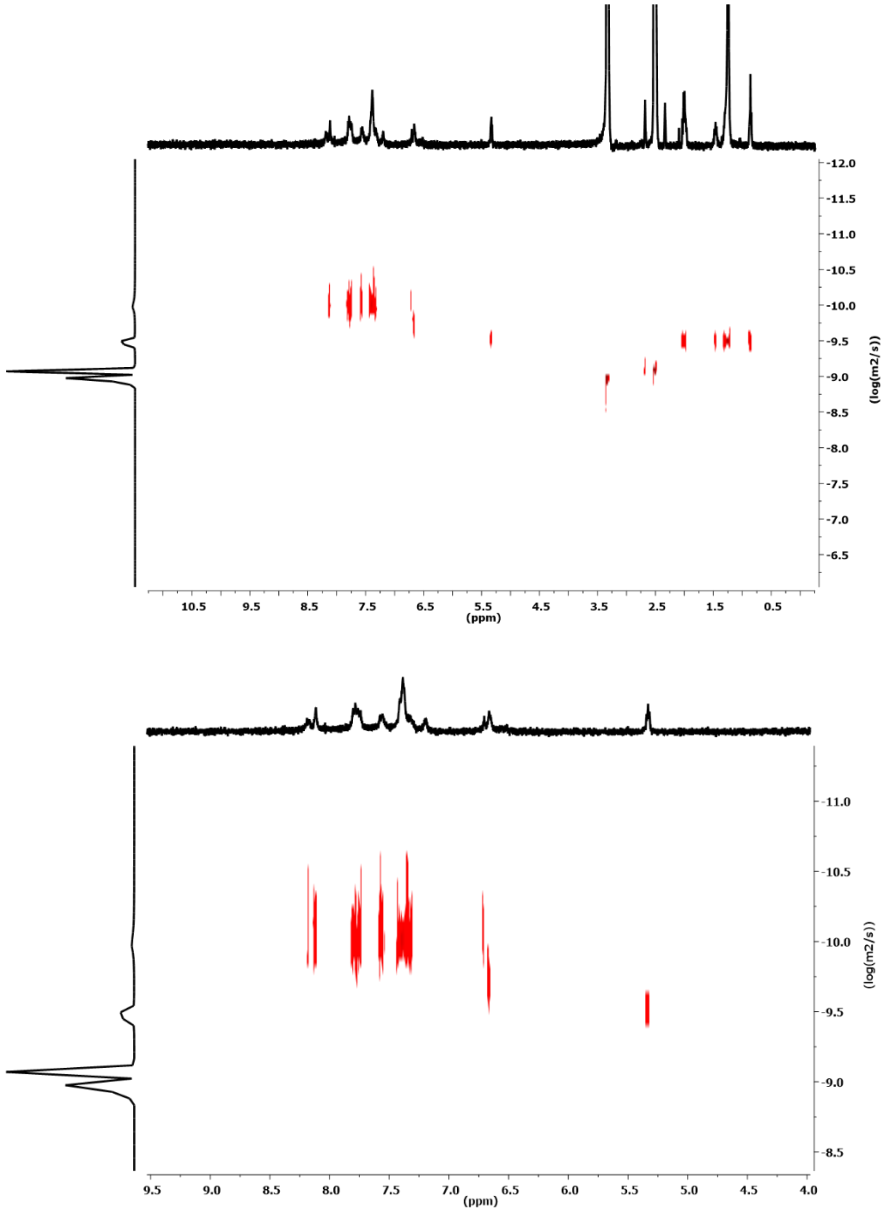

Figure S6.7. DOSY spectrum (400 MHz, DMSO-d_6) of $Rh_{12}\mathbf{L}^{\mathbf{6.1}}{}_6\mathbf{L}^{\mathbf{6.1'}}{}_6$.

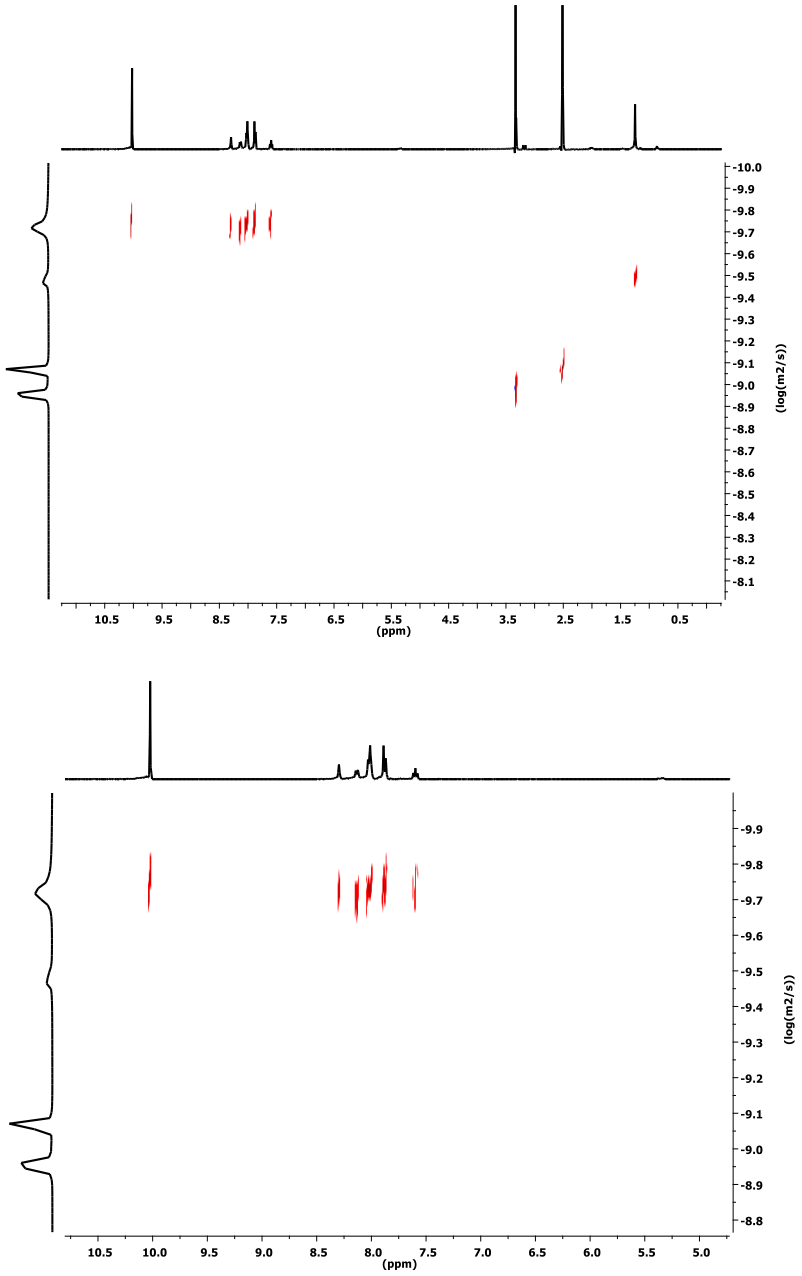

Figure S6.8. DOSY spectrum (400 MHz, DMSO-d_6) of *cis*-Rh_2-cluster.

Chapter 7

Conclusions

The main achievement of this Thesis has been to prove the feasibility of Clip-off Chemistry with the synthesis of a series of Rh_2-complexes from Rh_2-MOPs. Clip-off Chemistry is a novel synthetic methodology that involves the selective, rational cleavage of covalent bonds in pre-existing reticular materials.

Thus, to demonstrate the feasibility of our Clip-off Chemistry approach, we initially synthesized an homoleptic Rh_2-cluster by cleaving an homoleptic Rh_2-MOP precursor. For this, we first designed and synthesized a new lantern Rh_2-MOP with olefinic bonds in known crystallographic positions. Subsequently, ozonolysis was applied to this MOP precursor to produce the desired homoleptic Rh_2-cluster. From the ozonolysis reaction, a mixture of Rh_2-clusters functionalized with different amounts of aldehyde and carboxylic acid groups was initially obtained. However, this reaction crude was successfully purified by adding a basic aqueous solution. Under these conditions, we could isolate the homoleptic Rh_2-clusters fully functionalized with aldehyde groups.

After validating our Clip-off synthetic methodology, we expanded it to the synthesis of more complex structures. To do so, we first synthesized a new family of mixed-ligand Rh_2-MOPs, increasing the diversity of compounds suitable to be synthesized through Clip-off Chemistry. This new family of MOPs consists of 12 trigonal antiprismatic MOPs, each formed by six Rh_2-paddlewheel clusters, six ligands with a bridging angle of 90° and six ligands with a bridging angle of 120°. The trigonal antiprisms are formed by two trigonal macrocycles, each one built up from connecting three metal clusters through three ligands of the same type. Both trigonal macrocycles, which form the top and bottom facets of the antiprism, are connected through six ligands of the other type. Depending on the positions occupied by each kind of ligand, two possible isomers can be formed. Remarkably, we could

isolate these two isomers. Moreover, all these MOPs are microporous in the solid state, enlarging the still short-list of porous cages.

Once we synthesized these mixed-ligand Rh_2-MOPs, we proceeded to use them as precursors of our Clip-off Chemistry approach. We postulate that different types of Rh_2-complexes could be synthesized depending on the positions of the olefinic bonds within the MOP: (1) if the cleavable bonds are located in the equatorial positions of the MOP, a Rh_2-macrocycle can be synthesized; (2) if the cleavable bonds are located in the axial positions of the MOP, a Rh_2-crown type structure can be synthesized; and finally, (3) if the cleavable bonds are located in both axial and equatorial positions of the MOP, a mixed-ligand Rh_2-cluster can be synthesized. All these types of Rh_2-complexes are very difficult or impossible to synthesize by direct synthesis, as it would be very unlikely that the building blocks could be spontaneously assembled in this way.

We began by cleaving one of the previously synthesized antiprismatic Rh_2-MOPs with olefinic bonds in the equatorial positions. By cleaving this MOP in half, we were able to successfully synthesize a triangular Rh_2-macrocycle. Initially, a mixture of Rh_2-macrocycles with different amounts of aldehyde and carboxylic acid groups was obtained. Finally, we were able to obtain the Rh_2-macrocycle fully functionalized with carboxylic acid groups by performing the ozonolysis reaction under oxidative conditions.

Finally, we successfully synthesized a *cis*-Rh_2-cluster by the Clip-off cleavage of a trigonal antiprismatic Rh_2-MOP with olefinic bonds in both of its ligands. First, using reticular chemistry, we synthesized a trigonal antiprismatic Rh_2-MOP in which both types of ligands contained olefinic bonds. Then, we cleaved this new MOP releasing the expected *cis*-Rh_2-cluster fully functionalized with aldehyde groups.

In conclusion, we have successfully synthesized an homoleptic Rh_2-cluster, a Rh_2-macrocycle and a *cis*-Rh_2-cluster by selectively cleaving different kinds of Rh_2-MOPs. In these examples, we demonstrated that the cleavage in MOPs can be quantitative and selective. These results suggest that Clip-off Chemistry is ripe for further exploration. Clip-off Chemistry methodology offers the possibility to synthesize new molecules and materials via the controlled cleavage of MOPs, cages or other kinds of reticular materials. This cleavage can be carried out by ozonolysis or other reactions involving the cleavage of bonds (*e.g.*, photolysis). In summary, our results prove that controlled cleavage of reticular materials is feasible, and that Clip-off Chemistry could provide researchers with access to a myriad of new molecular architectures.

References

(1) A. J. Ihde, *J. Chem. Educ.*, 1956, **33**, 107–110.

(2) R. P. Feynman, *J. Microelectromech. Syst.*, 1995, **1**, 60–66.

(3) B. F. Hoskins and R. Robson, *J. Am. Chem. Soc.*, 1990, **112**, 1546–1554.

(4) A. F. Wells, *Structural Inorganic Chemistry*, Oxford Science Publications, 5th Ed., **1984**.

(5) B. F. Hoskins and R. Robson, *J. Am. Chem. Soc.*, 1989, **111**, 5962–5964.

(6) F. Containing and L. Rectangular, *J. Am. Chem. Soc.*, 1995, **117**, 10401–10402.

(7) O. M. Yaghi, M. J. Kalmutzki and C. S. Diercks, *Introduction to Reticular Chemistry: Metal-Organic Frameworks and Covalent Organic Frameworks*, Wiley, 1st Ed., **2019**.

(8) B. F. Abrahams, B. F. Hoskins, D. M. Michail and R. Robson, *Nature*, 1994, **369**, 727–729.

(9) M. Fujita, S. Washizu, K. Ogura and Y. J. Kwon, *J. Am. Chem. Soc.*, 1994, **116**, 1151–1152.

(10) R. W. Gable, B. F. Hoskins and R. Robson, *J. Chem. Soc., Chem. Commun.*, 1990, **96**, 762–763.

(11) H. Li, M. Eddaoudi, T. L. Groy and O. M. Yaghi, *J. Am. Chem. Soc.*, 1998, **120**, 8571–8572.

(12) A. Schoedel and S. Rajeh, *Top. Curr. Chem.*, 2020, **378**, 1–55.

(13) M. Eddaoudi, J. Kim, N. Rosi, D. Vodak, J. Wachter, M. O. Keeffe and O. M. Yaghi, *Science*, 2002, **295**, 32–34.

(14) N. W. Ockwig, M. O. Keeffe, A. J. Matzger and O. M. Yaghi, *Science*, 2005, **310**, 1166–1171.

(15) Y. Li, D. Zhang, F. Gai, X. Zhu, Y. N. Guo, T. Ma, Y. Liu and Q. Huo, *Chem. Commun.*, 2012, **48**, 7946–7948.

(16) M. A. Andrés, A. Carné-Sánchez, J. Sánchez-Laínez, O. Roubeau, J. Coronas, D. Maspoch and I. Gascón, *Chem. - Eur. J.*, 2020, **26**, 143–147.

(17) L. Hernández-López, J. Martínez-Esaín, A. Carné-Sánchez, T. Grancha, J. Faraudo and D. Maspoch, *Angew. Chem., Int. Ed.*, 2021, **60**, 11406–11413.

(18) T. Grancha, A. Carné-Sánchez, L. Hernández-López, J. Albalad, I. Imaz, J. Juanhuix and D. Maspoch, *J. Am. Chem. Soc.*, 2019, **141**, 18349–18355.

(19) A. Carné-Sánchez, J. Albalad, T. Grancha, I. Imaz, J. Juanhuix, P. Larpent, S. Furukawa and D. Maspoch, *J. Am. Chem. Soc.*, 2019, **141**, 4094–4102.

(20) J. Albalad, A. Carné-Sánchez, T. Grancha, L. Hernández-López and D. Maspoch, *Chem. Commun.*, 2019, **55**, 12785–12788.

(21) M. Eddaoudi, J. Kim, J. B. Wachter, H. K. Chae, M. O'Keeffe and O. M. Yaghi, *J. Am. Chem. Soc.*, 2001, **123**, 4368–4369.

(22) C. Avci, J. Ariñez-Soriano, A. Carné-Sánchez, V. Guillerm, C. Carbonell, I. Imaz and D. Maspoch, *Angew. Chem., Int. Ed.*, 2015, **54**, 14417–14421.

(23) S. Jeoung, I. T. Ju, J. H. Kim, S. H. Joo and H. R. Moon, *J. Mater. Chem. A*, 2018, **6**, 18906–18911.

(24) Z. Ou, X. Song, W. Huang, X. Jiang, S. Qu, Q. Wang, P. V. Braun, J. S. Moore, X. Li and Q. Chen, *ACS Appl. Mater. Interfaces*, 2018, **10**, 40990–40995.

(25) W. Liu, J. Huang, Q. Yang, S. Wang, X. Sun, W. Zhang, J. Liu and F. Huo, *Angew. Chem., Int. Ed.*, 2017, **56**, 5512–5516.

(26) M. Hu, Y. Ju, K. Liang, T. Suma, J. Cui and F. Caruso, *Adv. Funct. Mater.*, 2016, **26**, 5827–5834.

(27) M. Hu, S. Furukawa, R. Ohtani, H. Sukegawa, Y. Nemoto, J. Reboul, S. Kitagawa and Y. Yamauchi, *Angew. Chem.*, 2012, **124**, 1008–1012.

(28) Y. Kim, T. Yang, G. Yun, M. B. Ghasemian, J. Koo, E. Lee, S. J. Cho and K. Kim, *Angew. Chem., Int. Ed.*, 2015, **54**, 13273–13278.

(29) J. Koo, I. C. Hwang, X. Yu, S. Saha, Y. Kim and K. Kim, *Chem. Sci.*, 2017, **8**, 6799–6803.

(30) S. C. Qi, X. Y. Qian, Q. X. He, K. J. Miao, Y. Jiang, P. Tan, X. Q. Liu and L. B. Sun, *Angew. Chem., Int. Ed.*, 2019, **58**, 10104–10109.

(31) H. F. Drake, G. S. Day, S. W. Vali, Z. Xiao, S. Banerjee, J. Li, E. A. Joseph, J. E. Kuszynski, Z. T. Perry, A. Kirchon, O. K. Ozdemir, P. A. Lindahl and H. C. Zhou, *Chem. Commun.*, 2019, **55**, 12769–12772.

(32) P. Yang, F. Mao, Y. Li, Q. Zhuang and J. Gu, *Chem. - Eur. J.*, 2018, **24**, 2962–2970.

(33) S. Yuan, L. Zou, J. S. Qin, J. Li, L. Huang, L. Feng, X. Wang, M. Bosch, A. Alsalme, T. Cagin and H. C. Zhou, *Nat. Commun.*, 2017, **8**, 15356.

(34) L. Feng, S. Yuan, L. L. Zhang, K. Tan, J. L. Li, A. Kirchon, L. M. Liu, P. Zhang, Y. Han, Y. J. Chabal and H. C. Zhou, *J. Am. Chem. Soc.*, 2018, **140**, 2363–2372.

(35) V. Guillerm, H. Xu, J. Albalad, I. Imaz and D. Maspoch, *J. Am. Chem. Soc.*, 2018, **140**, 15022–15030.

(36) Y. Yang, A. Broto-Ribas, B. Ortín-Rubio, I. Imaz, F. Gándara, A. Carné-Sánchez, V. Guillerm, S. Jurado, F. Busqué, J. Juanhuix and D. Maspoch, *Angew. Chem., Int. Ed.*, 2022, **61**, e202111228.

(37) C. F. Schonbein, *J. Prakt. Chem.*, 1855, **66**.

(38) A. Houzeau, *Compt. rend.*, 1873, **76**.

(39) Dibckhoff, *Habilitationsschrift*, 1891, **56**.

(40) R. Criegee, *Angew. Chem., Int. Ed.*, 1975, **14**, 745–752.

(41) T. J. Fisher and P. H. Dussault, *Tetrahedron*, 2017, **73**, 4233–4258.

(42) L. R. Dix, J. R. Ebdon, N. J. Flinx and P. Hodge, *Eur. Polym. J.*, 1991, **27**, 581–588.

(43) W. T. M. Oligo-n, *J. Polym. Sci., Part A Polym. Chem.*, 1995, **33**, 593–597.

(44) D. M. Walba, R. M. Richards and R. C. Haltiwanger, *J. Am. Chem. Soc.*, 1982, **104**, 3219–3221.

(45) D. M. Walba, J. D. Armstrong III, A. E. Perry, R. M. Richards, T. C. Homan and R. C. Haltiwanger, *Tetrahedron*, 1986, **42**, 1883–1894.

(46) D. M. Walba, R. M. Richards and R. C. Haltiwanger, *J. Am. Chem. Soc.*, 1982, **104**, 3219–3221.

(47) J. Albalad, H. Xu, F. Gándara, M. Haouas, C. Martineau-Corcos, R. Mas-Ballesté, S. A. Barnett, J. Juanhuix, I. Imaz and D. Maspoch, *J. Am. Chem. Soc.*, 2018, **140**, 2028–2031.

(48) V. Guillerm, H. Xu, J. Albalad, I. Imaz and D. Maspoch, *J. Am. Chem. Soc.*, 2018, **140**, 15022–15030.

(49) B. Moulton, J. Lu, A. Mondal and M. J. Zaworotko, *Chem. Commun.*, 2001, **2**, 863–864.

(50) Z. Ni, A. Yassar, T. Antoun and O. M. Yaghi, *J. Am. Chem. Soc.*, 2005, **127**, 12752–12753.

(51) G. A. Craig, P. Larpent, S. Kusaka, R. Matsuda, S. Kitagawa and S. Furukawa, *Chem. Sci.*, 2018, **9**, 6463–6469.

(52) S. Kuwatan and R. Maehana, *Bull. Chem. Soc. Jpn.*, 2009, **1476**, 1470–1476.

(53) C. von Baeckmann, S. Ruiz-Relaño, I. Imaz, M. Handke, J. Juanhuix, F. Gándara, A. Carné-Sanchez and D. Maspoch, *Chem. Commun.*, 2023, **59**, 3423–3426.

(54) R. P. Bonar-Law, T. D. McGrath, N. Singh, J. F. Bickley and A. Steiner, *Chem. Commun.*, 1999, **8**, 2457–2458.

(55) S. Furukawa, N. Horike, M. Kondo, Y. Hijikata, A. Carné-Sánchez, P. Larpent, N. Louvain, S. Diring, H. Sato, R. Matsuda, R. Kawano and S. Kitagawa, *Inorg. Chem.*, 2016, **55**, 10843–10846.

(56) T. L. Jacobs, *J. Am. Chem. Soc.*, 1936, **58**, 2272–2273.

(57) E. Warzecha, T. C. Berto, C. C. Wilkinson and J. F. Berry, *J. Chem. Educ.*, 2019, **96**, 571–576.

(58) M. Higuchi, K. Matsuda, T. Hirose, P. Larpent, K. Urayama, A. Carné-Sánchez, G. A. Craig, S. Furukawa and S. Kitagawa, *Nat. Commun.*, 2018, **9**, 1–8.

(59) D. Cremer, R. Crehuet and J. Anglada, *J. Am. Chem. Soc.*, 2001, **123**, 6127–6141.

(60) A. Carné-Sánchez, G. A. Craig, P. Larpent, V. Guillerm, K. Urayama, D. Maspoch and S. Furukawa, *Angew. Chem., Int. Ed.*, 2019, **131**, 6413–6416.

(61) Bruker. APEX2, SAINT SADABS; Bruker AXS Inc. Madison, Wisconsin, USA 2012.

(62) J. Juanhuix, F. Gil-Ortiz, G. Cuní, C. Colldelram, J. Nicolás, J. Lidón, E. Boter, C. Ruget, S. Ferrer and J. Benach, *J. Synchrotron Radiat.*, 2014, **21**, 679–689.

(63) W. Kabsch, *Acta Crystallogr., Sect. D: Biol. Crystallogr.*, 2010, **66**, 125–132.

(64) G. M. Sheldrick, *Acta Crystallogr., Sect. C: Struct. Chem.*, 2015, **71**, 3–8.

(65) L. J. J. Farrugia, *J. Appl. Crystallogr.*, 2012, **45**, 849–854.

(66) H. Dolomanov, O. V. Bourhis, L. J. Gildea, R. J. Howard, J. A. K. Puschmann, *J. Appl. Crystallogr.*, 2009, **42**, 339–341.

(67) A. Spek, *Acta Crystallogr., Sect. D: Biol. Crystallogr.*, 2003, **36**, 7–13.

(68) G. Liu, Y. Di Yuan, J. Wang, Y. Cheng, S. B. Peh, Y. Wang, Y. Qian, J. Dong, D. Yuan and D. Zhao, *J. Am. Chem. Soc.*, 2018, **140**, 6231–6234.

(69) S. Lee, H. Jeong, D. Nam, M. S. Lah and W. Choe, *Chem. Soc. Rev.*, 2021, **50**, 528–555.

(70) E. J. Gosselin, C. A. Rowland and E. D. Bloch, *Chem. Rev.*, 2020, **120**, 8987–9014.

(71) G. Liu, Z. Ju, D. Yuan and M. Hong, *Inorg. Chem.*, 2013, **52**, 13815–13817.

(72) J. R. Li, A. A. Yakovenko, W. Lu, D. J. Timmons, W. Zhuang, D. Yuan and H. C. Zhou, *J. Am. Chem. Soc.*, 2010, **132**, 17599–17610.

(73) J. Park, Z. Perry, Y. P. Chen, J. Bae and H. C. Zhou, *ACS Appl. Mater. Interfaces*, 2017, **9**, 28064–28068.

(74) Z. Ju, G. Liu, Y. S. Chen, D. Yuan and B. Chen, *Chem. - Eur. J.*, 2017, **23**, 4774–4777.

(75) L. J. Cheng, X. X. Fan, Y. P. Li, Q. H. Wei, F. R. Dai, Z. N. Chen and Z. Wang, *Inorg. Chem. Commun.*, 2017, **78**, 61–64.

(76) K. Su, F. Jiang, J. Qian, L. Chen, J. Pang, S. M. Bawaked, M. Mokhtar, S. A. Al-Thabaiti and M. Hong, *Inorg. Chem.*, 2015, **54**, 3183–3188.

(77) D. Geng, X. Han, Y. Bi, Y. Qin, Q. Li, L. Huang, K. Zhou, L. Song and Z. Zheng, *Chem. Sci.*, 2018, **9**, 8535–8541.

(78) Z. Lu, C. B. Knobler, H. Furukawa, B. Wang, G. Liu and O. M. Yaghi, *J. Am. Chem. Soc.*, 2009, **131**, 12532–12533.

(79) H. Furukawa, U. Müller and O. M. Yaghi, *Angew. Chem., Int. Ed.*, 2015, **54**, 3417–3430.

(80) S. Pullen and G. H. Clever, *Acc. Chem. Res.*, 2018, **51**, 3052–3064.

(81) S. Pullen, J. Tessarolo and G. H. Clever, *Chem. Sci.*, 2021, **12**, 7269–7293.

(82) D. Fujita, K. Suzuki, S. Sato, M. Yagi-Utsumi, Y. Yamaguchi, N. Mizuno, T. Kumasaka, M. Takata, M. Noda, S. Uchiyama, K. Kato and M. Fujita, *Nat. Commun.*, 2012, **3**, 2–8.

(83) A. M. Johnson and R. J. Hooley, *Inorg. Chem.*, 2011, **50**, 4671–4673.

(84) D. Preston, J. E. Barnsley, K. C. Gordon and J. D. Crowley, *J. Am. Chem. Soc.*, 2016, **138**, 10578–10585.

(85) S. E. Walker, S. A. Boer, T. Malcomson, M. J. Paterson, K. L. Tuck and D. R. Turner, *Chem. Commun.*, 2021, **57**, 12456–12459.

(86) R. Zhu, W. M. Bloch, J. J. Holstein, S. Mandal, L. V. Schäfer and G. H. Clever, *Chem. - Eur. J.*, 2018, **24**, 12976–12982.

(87) Y. Liu, S. Liao, W. Dai, Q. Bai, S. Lu, H. Wang, X. Li, Z. Zhang, P. Wang, W. Lu and Q. Zhang, *Angew. Chem.*, 2023, **135**, e202217215.

(88) Q.-F. Sun, S. Sato and M. Fujita, *Angew. Chem.*, 2014, **126**, 13728–13731.

(89) J. R. Li and H. C. Zhou, *Nat. Chem.*, 2010, **2**, 893–898.

(90) S. Saha, B. Holzapfel, Y. T. Chen, K. Terlinden, P. Lill, C. Gatsogiannis, H. Rehage and G. H. Clever, *J. Am. Chem. Soc.*, 2018, **140**, 17384–17388.

(91) W. M. Bloch, Y. Abe, J. J. Holstein, C. M. Wandtke, B. Dittrich and G. H. Clever, *J. Am. Chem. Soc.*, 2016, **138**, 13750–13755.

(92) R. J. Li, J. Tessarolo, H. Lee and G. H. Clever, *J. Am. Chem. Soc.*, 2021, **143**, 3865–3873.

(93) J. Tessarolo, E. Benchimol, A. Jouaiti, M. W. Hosseini and G. H. Clever, *Chem. Commun.*, 2023, **4**, 3467–3470.

(94) K. E. Ebbert, L. Schneider, A. Platzek, C. Drechsler, B. Chen, R. Rudolf and G. H. Clever, *Dalton Trans.*, 2019, **48**, 11070–11075.

(95) K. Wu, J. Tessarolo, A. Baksi and G. H. Clever, *Angew. Chem., Int. Ed.*, 2022, **61**, 1–7.

(96) A. Platzek, S. Juber, C. Yurtseven, S. Hasegawa, L. Schneider, C. Drechsler, K. E. Ebbert, R. Rudolf, Q. Q. Yan, J. J. Holstein, L. V. Schäfer and G. H. Clever, *Angew. Chem., Int. Ed.*, 2022, **61**, 1–7.

(97) K. Wu, B. Zhang, C. Drechsler, J. J. Holstein and G. H. Clever, *Angew. Chem., Int. Ed.*, 2021, **60**, 6403–6407.

(98) W. M. Bloch, J. J. Holstein, W. Hiller and G. H. Clever, *Angew. Chem., Int. Ed.*, 2017, **56**, 8285–8289.

(99) S. Sudan, R. J. Li, S. M. Jansze, A. Platzek, R. Rudolf, G. H. Clever, F. Fadaei-Tirani, R. Scopelliti and K. Severin, *J. Am. Chem. Soc.*, 2021, **143**, 1773–1778.

(100) M. Do, D. Rogers, W. Kaminsky and D. J. Xiao, *Inorg. Chem.*, 2021, **60**, 7602–7606.

(101) N. Hosono, K. Omoto and S. Kitagawa, *Chem. Commun.*, 2017, **53**, 8180–8183.

(102) K. Omoto, N. Hosono, M. Gochomori, K. Albrecht, K. Yamamoto and S. Kitagawa, *Chem. Commun.*, 2018, **54**, 5209–5212.

(103) J. R. Li and H. C. Zhou, *Angew. Chem., Int. Ed.*, 2009, **48**, 8465–8468.

(104) R. J. Li, F. Fadaei-Tirani, R. Scopelliti and K. Severin, *Chem. - Eur. J.*, 2021, **27**, 9439–9445.

(105) A. Carné-Sánchez, J. Albalad, P. Larpent, S. Furukawa, J. Juanhuix, I. Imaz, D. Maspoch and T. Grancha, *J. Am. Chem. Soc.*, 2019, **141**, 4094–4102.

(106) S. Furukawa, N. Horike, M. Kondo, Y. Hijikata, A. Carné-Sánchez, P. Larpent, N. Louvain, S. Diring, H. Sato, R. Matsuda, R. Kawano and S. Kitagawa, *Inorg. Chem.*, 2016, **55**, 10843–10846.

(107) Y. Ke, D. J. Collins and H. C. Zhou, *Inorg. Chem.*, 2005, **44**, 4154–4156.

(108) S. S. Mishra, S. V. K. Kompella, S. Krishnaswamy, S. Balasubramanian and D. K. Chand, *Inorg. Chem.*, 2020, **59**, 12884–12894.

(109) D. Ogata and J. Yuasa, *Angew. Chem.*, 2019, **131**, 18595–18599.

(110) A. Tarzia, J. E. M. Lewis and K. E. Jelfs, *Angew. Chem.*, 2021, **133**, 21047–21055.

(111) H. Yu, J. Li, C. Shan, T. Lu, X. Jiang, J. Shi, L. Wojtas, H. Zhang and M. Wang, *Angew. Chem., Int. Ed.*, 2021, **60**, 26523–26527.

(112) J. E. M. Lewis, A. Tarzia, A. J. P. White and K. E. Jelfs, *Chem. Sci.*, 2020, **11**, 677–683.

(113) J. E. M. Lewis, *Chem. - Eur. J.*, 2021, **27**, 4454–4460.

(114) R. A. S. Vasdev, D. Preston, C. A. Casey-stevens, V. Mart, P. J. Lusby, A. L. Garden and J. D. Crowley, *Inorg. Chem.*, 2023, **62**, 1833−1844.

(115) R. Li, A. Tarzia, V. Posligua, K. E. Jelfs, N. Sanchez, A. Marcus, A. Baksi, G. H. Clever, F. Fadaei-Tirani and K. Severin, *Chem. Sci.*, 2022, **13**, 11912–11917.

(116) R. J. Li, A. Marcus, F. Fadaei-Tirani and K. Severin, *Chem. Commun.*, 2021, **57**, 10023–10026.

(117) H. Dasary, R. Jagan and D. K. Chand, *Inorg. Chem.*, 2018, **57**, 12222–12231.

(118) A. P. Birvé, H. D. Patel, J. R. Price, W. M. Bloch and T. Fallon, *Angew. Chem., Int. Ed.*, 2022, **61**, e202115468.

(119) A. W. Markwell-Heys, M. L. Schneider, J. M. L. Madridejos, G. F. Metha and W. M. Bloch, *Chem. Commun.*, 2021, **57**, 2915–2918.

(120) A. Broto-Ribas, M. S. Gutiérrez, I. Imaz, A. Carné-Sánchez, F. Gándara, J. Juanhuix and D. Maspoch, *Chem. Commun.*, 2022, **58**, 10480–10483.

(121) M. Fujita, *Acc. Chem. Res.*, 1999, **32**, 53–61.

(122) M. H. Chisholm, F. A. Cotton, L. M. Daniels, K. Folting, J. C. Hu, S. S. Iyer, C. Lin, M. Macintosh and C. A. Murillo, *Dalton Trans.*, 1999, **2**, 1387–1391.

(123) F. A. Cotton, J. P. Donahue, C. Lin and C. A. Murillo, *Inorg. Chem.*, 2001, **40**, 1234–1244.

(124) Q. Liang, M. Zhang, Z. Zhang, C. Liu, S. Xu and Z. Li, *J. Alloy. Compd.*, 2017, **690**, 123–130.

(125) F. A. Cotton, L. M. Daniels, C. Lin and C. A. Murillo, *J. Am. Chem. Soc.*, 1999, **121**, 4538–4539.

(126) F. A. Cotton, C. Lin and C. A. Murillo, *Inorg. Chem.*, 2001, **40**, 575–577.

(127) M. M. Deegan and E. D. Bloch, *Dalton Trans.*, 2021, **50**, 3127–3131.

(128) F. A. Cotton, C. Lin and C. A. Murillo, *Inorg. Chem.*, 2001, **40**, 472–477.

(129) M. Köberl, M. Cokoja, W. A. Herrmann and F. E. Kühn, *Dalton Trans.*, 2011, **40**, 6834–6859.

(130) F. A. Cotton, C. Lin and C. A. Murillo, *Chem. Commun.*, 2001, **708**, 11–12.

(131) F. A. Cotton, L. M. Daniels, C. Lin and C. A. Murillo, *Chem. Commun.*, 1999, 841–842.

(132) A. A. Ageshina, M. A. Uvarova and S. E. Nefedov, Russ. *J. Inorg. Chem.*, 2015, **60**, 1085–1092.

(133) Y. Sekine, W. Kosaka, H. Kano, C. Dou, T. Yokoyama and H. Miyasaka, *Dalton Trans.*, 2016, **45**, 7427–7434.

(134) M. H. Chisholm, A. S. Dann, F. Dielmann, J. C. Gallucci, N. J. Patmore, R. Ramnauth and M. Scheer, *Inorg. Chem.*, 2008, **47**, 9248–9255.

(135) Y. Lou, T. P. Remarchuk and E. J. Corey, *J. Am. Chem. Soc.*, 2005, **127**, 14223–14230.

(136) B. G. Anderson, D. Cressy, J. J. Patel, C. F. Harris, G. P. A. Yap, J. F. Berry and A. Darko, *Inorg. Chem.*, 2019, **58**, 1728–1732.

(137) F. P. Caló and A. Fürstner, *Angew. Chem., Int. Ed.*, 2020, **59**, 13900–13907.

(138) M. Ebihara, M. Nomura, S. Sakai and T. Kawamura, *Inorg. Chim. Acta*, 2007, **360**, 2345–2352.

(139) F. A. Cotton and J. L. Thompson, *Inorg. Chim. Acta*, 1984, **81**, 193–203.

Glossary

Acronyms and abbreviations

Acronyms and abbreviations

AZDC	Azobenzene-4,40-dicarboxylate
BDC	1,4-Benzenedicarboxylate
BDBA	Benzene-1,4-diboronic acid
CBAB	4-Carboxybenzylidene-4-aminobenzate
COFs	Covalent Organic Frameworks
COSY	Homonuclear correlation spectroscopy
DMA	*N*,*N*-Dimethylacetamide
DMF	*N*,*N*-Dimethylformamide
DMSO	Dimethyl sulfoxide
DOSY	Diffusion-Ordered Spectroscopy
ESI-MS	Electro-Spray Ionisation Mass Spectroscopy
SBUs	Secondary Building Units
S_{BET}	Brunauer-Emmett-Teller surface areas
HHTP	2,3,6,7,10,11-Hexahydroxytriphenylene
HKUST	Hong Kong University of Science and Technology
HSQC	Heteronuclear Single Quantum Coherence
IRMOFs	Isoreticular Metal-Organic Frameworks

MALDI-TOF	Matrix-Assisted Laser Desorption/Ionization coupled to Time-of-flight detector
MIL	Material Institut Lavoisier
MOF	Metal-Organic-Framework
MOP	Metal-Organic Polyhedra
NMR	Nuclear Magnetic Resonance
PB	Prussian Blue
PVP	Polyvinylpyrrolidone
PXRD	Powder X-ray diffraction
Rh_2-MOP	Rh(II)-based Metal-Organic Polyhedra
SCXRD	Single-crystal X-ray diffraction
THF	Tetrahydrofuran
UV-vis	Ultraviolet-visible spectroscopy
ZIF	Zeolitic Imidazolate Framework

Annex 1

Names of ligands and MOPs

Chapter 3

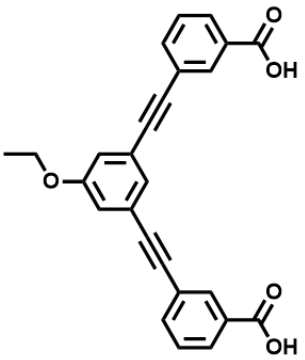

$L^{3.1}$

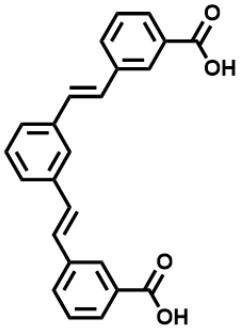

$L^{3.2}$

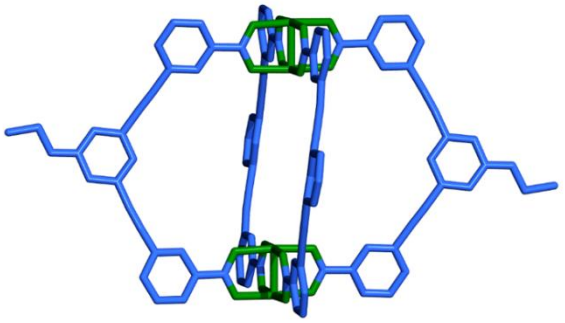

$Rh_4L^{3.1}{}_4$

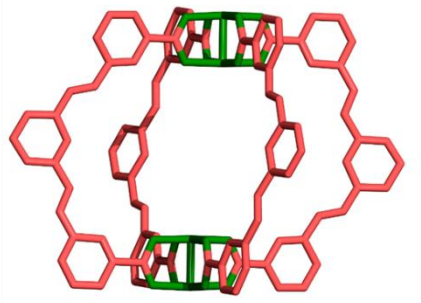

$Rh_4L^{3.2}{}_4$

Chapter 4

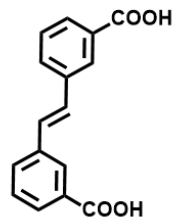

$L^{4.1}$
$L^{5.1}$
$L^{6.1}$

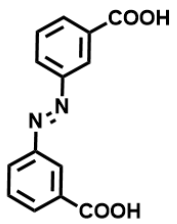

$L^{4.2}$

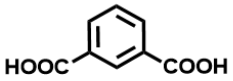

$L^{4.1'}$

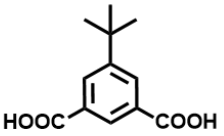

$L^{4.2'}$
$L^{5.1'}$

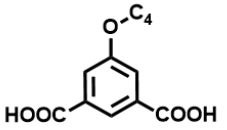

$L^{4.3'}$

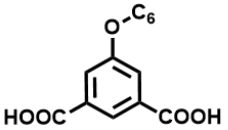

$L^{4.4'}$

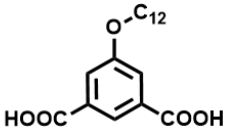

$L^{4.5'}$

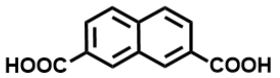

$L^{4.6'}$

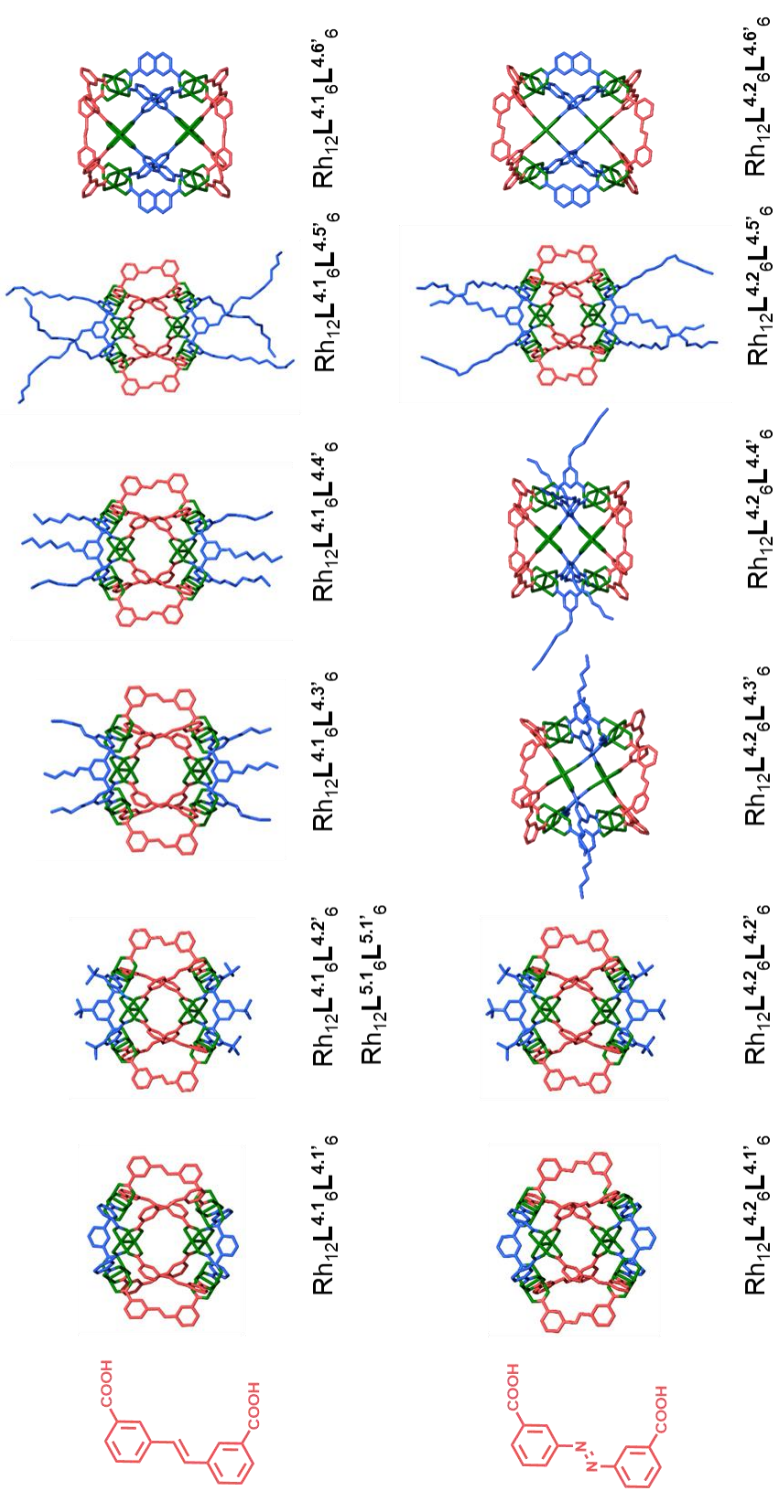
COOH
COOH
$Rh_{12}L^{4.1}{}_6L^{4.1'}{}_6$
$Rh_{12}L^{4.1}{}_6L^{4.2'}{}_6$
$Rh_{12}L^{5.1}{}_6L^{5.1'}{}_6$
$Rh_{12}L^{4.1}{}_6L^{4.3'}{}_6$
$Rh_{12}L^{4.1}{}_6L^{4.4'}{}_6$
$Rh_{12}L^{4.1}{}_6L^{4.5'}{}_6$
$Rh_{12}L^{4.1}{}_6L^{4.6'}{}_6$
COOH
COOH
$Rh_{12}L^{4.2}{}_6L^{4.1'}{}_6$
$Rh_{12}L^{4.2}{}_6L^{4.2'}{}_6$
$Rh_{12}L^{4.2}{}_6L^{4.3'}{}_6$
$Rh_{12}L^{4.2}{}_6L^{4.4'}{}_6$
$Rh_{12}L^{4.2}{}_6L^{4.5'}{}_6$
$Rh_{12}L^{4.2}{}_6L^{4.6'}{}_6$

Chapter 6

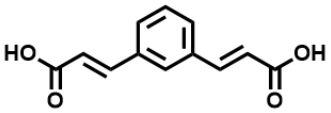

$L^{6.1'}$

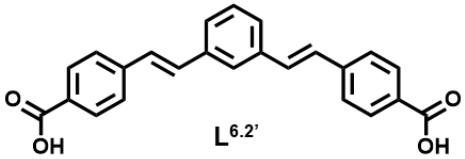

$L^{6.2'}$

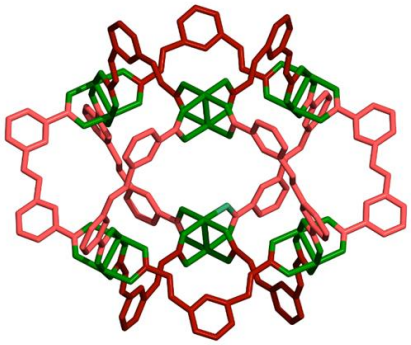

$Rh_{12}L^{6.1}{}_6L^{6.1'}{}_6$

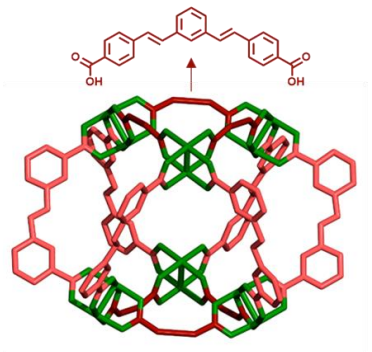

$Rh_{12}L^{6.1}{}_6L^{6.2'}{}_6$

Annex 2

List of Publications

List of Publications

The publications related to the main objectives of this PhD Thesis are listed below:

1. **Anna Broto-Ribas**,[§] Yunhui Yang,[§] Borja Ortín-Rubio,[§] Inhar Imaz, Felipe Gándara, Arnau Carné-Sánchez, Vincent Guillerm, Sergio Jurado, Félix Busqué, Judith Juanhuix, Daniel Maspoch. Clip-off Chemistry: Synthesis by Programmed Disassembly of Reticular Materials. *Angew. Chem., Int. Ed.* **2022**, 61, e202111228.

2. **Anna Broto-Ribas**, María Susana Gutiérrez, Inhar Imaz, Arnau Carné-Sánchez, Felipe Gándara, Judith Juanhuix, Daniel Maspoch. Synthesis of the Two Isomers of Heteroleptic $Rh_{12}L_6L'_6$ Metal-Organic Polyhedra by Screening of Complementary Linkers. *Chem. Commun.*, **2022**, 58, 10480–10483.

3. ***Anna Broto-Ribas***,[§] *Sara Ruiz-Relaño,*[§] *Jorge Albalad, Yunhui Yang, Felipe Gándara, Judith Juanhuix, Inhar Imaz, Daniel Maspoch. Retrosynthetic analysis applied to Clip-off Chemistry: synthesis of four Rh(II)-based complexes as proof-of-concept* ***(to be submitted)***

The author of this Thesis also contributed to the following publications:

4. Snezana Reljic, **Anna Broto-Ribas**, Carlos Cuadrado-Collados, Erika O. Jardim, Daniel Maspoch, Inhar Imaz, Joaquin Silvestre-Albero. Structural Deterioration of Well-Faceted MOFs upon H_2S Exposure and Its Effect in the Adsorption Performance. *Chem. Eur. J.* **2020**, 26, 17110 –17119.

5. **Anna Broto-Ribas**,[§] Claudia Vignatti,[§] Alicia Jimenez-Almarza, Javier Luis-Barrera, Zahra Dolatkhah, Felipe Gándara, Inhar Imaz, Rubén Mas-Ballesté, José Alemán, Daniel Maspoch. Heterogeneous catalysts with programmable topologies generated by reticulation of organocatalysts into metal-organic frameworks: The case of squaramide. *Nano Res.* **2021**, 14(2), 458–465.

[§] These authors contributed equally to this work.